Modelling IL-2 binding dynamics within and between T cell populations



Siting Miao
Linacre College
University of Oxford

A thesis submitted for the degree of
Doctor of Philosophy

Hilary 2026

Acknowledgements

I would like to express my sincere gratitude to my academic supervisors at Oxford, Eamonn Gaffney and Helen Byrne, and to my industrial supervisors at GSK, James Yates, Adam Nasim and Joey Leung, for their continuous support and thoughtful guidance; it has been a pleasure working with them throughout this project.

I am deeply grateful to my parents and grandmother for their enduring love during this journey, as always.

My heartfelt thanks also go to my friends in Oxford, who made my Oxford experience unique and truly memorable.

I owe my deepest thanks to my partner for his constant support and unshakable faith in me across the distance.

Abstract

The cytokine interleukin-2 (IL-2) is central to T-cell biology. Produced primarily by activated helper and cytotoxic T cells, it drives the proliferation of effector T, B and natural killer cells that promote immunity, yet simultaneously expands regulatory T cells that mediate immune tolerance. This dual capacity has sparked interest in generating different formulations of IL-2 such as IL-2/mAb immunocytokines and IL-2 mutants that preferentially stimulate particular types of T cells. In this thesis, we use mathematical approaches to increase understanding of how IL-2 mediates interactions within and between different types of T cells according to the density of different membrane based IL-2 receptors. In turn, this is important for the rational development of a range of immune-modulatory therapeutics.

We develop a series of mathematical models that could be used to test the efficacy of therapeutics that alter extracellular IL-2 levels or other factors, for example the binding rate constants, to preferentially stimulate certain types of T cells. Our study establishes practical criteria for deciding when a well-mixed ODE model can accurately approximate a spatially resolved model of IL-2 binding to α chains on a single T cell. By pinpointing model parameters that have the strongest influence on regulating the IL-2 competition between effector and regulatory T cells and highlighting the largest data gaps, this work provides a mechanistic basis for steering immune responses - towards immunoactivation in cancer and chronic infection or towards immunosuppression in autoimmunity and transplantation. It further proposes potential experiments that would support model predictions and refinement.

Contents

1 Introduction **1**

1.1 Biological background 1

1.1.1 The role of IL-2 1

1.1.2 Immune response or tolerance 3

1.1.3 Source of IL-2 4

1.1.4 IL-2 receptors and downstream signalling pathways 5

1.1.5 IL-2-based therapies 7

1.1.5.1 Low- and high-dose therapies 7

1.1.5.2 Engineered IL-2 therapeutics 7

1.2 Existing models 9

1.3 Mathematical techniques 11

1.3.1 Structural identifiability by GenSSI 2.0 11

1.3.2 Global sensitivity analysis 14

1.3.2.1 Extended Fourier Amplitude Sensitivity Test (eFAST) 15

1.3.2.2 The Sobol' method 15

1.4 Motivation, research aims and modelling scope 16

1.5 Thesis outline 17

2 Spatial PDE model of IL-2 binding to α chains **19**

2.1 Introduction 19

2.2 Model development 20

2.2.1 Dimensional 1D Model 20

2.2.2 Data available in literature and separation of time-scales . . . 22

2.2.3 Non-dimensionalisation 26

2.3 Analysis 27

2.3.1 Steady state analysis of the spatial model 27

2.4 Numerical simulations and global sensitivity analysis for the PDE model 29

2.4.1 Numerical simulations from the 1D PDE model varying R, S, C 29

2.4.2 Extended Fourier amplitude sensitivity testing (eFAST) 32
2.4.3 Sobol sensitivity analysis 33
2.4.3.1 Time-dependent Sobol sensitivity analysis 35
2.4.3.2 Sobol sensitivity analysis for the steady state solutions 35
2.5 Discussion 38

3 Simpler ODE models of IL-2 binding to α chains 40
3.1 Introduction 40
3.2 Quasi-steady state model 41
3.2.1 Model development 41
3.2.2 Structural identifiability analysis of the quasi-steady state model 44
3.2.3 Practical identifiability analysis of the quasi-steady state model 46
3.2.4 Parameter estimation of the quasi-steady state model by fitting to data generated by the 1D PDE model 51
3.3 Phenomenological ODE model 54
3.3.1 Model development 54
3.3.2 Analysis for the phenomenological ODE model 57
3.3.2.1 Steady state analysis for the phenomenological ODE model 57
3.3.2.2 Estimating $\hat{P}$ in the phenomenological ODE model . 58
3.3.2.3 Linearizing the phenomenological ODE model 59
3.3.3 Structural identifiability analysis of the phenomenological ODE model 60
3.3.3.1 Scaling invariance method 60
3.3.3.2 Generating series method by GenSSI 2.0 62
3.3.4 Practical identifiability analysis of the phenomenological ODE model 64
3.3.5 Parameter estimation 67
3.3.5.1 Matching steady states for the 1D PDE model and the phenomenological ODE model 67
3.3.5.2 Least squares estimation for the phenomenological ODE model using data generated by the 1D PDE model . 69
3.4 Comparison of the ODE models to the PDE model 72
3.5 Discussion 75

4 1D PDE model with α, β, γ chains **79**
4.1 Introduction . . . 79
4.2 Model development . . . 80
4.2.1 Dimensional model . . . 80
4.2.2 Non-dimensionalisation . . . 84
4.2.3 Model parametrization . . . 86
4.3 Preferential stimulation of IL-2 . . . 90
4.3.1 Preferential stimulation of different types of T cells with varying levels of IL-2 . . . 90
4.3.2 Effect of varying $\hat{G}_\beta$ and R across the range of S . . . 93
4.3.3 Results with different assumptions for the binding kinetics . . . 95
4.4 Global sensitivity analysis for the 1D PDE model with full binding kinetics . . . 97
4.5 Discussion . . . 103

5 Competition between T cell populations **106**
5.1 Introduction . . . 106
5.2 Models with only α chain . . . 107
5.2.1 Model formulation . . . 108
5.3 Model with full binding kinetics . . . 115
5.3.1 Model development . . . 115
5.3.2 Steady-state behaviour under parameter variation . . . 121
5.3.3 Global sensitivity analysis . . . 125
5.4 Discussion . . . 130

6 Discussion **132**
6.1 Summary of results . . . 132
6.2 Novelty and contributions . . . 134
6.3 Limitations and future work . . . 136

Bibliography **142**

Chapter 1

Introduction

The Introduction places the thesis within its biological and modelling context, articulates the research questions, and previews the methodological approach and structure that follow. Section 1.1 reviews the biological background of IL-2 binding dynamics, including its role in immunity and tolerance, sources of IL-2, receptor architecture and downstream signalling pathways, and therapeutic applications (low/high-dose regimens and engineered variants). Section 1.2 surveys existing mathematical models of IL-2 signalling dynamics. Section 1.3 describes the mathematical techniques used, introducing structural identifiability analysis by GenSSI 2.0 and variance-based global sensitivity analysis, with brief overviews of the eFAST and Sobol' methods. Section 1.4 states the motivation, research aims and modelling scope of the thesis and delineates the specific questions the thesis addresses. Section 1.5 provides an outline of the remainder of the thesis.

1.1 Biological background

1.1.1 The role of IL-2

The vertebrate immune system protects the host through two cooperating arms [61]. Innate immunity provides rapid, non-specific defence via phagocytes, natural-killer (NK) cells and soluble factors such as complement proteins. Adaptive immunity adds precision and memory through antigen-specific T and B lymphocytes.

Within the adaptive arm, T cell classification is often simplified with three main groups: helper, cytotoxic and regulatory T cells (see Table 1.1) [48].

T-cell subset	Marker	Principal function
Helper T cells (Th)	$CD4^+$	Orchestrate immune responses via cytokine secretion
Cytotoxic T cells (CTL)	$CD8^+$	Destroy virus-infected or malignant cells
Regulatory T cells (Treg)	$CD4^+FoxP3^+$	Restrain excessive or autoreactive immunity

Table 1.1: Major T-cell subsets and their principal functions.

All T-cell subsets depend on tightly regulated growth-factor signalling to balance population expansion and contraction during an immune response [97]. Key mediators of this signalling are cytokines - small, secreted proteins that enable immune cells to communicate and coordinate their behaviour.

The cytokine interleukin-2 (IL-2) is central to T-cell biology. IL-2 is produced primarily by activated helper and cytotoxic T cells (effector T cells). It promotes their proliferation and that of other cells, including B and NK cells [9, 50]. Thus, IL-2 has been used as a growth factor for effector T cells in cancer and immune-deficiencies induced by HIV, a human retrovirus that infects $CD4^+$ T cells, gradually weakening the immune system and leading to acquired immunodeficiency syndrome (AIDS) [66]. However, it also promotes the proliferation of regulatory T cells, which suppress the function of effector T cells and mediate immune tolerance. The complementary effects of IL-2 have stimulated interest in selectively activating regulatory (or effector) T cells to suppress (or promote) immune response by generating different formulations such as IL-2/mAb immunocytokines and IL-2 mutants that preferentially stimulate particular types of T cell [3]. When treating cancer or immune-deficiencies induced by HIV, we aim to preferentially stimulate effector T cells; while for autoimmune diseases such as multiple sclerosis that damage nerve myelin, we want to preferentially stimulate regulatory T cells. For the rational development of a range of immune-modulatory therapeutics, it is important to understand how IL-2 mediates interactions between different types of T cells. The aims of this thesis are to develop a mathematical modelling framework that describes IL-2 binding dynamics within and between T cell populations and to show how it can be used to increase understanding of dose-dependent preferential stimulation of T cell subsets and to inform the design principles for therapies that can manipulate this balance.

1.1.2 Immune response or tolerance

Competition between effector (Teffs) and regulatory T cells (Tregs) is central to the ability of the immune system to mount effective but proportionate and time-limited responses to pathogens while maintaining tolerance to self-antigens (endogenous host molecules) [28]. Effector T cells, including activated CD4+ helper T cells and CD8+ cytotoxic T cells, are critical for orchestrating immune responses. Upon antigen recognition, effector T cells rapidly proliferate and diversify into functional subsets, such as T helper type 1 (Th1) and T helper type 2 (Th2), that secrete signature cytokines (for example, IFN-γ is secreted by Th1 cells) [73]. These cytokines amplify inflammation, enhance the activity of other immune cells, and recruit additional leukocytes (white blood cells) to the infection site, while cytotoxic T cells eliminate infected or malignant cells [67]. Collectively, these actions heighten the inflammatory response needed for effective pathogen clearance. Memory T cells form following the resolution of acute infections, and contribute to long-term immune protection [90].

On the other hand, regulatory T cells play a critical role in maintaining immune homeostasis and preventing autoimmunity by exerting suppressive effects on effector T cells and other immune cells [84]. For example, they produce anti-inflammatory cytokines (including IL-10 and TGF-β), which inhibit the activation of effector T cells. They also form contact-dependent inhibitory synapses with dendritic cells or effector T cells through checkpoint molecules such as CTLA-4, LAG-3, and PD-1, which outcompete or remove the corresponding costimulatory ligands and transmit rapid suppressive signals [35, 54, 87, 93]. In healthy conditions, regulatory T cells ensure tolerance to self-antigens while allowing a robust response to foreign pathogens, highlighting their role in balancing immune reactivity and tolerance.

Interleukin-2 (IL-2) plays a central role in the immune system by promoting effector T cell responses while sustaining regulatory T cell-mediated immune tolerance [9]. IL-2 is essential for the activation, proliferation, and differentiation of effector T cells. Following antigen recognition, CD4+ and CD8+ T cells secrete IL-2, which acts in an autocrine and paracrine manner to drive clonal expansion of these cells and enhance cytotoxic activity of cytotoxic T cells. In CD8+ T cells, IL-2 drives a robust primary (first-exposure) response and promotes the formation and persistence of long-lived memory cells. Similarly, IL-2 signalling in CD4+ T cells supports the differentiation of distinct helper subsets (such as Th1 and Th2), which perform diverse functions that contribute to pathogen clearance. IL-2 is also important for the generation, maintenance, and function of regulatory T cells, although they do not secrete IL-2. These cells are characterized by the expression of the transcription

factor FoxP3 and are crucial for maintaining immune tolerance and preventing autoimmunity. Regulatory T cells actively compete for IL-2, limiting its availability for effector T cells; this interaction establishes a feedback loop that prevents excessive immune activation and prevents autoimmunity [42].

Given its central role in balancing immune activation and tolerance, understanding how IL-2 mediates interactions between different T cell subsets is an attractive target for developing therapeutic approaches in immunology [3]. Increased mechanistic understanding could aid in developing IL-2-based therapies for autoimmune diseases, cancer, and transplant acceptance by modulating T cell dynamics to either bolster effective immunity or enhance tolerance as appropriate.

1.1.3 Source of IL-2

Under homeostasis, CD4+ helper T cells in secondary lymphoid organs, such as the lymph nodes, serve as the primary source of low levels of interleukin-2 (IL-2) [9]. Low levels of IL-2 are crucial for the survival and function of regulatory T cells, which preserve immune tolerance and prevent autoimmune responses. By supporting the maintenance of homeostasis, where existing cells expand to restore normal cell counts after other cells have been depleted, low levels of IL-2 ensure a balanced and responsive T cell repertoire.

Upon immune response, IL-2 is produced rapidly by activated T cells, with CD4+ helper T cells being the most significant contributors, following stimulation of the T-cell receptor (TCR) and the costimulatory CD28 molecule [16]. IL-2 acts in an autocrine manner to support the proliferation and survival of the IL-2-secreting T cells, and in a paracrine manner to stimulate neighboring IL-2 receptor-positive cells, which include other effector T cells and regulatory T cells. IL-2 production by activated T cells is transient and tightly regulated at the transcriptional level [51]. Initially, on activation, effector T cells produce IL-2. However, sustained IL-2 production leads to the expression of transcriptional repressors like Blimp-1 and Aiolos, which reduce the rate of transcription of the IL-2 gene and decrease IL-2 production over time. This negative feedback prevents excessive, prolonged IL-2 expression, which could lead to uncontrolled T cell proliferation and potentially deleterious immune responses. Several other immune cells, including natural killer T (NKT) cells, dendritic cells and mast cells, also produce IL-2 [9].

Regulatory T cells are generally considered poor producers of IL-2, including after activation, and instead rely on external sources of IL-2 for their growth and survival

[3]. This reliance allows them to modulate immune responses without promoting T cell proliferation [2].

1.1.4 IL-2 receptors and downstream signalling pathways

IL-2 mediates its functions by binding to receptors (IL-2Rs) on the membrane of target cells [3, 70]. The building blocks of IL-2 receptors are α, β and γ chains (CD25, CD122 and CD132 respectively). The monomeric IL-2 receptor comprises only the α chain; the dimeric receptor consists of β and γ chains; the trimeric receptor comprises α, β and γ chains (see Figure 1.1).

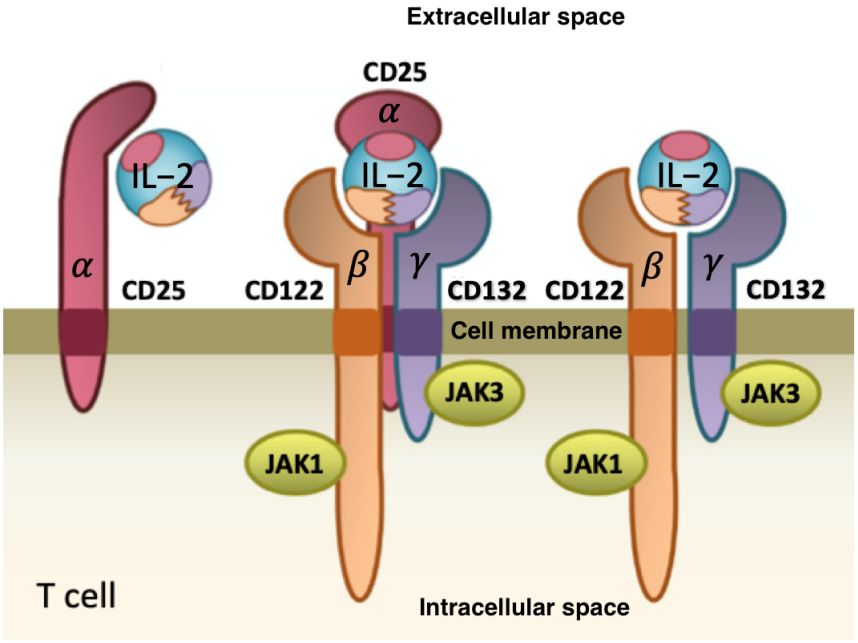


Figure 1.1: IL-2 binds to monomeric, dimeric and/or trimeric receptors on the cell membrane. The trimeric IL-2 receptor consists of α chain (CD25), β chain (CD122) and γ chain (CD132); the dimeric receptor comprises β and γ chains. IL-2 binding to β and γ chains induces heterodimerization of their cytoplasmic tails, activates Janus kinase 1 (JAK1) and Janus kinase 3 (JAK3) and initiates signalling of three downstream pathways (see Figure 1.2) [9, 16, 51]. Adapted from [3], Copyright (2015), with permission from Elsevier.

The dissociation constant K_d quantifies the binding affinity of a ligand and its receptor. For the formation of a ligand-receptor complex

$$\mathrm{L} + \mathrm{R} \underset{k_{\mathrm{off}}}{\overset{k_{\mathrm{on}}}{\rightleftharpoons}} \mathrm{LR},$$

the dissociation constant K_d is defined as $K_d = \frac{[\mathrm{L}][\mathrm{R}]}{[\mathrm{LR}]}$, where [L], [R] and [LR] are the concentrations of the ligand, the receptor and the ligand-receptor complex respectively at equilibrium, and k_{off} and k_{on} are the off and on binding rates. At equilibrium, mass action gives $k_{\mathrm{on}}[\mathrm{L}][\mathrm{R}] = k_{\mathrm{off}}[\mathrm{LR}]$, and hence $K_d = \frac{k_{\mathrm{off}}}{k_{\mathrm{on}}}$. Small K_d values denote strong binding affinity (i.e. a high propensity for association between the ligand and receptor). IL-2 binds to the α chain, with dissociation constant $K_d \sim 10^{-8}$ M [3]. The dimeric receptor is commonly described as low affinity ($K_d \sim 10^{-9}$ M) and the trimeric receptor as high affinity ($K_d \sim 10^{-11}$ M). Downstream signalling is initiated only when IL-2 binds to the β/γ dimer, with the α chain facilitating binding. When IL-2 binds to the trimeric receptor, the quaternary receptor complex (consisting of IL-2, α, β and γ chains) is internalised with a half-life of approximately 15 minutes. Internalised IL-2, β and γ chains undergo vesicular degradation while the α chain is recycled to the cell surface. By contrast the rate of internalisation of IL-2 bound to monomeric and dimeric receptors is very small [24, 96].

Different T cell subsets display distinct patterns of expression for the IL-2 receptor α and β chains [3, 27]. Regulatory T cells are characterized by high levels of α chains, enabling them to form high-affinity trimeric receptor complexes (in combination with β and γ chains) even when ambient IL-2 concentrations are low; this is essential for their survival and suppressive activity. Regulatory T cells express intermediate levels of β chains. In contrast, conventional effector and memory T cells typically express transient or lower levels of α chains upon activation and rely on the constant presence of β and γ chains to mediate IL-2 signalling. We hypothesise that differences in the numbers of α, β and γ chains on regulatory and effector T cells may explain differences in their behaviours when interacting with IL-2. We investigate this hypothesis in Chapters 4 and 5.

IL-2 binding to β and γ chains induces heterodimerization of their cytoplasmic tails, activates Janus kinase 1 (JAK1) and Janus kinase 3 (JAK3) and initiates signalling of three downstream pathways (see Figure 1.2) [9, 16, 51]. First, the Janus kinase (JAK)-signal transducer and activator of transcription (STAT) pathway is activated, leading primarily to STAT5 (signal transducer and activator of transcription 5) phosphorylation; phosphorylated STAT5 dimerizes and migrates to the nucleus where it induces transcription of genes responsible for T cell proliferation, survival, and differentiation. Second, the phosphoinositide 3-kinase (PI3K)-AKT pathway is activated, promoting cell metabolism, survival and the expression of key cell cycle regulators. Finally, the mitogen-activated protein kinase (MAPK) cascade is initiated,

which further contributes to the regulation of genes required for T cell activation and differentiation, adding an additional layer of control to the immune response. Importantly, IL-2 signalling induces the transcription of factor B lymphocyte-induced maturation protein 1 (Blimp1), encoded by the gene Prdm1, which downregulates IL-2 production in effector T cells, thus forming a negative feedback loop. IL-2 signalling also upregulates production of α chains, which promotes the binding and uptake of IL-2 by T cells [3]. This thesis develops mechanistic models of IL-2 diffusion and clearance and its binding dynamics with cell-surface receptors, and does not model downstream signalling pathways and feedback; nonetheless, we describe them here for contextual completeness and to delineate a natural extension of the modelling framework that we develop.

1.1.5 IL-2-based therapies

1.1.5.1 Low- and high-dose therapies

Low and high doses of IL-2 have been used to treat certain diseases [3, 25]. Low-dose IL-2 is used to treat autoimmune and chronic inflammatory diseases because low doses of IL-2 primarily activate regulatory T cells. High doses of IL-2 stimulate and enhance the activity of effector T cells and natural killer (NK) cells, and are thus used to treat metastatic cancer and immune deficiencies, including chronic HIV and other viral infections [21, 43].

However, both low- and high-dose IL-2 therapies present challenges [72]. High-dose IL-2 can also stimulate regulatory T cells, which suppress immune responses. Significant adverse effects associated with high doses of IL-2 (such as vascular leak syndrome, characterized by leakage of fluid and proteins from blood vessels into surrounding tissues) have limited its effectiveness in cancer treatment. Low-dose IL-2 therapies may stimulate effector T cells and NK cells in addition to regulatory T cells, thereby reducing selectivity and potentially undermining the intended tolerogenic effect. These limitations have motivated ongoing efforts to develop improved IL-2-based therapies that offer greater selectivity for certain types of T cells [3].

1.1.5.2 Engineered IL-2 therapeutics

IL-2 based therapies have undergone extensive re-engineering over the past decade to overcome the limitations of native IL-2, such as its short half-life and non-selective activation of immune cells (notably the undesired expansion of regulatory T cells) [3].

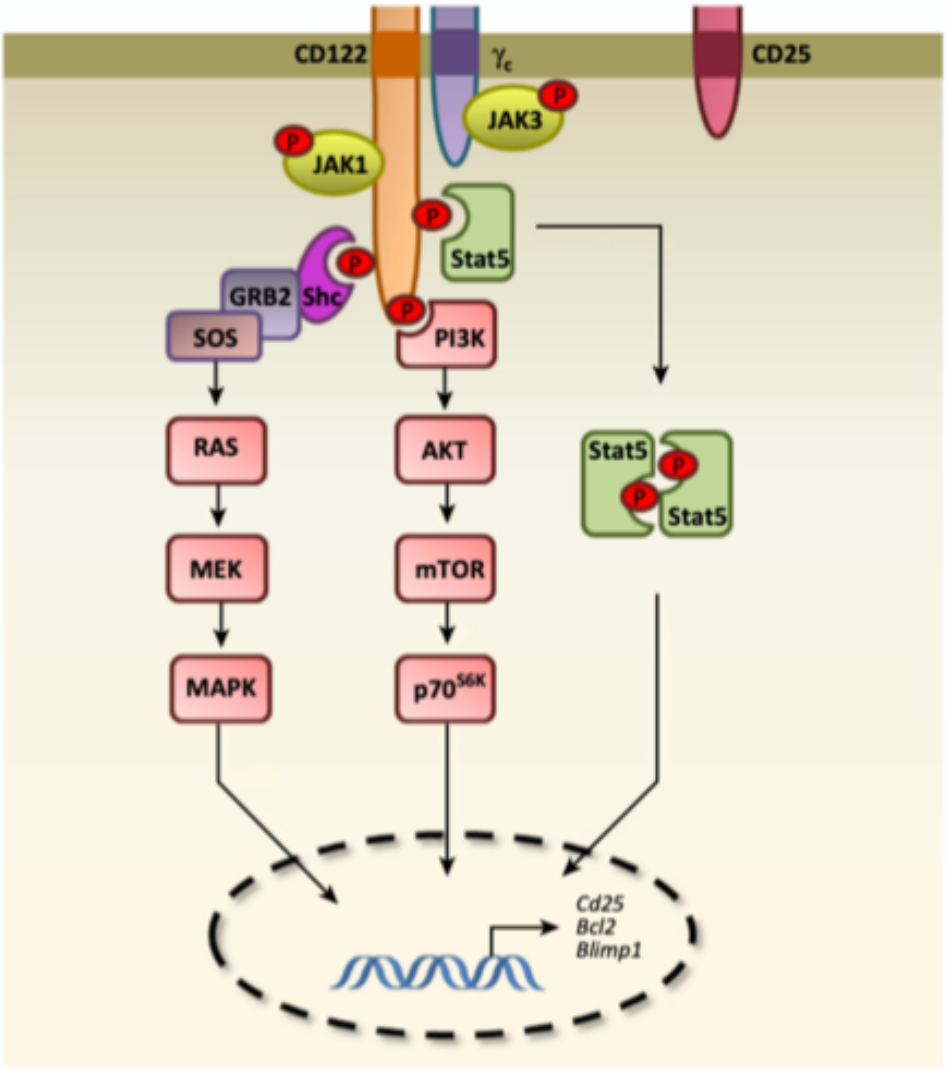


Figure 1.2: The subcellular IL-2 signalling pathways. There are three major signalling pathways: mitogen-activated protein kinase (MAPK), phosphoinositide 3-kinase (PI3K)-AKT and Janus kinase (JAK)-signal transducer and activator of transcription (STAT). Refer to the main text in Section 1.1.4 for detailed description of the signalling pathways. P $\equiv$ phosphorylated. IL-2 signalling induces the transcription of α chains (CD25s), B-cell lymphoma 2 (Bcl2) and B lymphocyte-induced maturation protein 1 (Blimp1). Bcl2 prevents programmed cell death (apoptosis). Blimp1 downregulates IL-2 production. Reprinted from [3], Copyright (2015), with permission from Elsevier.

By modifying the specific molecular properties of IL-2, next-generation therapies aim to bias receptor engagement, extend retention time and reduce systemic toxicities.

One major strategy involves re-engineering the receptor binding specificity of IL-

2. Early work by Levin et al. [47] introduced IL-2 "superkines" that show enhanced binding to dimeric IL-2 receptors while reducing dependency on α chains, thus favoring the activation of effector T cells over regulatory T cells. Additionally, Spangler et al. [86] demonstrated that binding of specific antibodies to IL-2 could induce conformational changes that modulate IL-2 engagement with its receptor subunits, selectively enhancing desired T cell subsets. Other designs, such as fusion proteins that combine IL-2 with decoy or engineered receptor domains [65] and multivalent IL-2-Fc fusions [68], illustrate how modifications in receptor-binding surfaces can redirect cytokine activity toward effector cell expansion or regulatory cell bias, depending on therapeutic goals.

Beyond receptor specificity, extending the half-life and improving the pharmacokinetic profile of IL-2 are vital. The native cytokine is rapidly cleared, necessitating high or frequent dosing, which exacerbates toxicity. Approaches such as PEGylation, Fc-fusion, and conjugation with long-acting carriers have been employed to increase persistence in vivo. Rosen et al. [74] describe a TransCon IL-2 β/γ prodrug that achieves sustained release and preferential expansion of effector lymphocytes through strategic modifications that also minimize the affinity of IL-2 for the α chain. Furthermore, engineered fusion proteins reviewed by Overwijk et al. [69] harness half-life extension domains to balance efficacy with reduced systemic exposure.

Another innovative approach has been the development of conditionally active or "masked" IL-2 molecules that are selectively activated in the tumor microenvironment. For instance, Quijano-Rubio et al. [71] designed a split, conditionally active IL-2 mimetic that minimizes systemic activation by remaining inactive until it encounters specific proteolytic conditions or receptor environments in the target tissue. Similarly, Hsu et al. [33] developed cytokine receptor-masked IL-2 prodrugs that are activated upon binding to tumor-infiltrating lymphocytes. These strategies aim to confine IL-2 activity spatially and temporally, reducing off-target effects while maximizing local immunostimulation.

1.2 Existing models

Mathematical models have played an important role in elucidating how IL-2 mediates interactions within and between different types of T cells.

One class of models focus on the initial binding of IL-2 to its receptors. In [70], a well-mixed mass-action ordinary differential equation (ODE) model that explicitly tracks the γ chain was developed. It was shown that γ chain abundance modulates

both the apparent IL-2 binding affinity and the signalling capacity. In this thesis, our focus is on how ligand supply, geometry, and α/β chain availability shape subset responses; accordingly, we adopt the standard reduction in which β and γ are treated as a pre-formed β/γ dimer with the γ chain assumed non-limiting. This choice reduces dimensionality while preserving the regimes we analyse (e.g., α-controlled sensitivity at low exposure of IL-2 and β-limited capacity at higher exposure). We note, however, that in contexts where γ chain is limiting or competes with other γ chains for shared cytokines (e.g., IL-7, IL-15), the dimer approximation may break down; extending the framework to track γ chains explicitly and account for cytokine competition constitutes a natural direction for future work. In [68], an equilibrium multivalent binding model (multivalent binding evaluated at quasi-equilibrium; equivalent to a reduced ODE mass-action scheme) was employed to explain how asymmetric, multivalent IL-2–Fc fusion proteins enhance regulatory T cell selectivity through cell surface interactions.

Another class of models couple receptor engagement to intracellular cascades, most commonly JAK/STAT5, and account for transcriptional feedback (e.g., α chain upregulation and IL-2 production) and fate outputs (proliferation/survival) [11, 31, 45, 95]. Joint modelling-experiment studies established how competing positive/negative feedbacks shape responses and subset asymmetries, providing a map from receptor occupancy to function. Many such models assume simplified binding kinetics [27, 45, 95]. For example, in [27], IL-2 binding to β chains was not considered; in [95], the binding between [IL-2 : β] complexes and free α chains was neglected. In [27], single-cell experiments were combined with a well-mixed mass-action ODE model of IL-2 receptor engagement and consumption to explain how heterogeneous expression of α and β chains shapes population responses. They showed that variability in receptor levels creates significant single-cell differences in IL-2 capture and pSTAT5 signalling. Further, at the population level, regulatory and effector T cells engage in a "tug-of-war" for IL-2: regulatory T cells deplete IL-2 and upregulate α chains, selectively suppressing weakly activated effector T cells while sparing strongly activated ones; early exogenous IL-2 further biases this suppression. The key insight is a mechanistic, quantitative link from receptor stoichiometry to collective outcomes. They established when IL-2 depletion by regulatory T cells is sufficient to curtail effector survival and proliferation and provided testable predictions for manipulating regulatory T cell suppression in vitro and in vivo. In [45], an ODE model was developed to investigate how interactions between helper, memory, regulatory T cells and IL-2 impact their

dynamics. Competition for IL-2 between effector and regulatory T cells was studied in [31].

While many studies employ ODE-based frameworks to describe the temporal dynamics of receptor activation and intracellular response, there is growing interest in incorporating spatial effects using partial differential equations (PDEs) because cytokine transport is spatially structured: diffusion, consumption, and cell-surface capture generate pericellular gradients that shape receptor occupancy, autocrine versus paracrine reach, and intercellular competition - phenomena that well-mixed ODEs may not be able to represent. In [11], a reaction-diffusion PDE model that describes the initial binding of IL-2 to α chains between a single helper T cell and a single regulatory T cell was developed to study how competing extracellular feedback loops between helper and regulatory T cells shape the IL-2 signal and affect immune homeostasis. They showed that IL-2-driven α chain up-regulation created a digital (on/off) switch for helper T cell proliferation, whereas it acts as an analog amplifier that increases IL-2 uptake capacity of regulatory T cells. A parameter-space diagram in cell-cell distance and IL-2 secretion rate identified conditions under which helper T cell autocrine signalling was sustained and contrasting conditions where it was suppressed by the regulatory T cell, underscoring the role of micro-scale geometry and timing in determining signalling outcomes.

1.3 Mathematical techniques

In this section, we introduce the mathematical techniques applied in the thesis. These techniques are broadly applicable to the analysis of mathematical models in immunology and, more generally, in biology.

1.3.1 Structural identifiability by GenSSI 2.0

For a dynamical system, structural identifiability asks whether unknown model parameters can be inferred uniquely from ideal (noise-free and continuous in time) measurements of its observables [6]. Consider an ODE model with inputs $u(t)$, states $x(t) \in \mathbb{R}^n$, outputs $y(t) \in \mathbb{R}^m$, and unknown parameters $\theta \in \mathbb{R}^p$:

$$\dot{x} = f(x, u, \theta), \qquad y = h(x, \theta), \qquad x(0) = x_0. \tag{1.1}$$

A parameter (or parameter vector) is globally identifiable when the mapping, $(\theta, x_0) \mapsto y(t)$, from the parameter space to noise-free, continuous output trajectories is injective (one-to-one) over the entire domain, ensuring that only a single parameter

set can reproduce the observations; it is locally identifiable when this mapping is injective in a neighbourhood of the true values; conversely, it is structurally non-identifiable when the mapping is not injective. Establishing structural identifiability is important because if this property is not satisfied, practical identifiability studies merely quantify uncertainty around intrinsically ambiguous parameters, and sensitivity analyses rank the influence of interchangeable values, leading to spurious conclusions [4]. Structural identifiability analysis informs experimental design by revealing which additional observables or concurrent experiments will most efficiently resolve parameter ambiguities, thereby directing laboratory resources toward the highest information gain [10].

We use GenSSI 2.0 [52], the updated version of the Generating Series for Testing Structural Identifiability (GenSSI) toolbox [17], to evaluate the structural identifiability of the models. GenSSI 2.0 is an open-source MATLAB toolbox that automates structural identifiability analysis for linear and non-linear ODE models. The toolbox builds on the generating-series framework coupled with identifiability tableaus [4]. It computes successive Lie derivatives of the model outputs along the vector field of the ODE system and uses them to construct a finite algebraic system whose unknowns are the model parameters and initial conditions. This algebraic system is then analysed to assess whether the unknown parameters and initial conditions are globally identifiable, locally identifiable, or potentially non-identifiable from the model outputs. We note that we can only conclude local or global identifiability from GenSSI 2.0 but not non-identifiability, because in theory infinitely many Lie derivatives could be utilised to generate the algebraic system.

Generating-series approach. GenSSI 2.0 implements a generating-series approach [4]. While Equation (1.1) represents a general dynamical system, the generating series method is formally defined for systems that are affine in inputs:

$$\dot{x} = g_0(x,\theta) + \sum_{i=1}^{r} g_i(x,\theta)u_i(t), \qquad y = h(x,\theta), \qquad x(0) = x_0. \tag{1.2}$$

Under analyticity, each output admits a time-series expansion about $t = 0$:

$$y(t) = \sum_{k=0}^{\infty} \frac{c_k(\theta, x_0, u^{(0:k-1)}(0))}{k!}\, t^k.$$

Here $u(t) = (u_1(t), \ldots, u_r(t))$ denotes the input vector, and $u^{(j)}$ denotes the j-th time derivative of the input, $u^{(j)}(t) = \frac{\mathrm{d}^j u}{\mathrm{d}t^j}$. The notation $u^{(0:k-1)}(0)$ represents the collection of these input derivatives up to order $k-1$ evaluated at $t = 0$.

The series coefficients c_k are the output time derivatives at $t = 0$, $c_k = \frac{\mathrm{d}^k}{\mathrm{d}t^k} y(t)\Big|_{t=0}$. They are computed recursively via Lie derivatives of the output map h along the vector fields g_0 and g_i. The Lie derivative of a scalar-valued function h along a vector field g is:

$$L_g h(x, \theta) = \frac{\partial h}{\partial x}(x, \theta)\, g(x, \theta) = \sum_{j=1}^{n} \frac{\partial h}{\partial x_j}(x, \theta)\, g_j(x, \theta).$$

Accordingly, the first two coefficients are given by:

$$c_0 = h(x_0, \theta), \qquad c_1 = \dot{y}(0) = L_{g_0} h(x_0, \theta) + \sum_{i=1}^{r} u_i(0) L_{g_i} h(x_0, \theta).$$

Higher-order coefficients c_k are determined by iteratively differentiating the output, resulting in linear combinations of higher-order Lie derivatives weighted by the inputs and their time derivatives. These coefficients depend algebraically on (θ, x_0) and a finite set of input derivatives evaluated at $t = 0$. Under the structural-identifiability assumption that the outputs are observed continuously in time, the values of the outputs and their successive time derivatives at $t = 0$ are treated as known quantities. The coefficients c_k therefore provide algebraic equations relating these known output-derivative values to the unknown parameters and, when applicable, unknown initial conditions. Collecting the first $K + 1$ coefficients for all m outputs and, if desired, for several experiments with different inputs and/or initial conditions, defines the coefficient map:

$$C(\theta, x_0) = \left(c_0^{(1)}, \ldots, c_K^{(1)},\ \ldots\ ,\ c_0^{(m)}, \ldots, c_K^{(m)}\right)^{\top},$$

which constitutes the algebraic system analysed by GenSSI.

Rank tests and classification. GenSSI 2.0 constructs the Jacobian of the coefficient map with respect to the unknowns $\phi = (\theta, x_0^{\mathrm{u}})$, where x_0^{u} denotes the subset of initial conditions that are unknown:

$$J(\phi) = \frac{\partial C(\phi)}{\partial \phi}.$$

The Jacobian is then evaluated at generic points (symbolically or by randomized numeric evaluation) and the truncation order K is increased until the resulting rank stabilizes. If J has full column rank, all components of ϕ are locally identifiable; a rank deficiency signals non-identifiability or the presence of identifiable combinations. By stacking coefficients from multiple experiments, GenSSI can exploit input

variation to restore identifiability. When feasible, additional algebraic checks distinguish global from local identifiability by verifying that the resulting algebraic system has no residual discrete symmetries - i.e., it admits a unique generic solution for the parameter.

Workflow in practice. The user supplies the symbolic model (f, h), declares unknown parameters and unknown initial conditions, specifies measured outputs and admissible inputs, and optionally defines multiple experiments. GenSSI 2.0 then (i) computes series coefficients up to order K for each experiment, (ii) assembles and analyzes the Jacobian J, (iii) classifies each unknown as globally identifiable, locally identifiable, or non-identifiable. The outcome guides model redesign (e.g. reparameterization, additional outputs) and experimental planning (e.g. input profiles or multi-experiment designs) before quantitative calibration.

1.3.2 Global sensitivity analysis

Global sensitivity analysis quantifies the importance of model parameters and their interactions with model outputs of interest [13, 59, 92]. Among the families of global sensitivity analysis algorithms, variance-based techniques partition the total output variance into proportions attributable to each model input and their interactions. Let $Y = f(\mathbf{X})$ be the model output and $\mathbf{X} = (X_1, \ldots, X_p)$ be the independent model parameters with prescribed distributions. The total variance $\mathrm{Var}(Y)$ admits an ANOVA/HDMR decomposition into main effects and interactions. Two indices are reported:

$$S_i \;=\; \frac{\mathrm{Var}\big(\mathbb{E}[\,Y \mid X_i\,]\big)}{\mathrm{Var}(Y)} \qquad \text{and} \qquad S_{T_i} \;=\; 1 - \frac{\mathrm{Var}\big(\mathbb{E}[\,Y \mid \mathbf{X}_{\sim i}\,]\big)}{\mathrm{Var}(Y)}\,,$$

where S_i (first-order sensitivity index) measures the isolated effect of X_i, and S_{T_i} (total-order sensitivity index) measures the effect of X_i including all its interactions. Higher values of the sensitivity indexes indicate parameters that have a greater effect on the quantities of interest. Comparing S_i and S_{T_i} indicates whether X_i acts mainly additively ($S_i \approx S_{T_i}$) or through interactions ($S_{T_i} \gg S_i$). In this project, we use two variance-based methods: extended Fourier Amplitude Sensitivity Test (eFAST) and Sobol' sensitivity analysis.

1.3.2.1 Extended Fourier Amplitude Sensitivity Test (eFAST)

eFAST estimates S_i and S_{T_i} by sampling along sinusoidal trajectories and analysing the Fourier spectrum of the resulting output signal [20, 59, 80]. Each parameter X_i is assigned a unique angular frequency ω_i. A one-dimensional path $s \mapsto \mathbf{X}(s)$ is then constructed by transforming phase-shifted sinusoidal functions through the inverse cumulative distribution function of each parameter, so that the resulting samples follow the prescribed marginal distributions. Evaluating $Y(s_k)$ on a uniform grid s_k yields a discrete signal. Its discrete Fourier transform exhibits peaks at ω_i (and harmonics); the normalised spectral power at ω_i estimates the first-order contribution S_i. Total-order indices S_{T_i} are obtained by allocating complementary frequency bands to the combined effects of all factors other than X_i, and then computing the associated normalised spectral power. Multiple phase shifts and replicate trajectories reduce aliasing and provide uncertainty for S_i and S_{T_i}.

In eFAST, a dummy parameter that does not appear in the system is included for benchmarking [59]. The dummy parameter is introduced as an artificial input in the sampling design and assigned its own frequency, phase, and inverse cumulative distribution mapping, while the model outputs are strictly independent of this variable. Since its true first and total order sensitivity indices are zero, the estimated indices associated with the dummy parameter quantify the background noise floor in the sensitivity-index estimates arising from finite sampling, numerical noise, and spectral aliasing. Consequently, the dummy parameter provides a significance benchmark: parameters whose S_i or S_{T_i} are less than the corresponding dummy indices can be regarded as possessing negligible sensitivity when the dummy indices are small. In contrast, inflated values of the dummy indices indicate inadequate sample size, suboptimal frequency allocation, or other deficiencies in the design and motivate increasing trajectory length, adding phase shifts and replicates, or revising the frequency set.

1.3.2.2 The Sobol' method

The Sobol' method estimates the same indices as eFAST but uses low-discrepancy sampling and Monte Carlo estimators derived from the ANOVA decomposition [38, 78, 85]. Two independent $N \times p$ sampling matrices A and B are constructed using independent Monte Carlo or Sobol' low-discrepancy (quasi-MC) sequences. For each parameter i, a hybrid matrix $A_B^{(i)}$ is constructed by replacing the i-th column of A with the i-th column of B. After evaluating $f(A)$, $f(B)$ and $f(A_B^{(i)})$, standard estimators

are:

$$\text{(Saltelli first-order)} \quad \widehat{S}_i \;=\; \frac{1}{N\,\widehat{\mathrm{Var}}(Y)} \sum_{j=1}^{N} f(B_j)\left(f\big(A_{B,j}^{(i)}\big) - f(A_j)\right),$$

$$\text{(Jansen total-order)} \quad \widehat{S}_{T_i} \;=\; \frac{1}{2N\,\widehat{\mathrm{Var}}(Y)} \sum_{j=1}^{N} \left(f(A_j) - f\big(A_{B,j}^{(i)}\big)\right)^2,$$

where the sample variance $\widehat{\mathrm{Var}}(Y)$ is estimated from $f(A)$ and $f(B)$. This design requires $(2+p)N$ model evaluations; bootstrap resampling of the N replicates provides confidence intervals and convergence checks [79].

Using both eFAST and Sobol' method provides a cross-check: eFAST is sample-efficient and robust for first-order structure via spectral separation, while Sobol' offers transparent Monte-Carlo estimators with widely used diagnostics for variance and bias. We implement eFAST in MATLAB with algorithm developed by [59]. We implement Sobol' sensitivity analysis in MATLAB using the software tool GSAT [13].

1.4 Motivation, research aims and modelling scope

Most existing models of IL-2 signalling are formulated as time-dependent ODEs, which assume that the concentration of IL-2 in the extracellular space is spatially uniform. Consequently, the potential influence of bulk spatial heterogeneity remains largely unexplored. Additionally, existing models make varying assumptions about the assembly mechanism of the quaternary complex (IL-2 bound to α, β and γ chains) [27, 45, 95]. The neglect of spatial dynamics and the varying assumptions regarding binding mechanisms highlight a gap in the current theoretical understanding of IL-2 capture.

Clinically, the limitations of low-dose and high-dose IL-2 therapies have motivated ongoing efforts to develop improved IL-2-based therapies that offer greater selectivity for certain type of T cells. This raises the important question of which factors, for example the kinetic rate constants associated with binding, should be targeted to achieve this goal. This question has not been the focus of mathematical modelling studies in this area.

The primary aim of this thesis is to use mathematical modelling to bridge these gaps and to increase mechanistic understanding of how IL-2 interacts with different types of T cells. The modelling framework is intended primarily as a mechanistic

tool that can be parameterised and tested against data from a range of experimental and physiological contexts, including controlled in vitro or ex vivo settings, and in vivo-motivated microenvironments. While the models are not constructed as patient-specific clinical predictors, the mechanisms they capture are chosen to be sufficiently general to inform interpretation of in vivo phenomena and to support the rational design of IL-2-based therapies by identifying qualitative regimes and intervention points that may translate across contexts.

To implement this aim, we parametrize the framework using parameter values and ranges drawn from the available literature, with an emphasis on data from controlled in vitro human T-cell experiments. To ensure physiological plausibility of transport and clearance, we also use complementary in vivo/tissue-based measurements where appropriate. It is important to note that this hybrid parameterisation is designed to represent the dynamics of a local microenvironment, analogous to continuous in vitro perfusion systems or active tissue niches, rather than closed batch systems. This approach allows us to investigate how T cells behave under homeostatic conditions, where constant IL-2 supply is balanced by cellular consumption and environmental decay. These choices define a concrete baseline scenario for our analyses while leaving the framework adaptable to other species, tissues and experimental designs. Accordingly, we consider IL-2 dynamics at two organisational scales: (i) the individual cell scale, modelling IL-2 diffusion and receptor-binding kinetics in the pericellular environment; and (ii) the population scale, modelling how different types of T cells compete for IL-2 in a shared extracellular milieu.

1.5 Thesis outline

The remainder of this thesis is organised as follows. Chapters 2, 3, 4 and 5 are the research chapters. In Chapters 2, 3 and 4, we develop single-cell models of how IL-2 binds to its receptors. In Chapter 5, we extend this work by constructing a model for IL-2 competition between well-mixed populations of effector and regulatory T cells. The thesis concludes in Chapter 6 where we discuss our results.

In Chapter 2, we develop and analyse a 1D, radially symmetric spatial PDE model capturing the initial binding of IL-2 to α chains on the membrane of a single T cell. We examine the importance of bulk spatial effects (spatial heterogeneity of IL-2 and its changes with cell density) and identify those model features, including IL-2 levels, the availability of α chains and cell density, that dominate the temporal dynamics and steady state levels of IL-2 bound to α chains.

The focus of Chapter 3 is to determine whether simpler ODE models can accurately describe the behaviour of spatially resolved PDE models of IL-2 binding to α chains. We develop and analyse two distinct ODE models, a quasi-steady state model based on the PDE model from Chapter 2 (assuming the concentration of IL-2 is at its quasi-steady state) and a phenomenological model. We identify conditions under which the ODE models can (and cannot) describe the steady-state behaviour and system dynamics of the PDE model introduced in Chapter 2.

In Chapter 4, we extend the binding kinetics in the 1D PDE model from Chapter 2 to account for β and γ chains. We use this model to investigate how different types of T cells respond to different levels of IL-2, noting how the availability of α and β chains varies between different types of T cells. To examine the effects of eliminating the possibility of IL-2 binding to β chains or the possibility of IL-2β complex and α chain binding, we compare steady-state solutions of the signalling complexes for the simplified models to those for the full PDE model. To highlight critical parameters for experimental measurement and identify potential targets for intervention, we use global sensitivity analysis to identify the parameters that have the most significant effect on the levels of signalling complexes formed by different types of T cells.

In Chapter 5, we introduce a spatially well-mixed mathematical model which we use to investigate how competition affects the response of a heterogeneous population of T cells to stimulation with IL-2. We use this model to examine how different factors, including IL-2 concentration, the availability of α and β chains and kinetic rate constants of binding, skew stimulation towards one subset.

In Chapter 6, we discuss our results, explain how they relate to the original thesis aims, discuss their relationship to the existing literature, and identify directions for future work.

Chapter 2

Spatial PDE model of IL-2 binding to α chains

2.1 Introduction

The α chain binds IL-2 with low affinity when it is not part of the full receptor complex. However, this initial interaction is crucial for capturing IL-2 molecules and is the first step toward forming the high-affinity receptor complex with β and γ chains. Understanding this initial step is essential for comprehending how IL-2 signalling is initiated. The primary aim of this chapter is to develop a mathematical framework to investigate the interplay between extracellular IL-2 diffusion and initial binding of IL-2 to α chains. To achieve this, we develop a 1D, radially-symmetric model that captures binding of IL-2 to α chains on the surface of a generic T cell. The model describes the spatial distribution of IL-2 in the extracellular space, while the membrane receptor species (α chains and complexes formed by IL-2 binding to α chains) are treated as uniformly distributed over the cell surface and represented by surface-averaged concentrations. Specifically, this chapter addresses two key research questions: (i) the extent to which the effective cell density, represented by varying domain sizes, influences the availability and spatial heterogeneity of extracellular IL-2; and (ii) the identification of those parameters that have the greatest influence on the efficiency of IL-2 capture. To this end, we analyse our model using a variety of mathematical techniques including steady states analysis, numerical simulations and global parameter sensitivity analysis via Extended Fourier amplitude sensitivity testing (eFAST) and Sobol sensitivity analysis.

The remainder of the chapter is organised as follows. In Section 2.2, we introduce our spatial PDE model and estimate model parameters using data from the literature. In Section 2.3, we identify and characterise the steady state solutions of the PDE

model. In Section 2.4, we present results from numerical simulations and global parameter sensitivity analysis. The chapter ends in Section 2.5, where we discuss our results and possible directions for future work.

2.2 Model development

2.2.1 Dimensional 1D Model

For simplicity, we consider only α chains and model a single isolated T cell, assuming spherical symmetry of the surrounding cell–environment system; that is, IL-2 concentrations vary only with distance from the cell surface, and any spatial variation along the membrane is not considered. In Figure 2.1, we present a schematic of the radially symmetric geometry that we use. Let the cell membrane be the surface of a sphere with its centre located at the origin of a spherical domain. We work in spherical polar coordinates (r, θ, ϕ); by symmetry, all fields depend only on radial coordinate, r, with units cm and time, t, with units s. The extracellular region is the spherical annulus $\Omega = \{ r : R_{\text{cell}} < r < R_{\text{outer}} \}$, with the membrane at $r = R_{\text{cell}}$ and the outer boundary at $r = R_{\text{outer}}$. We make the following modelling assumptions: IL-2 diffuses and decays in the extracellular space that surrounds the cells; α chains do not move and are uniformly distributed on the cell membrane at $r = R_{\text{cell}}$; IL-2 binds reversibly to α chains, and the resulting complexes remain on the cell membrane. We also neglect receptor internalisation, recycling, and downstream signalling, focusing solely on ligand–receptor binding dynamics.

The dependent variables of the system are $N_L(r, t)$ (the concentration of free IL-2 in the bulk) with unit Number/cm^3, $N_\alpha(t)$ (the concentration of free α chain on the cell membrane) with unit Number/cm^2 and $N_{\alpha L}(t)$ (the concentration of the complex formed by IL-2 and α chain or the occupied α chain) with units Number/cm^2. The dependent variables defined on the cell membrane are t-dependent; only $N_L(r, t)$ varies with position. The physical interpretation and units of the dependent variables and model parameters are summarized in Tables 2.1 and 2.2 respectively. By appealing to mass conservation and using the Law of Mass Action to model the binding kinetics, we arrive at the following equations, which describe the evolution of the dependent variables:

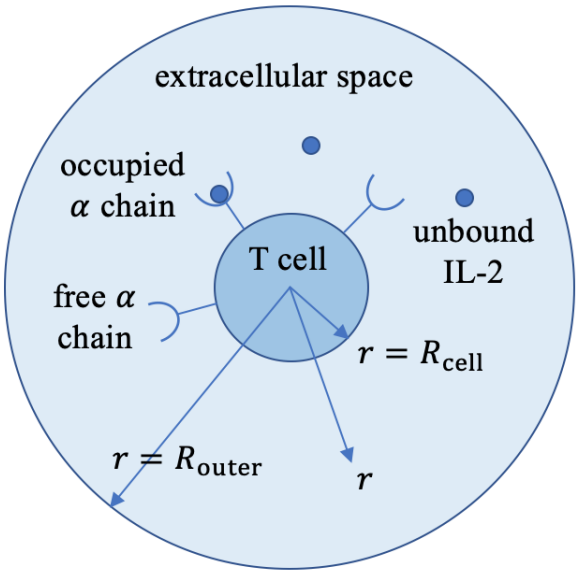


Figure 2.1: Schematic of the model geometry. A spherical T cell of radius R_{cell} is centered at the origin of a larger spherical domain of radius R_{outer}. Free IL-2 molecules diffuse in the extracellular space ($R_{\text{cell}} < r < R_{\text{outer}}$) and interact with receptors located on the cell membrane ($r = R_{\text{cell}}$).

$$\frac{\partial N_L}{\partial t} = D_L \frac{1}{r^2}\frac{\partial}{\partial r}\left(r^2 \frac{\partial N_L}{\partial r}\right) - \Lambda N_L, \tag{2.1}$$

$$\frac{dN_\alpha}{dt} = -\left(k_{\alpha L} N_L\left(R_{\text{cell}}, t\right) N_\alpha - k_{-\alpha L} N_{\alpha L}\right), \tag{2.2}$$

$$\frac{dN_{\alpha L}}{dt} = +\left(k_{\alpha L} N_L\left(R_{\text{cell}}, t\right) N_\alpha - k_{-\alpha L} N_{\alpha L}\right). \tag{2.3}$$

In Equation (2.1), IL-2 diffuses in the extracellular space with diffusion coefficient D_L (unit: cm^2/s), where it also undergoes linear decay with rate Λ (unit: s^{-1}). In Equation (2.2), a free α chain on the cell membrane binds with IL-2 from the bulk. R_{cell} is the radius of the cell (units: cm). Similarly in Equation (2.3), a complex forms when IL-2 binds to a free α chain on the cell membrane.

We close Equations (2.1)–(2.3) by imposing the following boundary and initial conditions. For the boundary conditions, with R_{outer} being the radius of the extracellular space (units: cm),

$$D_L \frac{\partial N_L}{\partial r}\left(R_{\text{cell}}, t\right) = +\left(k_{\alpha L} N_L\left(R_{\text{cell}}, t\right) N_\alpha - k_{-\alpha L} N_{\alpha L}\right), \tag{2.4}$$

$$N_L\left(R_{\text{outer}}, t\right) = S_{\text{outer}}, \tag{2.5}$$

we have IL-2 docking onto the cell membrane by binding to a free α chain. On the cell membrane, we capture this interaction between the bulk and the surface via the normal component of the flux for IL-2 balancing its surface reaction rate (see Equation (2.4)). We also impose a Dirichlet boundary condition for the concentration of IL-2 (N_L) at the outer boundary ($r = R_{\text{outer}}$) representing a well-mixed reservoir of IL-2 that is maintained at a baseline concentration (see Equation (2.5)). IL-2 is produced by multiple T cells and this boundary condition reflects a background concentration.

We impose the initial conditions:

$$N_L\left(r,0\right) = F\left(r\right), R_{\text{cell}} < r < R_{\text{outer}}, \tag{2.6}$$

$$N_\alpha(0) = N_{\alpha,0}, \tag{2.7}$$

$$N_{\alpha L}(0) = N_{\alpha L,0}. \tag{2.8}$$

Here, $F(r) \geq 0$ denotes the initial extracellular IL-2 concentration profile (unit: Number/cm^3) in the radially symmetric domain. Unless stated otherwise, we assume a uniform bath:

$$F(r) \equiv S_{\text{outer}},$$

which is consistent with the outer boundary condition. If the domain is initially devoid of IL-2, then we set

$$F(r) \equiv 0.$$

In Equations (2.7) and (2.8), $N_{\alpha,0}$ and $N_{\alpha L,0}$ denote the initial concentrations of free α chains and [IL-2 : α] complexes on the cell membrane respectively.

From Equations (2.2) and (2.3), it is straightforward to show that the total concentration of α chains is conserved:

$$N_\alpha\left(t\right) + N_{\alpha L}\left(t\right) = N_\alpha(0) + N_{\alpha L}(0) = N_{\alpha,\text{TOT}}, \tag{2.9}$$

where $N_{\alpha,\text{TOT}}$ is the total concentration of α chains on a cell's outer surface. Without loss of generality, we can use Equation (2.9) to eliminate $N_{\alpha L}$ $\left(N_{\alpha L} = N_{\alpha,\text{TOT}} - N_\alpha\right)$ and simplify subsequent analysis.

2.2.2 Data available in literature and separation of time-scales

Data available for estimating model parameters and typical values for N_L and N_α are summarized in Tables 2.3 and 2.4 respectively, with literature sources cited therein.

Variable	Interpretation	Unit
N_L	Concentration of free IL-2 in the bulk	Number/cm^3
N_α	Concentration of free α chain on the cell membrane	Number/cm^2
$N_{\alpha L}$	Concentration of occupied α chain	Number/cm^2

Table 2.1: Dependent variables and their units for the dimensional 1D PDE models.

Parameter	Interpretation	Unit
R_{cell}	Cell radius	cm
R_{outer}	Radius of the domain that the cell lies in	cm
D_L	Diffusion coefficient of IL-2 in the bulk	cm^2/s
$k_{\alpha L}$	Binding on rate of IL-2 and α chain	cm^3/ (Number$*$s)
$k_{-\alpha L}$	Binding off rate of IL-2 and α chain	1/s
Λ	Decay rate of IL-2	1/s
S_{outer}	Concentration of IL-2 at the outer boundary	Number/cm^3
$N_{\alpha,\text{TOT}}$	Total concentration of the α chain on the cell membrane	Number/cm^2

Table 2.2: Parameters and their units for the radially symmetric PDE model.

Selected values of the model parameters are stated in Table 2.5. These values yield a range of characteristic time-scales which are summarized in Table 2.6. A separation of time-scales is observed between the binding and unbinding processes. When the distance between the cells is very small ($R_{\text{outer}} \sim R_{\text{cell}}$), the time-scale for IL-2 to diffuse between the cells is much shorter than the time-scale for binding; when the distance is large (e.g. $R_{\text{outer}} \sim 10R_{\text{cell}}$), unbinding occurs on a shorter time-scale than IL-2 diffusion and binding. We will explore these observations when we develop the quasi-steady state model in Chapter 3.

Parameter	Data	Note	Description and Citation
R_{cell}	2.5–5 μm	Range	In vitro activated human T cells [39]
D_L	$9.2 \pm 2\,(10^{-7})\,\text{cm}^2/\text{s}$	Mean ± SEM	Diffusion of human IL-2 from HEK 293 cells in live mouse lymph node tissue [76]
Λ	5–7 min	Range for half life of IL-2	In vivo half life of human IL-2 from a Jurkat cell line in serum [56]
	3.7 ± 0.8 min	Mean ± SD for half life of IL-2	In vivo half life of IL-2 in murine serum [22]
$k_{\alpha L}$	$1.4 \times 10^7\ \text{M}^{-1}\text{s}^{-1}$		In vitro for human IL-2 from E. coli, MT-1 cells [94]
	$1.06 \pm 0.02\,(10^7)$ $\text{M}^{-1}\text{s}^{-1}$	Mean ± SD	Biosensor analysis (surface plasmon resonance) for recombinant human IL-2 and α chain [55]
$k_{-\alpha L}$	$0.4\ \text{s}^{-1}$		In vitro for human IL-2 from E. coli, MT-1 cells [94]
	$0.298 \pm 0.004\ \text{s}^{-1}$	Mean ± SD	Biosensor analysis (surface plasmon resonance) for recombinant human IL-2 and α chain [55]

Table 2.3: Data available in the literature for estimating parameters in the spatial PDE model of IL-2 binding to α chains.

Variable	Data	Data type	Description and Citation
N_L	$[10^{-4}, 10^4]$ pM	Range	IL-2 concentrations to which T cells are exposed in vitro [27]
	125 pM		Concentration of IL-2 used to culture PBMCs in vitro [39]
	2×10^4 pM		High-dose IL-2 concentration for LAK cell expansion [75]
N_α	2000 per cell		In vitro activated human effector T cells [3]
	$[0,10^3]$ per cell	Range	In vitro human effector T cells with peptide stimulation [27]
	10^4 per cell	Geometric mean	In vitro human regulatory T cells [27]

Table 2.4: Typical values of N_L and N_α. The N_L values correspond to IL-2 concentrations used in cell culture experiments, except for the highest value, which reflects a clinically administered concentration. These concentrations were obtained by dilution from recombinant IL-2 solutions of known concentration rather than by direct assay. The N_α values denote receptor numbers per cell and were measured using antibody staining and quantitative flow cytometry, with fluorescence intensities converted to receptor counts through calibration.

Parameter	Dimension	Value
R_{cell}	Length	5×10^{-4} cm
R_{outer}	Length	Varied
D_L	Length^2/Time	10^{-6} cm^2/s
$k_{\alpha L}$	Length^3/(Number$\times$Time)	1.760×10^{-14} cm^3/(Number$\times$s) $\left(1.06 \times 10^7\ \text{M}^{-1}\text{s}^{-1}\right)$
$k_{-\alpha L}$	1/Time	0.298 s^{-1}
Λ	1/Time	0.00231 s^{-1} (Half life of IL-2: 5 min)
S_{outer}	Number/Length^3	Varied
$N_{\alpha,\text{TOT}}$	Number/Length^2	Varied
$\overline{N_L}$	Number/Length^3	3.885×10^8 Number/cm^3 (or $\sim 10^{-12}$ M) (IL-2 typical: 10 pg/ml, molecular weight of IL-2: 15.5 kDa [77])
$\overline{N_\alpha}$	Number/Length^2	3.183×10^9 Number/cm^2 (Number of α chains per cell: 10^4)

Table 2.5: Selected values for the dimensional parameters in the 1D model based on data from Tables 2.3 and 2.4. $\overline{N_L}$ and $\overline{N_\alpha}$ are chosen typical values of N_L and N_α respectively to non-dimensionalise these two variables.

Time-scale	Expression	Value
Diffusion of IL-2 between two cells	$\sim \frac{R_{\text{outer}}^2}{D_L}$	~ 0.25 s ($R_{\text{outer}} \sim R_{\text{cell}}$) ~ 25 s ($R_{\text{outer}} \sim 10R_{\text{cell}}$)
Binding	$\sim \frac{1}{k_{\alpha L} \times N_L}$	~ 30 h ($N_L \sim 10^{-11}$ M or 155 pg/ml)
Unbinding	$\sim \frac{1}{k_{-\alpha L}}$	~ 3 s
Decay of IL-2	$\sim \frac{1}{\Lambda}$	~ 7.21 min

Table 2.6: Estimates of model time-scales. Parameter values are from Table 2.5.

2.2.3 Non-dimensionalisation

We non-dimensionalise time and length in our 1D model using the time for IL-2 to diffuse the distance of a cell radius ($\frac{R_{\text{cell}}^2}{D_L}$) and the cell radius ($R_{\text{cell}}$) respectively. The scaling constant for the concentration of IL-2 in the bulk (N_L) is a typical concentration ($\overline{N_L}$). We rescale the concentration of α chains (N_α) and the concentration of the complex formed by IL-2 binding to an α chain on the cell membrane ($N_{\alpha L}$) using a typical concentration of α chains on the cell membrane ($\overline{N_\alpha}$). In summary, we have the scalings:

$$\tau = \frac{D_L}{R_{\text{cell}}^2} t,\ r^* = \frac{r}{R_{\text{cell}}},\ n_L = \frac{N_L}{\overline{N_L}},\ n_\alpha = \frac{N_\alpha}{\overline{N_\alpha}},\ n_{\alpha L} = \frac{N_{\alpha L}}{\overline{N_\alpha}}. \tag{2.10}$$

We also introduce the following dimensionless parameters:

$$\hat{k}_{\alpha L} = \frac{R_{\text{cell}}^2}{D_L} \overline{N_L} k_{\alpha L},\ \hat{k}_{-\alpha L} = \frac{R_{\text{cell}}^2}{D_L} k_{-\alpha L},\ \lambda^2 = \frac{R_{\text{cell}}^2}{D_L} \Lambda, \tag{2.11}$$

$$R = \frac{R_{\text{outer}}}{R_{\text{cell}}},\ S = \frac{S_{\text{outer}}}{\overline{N_L}},\ C = \frac{N_{\alpha,\text{TOT}}}{\overline{N_\alpha}},\ \hat{T} = \frac{\overline{N_\alpha}}{R_{\text{cell}} \overline{N_L}}, \tag{2.12}$$

and the dimensionless initial conditions:

$$f(r) = \frac{F(r)}{\overline{N_L}},\ n_{\alpha,0} = \frac{N_{\alpha,0}}{\overline{N_\alpha}},\ n_{\alpha L,0} = \frac{N_{\alpha L,0}}{\overline{N_\alpha}}. \tag{2.13}$$

Under these rescalings, Equations (2.1)–(2.9) transform to the dimensionless 1D model:

$$\frac{\partial n_L}{\partial \tau} = \frac{1}{r^2} \frac{\partial}{\partial r} \left(r^2 \frac{\partial n_L}{\partial r} \right) - \lambda^2 n_L, \tag{2.14}$$

$$\frac{dn_\alpha}{d\tau} = -\left(\hat{k}_{\alpha L} n_L(1,\tau)\, n_\alpha - \hat{k}_{-\alpha L} n_{\alpha L} \right), \tag{2.15}$$

$$\frac{dn_{\alpha L}}{d\tau} = +\left(\hat{k}_{\alpha L} n_L(1,\tau)\, n_\alpha - \hat{k}_{-\alpha L} n_{\alpha L} \right), \tag{2.16}$$

with boundary conditions,

$$\frac{\partial n_L}{\partial r}(1,\tau) = +\hat{T}\left(\hat{k}_{\alpha L} n_L(1,\tau)\, n_\alpha(\tau) - \hat{k}_{-\alpha L} n_{\alpha L}(\tau)\right), \tag{2.17}$$

$$n_L(R,\tau) = S, \tag{2.18}$$

conservation of α chain,

$$n_\alpha(\tau) + n_{\alpha L}(\tau) = n_\alpha(0) + n_{\alpha L}(0) = C, \tag{2.19}$$

and initial conditions,

$$n_L(r,0) = f(r), 1 < r < R, \tag{2.20}$$

$$n_\alpha(0) = n_{\alpha,0}, \tag{2.21}$$

$$n_{\alpha L}(0) = n_{\alpha L,0}. \tag{2.22}$$

In our model, R is the radius of the domain in which the T cell lies and represents the distance between T cells in the system. Small values of R correspond to cases for which T cells are densely packed. This scenario is relevant, as found in secondary lymphoid tissues (lymph nodes and spleen) and high-density in-vitro cultures, where T cells are densely packed. Large values of R represent sparse cellular configurations, which are relevant in peripheral non-lymphoid tissues, early infiltration of tumors or inflamed sites with low T-cell density, and in-vitro assays with low seeding densities.

2.3 Analysis

2.3.1 Steady state analysis of the spatial model

To characterise the long-time behaviour of the PDE model defined by Equations (2.14)–(2.22), we assume that

$$n_L(r,t) \to n_L^\infty(r), \qquad n_\alpha(t) \to n_\alpha^\infty, \qquad n_{\alpha L}(t) \to n_{\alpha L}^\infty \qquad \text{as } t \to \infty,$$

where $n_L^\infty(r)$, n_α^∞ and $n_{\alpha L}^\infty$ denote the steady-state solutions of the model, obtained by setting the time derivatives to zero. Imposing the boundary conditions and exploiting conservation of α chain, it is possible to show that,

$$n_L^\infty(r) = A_1\frac{e^{-\lambda r}}{r} + A_2\frac{e^{\lambda r}}{r},\ n_\alpha^\infty = \frac{C}{\frac{\hat{k}_{\alpha L}}{\hat{k}_{-\alpha L}}\frac{2S\lambda R e^{\lambda(R+1)}}{e^{2\lambda}(\lambda-1)+e^{2\lambda R}(\lambda+1)}+1},\ n_{\alpha L}^\infty = C - n_\alpha^\infty, \tag{2.23}$$

where

$$A_1 = \frac{SRe^{\lambda(R+2)}(\lambda-1)}{e^{2\lambda}(\lambda-1)+e^{2\lambda R}(\lambda+1)},\ A_2 = \frac{SRe^{\lambda R}(\lambda+1)}{e^{2\lambda}(\lambda-1)+e^{2\lambda R}(\lambda+1)}.$$

The values of the fixed dimensionless parameters are summarized in Table 2.7. We note that λ is very small ($\lambda \approx 0.024$), so we can approximate the steady state solutions as follows:

$$n_L^\infty(r) \approx \frac{S\lambda R}{\sinh\lambda R}\frac{\sinh\lambda r}{\lambda r},\ n_\alpha^\infty \approx C\left(\frac{\hat{k}_{\alpha L}}{\hat{k}_{-\alpha L}}\frac{S\lambda R}{\sinh\lambda R}+1\right)^{-1},\ n_{\alpha L}^\infty \approx C - n_\alpha^\infty. \quad (2.24)$$

If the domain size R is small, then for $0 \le r \le R$, $\sinh\lambda r \sim \lambda r$, and Equations (2.24) simplify to give:

$$n_L^\infty(r) \sim S,\ n_\alpha^\infty \sim C\left(S\frac{\hat{k}_{\alpha L}}{\hat{k}_{-\alpha L}}+1\right)^{-1},\ n_{\alpha L}^\infty \sim C - n_\alpha^\infty. \quad (2.25)$$

From Equations (2.24) and (2.25), we conclude that when the domain size R is small, the steady-state concentrations of the free α chain and the occupied α chain are determined by C and the parameter grouping, $S\frac{\hat{k}_{\alpha L}}{\hat{k}_{-\alpha L}}$. They are proportional to the total concentration of α chain (C). $S\frac{\hat{k}_{\alpha L}}{\hat{k}_{-\alpha L}}$ quantifies how the IL-2 concentration compares to the dissociation constant $\hat{K}_d$ ($\hat{K}_d = \frac{\hat{k}_{-\alpha L}}{\hat{k}_{\alpha L}}$). When $S \ll K_d$, minimal binding occurs; when $S = \hat{K}_d$, half of the α chains are occupied by IL-2; when $S \gg \hat{K}_d$, most of the α chains are bound to IL-2. Further, the steady-state concentration of free IL-2 in the bulk is independent of the radial coordinate r in this limit.

Parameter	Expression	Value
$\hat{k}_{\alpha L}$	$\frac{R_{\text{cell}}^2}{D_L}\overline{N_L}k_{\alpha L}$	1.710×10^{-6}
$\hat{k}_{-\alpha L}$	$\frac{R_{\text{cell}}^2}{D_L}k_{-\alpha L}$	0.0745
$\hat{T}$	$\frac{\overline{N_\alpha}}{R_{\text{cell}}\overline{N_L}}$	1.639×10^4
λ	$\sqrt{\frac{R_{\text{cell}}^2}{D_L}\Lambda}$	0.024

Table 2.7: The fixed dimensionless parameters in the 1D spatial model/non-spatial models and estimates of their values based on the dimensional parameter values stated in Table 2.5. For later consideration, the fixed parameters in the phenomenological non-spatial ODE model, $\hat{k}_{\alpha L}$, $\hat{k}_{-\alpha L}$ and λ, are identical to those from the 1D spatial model (they have the same expressions and values).

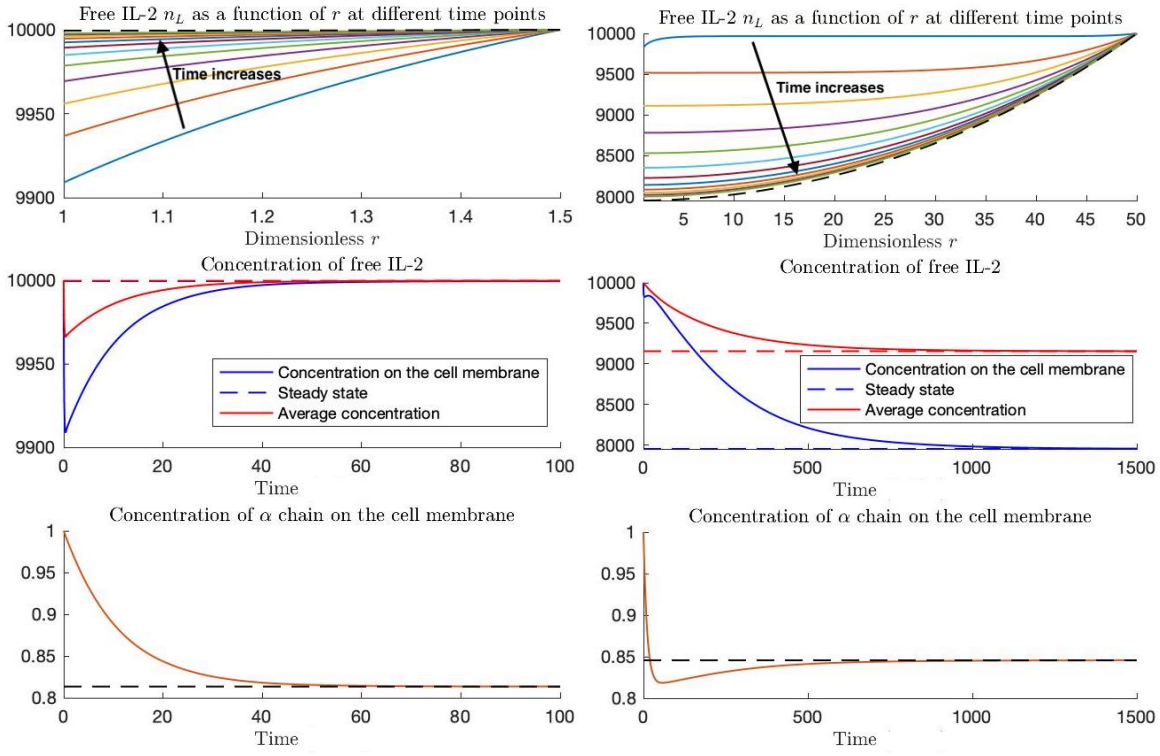
2.4 Numerical simulations and global sensitivity analysis for the PDE model

2.4.1 Numerical simulations from the 1D PDE model varying R, S, C

To understand the behavior of the PDE model, numerical simulations are generated for different values of the domain size (R), the source of IL-2 on $r = R$ (S) and the total concentration of α chain in the system (C). The PDE model is solved in MATLAB using the solver `pde1dM` [29]. `pde1dM` extends the MATLAB function `pdepe` [62] to solve systems of partial differential equations (PDEs) coupled to ordinary differential equations (ODEs). `pde1dM` implements a method-of-lines scheme [83]: the spherical diffusion operator $\frac{1}{r^2}\partial_r\big(r^2 D_L\, \partial_r N_L\big)$ is written in conservative form and discretized on a radial mesh using second-order centered finite differences. The resulting stiff semi-discrete ODE system is advanced in time with MATLAB's stiff ODE solver `ode15s`, as wrapped by `pde1dM`. We simulate the model for two different initial conditions, $n_L(r,0) = S$ and $n_L(r,0) = 0$ for $r \neq R$. Simulation results with $n_L(r,0) = S$ are shown in Figure 2.2. In Figure 2.3, we present simulation results for the concentration of occupied α chain ($n_{\alpha L}$) as R, S and C vary. Steady state solutions for $n_{\alpha L}$ as R, S and C vary are estimated by simulating the PDE model at long times and are plotted in Figure 2.4.

Figure 2.2 shows good agreement between the long time numerical simulations and the analytical expressions for the steady state solutions. As expected, the steady state solutions are independent of the initial conditions. When we fix $n_L(r,0) = 0$ for $r \neq R$ and $n_\alpha(0) = 1$, if the domain size R is small, there is a rapid increase in the concentration of IL-2 on the cell membrane, as the timescale for IL-2 to diffuse from the outer boundary to the cell surface is shorter than the timescale for binding. We observe a discrepancy between the concentration of IL-2 on the cell membrane and its average concentration in the bulk and the discrepancy increases as the domain size R increases, indicating spatial effects may be important.

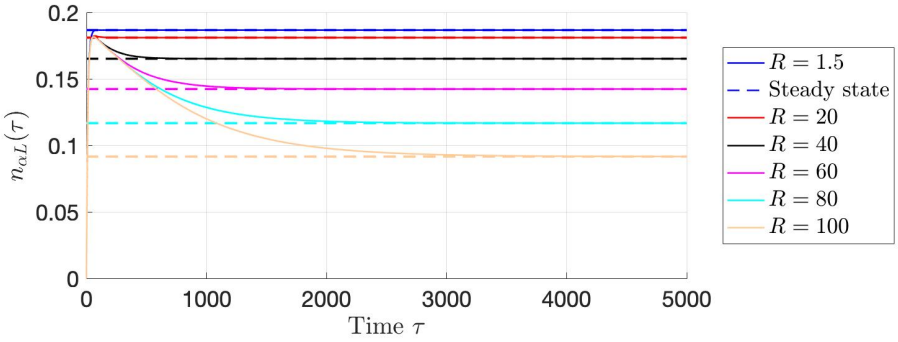
In Figures 2.3 and 2.4, we show how the model behaviour changes as we vary parameters R, S and C. As the domain size R increases, the system takes longer to attain its steady state. We observe that changes to S and C contribute significantly to changes in the concentration of occupied α chains on the cell membrane and that changes in the domain size R do not. We conclude that geometry may not be important for system outputs that are of interest to us. To verify this, below we perform global sensitivity analysis of the 1D PDE model.



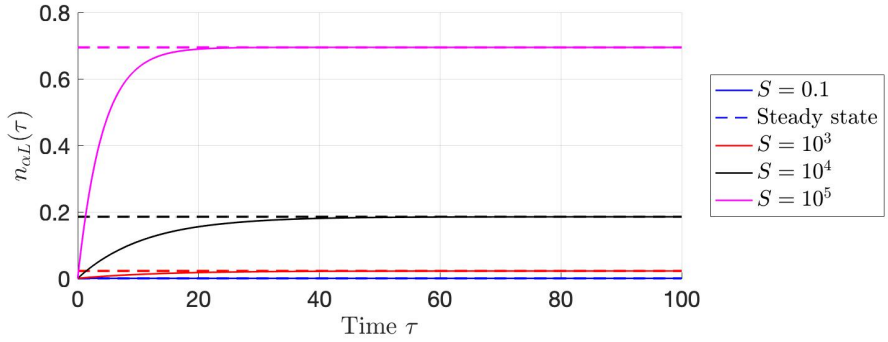
(a) $R = 1.5$. $n_L(r, 0) = S$.

(b) $R = 50$. $n_L(r, 0) = S$.

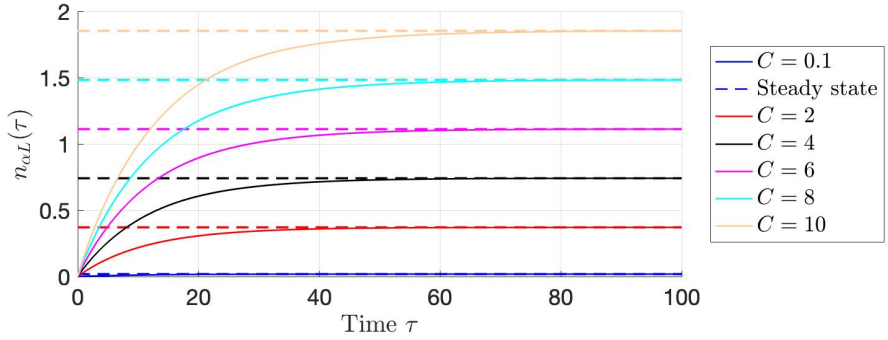
Figure 2.2: Data generated by the PDE model with different values of domain size R. Results for $R = 1.5$ and $R = 50$ are in Panels (a) and (b) respectively. $S = 10000, C = 1$. The values of other fixed parameters are in Table 2.7. Initial condition for IL-2 and free α chain: $n_L(r, 0) = S, n_\alpha(0) = 1$. In the first panel of each plot, for the concentration of free IL-2 in the bulk (n_L), different lines represent simulation results as a function of r at different time points with time increasing in the direction of the arrow. In the middle panel, the concentration of free IL-2 on the cell membrane and the average concentration are plotted as a function of time. In the third panel, for the dimensionless concentration of free α chain (n_α), the results are plotted as a function of time. Note that time is dimensionless here and each dimensionless time unit represents 0.25 s. The analytical steady state solutions are plotted in dashed lines. Simulated results for the average concentration of IL-2 and concentration of free α chain at the end time point are used later to calculate $\hat{k}_{-\alpha L}$ and $\hat{P}$ in the ODE model in Section 3.3.5.1.



(a) Results with varying R. $S = 10^4$, $C = 1$.

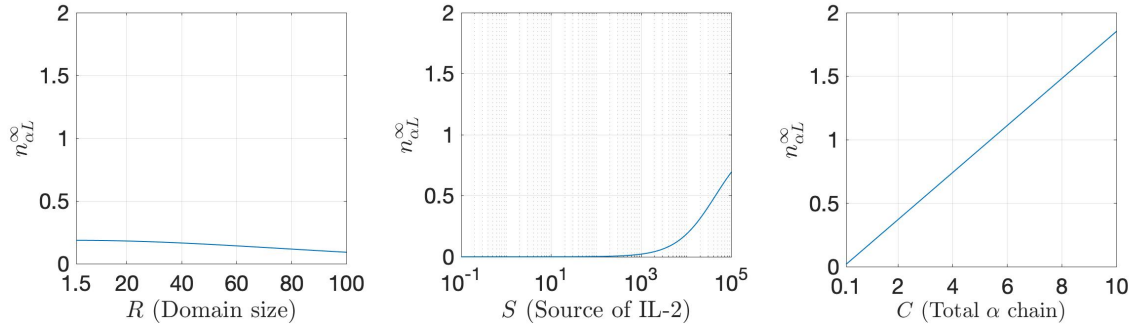


(b) Results with varying S. $R = 10$, $C = 1$.



(c) Results with varying C. $R = 10$, $S = 10^4$.

Figure 2.3: Simulation results for the concentration of occupied α chains ($n_{\alpha L}$), which controls the level of signalling in the system, from the 1D PDE model with varying values of the domain size (R), the source of IL-2 (S) and total concentration of α chain available (C). Results with varying value of R, S or C are shown in Panels (a), (b) and (c) respectively. The analytical steady state solutions are plotted in dashed lines. The values of fixed parameters are in Table 2.7. Initial conditions: $n_\alpha(0) = C$, $n_L(r, 0) = S$.



(a) Results with varying R. $S = 10^4$, $C = 1$.

(b) Results with varying S. $R = 10$, $C = 1$.

(c) Results with varying C. $R = 10$, $S = 10^4$.

Figure 2.4: Series of plots showing how the steady state values of the concentration of occupied α chains ($n_{\alpha L}$) change as we vary the domain size (R) (a), the source of IL-2 (S) (b) and the total concentration of α chains in the system (C) (c). The values of fixed parameters are stated in Table 2.7.

2.4.2 Extended Fourier amplitude sensitivity testing (eFAST)

To quantify what model parameters are important for the concentration of occupied α chains and the level of IL-2 binding, we perform a global sensitivity analysis, using the Extended Fourier Amplitude Sensitivity Test (eFAST) and the Sobol sensitivity analysis introduced in Section 1.3.2.

We implement time-dependent eFAST in MATLAB with the algorithm developed by [59]. The time-dependent quantities of interest are the concentration of the complex formed by IL-2 and α chains ($n_{\alpha L}$), the proportion of α chains that are occupied ($P_{\alpha,\text{occupied}} = \frac{n_{\alpha L}}{C}$, where C is the total concentration of α chains) and the proportion of IL-2 that is bound to an α chain ($P_{L,\text{bound}}$),

$$P_{L,\text{bound}}(\tau) = \frac{n_{\alpha L}(\tau)}{n_{\alpha L}(\tau) + \frac{1}{\hat{T}} \int_{r=1}^{R} n_L(r,\tau)\, r^2 dr}, \tag{2.26}$$

where $\hat{T} = \frac{\overline{N_\alpha}}{R_{\text{cell}} \overline{N_L}}$.

The dimensionless parameters that we vary are S (dimensionless source term of IL-2 at our boundary), C and R (the dimensionless domain size). The values of the fixed dimensionless parameters are summarized in Table 2.7. The values of R, S and C are varied by changing the values of their dimensional analogues $R_{\text{outer}}, S_{\text{outer}}$ and $N_{\alpha,\text{TOT}}$ respectively. The ranges of the dimensionless parameters are summarized in Table 2.8.

eFAST results from simulations for the model are shown in Figure 2.5. For the quantities of interest (the concentration of occupied α chains, the proportion of oc-

Parameter	Expression	Range
R	$\frac{R_{\text{outer}}}{R_{\text{cell}}}$	$[1.5, 100]$
S	$\frac{S_{\text{outer}}}{\overline{N_L}}$	$[0.1, 10^5]$
C	$\frac{N_{\alpha,\text{TOT}}}{\overline{N_\alpha}}$	$[0.1, 10]$

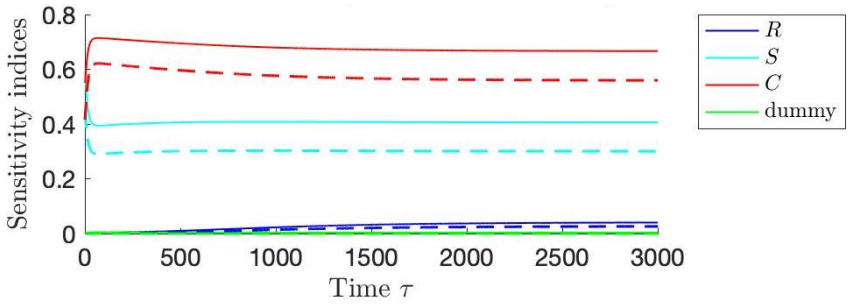
Table 2.8: Ranges for the dimensionless parameters that are varied in the sensitivity analysis of the 1D dimensionless model. The values of R, S and C are varied by changing the values of their dimensional analogues $R_{\text{outer}}, S_{\text{outer}}$ and $N_{\alpha,\text{TOT}}$ respectively. The values of $R_{\text{cell}}, \overline{N_L}$ and $\overline{N_\alpha}$ are fixed at the values stated in Table 2.5.

cupied α chains and the proportion of bound IL-2), the sensitivity indices, first-order sensitivity index (S_i) and total-order sensitivity index (S_{T_i}), are plotted in dashed and solid lines respectively for each varying parameter (dimensionless radius of the domain (R), dimensionless source of IL-2 (S) and dimensionless total amount of α chain (C)) and the dummy parameter over time.

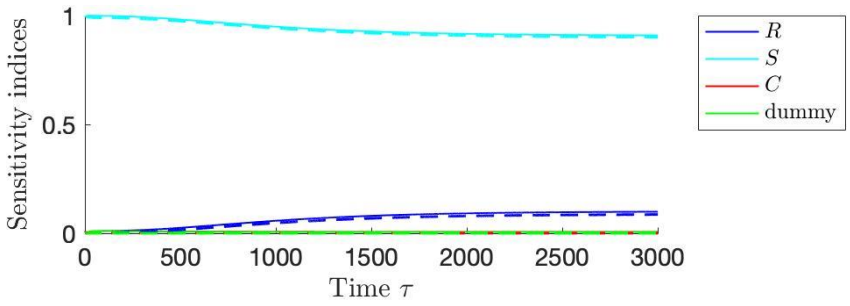
As the time-dependent simulations reach equilibrium, the eFAST sensitivity indices converge to those obtained for the steady state solutions (results not shown). Sensitivity indices are constant after an early transient period that reflects the rapid, binding-dominated equilibration following the imposed initial conditions. For the variance in the concentration of occupied α chains, C contributes the most to sensitivity, S (source of IL-2) also contributes, while spatial effects, via R, have a negligible effect on the concentration of occupied α chains. For the variance in the proportion of occupied α chains, C does not play a role, as expected from our analysis of the steady states, and S contributes the most to the variance. The effects of R are negligible. For the proportion of bound IL-2, the total-order sensitivity index for the dummy variable is high (plotted in green solid line), which indicates that the results are unreliable and we cannot conclude anything from the total-order indices. From the first-order sensitivity indices, we conclude that R contributes the most (approximately 20%) to the variance in the proportion of bound IL-2. The total-order indices are unreliable in this case probably due to two reasons. First, the parameters are highly correlated (the first-order indices are low), which is why the total-order index of the dummy variable is large, as explained in the supplementary material for [59]. Secondly, the proportion of bound IL-2 is small because a significant amount of IL-2 is in the bulk.

2.4.3 Sobol sensitivity analysis

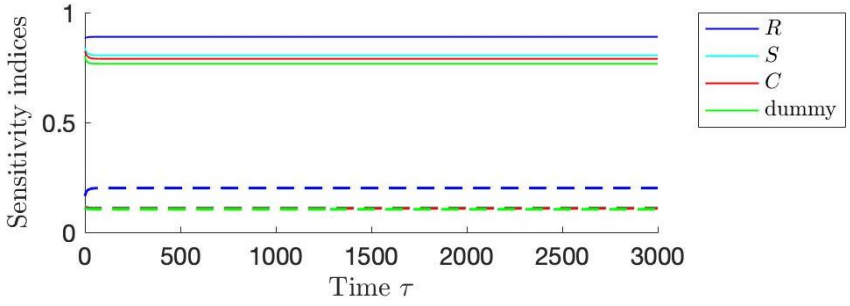
To cross-check the results from eFAST and to further investigate the important parameters for the proportion of bound IL-2, we also performed Sobol sensitivity anal-



(a) For the concentration of occupied α chain.



(b) For the proportion of occupied α chain.



(c) For the proportion of bound IL-2.

Figure 2.5: eFAST results from simulations of the dimensionless model varying R, S and C (see Table 2.8 for their ranges). In the eFAST sampling scheme, 5 search curves and 65 samples per curve are used. For model outputs of interest, the dimensionless concentration of occupied α chains (a), the proportion of occupied α chains (b) and the proportion of bound IL-2 (c), the first-order sensitivity indices (S_i) and total-order sensitivity indices (S_{T_i}) are plotted in dashed and solid lines respectively for each varying parameter (dimensionless radius of the domain (R), dimensionless source of IL-2 (S) and dimensionless total concentration of α chains (C)) and the dummy parameter over time.

ysis in MATLAB using the software tool GSAT ([13]), with the same parameter values/ranges and outputs of interest as for the eFAST analysis (see Section 2.4.2). Both methods are variance-based global sensitivity techniques, but they rely on different sampling strategies. eFAST estimates the sensitivity indices from a frequency-based sampling scheme, which is computationally efficient but sensitive to the choice of frequencies and can be unreliable under strong parameter interactions [59, 80]. The Sobol method estimates the same indices by (quasi-)Monte Carlo sampling [85]. This avoids the aliasing that affects frequency-based schemes, at the cost of slower convergence and a substantially higher computational load. Because the errors of the two methods differ in nature, systematic in the case of eFAST and stochastic in the case of Sobol, their agreement provides greater confidence in the resulting parameter rankings than either method alone.

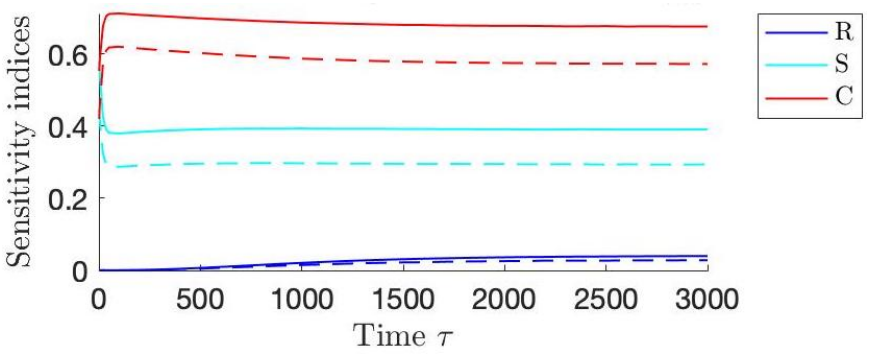
2.4.3.1 Time-dependent Sobol sensitivity analysis

Results from the time-dependent Sobol sensitivity analysis of the dimensionless model are shown in Figure 2.6. Comparison with the results from eFAST (see Figure 2.5) shows good agreement for the amount of occupied α chain and the proportion of occupied α chain. For the proportion of bound IL-2, the domain size R contributes the most to its variance. This is consistent with the Sobol sensitivity analysis for the steady states of the model, as we highlight below.

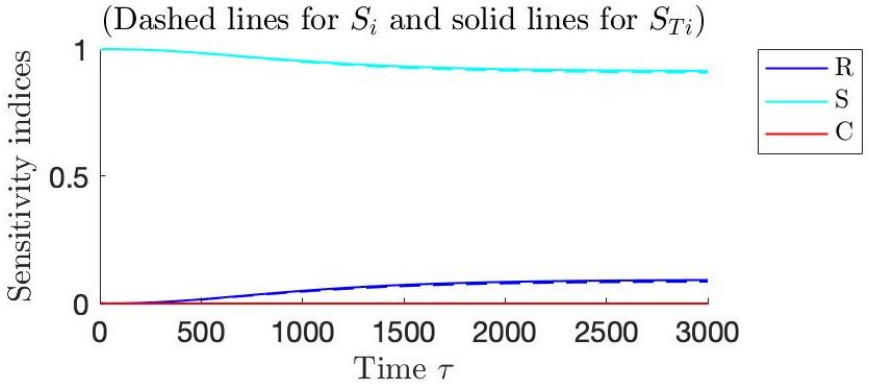
2.4.3.2 Sobol sensitivity analysis for the steady state solutions

Sobol indices for the steady states of the dimensionless model varying parameters of interest were calculated with the number of samples $n = 10000$ or $n = 50000$. Results for $n = 50000$ are shown in Table 2.9 for the reference variables of interest.

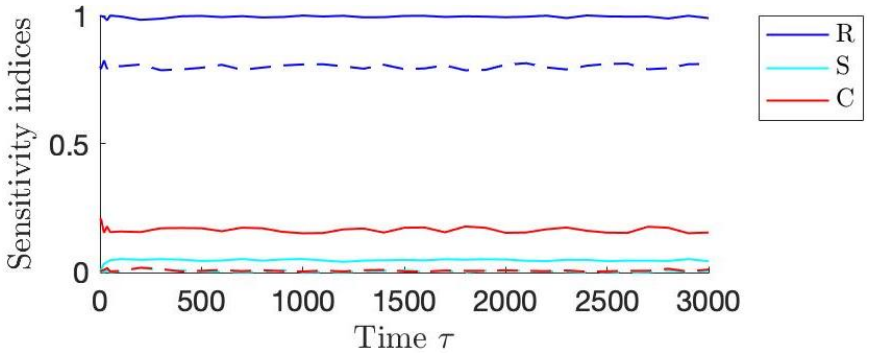
The Sobol indices attain numerical convergence when the number of samples is increased from $n = 10000$ to $n = 50000$, with a corresponding reduction in the associated 50% confidence intervals. For the variance in the concentration of occupied α chains, C contributes the most, S is the second-largest contributor, and R contributes the least. For the variance in the proportion of occupied α chains, C does not play a role anymore, which is consistent with our analysis for the analytical steady states, and it is S that contributes the most to the variance. For the proportion of bound IL-2, R plays the most significant role in its change. However, the fraction of bound IL-2 in the system has marginal impact because it does not control signalling. The associated 50% confidence intervals are relatively high for some Sobol indices for the proportion of bound IL-2. In the table, some small negative values exist, highlighting



(a) For the concentration of occupied α chain.



(b) For the proportion of occupied α chain.



(c) For the proportion of bound IL-2.

Figure 2.6: Results from Sobol sensitivity analysis for the dimensionless model with parameters varying in their original ranges. Number of samples for the quasi-random Monte Carlo simulation = 20000. For the reference variables of interest in the system (the dimensionless concentration of occupied α chains, the proportion of occupied α chains and the proportion of bound IL-2), the first-order sensitivity indices (S_i) and total-order sensitivity indices (S_{T_i}) are plotted in dashed and solid lines respectively for each varying parameter (dimensionless radius of the domain (R), dimensionless source of IL-2 (S) and dimensionless total concentration of α chains (C)) over time. The parameters in the system and their corresponding representative colours in the figure are given in the legends.

Output\Parameter	R	S	C
Occupied α chains	0.0282 (3.3460×10^{-4})	0.2936 (0.0035)	0.5721 (0.0070)
Occupied α chain ratio	0.0875 (0.0061)	0.9061 (0.0638)	-2.2434×10^{-5} (-1.5759×10^{-6})
Proportion of bound IL-2	0.7974 (0.2819)	-4.5800×10^{-4} (-1.5718×10^{-4})	0.0022 (7.4986×10^{-4})

(a) First order Sobol index (50% confidence interval).

Output\Parameter	R	S	C
Occupied α chains	0.0402 (0.0123)	0.3905 (0.0076)	0.6760 (0.0039)
Proportion of occupied α chains	0.0939 (0.0638)	0.9125 (0.0061)	0 (0.0704)
Proportion of bound IL-2	0.9953 (0.0016)	0.0444 (0.3401)	0.1622 (0.2967)

(b) Total order Sobol index (50% confidence interval).

Table 2.9: Sobol indices for the steady states of the dimensionless model varying parameters of interest in the original ranges. Number of samples = 50000. For the reference variables of interest, the first order and total order Sobol indices are calculated and summarized in Tables 2.9a and 2.9b respectively.

error incurred from the algorithm. The conclusions are consistent with those drawn from eFAST.

2.5 Discussion

In this chapter, we have used mathematical modelling to study the binding of IL-2 to α chains on the membrane of a T cell. To examine the importance of spatial heterogeneity and identify the main parameters governing the level of signalling in the system, we developed a 1D, radially-symmetric model which describes the spatial distribution of IL-2 in the bulk and treats the α chain and the [IL-2 : α] complex as uniform, surface-averaged membrane concentrations. We estimated parameter values from the literature, and then non-dimensionalized the model. We used a variety of techniques including steady state analysis and numerical simulations to investigate the model. We also performed global parameter sensitivity analysis including extended Fourier amplitude sensitivity testing (eFAST) and Sobol sensitivity analysis for the model and examined the impact of varying the domain size and concentration of IL-2 on the domain boundary.

The numerical simulations and steady state analysis of the 1D PDE model are in good agreement. For the analytical estimates for the steady states of the dimensionless 1D model, the expressions are simple, and can be understood in terms of a small number of parameter groupings. The model parameters are not identifiable from steady-state data because only the ratio of the binding on and off rates influences the steady states. Simulations of the 1D model revealed a difference between the concentration of IL-2 on the cell membrane and the concentration at the outer boundary, which is accentuated at larger domain sizes, indicating that geometry may be important.

We performed a global parameter sensitivity analysis using eFAST and Sobol sensitivity analysis. The eFAST results relating to the proportion of bound IL-2 are not reliable because the sensitivity indices for the dummy variable are high. Thus, Sobol sensitivity analysis was also considered. Overall, sensitivity indices are constant after an early transient period that reflects the rapid, binding-dominated equilibration following the imposed initial conditions. The concentrations of bound α chains or bound IL-2 is most sensitive to the concentration of α chains available, and the proportion of occupied α chains is most sensitive to the source of IL-2 introduced to the system. Both metrics are relatively insensitive to changes in the size of the domain, i.e. geometry. These results suggest that the availability of α chains determines how much IL-2 a cell can bind, while the supply of IL-2 determines how much of this binding capacity is used.

From the global sensitivity analysis, we conclude that the level of bound α chains is insensitive to geometry. Instead, the level of IL-2 introduced and the concentration of α chains available on the cell membrane are the key parameters. Similarly the temporal dynamics are not important when the initial binding period is not of primary interest. In this case, we can understand the overall response of bound α chain density, and what this is sensitive to, from the steady state solutions.

In the literature, simpler non-spatial ODE models are often used to model IL-2 binding dynamics, raising the question of whether spatial heterogeneity is important and whether we could approximate the spatial model with a simpler non-spatial model. In summary, the core result of this chapter is that the density of bound α chains is insensitive to spatial constraints. This provides a strong rationale for well-mixed approximations. However, we are also interested in whether the general temporal dynamics of the 1D PDE model can be captured by simpler models. Thus, in the next chapter, we will develop two simpler ODE models to further examine the importance of spatial heterogeneity and whether simpler models can be used to represent the spatial PDE model.

Chapter 3

Simpler ODE models of IL-2 binding to α chains

3.1 Introduction

In Chapter 2, we developed a 1D PDE model that describes the binding dynamics of IL-2 to α chains on the surface of a T cell. In the literature, non-spatial ODE models are often used to model this system [15, 31, 45, 70, 95]. This raises the question of whether simpler ODE models can be used to approximate the 1D PDE model. In this chapter, our aims are to assess whether simpler ODE models provide an adequate approximation to the spatial model and to examine whether parameter values for these models can be estimated from the spatial model representing experimental data.

In pursuit of our aims, we develop two distinct ODE models, a quasi-steady state model and a phenomenological one. We start by comparing the steady states of the phenomenological model and the 1D PDE model to see how this may constrain the phenomenological ODE model and to give a first indication of the quality of approximation that it provides. We do not compare the steady states of the quasi-steady state model and the 1D PDE model because they are identical by construction. We analyse the relaxation time-scale of the phenomenological ODE model, by linearising it around its steady state. We examine the structural identifiability of the two simpler models using the scaling invariance method and the generating series method by GenSSI 2.0 [14, 52]. We then examine the practical identifiability of the two ODE models using synthetic data with different levels of noise. We estimate parameter values for the two ODE models using a least squares approach with synthetic datasets generated from the 1D PDE model, to identify model misspecification. The

parameter values in the phenomenological ODE model are also estimated by matching its steady states to those simulated from the PDE model. To assess whether the behaviour of the spatial model can be represented by the simpler ODE models, we compare time-dependent simulation results from the three models, ensuring that each model is run using the same parameter values.

The remainder of this chapter is organised as follows. In Section 3.2, we develop the quasi-steady state model, investigate its structural and practical identifiability and perform parameter estimation using a least squares approach. In Section 3.3, we develop the phenomenological ODE model, identify its steady state solutions, estimate an undetermined constant and linearize the model around its steady state. Then we investigate its structural and practical identifiability and estimate its parameter values by matching its steady state solutions to those simulated from the PDE model and by least squares estimation. In Section 3.4, we present results from the comparison of simulation results from the three models. The chapter ends in Section 3.5, where we discuss our results and outline next steps for this work.

3.2 Quasi-steady state model

3.2.1 Model development

In Chapter 2, we developed the 1D PDE model (Equations (2.14)–(2.22)). In Section 2.2.2, we observed a separation of time-scales between the diffusion of IL-2 in the extracellular space and its binding to the α chains; although this time-scale separation diminishes when the domain size is large and the IL-2 concentration is high, it is pronounced in the parameter regimes of primary interest. This is reflected in the dimensionless parameter $\hat{k}_{\alpha L}$:

$$\hat{k}_{\alpha L} = \frac{t_{\text{diff}}^{\text{cell}}}{t_{\text{on}}}, \text{ where } t_{\text{diff}}^{\text{cell}} = \frac{R_{\text{cell}}^2}{D_L} \text{ and } t_{\text{on}} = \frac{1}{k_{\alpha L}\,\overline{N_L}},$$

and $\hat{k}_{\alpha L} \ll 1$ for typical values.

In such regimes, the extracellular IL-2 concentration relaxes rapidly, on the fast diffusion time-scale, to a profile that is close to steady state for each fixed value of the (more slowly varying) membrane variables. We therefore introduce a quasi-steady state approximation for the bulk IL-2 field.

To make the time-scale separation explicit, we introduce the longer binding time-scale

$$\sigma := \hat{k}_{\alpha L}\,\tau. \tag{3.1}$$

The dimensionless bulk equation in the 1D PDE model is

$$\hat{k}_{\alpha L}\frac{\partial n_L(r,\sigma)}{\partial \sigma}=\frac{\partial n_L(r,\tau)}{\partial \tau}=\frac{1}{r^2}\frac{\partial}{\partial r}\left(r^2\frac{\partial n_L}{\partial r}\right)-\lambda^2 n_L\to 0 \text{ as } \hat{k}_{\alpha L}\to 0, \tag{3.2}$$

for $1<r<R$, where $\tau=\frac{D_L}{R_{\text{cell}}^2}t$ is time scaled by $t_{\text{diff}}^{\text{cell}}$. Intuitively, for each fixed value of $(n_\alpha, n_{\alpha L})$, the extracellular IL-2 profile relaxes rapidly to the stationary diffusion-decay balance, while the membrane variables evolve on the slower time-scale σ. This approximation does not hold during the initial transient, when the bulk IL-2 field adjusts rapidly on the diffusion time-scale.

The quasi-steady state model is obtained by replacing the bulk equation (2.14) in the 1D PDE model with the elliptic problem, while retaining the same coupling to the membrane. Returning to the original dimensionless time variable τ, the reduced model is:

$$0=\frac{1}{r^2}\frac{\partial}{\partial r}\left(r^2\frac{\partial n_L}{\partial r}\right)-\lambda^2 n_L, \tag{3.3}$$

$$\frac{dn_\alpha(\tau)}{d\tau}=-\left(\hat{k}_{\alpha L}n_L\left(1,\tau\right)n_\alpha-\hat{k}_{-\alpha L}n_{\alpha L}\right), \tag{3.4}$$

$$\frac{dn_{\alpha L}(\tau)}{d\tau}=+\left(\hat{k}_{\alpha L}n_L\left(1,\tau\right)n_\alpha-\hat{k}_{-\alpha L}n_{\alpha L}\right), \tag{3.5}$$

with boundary conditions,

$$\frac{\partial n_L}{\partial r}\left(1,\tau\right)=+\hat{T}\left(\hat{k}_{\alpha L}n_L\left(1,\tau\right)n_\alpha\left(\tau\right)-\hat{k}_{-\alpha L}n_{\alpha L}\left(\tau\right)\right), \tag{3.6}$$

$$n_L\left(R,\tau\right)=S, \tag{3.7}$$

and initial conditions,

$$n_\alpha(0)=n_{\alpha,0}, \tag{3.8}$$

$$n_{\alpha L}(0)=n_{\alpha L,0}. \tag{3.9}$$

For the quasi-steady state model, we can determine an implicit solution for $n_L(r,\tau)$ in terms of $n_\alpha(t)$. Integrating Equation (3.3) twice with respect to r, we have that:

$$n_L\left(r,\tau\right)=A(\tau)\frac{\sinh\lambda\left(R-r\right)}{r}+B(\tau)\frac{\cosh\lambda\left(R-r\right)}{r},$$

where the coefficients $A(\tau)$ and $B(\tau)$ are determined by imposing Equations (3.6) and (3.7). By substitution for $n_L\left(r,\tau\right)$ in Equation (3.4), we obtain our reduced formulation of the quasi-steady state model as a non-linear ODE for $n_\alpha(\tau)$:

$$\frac{dn_\alpha(\tau)}{d\tau} = f(\underline{\theta}; n_\alpha) \equiv \frac{1}{\hat{T}}\left[\theta_0 - \theta_1 \frac{\eta_0 n_\alpha + \eta_1}{\eta_2 n_\alpha + \theta_1}\right], \tag{3.10}$$

with,

$$n_\alpha(0) = n_{\alpha,0}, \tag{3.11}$$

where

$$n_L(r,\tau) = -\left(\frac{\eta_0 n_\alpha(\tau) + \eta_1}{\eta_2 n_\alpha(\tau) + \theta_1}\right) \cdot \frac{\sinh\lambda(R-r)}{r} + SR\frac{\cosh\lambda(R-r)}{r}, \tag{3.12}$$

$$n_{\alpha L}(\tau) = C - n_\alpha(\tau), \tag{3.13}$$

and

$$\begin{aligned}
\theta_0 &= SR\eta_3,\\
\theta_1 &= \lambda\cosh\lambda(R-1) + \sinh\lambda(R-1),\\
\eta_0 &= \hat{T}\left[SR\hat{k}_{\alpha L}\cosh\lambda(R-1) + \hat{k}_{-\alpha L}\right],\\
\eta_1 &= \theta_0 - \hat{T}\hat{k}_{-\alpha L}C,\\
\eta_2 &= \hat{T}\hat{k}_{\alpha L}\sinh\lambda(R-1),\\
\eta_3 &= \lambda\sinh\lambda(R-1) + \cosh\lambda(R-1).
\end{aligned}$$

Assuming all α chains are unbound initially, we have $n_{\alpha,0} = C$. By construction, the steady state of the quasi-steady state model is identical to the steady state of the PDE model, with

$$n_{\alpha L}^{\infty} = \frac{\theta_1(\eta_1 - \theta_0)}{\theta_0\eta_2 - \theta_1\eta_0}. \tag{3.14}$$

Values of the fixed model parameters and ranges for those that vary are stated in Tables 2.7 and 2.8 respectively.

Considering the case when the domain size R is small:

We note from Table 2.7 that λ is small ($\lambda \approx 0.024$). If the domain size R is also small, then $\sinh\lambda r \sim \lambda r$, and the quasi-steady model reduces to give:

$$\frac{dn_\alpha}{d\tau} = \frac{-\left(\hat{k}_{-\alpha L} + \hat{k}_{\alpha L}S\right)n_\alpha + \hat{k}_{-\alpha L}C}{\left(\frac{R-1}{R}\right)\hat{T}\hat{k}_{\alpha L}n_\alpha + 1}, \tag{3.15}$$

with

$$n_L(r,\tau) = S + \frac{-\left(\hat{k}_{-\alpha L} + \hat{k}_{\alpha L} S\right) n_\alpha + \hat{k}_{-\alpha L} C}{\left(\frac{R-1}{R}\right) \hat{k}_{\alpha L} n_\alpha + \frac{1}{\hat{T}}} \left(\frac{1}{r} - \frac{1}{R}\right), \; 1 < r < R, \tag{3.16}$$

and

$$n_{\alpha L} = C - n_\alpha. \tag{3.17}$$

3.2.2 Structural identifiability analysis of the quasi-steady state model

A wide range of data could in principle be used for model calibration, obtained in diverse formats and under different experimental conditions. This raises the question of which types and quantities of data should be collected to achieve structural and practical identifiability of the model. Structural identifiability guarantees that the parameters of the model can be uniquely determined from idealized noise-free data, while practical identifiability ensures that parameter estimates remain reliable under real-world constraints such as measurement noise and data limitations [18, 60]. If structural or practical identifiability does not hold, different parameter sets may produce indistinguishable model outputs, making parameter estimates unreliable and undermining the predictive value of the model.

We examine the structural identifiability of the quasi-steady state model using GenSSI 2.0 implemented in MATLAB [52] (introduced in Section 1.3.1). We examine the structural identifiability of the model assuming different observables and unknown parameters. The results are summarized in Table 3.1.

We assume that in all cases, the concentration of free α chains (n_α) is observed; different cases depend on whether the concentration of free IL-2 in the extracellular space at the cell surface ($n_L(1,\tau)$) and the average concentration of IL-2 in the bulk ($n_{L,\text{avg}}(\tau)$) are also observed. In all cases considered, if all parameter values are assumed unknown, the Jacobian matrix remains rank deficient when the order of Lie derivatives is up to 7, suggesting potential non-identifiability across these observation schemes. However, this result is not strictly conclusive, because the generating-series approach is only guaranteed to decide identifiability in the limit of infinitely many Lie derivatives; with a finite truncation (here, order 7), it remains theoretically possible that full rank could be recovered at higher orders. In our case, the parameters R and λ enter the input-output relations through hyperbolic functions (arising from the analytic solution of the bulk equation), so the resulting identifiability equations

Observables	Unknown parameters							Identifiability
	R	S	C	$\hat{k}_{-aL}$	$\hat{k}_{aL}$	$\hat{T}$	λ	
$n_\alpha(\tau), n_L(1,\tau)$	✓	✓	✓	✓	✓	✓	✓	NI
		✓	✓	✓	✓	✓		GI
$n_\alpha(\tau), n_{L,\text{avg}}(\tau)$	✓	✓	✓	✓	✓	✓	✓	NI
		✓	✓	✓	✓	✓		LI
		✓	✓	✓	✓			LI
			✓	✓	✓			LI
		✓		✓	✓			GI
		✓	✓		✓			GI
		✓	✓	✓				GI
$n_\alpha(\tau)$		✓	✓	✓				NI
			✓	✓	✓			GI
		✓		✓	✓			GI
		✓	✓		✓			GI

GI Globally identifiable LI Locally identifiable NI Non-identifiable

Table 3.1: Structural identifiability of the quasi-steady state model (Equations (3.10)–(3.13)) assuming different observables and unknown parameters by GenSSI 2.0. In all cases, the concentration of free α chains (n_α) is observed; different cases depend on whether the concentration of free IL-2 in the extracellular space at the cell surface ($n_L(1,\tau)$), the average concentration of IL-2 in the bulk ($n_\alpha, n_{L,\text{avg}}(\tau)$)) are also observed (or not). The unknown parameters are marked with a checkmark (✓). The color-coded column shows the resulting identifiability: GI (globally identifiable), LI (locally identifiable), or NI (non-identifiable). The average concentration of IL-2 in the bulk $n_{L,\text{avg}}(\tau) = \frac{4\pi}{\hat{V}} \int_1^R n_L(r,\tau)\, r^2 dr$, where $\hat{V} = \frac{4}{3}\pi(R^3 - 1)$ is the volume of the bulk.

are transcendental rather than purely polynomial or rational in the parameters. As a consequence, the symbolic solver in GenSSI cannot derive closed-form global solutions for R or λ, and we can only certify that they are locally identifiable. The value of R can be estimated from the concentration of T cells, and the value of the decay rate λ can be measured separately.

When the concentration of α chains and the concentration of free IL-2 in the extracellular space at the cell surface are observed, the other model parameters $(S, C, \hat{k}_{-\alpha L}, \hat{k}_{\alpha L}, \hat{T})$ are globally structurally identifiable. If we assume instead that the concentration of α chains and the average concentration of IL-2 in the bulk are observable, the same parameter set $(S, C, \hat{k}_{-\alpha L}, \hat{k}_{\alpha L}, \hat{T})$ is only locally identifiable; global identifiability cannot be guaranteed because the algorithm cannot solve the transcendental equations. Since $\hat{T}$ depends on the cell radius, it can in principle be

measured independently. If $\hat{T}$ is treated as known, then the subsets $S, C, \hat{k}_{-\alpha L}, \hat{k}_{\alpha L}$ or $C, \hat{k}_{-\alpha L}, \hat{k}_{\alpha L}$ are also locally identifiable; $S, C, \hat{k}_{-\alpha L}$ or $S, \hat{k}_{-\alpha L}, \hat{k}_{\alpha L}$ or $S, C, \hat{k}_{\alpha L}$ are globally identifiable. We conclude that, in addition to R, λ and $\hat{T}$, one of $C, \hat{k}_{-\alpha L}, \hat{k}_{\alpha L}$ should also be measured to ensure that the remaining parameters are globally identifiable. The total concentration of α chains, C, can be measured by flow cytometry, and the dissociation rate, $\hat{k}_{-\alpha L}$, can be determined from an off-rate assay [8, 34]. When only the concentration of α chains is observable and the unknown parameters are $S, C, \hat{k}_{-\alpha L}$, the Jacobian matrix is rank deficient, suggesting non-identifiability. $S, C, \hat{k}_{\alpha L}$ or $C, \hat{k}_{-\alpha L}, \hat{k}_{\alpha L}$ or $S, \hat{k}_{-\alpha L}, \hat{k}_{\alpha L}$ are globally identifiable. As for the case when the average concentration of IL-2 is known, one of $S, C, \hat{k}_{-\alpha L}$ must be determined separately to guarantee global identifiability of the model.

We conclude that the quasi-steady state model maximizes the number of identifiable parameters when the concentrations of unbound α chains and free IL-2 in the extracellular space at the cell surface are observable. Further, knowledge of the average concentration of free IL-2 in the extracellular domain reduces the number of parameters for which global identifiability can be established. When only the concentration of α chains is observed, the model shows the weakest structural identifiability, with several parameter combinations remaining non-identifiable compared with the other observation scenarios. In practice, measuring the concentration of free IL-2 in the extracellular domain at the cell membrane requires advanced imaging techniques, which may not be readily accessible. Depending on what data are available, some parameters may need to be measured separately to ensure global structural identifiability of the model. In cases where GenSSI does not establish global identifiability, its conclusions about non-identifiability are not strictly definitive, because the generating-series approach relies on a finite truncation of Lie derivatives. Complementary structural identifiability techniques, such as tools based on differential algebra (e.g. DAISY [7]), could be used to further investigate these cases, as they provide an independent check on structural non-identifiability. A full comparison with these alternative approaches is beyond the scope of this chapter and is left for future work.

3.2.3 Practical identifiability analysis of the quasi-steady state model

To evaluate the practical identifiability of the quasi-steady state model, we use it to generate synthetic data under different conditions. We then use a least squares approach to estimate the model parameters in each case. By comparing the recovered

parameters with their true values, we gain insight into how well the model can be identified under different conditions. We focus on estimating the parameter $\hat{k}_{-\alpha L}$ since this is of interest in drug development [19, 58].

We use the quasi-steady state model to generate synthetic time series data for n_α and n_L at P_τ time-points (times $\tau = 0, \delta\tau, 2\delta\tau, ..., (P_\tau - 1)\,\delta\tau$) for different values of $\hat{k}_{-\alpha L}$ from 0.01 to 1 ($\hat{k}_{-\alpha L} = [0.01,\ 0.05 : 0.05 : 1]$). We use a multiplicative noise model to introduce variability in the observed data for n_α and n_L:

$$y_i^{\text{obs}}(\tau) = y_i^{\text{true}}(\tau) \times (1 + \epsilon_i(\tau)), \tag{3.18}$$

where each independent random variable $\epsilon_i(\tau)$ is sampled from a Gaussian distribution with variance σ^2 ($\epsilon_i(\tau) \sim \mathcal{N}(0, \sigma^2)$), $y_1(\tau) = n_\alpha(\tau)$, and $y_2(\tau) = n_L(1, \tau)$ or $n_{L,\text{avg}}(\tau)$. We use a multiplicative noise model to capture the constant coefficient of variation often observed in biological data, where measurement error scales with signal intensity [44]; this also accommodates the difference in scale between n_α and n_L. The values of the fixed parameters are stated in Table 2.7.

To facilitate application of least squares estimation, we apply a logarithmic transformation to the noise model, converting the multiplicative noise into an additive form:

$$\ln\left(y_i^{\text{obs}}(\tau)\right) = \ln\left(y_i^{\text{true}}(\tau)\right) + \ln\left(1 + \epsilon_i(\tau)\right) \approx \ln\left(y_i^{\text{true}}(\tau)\right) + \epsilon_i(\tau), \tag{3.19}$$

assuming $\epsilon_i(\tau) \ll 1$.

To explore the effect of data sampling, we consider different temporal discretizations by varying the time steps ($\delta\tau$) and the time ranges ($[0, T]$). $P_\tau = \frac{T}{\delta\tau} + 1$ is the total number of time points. We generate M replicates of the synthetic data to mimic repeated experiments. We apply a least squares approach to the logarithmically transformed data to estimate the parameter $\hat{k}_{-\alpha L}$:

$$\hat{k}_{-\alpha L}^{\text{inf}} = \arg\min_{\hat{k}_{-\alpha L}} \sum_{i=1}^{2} \sum_{j=1}^{P_\tau} \sum_{m=1}^{M} \left(\ln y_{i,j,m}^{\text{obs}} - \ln y_{i,j}^{\text{model}}(\hat{k}_{-\alpha L})\right)^2, \tag{3.20}$$

where

$y_{i,j,m}^{\text{obs}}$	is the observed value of y_i at time $\tau_j = (j-1)\,\delta\tau$ for replicate m;
$y_{i,j}^{\text{model}}(\hat{k}_{-\alpha L})$	is the model prediction of y_i at time τ_j given parameter $\hat{k}_{-\alpha L}$;
P_τ	is the total number of time points;
M	is the number of replicates for each time point.

For each fit, we compute the ratio of inferred to real values of $\hat{k}_{-\alpha L}$ ($\frac{\hat{k}^{\text{inf}}_{-\alpha L}}{\hat{k}^{\text{true}}_{-\alpha L}}$) and the associated mean squared error (MSE):

$$\text{MSE} = \frac{1}{2P_\tau M} \sum_{i=1}^{2} \sum_{j=1}^{P_\tau} \sum_{m=1}^{M} \left(\ln y^{\text{obs}}_{i,j,m} - \ln y^{\text{model}}_{i,j}(\hat{k}^{\text{inf}}_{-\alpha L}) \right)^2, \tag{3.21}$$

to assess the goodness-of-fit. We repeat this process N times, each time generating a new synthetic data set with an independent stochastic noise realisation (i.e. new random draws for the measurement noise). We then calculate the mean and 95% confidence intervals of the ratio of the inferred and real values of $\hat{k}_{-\alpha L}$ and the mean squared error across the N fittings to assess the variability and uncertainty in the parameter estimates. We examine how different experimental conditions can influence the results by changing the noise level (σ), the time step ($\delta\tau$), the time range (T) and the number of replicates (M).

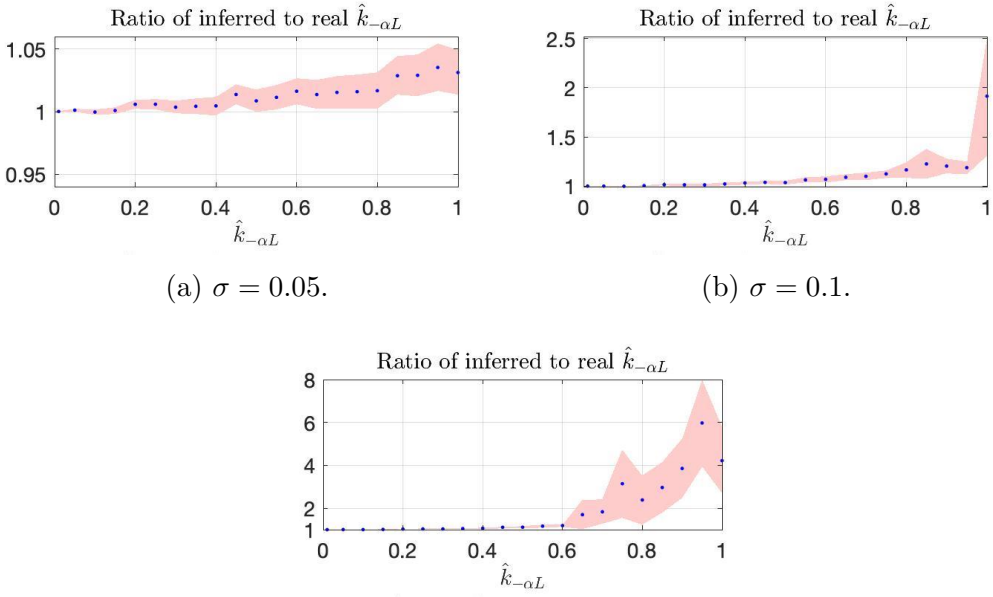
We obtain results for varying values of $\hat{k}_{-\alpha L}$ ($\hat{k}_{-\alpha L} = [0.01,\ 0.05 : 0.05 : 1]$) and different noise levels ($\sigma = 0, 0.05, 0.1, 0.15$) in the synthetic data. The results with $\sigma = 0.05, 0.1, 0.15$ are shown in Figure 3.1. When $\sigma = 0$ for the synthetic data, the inferred values of $\hat{k}_{-\alpha L}$ are the same as the ground truth (the ratio of inferred to real $\hat{k}_{-\alpha L}$ is 1) with small mean squared errors ($\sim 10^{-25}$) (results not shown). As we increase the noise level, the inferred values of $\hat{k}_{-\alpha L}$ deviate from the ground truth (the ratio deviates from 1) and the associated mean squared error increases. The accuracy of the estimation for $\hat{k}_{-\alpha L}$ decreases as the ground truth value of $\hat{k}_{-\alpha L}$ increases. When $\sigma = 0.05$, the inferred values of $\hat{k}_{-\alpha L}$ are within 5% of the real values, with associated average least squares at the order of 10^{-3}. When $\sigma = 0.1$, the mean values of most estimates are within 50% of the ground truth values, and the associated least squares error is approximately 0.01. When $\sigma = 0.15$, especially for larger values of $\hat{k}_{-\alpha L}$, the inferred value is not accurate, with associated least squares error of approximately 0.0225. For example, when $\hat{k}_{-\alpha L} = 1$, the inferred value is approximately 4 times the true value. We also observe that the value of $\hat{k}_{-\alpha L}$ is consistently overestimated. Estimating $\hat{k}_{-\alpha L}$ becomes more difficult as its value increases because high values of $\hat{k}_{-\alpha L}$ lead to rapid dissociation events and short-lived binding events that are difficult to capture accurately, resulting in missed events due to limited sampling resolution and increased noise impact. Missed short events and noise make dissociation appear faster because they reduce observed binding times and blur transition points. This indicates that we can mitigate these effects by using a smaller time step to minimize missed short events or increasing the time range to capture more events and average out noise and variability.

The results with different data availability for the concentration of α chains (n_α) and the concentration of IL-2 (n_L) are presented in Figure 3.2 for noise level $\sigma = 0.15$. Estimates of the values of $\hat{k}_{-\alpha L}$ are most accurate with data for the concentration of IL-2 on the cell surface ($n_L(1,\tau)$), less accurate with data for the average concentration of IL-2 ($n_{L,\text{avg}}$), and least accurate with data only for the concentration of α chains (n_α). When $n_L(1,\tau)$ or $n_{L,\text{avg}}$ is available or only n_α is observed, the worst estimation exceeds the true value by a factor of approximately 3, 6 and 27 respectively. We conclude that best estimates can be achieved with data for n_α and $n_L(1,\tau)$. Data for n_α and $n_{L,\text{avg}}$ also generate reasonable estimates.

We also examine the effects of changing the noise level (σ), the number of replicates (M), the number of simulations (N), the time steps ($\delta\tau$) and the time ranges (T); the results are shown in Figure 3.3. As the level of noise (σ) increases, the estimation of $\hat{k}_{-\alpha L}$ deteriorates, as indicated by a less accurate mean value, wider confidence intervals, and an increased mean squared error. When $\sigma = 0.3$, the inferred $\hat{k}_{-\alpha L}$ is approximately 20 times larger than the true value, and the mean squared error is approximately 0.1. We can obtain more accurate estimates of $\hat{k}_{-\alpha L}$ by increasing the number of replicates (M), decreasing the time step for sampling ($\delta\tau$) or increasing the time range (T). When increasing the number of simulations (N), we obtain more stable and accurate estimates of the mean and the confidence interval.

We conclude that $\hat{k}_{-\alpha L}$ is practically identifiable under noise-free conditions for the synthetic datasets analyzed. When noise is introduced, achieving practical identifiability requires a careful selection of experimental design parameters, including the number of replicates, the time step for sampling, and the sampling time range. Higher levels of noise or larger values of $\hat{k}_{-\alpha L}$ exacerbate accurate estimation. In such cases, increasing the number of replicates, refining the sampling intervals, and prolonging the observation period are necessary to maintain practical identifiability. Practically, these enhancements are often limited by available resources and limitations of the measurement methods. We also observe that, among all data-collection protocols considered, practical identifiability of $\hat{k}_{-\alpha L}$ is most pronounced when data for both the concentration of the α chain and the concentration of IL-2 on the cell membrane are available. However, in practice, acquiring measurements of the free concentration of IL-2 on the cell membrane is challenging and typically requires advanced imaging techniques, which may not be accessible. We find that utilizing data for the average concentration of IL-2 is a viable alternative and can produce satisfactory results in $\hat{k}_{-\alpha L}$.

In summary, while the ideal conditions for practical identifiability of $\hat{k}_{-\alpha L}$ involve noise-free data and comprehensive measurements, real-world applications must contend with noise and resource limitations. By strategically selecting the number of replicates, refining sampling strategies, and utilizing accessible forms of data, we have demonstrated that it is possible to achieve reliable parameter estimation under less-than-ideal conditions.

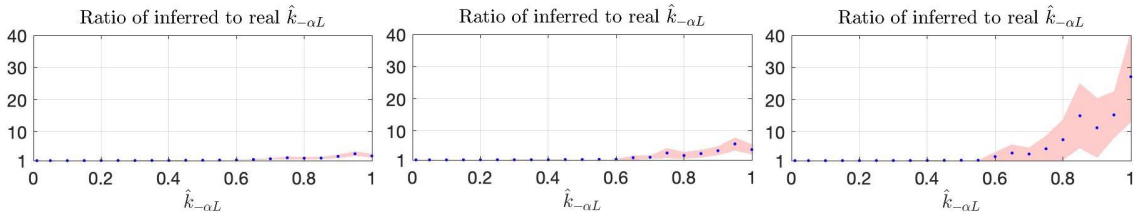


(a) $\sigma = 0.05$.

(b) $\sigma = 0.1$.

(c) $\sigma = 0.15$.

Figure 3.1: Practical identifiability of the quasi-steady state model (Equations (3.10)–(3.13)) with different levels of noise (σ) in the synthetic data. Results from least squares estimation, varying the value of $\hat{k}_{-\alpha L}$ from 0.01 to 1, adding different levels of noise to synthetic data generated from the quasi-steady state model and then inferring parameter estimates in the same model. Mean value and 95% confidence interval for the ratio of inferred to real values of $\hat{k}_{-\alpha L}$ with $\sigma = 0.05, 0.1, 0.15$ are plotted in Panels (a), (b) and (c) respectively. The corresponding mean squared errors are calculated but are not included in the figure for simplicity because they present narrow 95% confidence intervals and exhibit marginal variation across different values of $\hat{k}_{-\alpha L}$. Their values vary for different values of σ. Results for $\sigma = 0$ are omitted because the ratio of inferred to real $\hat{k}_{-\alpha L}$ remains 1 for all $\hat{k}_{-\alpha L}$. Data for n_α and $n_{L,\text{avg}}$ are used. $R = 10, S = 10^4, C = 1$. $\delta\tau = 6, T = 300, M = 5, N = 500$.



(a) Data for $n_\alpha(\tau)$ and $n_L(1,\tau)$.

(b) Data for $n_\alpha(\tau)$ and $n_{L,\text{avg}}(\tau)$.

(c) Data for only $n_\alpha(\tau)$.

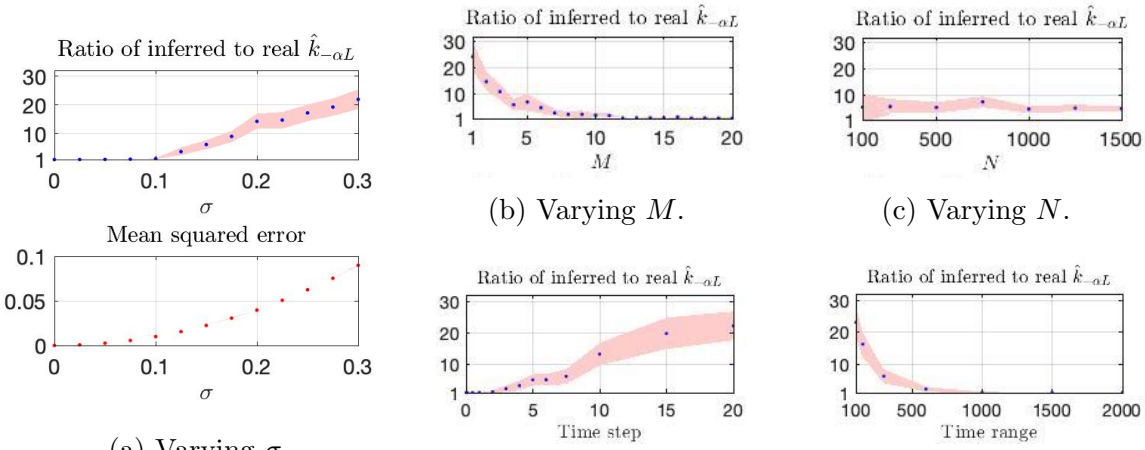
Figure 3.2: Practical identifiability of the quasi-steady state model (Equations (3.10)–(3.13)) with different availability of data. Results from the least squares estimation, varying the value of $\hat{k}_{-\alpha L}$ from 0.01 to 1, adding noise ($\sigma = 0.15$) to different availability of synthetic data for n_α and n_L generated from the quasi-steady state model and then inferring parameter estimates in the same model. Mean value and 95% confidence interval for the ratio of inferred to real values of $\hat{k}_{-\alpha L}$ with data for $n_\alpha(\tau)$ and $n_L(1,\tau)$, $n_\alpha(\tau)$ and $n_{L,\text{avg}}(\tau)$, or only $n_\alpha(\tau)$ are plotted in Panels (a), (b) and (c) respectively. The corresponding mean squared errors are calculated but are omitted from the figure for simplicity because they exhibit narrow 95% confidence intervals and present marginal variation across different values of $\hat{k}_{-\alpha L}$. $R = 10, S = 10^4, C = 1$. $\sigma = 0.15, \delta\tau = 6, T = 300, M = 5, N = 500$.

3.2.4 Parameter estimation of the quasi-steady state model by fitting to data generated by the 1D PDE model

We now examine whether the parameter values in the quasi-steady state model can be estimated accurately by fitting to data generated by the 1D PDE model. We generate data for n_α and n_L from the PDE model for different domain sizes R but assume R is known and estimate the value of $\hat{k}_{-\alpha L}$ in the quasi-steady model using a least squares approach.

We consider two types of initial conditions for the PDE model, corresponding to cases with and without an initial quasi-steady bulk IL-2 profile. In both cases we impose $n_\alpha(0) = C$ in both models. For the PDE model, when the initial conditions are quasi-steady, we initialise the bulk IL-2 concentration with the quasi-steady profile obtained from the quasi-steady state model. In the non-quasi-steady case, we instead initialise the PDE model with a spatially uniform IL-2 concentration, $n_L(r,0) = S$.

For different values of the domain size ($R = 1.5$ and 50), we use the PDE model to generate noise-free data for n_α and n_L at P_τ regularly spaced time-points in the range $[0,T]$ ($\tau = 0, \delta\tau, 2\delta\tau, ..., (P_\tau - 1)\,\delta\tau$). The data here are noise-free, so the logarithmic transformation used in Section 3.2.3 to convert multiplicative noise into an additive form is not required, and only the difference in scale between n_α and n_L remains to be



(a) Varying σ. (b) Varying M. (c) Varying N. (d) Varying $\delta\tau$. (e) Varying T.

Figure 3.3: Practical identifiability of the quasi-steady state model (Equations (3.10)–(3.13)) with different experimental conditions and the number of simulations (N). The effects of changing the noise level (σ), the number of replicates (M), the number of simulations (N), the time steps ($\delta\tau$) and the time ranges (T) are shown in Panels (a), (b), (c), (d) and (e) respectively. The corresponding mean squared errors are omitted for all panels other than the one for varying σ because they exhibit narrow 95% confidence intervals and present marginal variation across different values of $M, N, \delta\tau$ or T. The value of $\hat{k}_{-\alpha L}$ is fixed at 1. Data for n_α and $n_{L,\text{avg}}$ are used. $R = 10, S = 10^4, C = 1$. $\sigma = 0.15, \delta\tau = 6, T = 300, M = 5$ if they are not the varying factor. When varying σ, $N = 1000$ is used to ensure more stable mean values and confidence intervals for high levels of noise; $N = 500$ for varying other factors. The varying time steps are [0.1,0.5,1,2,3,4,5,6,7.5,10,15,20].

addressed. To account for this, we use weighted least squares to fit the quasi-steady state model to these data, normalising each residual by the observed value. In more detail, we define the relative squared error (RSE) for a given value of $\hat{k}_{-\alpha L}$ as:

$$\text{RSE}(\hat{k}_{-\alpha L}) = \sum_{i=1}^{P_\tau} \left[\left(\frac{n_\alpha^{\text{obs}}(\tau_i) - n_\alpha^{\text{model}}(\tau_i; \hat{k}_{-\alpha L})}{n_\alpha^{\text{obs}}(\tau_i)} \right)^2 + \left(\frac{n_L^{\text{obs}}(1, \tau_i) - n_L^{\text{model}}(1, \tau_i; \hat{k}_{-\alpha L})}{n_L^{\text{obs}}(1, \tau_i)} \right)^2 \right], \tag{3.22}$$

where

$n_\alpha^{\text{obs}}(\tau_i)$	is the observed value of n_α at time $\tau_i = (i-1)\,\delta\tau$, generated by the 1D PDE model;
$n_\alpha^{\text{model}}(\tau_i; \hat{k}_{-\alpha L})$	is the predicted value of n_α at time τ_j, given parameter $\hat{k}_{-\alpha L}$, generated by the quasi-steady state model;
$n_L^{\text{obs}}(1, \tau_i)$	is the observed value of n_L on the cell membrane ($r = 1$), at time τ_i, generated by the 1D PDE model;
$n_L^{\text{model}}(1, \tau_i; \hat{k}_{-\alpha L})$	is the predicted value of n_L on the cell membrane ($r = 1$), at time τ_i, given parameter $\hat{k}_{-\alpha L}$, generated by the quasi-steady state model;
P_τ	is the total number of time points,

We define the inferred value of $\hat{k}_{-\alpha L}$ as the minimiser of the relative squared error:

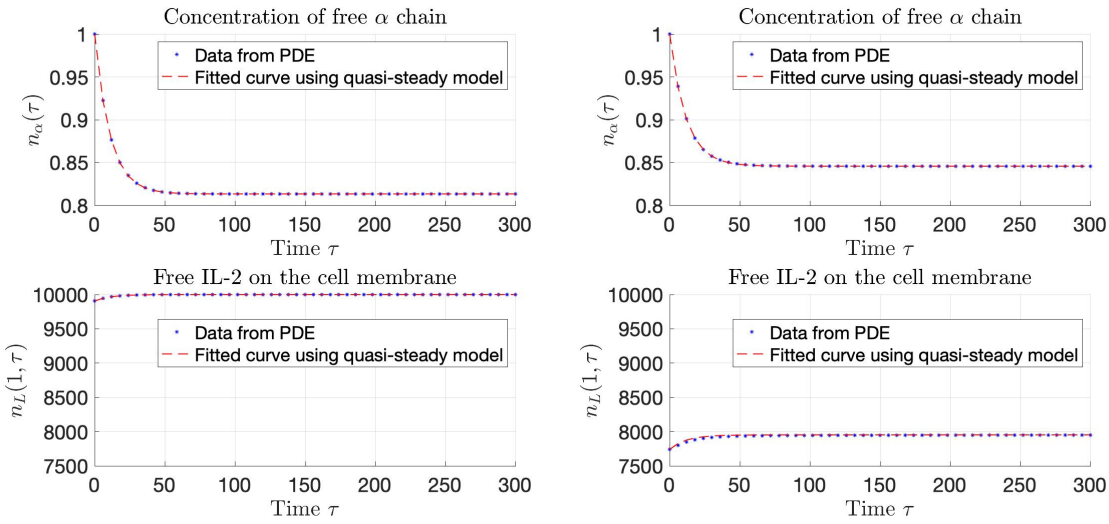
$$\hat{k}_{-\alpha L}^{\text{inf}} = \arg\min_{\hat{k}_{-\alpha L}} \text{RSE}(\hat{k}_{-\alpha L}). \tag{3.23}$$

We then quantify the goodness-of-fit using the mean relative squared error (MRSE), defined as

$$\text{MRSE} = \frac{1}{2P_\tau} \sum_{i=1}^{P_\tau} \left[\left(\frac{n_\alpha^{\text{obs}}(\tau_i) - n_\alpha^{\text{model}}(\tau_i; \hat{k}_{-\alpha L}^{\text{inf}})}{n_\alpha^{\text{obs}}(\tau_i)} \right)^2 + \left(\frac{n_L^{\text{obs}}(1, \tau_i) - n_L^{\text{model}}(1, \tau_i; \hat{k}_{-\alpha L}^{\text{inf}})}{n_L^{\text{obs}}(1, \tau_i)} \right)^2 \right]. \tag{3.24}$$

Results with quasi-steady initial conditions with varying domain size R are shown in Figure 3.4. Results for initial conditions that are not quasi-steady in IL-2 for the PDE model, with $n_L(r, 0) = S$ and varying domain size R, are shown in Figure 3.5.

The results presented in Figure 3.4 show that the quasi-steady state model is a very good representation of the PDE model, with accurate estimation of parameter values and small MRSE when the PDE initial conditions are quasi-steady. From Figure 3.5, when the initial conditions for IL-2 for the PDE model are not quasi-steady, the quasi-steady model fits the 1D PDE model well when the domain size ($R = 1.5$) is small but not when the domain size gets large ($R = 50$). As the domain size increases, the estimates for $\hat{k}_{-\alpha L}$ and the corresponding MRSE get worse, with poor fitting to the initial transient. As the time span T increases, the estimates for $\hat{k}_{-\alpha L}$ improve because the steady state solutions contribute more to the fitting. However, fitting to the initial transient does not improve.



(a) $R = 1.5$. $\hat{k}^{\text{inf}}_{-\alpha L} = 0.0745$ in the quasi-steady model. Mean relative squared error is 1.8374×10^{-8}.

(b) $R = 50$. $\hat{k}^{\text{inf}}_{-\alpha L} = 0.0746$ in the quasi-steady model. Mean relative squared error is 9.1068×10^{-7}.

Figure 3.4: Results from least squares fits of the quasi-steady state model (Equations (3.10)–(3.13)) to data generated from the PDE model (Equations (2.14)–(2.22)) with quasi-steady initial conditions. Results for $R = 1.5$ and $R = 50$ are in Panels (a) and (b) respectively. For both models: $n_\alpha(0) = C$ and $n_L(r, 0)$ is calculated from the quasi-steady model. $T = 300, P_\tau = 51$. $S = 10^4$, $C = 1$. The values of the other parameters are in Table 2.7.

3.3 Phenomenological ODE model

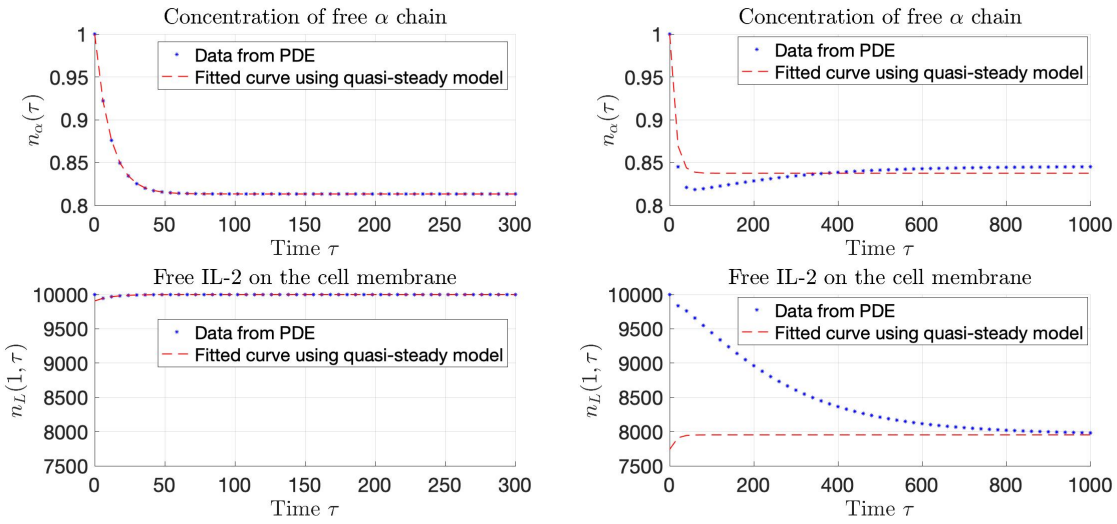
3.3.1 Model development

To understand the significance of spatial effects in the 1D PDE model, we now introduce a spatially uniform ODE model which is similar to existing ODE models [15, 95]. We use the same dependent variables (N_L, N_α and $N_{\alpha L}$) and the domain as for the 1D PDE model (see Section 2.2). Although the ODE model is spatially homogeneous, the domain enters the model formulation through geometric and volume-averaging factors. We assume that the dynamics of N_L, N_α and $N_{\alpha L}$ are governed by the following t-dependent ODEs, with the dimensional parameters listed in Table 2.5:

$$\frac{dN_L(t)}{dt} = -\frac{A}{V}\left(k_{\alpha L} N_L N_\alpha - k_{-\alpha L} N_{\alpha L}\right) - \Lambda N_L + P, \tag{3.25}$$

$$\frac{dN_\alpha(t)}{dt} = -\left(k_{\alpha L} N_L N_\alpha - k_{-\alpha L} N_{\alpha L}\right), \tag{3.26}$$

$$\frac{dN_{\alpha L}(t)}{dt} = +\left(k_{\alpha L} N_L N_\alpha - k_{-\alpha L} N_{\alpha L}\right). \tag{3.27}$$



(a) $R = 1.5$. $\hat{k}^{\text{inf}}_{-\alpha L} = 0.0745$ in the quasi-steady model. Mean relative squared error is 8.5101×10^{-7}.

(b) $R = 50$. $\hat{k}^{\text{inf}}_{-\alpha L} = 0.0701$ in the quasi-steady model. Mean relative squared error is 0.036.

Figure 3.5: Results from least squares fits of the quasi-steady model (Equations (3.10)–(3.13)) to data generated from the PDE model (Equations (2.14)–(2.22)) with initial conditions that are not quasi-steady. Results for $R = 1.5$ and $R = 50$ are in Panels (a) and (b) respectively. For both models: $n_\alpha(0) = C$. For the PDE model: $n_L(r, 0) = S$. When $R = 1.5$, $T = 300$ and $P_\tau = 51$; when $R = 50$, $T = 1000$ and $P_\tau = 51$. In both cases, $S = 10^4$, $C = 1$. The values of the other parameters are in Table 2.7.

Equation (3.25) describes the dynamics of $N_L(t)$, the concentration of IL-2 in the bulk. The term modelling reversible binding of IL-2 to free α chains on the cell membrane includes a prefactor $\frac{A}{V}$ to convert the cell surface concentration to a bulk concentration because units of N_L are different from those for N_α and $N_{\alpha L}$, where $A = 4\pi R^2_{\text{cell}}$ is the area of the cell membrane and $V = \frac{4}{3}\pi\left(R^3_{\text{outer}} - R^3_{\text{cell}}\right)$ is the volume of the bulk. R_{cell} is the radius of the cell (units cm) and R_{outer} is the outer radius of the extracellular space (units cm). We assume that IL-2 undergoes linear decay, with rate Λ (units: s^{-1}), and that it is produced at a constant rate P (units: Number/($\text{cm}^3 \times \text{s}$)). This source term mimics the supply of IL-2 from the bulk in the 1D PDE model. In Equation (3.26), free α chain on the cell membrane binds reversibly with free IL-2 from the bulk. Similarly in Equation (3.27), the complex forms when IL-2 binds reversibly to a free α chain on the cell membrane.

We note from adding Equations (3.26) and (3.27) that the total number of α chains in the system is constant. We can exploit this identity to eliminate $N_{\alpha L}$ from

the model, noting that

$$N_{\alpha L}(t) = N_{\alpha,\mathrm{TOT}} - N_{\alpha}(t), \tag{3.28}$$

where $N_{\alpha,\mathrm{TOT}}$ is the total concentration of α chains on the cell membrane.

We close Equations (3.25) and (3.26) by imposing the initial conditions,

$$N_L(0) = N_{L,0}, \tag{3.29}$$

$$N_{\alpha}(0) = N_{\alpha,0}, \tag{3.30}$$

where $N_{L,0}$ and $N_{\alpha,0}$ are respectively the initial concentration of IL-2 in the extracellular space and the initial concentration of free α chain on the cell membrane.

One question about this model is how to relate the parameter P to the rate of production of IL-2 (S) in the spatial model where IL-2 is supplied to the domain by prescribing the IL-2 concentration on the outer domain boundary, which we will investigate in the next section.

Non-dimensionalisation of the phenomenological ODE model

To facilitate comparison with the 1D PDE model and the quasi-steady state model, we use the same scalings (see Equation (2.10)) to non-dimensionalize the phenomenological ODE model defined by Equations (3.25)–(3.30). Thus, we introduce the following scalings:

$$\begin{aligned} \tau &= \frac{t}{\overline{\tau}}, \text{ where } \overline{\tau} = \frac{R_{\mathrm{cell}}^2}{D_L}, \\ n_L &= \frac{N_L}{\overline{N_L}}, n_{\alpha} = \frac{N_{\alpha}}{\overline{N_{\alpha}}}, n_{\alpha L} = \frac{N_{\alpha L}}{\overline{N_{\alpha}}}, \end{aligned} \tag{3.31}$$

where $\overline{N_L}$ and $\overline{N_{\alpha}}$ are typical values of the concentrations of free IL-2 in the bulk and free α chain on the cell membrane respectively, and D_L is the diffusion coefficient of IL-2 in the bulk with units cm^2/s. We also introduce the following dimensionless parameter groupings:

$$\begin{aligned} &\hat{k}_{\alpha L} = \overline{\tau}\overline{N_L}k_{\alpha L}, \hat{k}_{-\alpha L} = \overline{\tau}k_{-\alpha L}, \lambda^2 = \overline{\tau}\Lambda, \hat{P} = \frac{\overline{\tau}}{\overline{N_L}}P, C = \frac{N_{\alpha,\mathrm{TOT}}}{\overline{N_{\alpha}}}, \\ &\hat{F} = \frac{A}{V}\frac{\overline{N_{\alpha}}}{\overline{N_L}}, A = 4\pi R_{\mathrm{cell}}^2, V = \frac{4}{3}\pi R_{\mathrm{cell}}^3\left(R^3 - 1\right), R = \frac{R_{\mathrm{outer}}}{R_{\mathrm{cell}}}, \end{aligned}$$

and the dimensionless initial conditions,

$$n_{L,0} = \frac{N_{L,0}}{\overline{N_L}}, n_{\alpha,0} = \frac{N_{\alpha,0}}{\overline{N_{\alpha}}}.$$

Under the above rescaling, Equations (3.25)–(3.30) transform to give:

$$\frac{dn_L(\tau)}{d\tau} = -\hat{F}\left(\hat{k}_{\alpha L} n_L n_\alpha - \hat{k}_{-\alpha L} n_{\alpha L}\right) - \lambda^2 n_L + \hat{P}, \tag{3.32}$$

$$\frac{dn_\alpha(\tau)}{d\tau} = -\left(\hat{k}_{\alpha L} n_L n_\alpha - \hat{k}_{-\alpha L} n_{\alpha L}\right), \tag{3.33}$$

where

$$n_{\alpha L}(\tau) = C - n_\alpha(\tau), \text{ and } n_L(0) = n_{L,0},\ n_\alpha(0) = C. \tag{3.34}$$

We assume that initially all α chains are unbound, so that $N_{\alpha,0} = N_{\alpha,\mathrm{TOT}}$. The dimensionless production rate of IL-2, $\hat{P}$, is treated as an unknown. This choice follows from the fact that the 1D PDE formulation does not contain an explicit volumetric secretion term for IL-2. We estimate the value of $\hat{P}$ in Section 3.3.2.2.

The values of the fixed parameters and the ranges of the varying parameters in the phenomenological ODE model are stated in Tables 2.7 and 2.8 respectively.

3.3.2 Analysis for the phenomenological ODE model

3.3.2.1 Steady state analysis for the phenomenological ODE model

We determine the steady state solutions of the phenomenological ODE model, by setting the right hand side of Equations (3.32)–(3.33) to zero, giving:

$$n_L^\infty = \frac{\hat{P}}{\lambda^2},\ n_\alpha^\infty = \frac{C}{\frac{\hat{P}}{\lambda^2}\frac{\hat{k}_{\alpha L}}{\hat{k}_{-\alpha L}} + 1},\ n_{\alpha L}^\infty = C - n_\alpha^\infty, \tag{3.35}$$

where n_L^∞, n_α^∞ and $n_{\alpha L}^\infty$ represent the steady state solutions for the concentration of free IL-2 in the bulk, the concentration of free α chain and the concentration of occupied α chain on the cell membrane respectively.

The steady-state solution for n_L^∞ is governed by balancing its production rate ($\hat{P}$) and its decay rate ($\lambda^2 n_L^\infty$). The expression for n_α^∞ can be written as: $n_\alpha^\infty = \frac{C}{\frac{n_L^\infty}{\hat{K}_d}+1}$, where $\hat{K}_d$ is the dissociation constant and $\hat{K}_d = \frac{\hat{k}_{-\alpha L}}{\hat{k}_{\alpha L}}$. n_α^∞ and $n_{\alpha L}^\infty$ are proportional to the total concentration of α chain (C). $\frac{n_L^\infty}{\hat{K}_d}$ quantifies how steady-state IL-2 concentration compares with $\hat{K}_d$. When $n_L^\infty \ll \hat{K}_d$, most α chains are free; when $n_L^\infty = \hat{K}_d$, half of the α chains are occupied by IL-2; when $n_L^\infty \gg \hat{K}_d$, the majority of the α chains are occupied by IL-2. Using the values of $\hat{k}_{-\alpha L}$ and $\hat{k}_{\alpha L}$ listed in Table 2.7, the concentration of IL-2 must reach approximately 4×10^{-8} M for half of the α chains to be occupied. In the context of our model, this value is of the same order of magnitude as the high-dose IL-2 protocols employed in T cell expansion in vitro and the localized IL-2 concentrations characteristic of active tissue niches [11].

3.3.2.2 Estimating $\hat{P}$ in the phenomenological ODE model

We estimate $\hat{P}$ by matching the steady states of the phenomenological ODE model and the 1D PDE model.

Estimating $\hat{P}$ when the domain size (R) is small

For the 1D PDE model, when the domain size (R) is small, the profile of the steady state solution of $n_L(r,\tau)$ is approximately spatially uniform. Equating the steady states of the phenomenological ODE system, Equation (3.35), to those of the 1D PDE model when the domain size (R) is small:

$$n_L^\infty(r) \sim S,\ n_\alpha^\infty \sim \frac{C}{S\dfrac{\hat{k}_{\alpha L}}{\hat{k}_{-\alpha L}}+1},\ n_{\alpha L}^\infty \sim C - n_\alpha, \tag{3.36}$$

we have that:

$$\hat{P} = \lambda^2 S, \tag{3.37}$$

or, equivalently,

$$P = S_{\text{outer}}\Lambda, \tag{3.38}$$

in terms of dimensional parameters.

Thus, when the domain size is small, the steady states of the phenomenological ODE model and the spatial model are consistent if $\hat{P} = \lambda^2 S$. Then the steady states of the phenomenological ODE model are:

$$n_L^\infty = S,\ n_\alpha^\infty = \frac{C}{\frac{S}{\hat{K}_d}+1},\ n_{\alpha L}^\infty = C - n_\alpha^\infty. \tag{3.39}$$

Estimating $\hat{P}$ for more general cases

More generally, the domain size (R) may not be small, and we match the steady state solutions for free α chain in the ODE model and 1D PDE models as follows:

$$n_\alpha^\infty \approx \frac{C}{\dfrac{S}{\hat{K}_d}\dfrac{\lambda R}{\sinh \lambda R}+1}, \tag{3.40}$$

to get:

$$\hat{P} = \left(\lambda^2 S\right)\frac{\lambda R}{\sinh \lambda R}, \tag{3.41}$$

or, in dimensional terms,

$$P = \Lambda S_{\text{outer}} \frac{R_{\text{outer}} \sqrt{\frac{\Lambda}{D_L}}}{\sinh\left(R_{\text{outer}} \sqrt{\frac{\Lambda}{D_L}}\right)} \tag{3.42}$$

Using Equation (3.41), we deduce that the steady state solution for IL-2 in the phenomenological ODE model is $n_L^\infty = \frac{S\lambda R}{\sinh \lambda R}$. The steady state solution for IL-2 in the bulk for the 1D PDE model is $n_L^\infty \approx \frac{S\lambda R}{\sinh \lambda R} \frac{\sinh \lambda r}{\lambda r}$, which depends on the radial component r. If we consider the concentration of IL-2 close to the cell membrane in the spatial model, because $\lambda \ll 1$, $\frac{\sinh \lambda r}{\lambda r} \sim 1$ when $r = 1$, then $n_L^\infty \approx \frac{S\lambda R}{\sinh \lambda R}$, which matches with the steady state solution for the concentration of IL-2 in the ODE model.

Thus, in general, if we fix $\hat{P} = \frac{S\lambda^3 R}{\sinh \lambda R}$, the steady state concentration of free α chain and the complex formed by IL-2 binding with α chain for the ODE and 1D PDE models can be matched. The steady state solution for the concentration of IL-2 in the phenomenological model is matched with that close to the cell membrane in the 1D PDE model. The steady state solutions of the phenomenological ODE model when $\hat{P} = \frac{S\lambda^3 R}{\sinh \lambda R}$ are:

$$n_L^\infty = \frac{S\lambda R}{\sinh \lambda R},\ n_\alpha^\infty = \frac{C}{\frac{\hat{k}_{\alpha L}}{\hat{k}_{-\alpha L}} \frac{S\lambda R}{\sinh \lambda R} + 1},\ n_{\alpha L}^\infty = C - n_\alpha^\infty. \tag{3.43}$$

3.3.2.3 Linearizing the phenomenological ODE model

When simulating system dynamics for the phenomenological ODE model, we observe that the system approaches its steady state slowly. This raises the question of what governs the relaxation time-scale to the steady state for the model. The relaxation time-scale is also biologically relevant because it provides insights for immune response timing and drug dosing strategies.

To determine the time-scale on which the ODE model (Equations (3.32)–(3.34)) relaxes to its steady state, we linearize about the steady state solution.

The Jacobian matrix of the two dimensional system for n_L and n_α is:

$$J = \begin{bmatrix} -\hat{F}\hat{k}_{\alpha L} n_\alpha^\infty - \lambda^2 & -\hat{F}\left(\hat{k}_{\alpha L} n_L^\infty + \hat{k}_{-\alpha L}\right) \\ -\hat{k}_{\alpha L} n_\alpha^\infty & -\left(\hat{k}_{\alpha L} n_L^\infty + \hat{k}_{-\alpha L}\right) \end{bmatrix}, \tag{3.44}$$

where

$$n_L^\infty = \frac{\hat{P}}{\lambda^2},\ n_\alpha^\infty = \frac{C}{\frac{\hat{P}}{\lambda^2} \frac{\hat{k}_{\alpha L}}{\hat{k}_{-\alpha L}} + 1}. \tag{3.45}$$

The trace T and determinant D of J are:

$$T = -\hat{F}\hat{k}_{\alpha L}n_{\alpha}^{\infty} - \lambda^2 - \left(\hat{k}_{\alpha L}n_L^{\infty} + \hat{k}_{-\alpha L}\right) < 0,\ D = \lambda^2\left(\hat{k}_{\alpha L}n_L^{\infty} + \hat{k}_{-\alpha L}\right) > 0, \quad (3.46)$$

and the two eigenvalues of J are given by:

$$\mu_{\pm} = \frac{T \pm \sqrt{T^2 - 4D}}{2}. \quad (3.47)$$

If λ^2 is small ($\lambda^2 = 5.76 \times 10^{-4}$), $T^2 \gg D$, and

$$\mu_{\pm} = \frac{T \pm |T|\sqrt{1 - \frac{4D}{T^2}}}{2} \sim \frac{T \pm |T|\left(1 - \frac{2D}{T^2}\right)}{2} \sim T \text{ or } \frac{D}{T}. \quad (3.48)$$

Both eigenvalues are real and negative, with $|\mu_+| \sim |T|$ corresponding to a short time-scale and $|\mu_-| \sim |\frac{D}{T}|$ corresponding to a long time-scale. This analysis explains the results generated by the ODE model in Section 3.4. The magnitude of μ_- is very small, and, hence, the ODE model approaches its steady state very slowly. As the domain size R increases and $\hat{F}$ decreases, the long time-scale decreases. We also note that $|\frac{D}{T}| = O(\lambda^2)$ (see Equation (3.46)). For the ODE model, the long time-scale is of order $\frac{1}{\lambda^2}$.

3.3.3 Structural identifiability analysis of the phenomenological ODE model

3.3.3.1 Scaling invariance method

The Scaling Invariance Method (SIM) tests local structural identifiability of ODE models by searching for scaling symmetries [14]. Since it only probes this class of symmetries, it can prove non-identifiability when a scaling symmetry is found, but it cannot guarantee identifiability when no scaling symmetry is detected [91]. Thus, SIM is best used as a screening tool that provides certificates of non-identifiability when applicable, and as a complement to the generating-series approach introduced in Section 1.3.1, which can then be used to establish identifiability more generally.

Following the method described in [14], we write the right-hand side of the ODE model (Equations (3.32)–(3.34)) as functionally independent functions, scale all parameters and variables by unknown scaling factors, u_x, where x is the corresponding parameter or variable, and substitute into the ODE equations. We then equate each functionally independent function to its scaled version and find relations between the

scaling factors u_x that leave the system invariant. We obtain the following identifiability conditions for the phenomenological ODE model:

$$u_{\hat{F}}u_{\hat{k}_{\alpha L}}u_{n_\alpha} = 1, u_{\hat{F}}u_{\hat{k}_{-\alpha L}}u_{n_\alpha} = u_{n_L}, u_{\lambda^2} = 1, u_{\hat{F}}u_{\hat{k}_{-\alpha L}}u_C = u_{n_L}, u_{\hat{P}} = u_{n_L}, \tag{3.49}$$

$$u_{\hat{k}_{\alpha L}}u_{n_L} = 1, u_{\hat{k}_{-\alpha L}} = 1, u_{\hat{k}_{-\alpha L}}u_C = u_{n_\alpha}, \tag{3.50}$$

$$u_{n_{L,0}} = u_{n_L}, u_{n_{\alpha,0}} = u_{n_\alpha}. \tag{3.51}$$

The identifiability equations in (3.49), (3.50) and (3.51) are obtained by equating terms in the equations for n_L (Equation (3.32)), n_α (Equation (3.33)) and the initial conditions (Equation (3.34)) respectively.

For variables and parameters that are assumed to be known, the corresponding scaling factors are set to be 1. Then we solve the resulting identifiability equations for the scaling factors associated with the unknown parameters and variables. Parameter x is non-identifiable if the trivial solution, with $u_x = 1$, is not the only solution for its scaling factor. Below we will discuss results for cases when different combinations of the dependent variables n_L and n_α are observed.

Case I: Both n_L and n_α are observed In this case, we fix $u_{n_L} = 1$ and $u_{n_\alpha} = 1$, and the identifiability equations reduce to give:

$$u_{\hat{F}}u_{\hat{k}_{\alpha L}} = 1, u_{\hat{F}}u_{\hat{k}_{-\alpha L}} = 1, u_{\lambda^2} = 1, u_{\hat{F}}u_{\hat{k}_{-\alpha L}}u_C = 1, u_{\hat{P}} = 1, \tag{3.52}$$

$$u_{\hat{k}_{\alpha L}} = 1, u_{\hat{k}_{-\alpha L}} = 1, u_{\hat{k}_{-\alpha L}}u_C = 1, \tag{3.53}$$

$$u_{n_{L,0}} = 1, u_{n_{\alpha,0}} = 1, \tag{3.54}$$

and the only solution is the trivial solution:

$$u_{\hat{F}} = u_{\hat{k}_{-aL}} = u_{\hat{k}_{aL}} = u_{\lambda^2} = u_{\hat{P}} = u_C = u_{n_{L,0}} = u_{n_{\alpha,0}} = 1. \tag{3.55}$$

We conclude that no scaling symmetries exist and thus no conclusion about non-identifiability can be drawn when both n_L and n_α are observed.

Case II: Only n_α is observed In this case, we fix $u_{n_\alpha} = 1$, and the identifiability equations reduce to:

$$u_{\hat{F}}u_{\hat{k}_{\alpha L}} = 1, u_{\hat{F}}u_{\hat{k}_{-\alpha L}} = u_{n_L}, u_{\lambda^2} = 1, u_{\hat{F}}u_{\hat{k}_{-\alpha L}}u_C = u_{n_L}, u_{\hat{P}} = u_{n_L}, \tag{3.56}$$

$$u_{\hat{k}_{\alpha L}}u_{n_L} = 1, u_{\hat{k}_{-\alpha L}} = 1, u_{\hat{k}_{-\alpha L}}u_C = 1, \tag{3.57}$$

$$u_{n_{L,0}} = u_{n_L}, u_{n_{\alpha,0}} = 1, \tag{3.58}$$

from which we obtain:

$$u_{\hat{k}_{-\alpha L}} = u_{\lambda^2} = u_C = u_{n_{\alpha,0}} = 1 \tag{3.59}$$

$$u_{\hat{F}} u_{\hat{k}_{\alpha L}} = 1, u_{\hat{P}} = u_{n_L}, u_{\hat{k}_{\alpha L}} u_{n_L} = 1, u_{n_{L,0}} = u_{n_L}. \tag{3.60}$$

We observe that non-trivial solutions exists for $u_{\hat{F}}, u_{\hat{k}_{\alpha L}}, u_{\hat{P}}, u_{n_{L,0}}$ and u_{n_L}. Thus, the model is non-identifiable when only u_{n_α} is observed. From equations in (3.60), we conclude that, if one of $\hat{F}, \hat{k}_{\alpha L}, \hat{P}$ or $u_{n_{L,0}}$ is known, then scaling symmetry can be eliminated from the model and the trivial solution is the only solution of the identifiability equations.

Case III: Only n_L is observed In this case, $u_{n_L} = 1$, and the identifiability equations are:

$$u_{\hat{F}} u_{\hat{k}_{\alpha L}} u_{n_\alpha} = 1, u_{\hat{F}} u_{\hat{k}_{-\alpha L}} u_{n_\alpha} = 1, u_{\lambda^2} = 1, u_{\hat{F}} u_{\hat{k}_{-\alpha L}} u_C = 1, u_{\hat{P}} = 1, \tag{3.61}$$

$$u_{\hat{k}_{\alpha L}} = 1, u_{\hat{k}_{-\alpha L}} = 1, u_{\hat{k}_{-\alpha L}} u_C = u_{n_\alpha}, \tag{3.62}$$

$$u_{n_{L,0}} = 1, u_{n_{\alpha,0}} = u_{n_\alpha}, \tag{3.63}$$

from which we obtain:

$$u_{\hat{k}_{-\alpha L}} = u_{\hat{k}_{\alpha L}} = u_{\lambda^2} = u_{\hat{P}} = u_{n_{L,0}} = 1, \tag{3.64}$$

$$u_{\hat{F}} u_{n_\alpha} = 1, u_{\hat{F}} u_C = 1, u_{n_{\alpha,0}} = u_{n_\alpha}. \tag{3.65}$$

We conclude that non-trivial solutions exist for $u_{\hat{F}}, u_C, u_{n_{\alpha,0}}$ and u_{n_α}, and thus the model is non-identifiable. We note further that if $u_{\hat{F}} = 1$ or $u_C = 1$ or $u_{n_{\alpha,0}} = 1$, then the trivial solution (u_x=1 for any x) is the only solution for the identifiability equations. Thus, we can eliminate the scaling symmetries in the model if one of $\hat{F}, C$ or $n_{\alpha,0}$ is known.

3.3.3.2 Generating series method by GenSSI 2.0

As for the quasi-steady state model (see Section 3.2.2), we use GenSSI 2.0 to assess the structural identifiability of the phenomenological ODE model [52] (see also Section 1.3.1). Results assuming different observables, different unknown parameters and different initial conditions for the ODE model are shown in Table 3.2.

When the concentrations of IL-2 (n_L) and α chain (n_α) are observable, the phenomenological ODE model is globally identifiable, with all the parameters unknown ($\hat{F}, \hat{k}_{-aL}, \hat{k}_{aL}, \lambda^2, \hat{P}, C$).

Observables	Unknown parameters/ICs								Identifiability
	$\hat{F}$	$\hat{P}$	C	$\hat{k}_{-aL}$	$\hat{k}_{aL}$	λ^2	$n_{L,0}$	$n_{\alpha,0}$	
$n_L(\tau), n_\alpha(\tau)$	✓	✓	✓	✓	✓	✓			GI
$n_\alpha(\tau)$	✓	✓	✓	✓	✓	✓	✓		NI
		✓	✓	✓		✓	✓		NI
		✓	✓	✓	✓		✓		NI
		✓		✓	✓	✓	✓		LI
		✓	✓		✓	✓	✓		LI
		✓	✓	✓	✓	✓			LI
		✓		✓	✓		✓		GI
		✓	✓		✓		✓		GI
		✓	✓	✓	✓				GI
$n_L(\tau)$	✓	✓	✓	✓	✓	✓		✓	NI
		✓	✓	✓	✓	✓		✓	LI
		✓		✓					LI
		✓			✓				LI
		✓	✓					✓	GI

GI Globally identifiable LI Locally identifiable NI Non-identifiable

Table 3.2: Structural identifiability of the phenomenological ODE model (Equations (3.32)–(3.34)) assuming different observables and unknown parameters or initial conditions by GenSSI 2.0. The observables are from $n_L(\tau)$ and $n_\alpha(\tau)$. The unknown parameters or initial conditions are marked with a checkmark (✓). The color-coded column shows the resulting identifiability: GI (globally identifiable), LI (locally identifiable), or NI (non-identifiable).

When only n_α is observed, the model, with unknown parameters $\hat{F}, \hat{k}_{-aL}, \hat{k}_{aL}, \lambda^2, \hat{P}, C$ and $n_{L,0}$ (the initial condition of the concentration of IL-2), is not locally structural identifiable because scaling symmetries exist (see analysis in Section 3.3.3.1). This is consistent with results from GenSSI 2.0, where the Jacobian matrix stays rank deficient utilising Lie derivatives up to the order of 8, indicating non-identifiability. From the scaling method analysis, we conclude that if one of $\hat{F}, \hat{k}_{\alpha L}, \hat{P}$ or $u_{n_{L,0}}$ is known, scaling symmetry can be eliminated. To reduce the number of unknown parameters, we assume that $\hat{F}$ is known (it depends on the radius of the T cell and should be relatively easy to measure), and then scaling symmetries are eliminated and identifiability is possible but not definitive. We find that a further reduction in the number of unknown parameters is required to conclude identifiability from GenSSI. If we further assume that one of $\hat{k}_{-aL}, C$ or $n_{L,0}$ is known, then the remaining parameters are structurally locally identifiable; assuming $\hat{k}_{aL}$ or λ^2 is known is not sufficient to conclude identifiability. We do not consider the case when $\hat{P}$ is known because it is

a parameter that we introduce and is difficult to quantify separately. After assuming one of $\hat{k}_{-aL}, C$ or $n_{L,0}$ can be measured separately, if we further assume that λ^2 (the decay rate of IL-2) is known, we conclude from GenSSI that the model with unknown parameters, $\hat{k}_{aL}, \hat{P}, C, n_{L,0}$ or $\hat{k}_{-aL}, \hat{k}_{aL}, \hat{P}, n_{L,0}$ or $\hat{k}_{-aL}, \hat{k}_{aL}, \hat{P}, C$, is structurally globally identifiable.

When only n_L is observable, the scaling method predicts that the model, with unknown parameters $\hat{F}, \hat{k}_{-aL}, \hat{k}_{aL}, \lambda^2, \hat{P}, C$ and $n_{\alpha,0}$ (the initial condition of the concentration of free α chain), is not locally structural identifiable due to the existence of scaling symmetries. This is consistent with results from GenSSI, suggesting non-identifiability because the Jacobian matrix remains rank deficient. From the scaling method analysis, we also conclude that if one of $\hat{F}, C$ or $n_{\alpha,0}$ is known, the scaling symmetries can be eliminated. Thus, we further assume $\hat{F}$ is known. We then conclude from GenSSI that the model is locally identifiable with the remaining unknown parameters. We further assume that λ^2 is known and fix different combinations of the remaining model parameters. From GenSSI, we can conclude local structural identifiability for the model with unknown parameters, $\hat{k}_{-aL}, \hat{P}$ or $\hat{k}_{aL}, \hat{P}$. The model with unknown parameter, $\hat{P}, C, n_{\alpha,0}$, is globally identifiable.

We conclude that, for the phenomenological model, structural identifiability can be established for all parameters when both n_α and n_L are observed. When only one of n_α or n_L is observed, some model parameters must be measured separately to ensure global structural identifiability of the phenomenological ODE model. For cases where global identifiability cannot be concluded from GenSSI, other methods could be used to conduct further assessment.

3.3.4 Practical identifiability analysis of the phenomenological ODE model

To assess the practical identifiability of the phenomenological ODE model, we use it to generate synthetic data, and then attempt to estimate parameters by fitting the synthetic data to the phenomenological ODE model using a least squares approach. By comparing the estimated parameters with their true values, we gain insight into how well the model can be identified. We vary and infer $\hat{P}$ because it is unknown from the 1D PDE model and $\hat{k}_{-\alpha L}$ because it is of interest for drug development [19, 58].

We use the phenomenological ODE model to generate synthetic time series data for n_α and n_L at P_τ time-points in the time range $[0, T]$ (times $\tau = 0, \delta\tau, 2\delta\tau, ..., (P_\tau - 1)\delta\tau$) for different values of $\hat{k}_{-\alpha L}$ (0.01 to 1) and the production rate for IL-2, $\hat{P}$ (10^{-6}

to 10^2). We use a multiplicative noise model to introduce variability in the observed data for n_α and n_L:

$$y_i^{\text{obs}}(\tau) = y_i^{\text{true}}(\tau) \times (1 + \epsilon_i(\tau)), \tag{3.66}$$

where $\epsilon_i(\tau)$ are independent random variables following a Gaussian distribution with constant variance σ^2: $\epsilon_i(\tau) \sim \mathcal{N}(0, \sigma^2)$. $y_1(\tau) = n_\alpha(\tau)$, and $y_2(\tau) = n_L(\tau)$. The values of the fixed parameters are stated in Table 2.7. We fix $n_\alpha(0) = C$ and use Equation (3.41) to determine $n_L(0)$, solving for S given the value of $\hat{P}$. As before, to facilitate the application of least squares estimation, we apply a logarithmic transformation to the noise model, converting the multiplicative noise into an additive form, as in Equation (3.19).

We generate M replicates of the synthetic data to mimic repeated experiments. We apply a least squares approach to the logarithmically transformed data to estimate $\hat{k}_{-\alpha L}$ and $\hat{P}$:

$$\left(\hat{k}_{-\alpha L}^{\text{inf}}, \hat{P}^{\text{inf}}\right) = \arg \min_{(\hat{k}_{-\alpha L}, \hat{P})} \sum_{i=1}^{2} \sum_{j=1}^{P_\tau} \sum_{m=1}^{M} \left(\ln y_{i,j,m}^{\text{obs}} - \ln y_{i,j}^{\text{model}}(\hat{k}_{-\alpha L}, \hat{P})\right)^2, \tag{3.67}$$

where

$y_{i,j,m}^{\text{obs}}$	is the observed value of y_i at time $\tau_j = (j-1)\,\delta\tau$ for replicate m;
$y_{i,j}^{\text{model}}(\hat{k}_{-\alpha L}, \hat{P})$	is the model prediction of y_i at time τ_j given parameters $\hat{k}_{-\alpha L}$ and $\hat{P}$;
P_τ	is the total number of time points;
M	is the number of replicates for each time point.

For each fit, we compute the ratio of inferred to real values of $\hat{k}_{-\alpha L}$ and $\hat{P}$ $\left(\frac{\hat{k}_{-\alpha L}^{\text{inf}}}{\hat{k}_{-\alpha L}^{\text{true}}}, \frac{\hat{P}^{\text{inf}}}{\hat{P}^{\text{true}}}\right)$, and calculate the associated mean squared error (MSE):

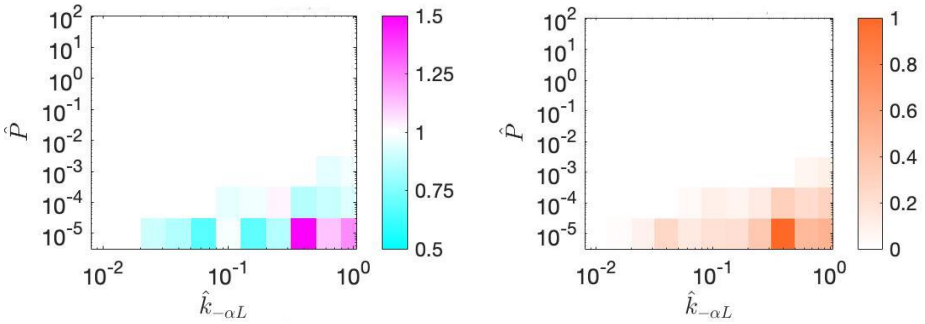
$$\text{MSE} = \frac{1}{2P_\tau M} \sum_{i=1}^{2} \sum_{j=1}^{P_\tau} \sum_{m=1}^{M} \left(\ln y_{i,j,m}^{\text{obs}} - \ln y_{i,j}^{\text{model}}(\hat{k}_{-\alpha L}^{\text{inf}}, \hat{P}^{\text{inf}})\right)^2, \tag{3.68}$$

to assess the goodness-of-fit. We repeat this process N times, each time generating a new synthetic data set with an independent stochastic noise realisation. We then calculate the mean and 95% confidence intervals of the ratio of the inferred and real values of $\hat{k}_{-\alpha L}$ and $\hat{P}$ and the mean squared error across the N fittings to assess the variability and uncertainty in the parameter estimates.

Results for noise-free synthetic data ($\sigma = 0$) and varying domain size R reveal similar patterns. The results for $R = 50$ are shown in Figure 3.6. We observe that the estimates for $\hat{k}_{-\alpha L}$ are not accurate for small values of $\hat{P}$ and large values of $\hat{k}_{-\alpha L}$. The mean values of the ratio of inferred to real values of $\hat{k}_{-\alpha L}$ range between 0.5 and 1.5, with margin of errors for 95% confidence interval of up to 1. This may be because, when IL-2 production is low and the dissociation rate is high, minimal binding occurs and changes in the dynamics are minimal, making it difficult to infer the parameter values. As the domain size increases, the parameter region in which the estimates are inaccurate expands. Estimates of $\hat{P}$ are always accurate, with mean values of the ratio of inferred to real values of $\hat{P}$ in the range 0.998 to 1.002, with a small margin of error. The mean values and margin of error for the mean squared error remain acceptable, with the highest observed values on the order of 10^{-5}.

Focusing on the parameter region where accurate estimation of $\hat{k}_{-\alpha L}$ is achieved using noise-free data, we increase the noise level in the synthetic data. As for the quasi-steady state model, we find that by appropriately selecting the time step ($\delta\tau$), the sampling time range (T), and the number of replicates (M), practical identifiability of $\hat{k}_{-\alpha L}$ and $\hat{P}$ can be achieved. Results for noise level $\sigma = 0.15$, with $\delta\tau = 10, T = 12000, M = 5$ and $R = 1.5$ are presented in Figure 3.7. We observe that, for noise levels up to $\sigma = 0.15$, the mean estimated values of $\hat{k}_{-\alpha L}$ and $\hat{P}$ deviate by less than 3% and 0.1% from their true values respectively with corresponding margin of errors for 95% confidence interval within 0.025 and 1.5×10^{-3} respectively. The mean values of the mean squared error are approximately 0.0225, with corresponding margin of error on the order of 10^{-5}.

We conclude that, even when noise is present in the synthetic datasets, the parameters $\hat{k}_{-\alpha L}$ and $\hat{P}$ are practically identifiable when the time step, the sampling time range and the number of replicates are suitably chosen, except in parameter regions where minimal binding of IL-2 to α chains occurs.



(a) Mean value of $\frac{\hat{k}_{-\alpha L,\text{inferred}}}{\hat{k}_{-\alpha L,\text{real}}}$. (b) MOE_{95} for $\frac{\hat{k}_{-\alpha L,\text{inferred}}}{\hat{k}_{-\alpha L,\text{real}}}$.

Figure 3.6: Practical identifiability of the phenomenological ODE model (Equations (3.32)–(3.34)) with noise-free synthetic data ($\sigma = 0$) with $R = 50$. Results for other values of R are omitted for brevity. Results from least squares estimation, generating synthetic data with $\hat{k}_{-\alpha L}$ from 0.01 to 1 and $\hat{P}$ from 10^{-5} to 10^2 and then inferring parameter estimates using the same model. Mean values and associated margin of errors for 95% confidence interval (MOE_{95}) for the ratio of inferred to real values of $\hat{k}_{-\alpha L}$ are presented in Panels (a) and (b) respectively. Mean values and associated margin of errors for 95% confidence interval for the ratio of inferred to real values of $\hat{P}$ and the mean squared error are omitted for brevity. $C = 1$. $\delta\tau = 10, T = 12000, M = 1, N = 5$. The values of the fixed parameters are stated in Table 2.7. We fix $n_\alpha(0) = C$ and use Equation (3.41) to determine $n_L(0)$, solving for S given the value of $\hat{P}$.

3.3.5 Parameter estimation

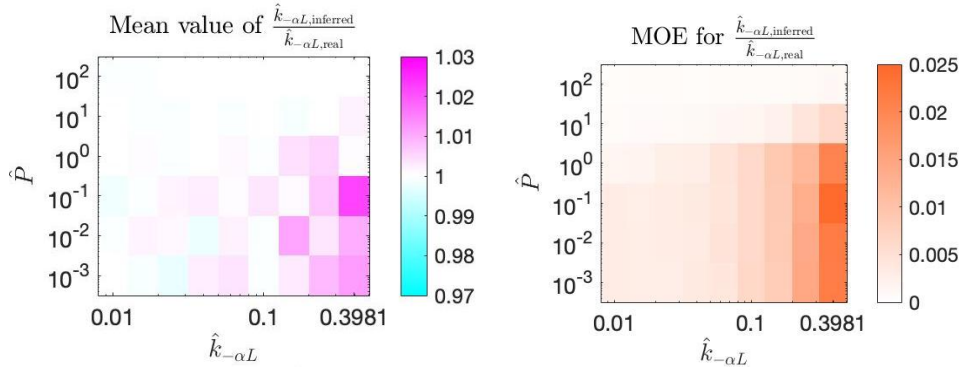
3.3.5.1 Matching steady states for the 1D PDE model and the phenomenological ODE model

For the phenomenological ODE model, the following expressions relate the parameters $\hat{k}_{-\alpha L}$ and $\hat{P}$ to the system steady states n_L^∞ and n_α^∞:

$$\hat{P} = \lambda^2 n_L^\infty, \tag{3.69}$$

$$\hat{k}_{-\alpha L} = \frac{\hat{k}_{\alpha L} n_L^\infty n_\alpha^\infty}{C - n_\alpha^\infty}. \tag{3.70}$$

We generate synthetic data by simulating the PDE model, with no noise, to estimate first the steady states, n_L^∞ and n_α^∞, and then $\hat{k}_{-\alpha L}$ and $\hat{P}$ in the ODE model, thus matching the steady states of the 1D PDE model and the ODE model. The numerical steady state for the average concentration of IL-2 in the bulk for the 1D PDE model is calculated to estimate n_L^∞. We simulate the ODE model with the estimated values for $\hat{k}_{-\alpha L}$ and $\hat{P}$ to determine whether the system dynamics agree with the PDE

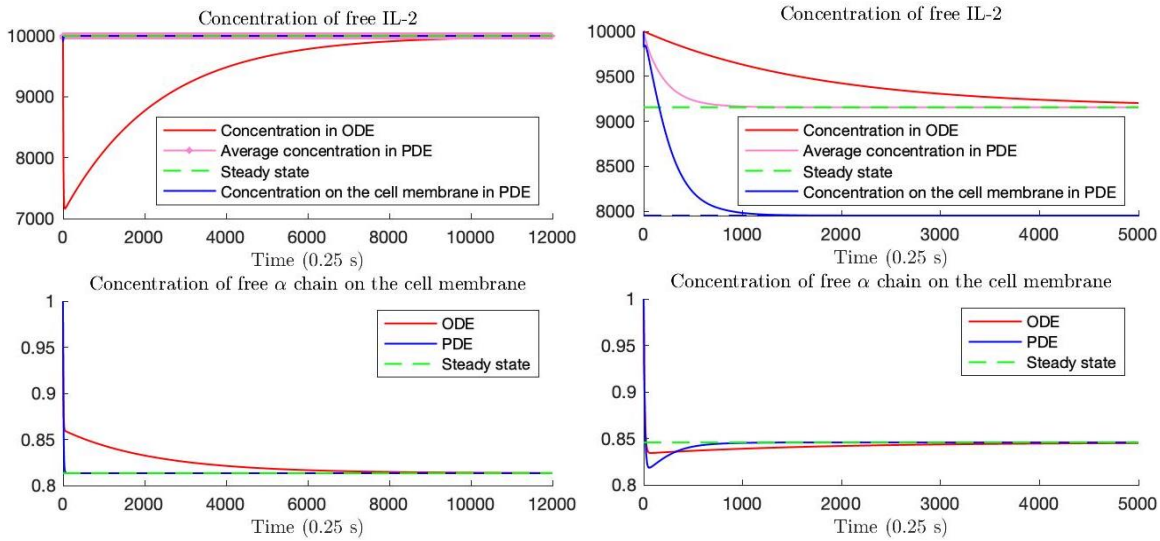


(a) Mean value of $\frac{\hat{k}_{-\alpha L,\text{inferred}}}{\hat{k}_{-\alpha L,\text{real}}}$. (b) MOE_{95} for $\frac{\hat{k}_{-\alpha L,\text{inferred}}}{\hat{k}_{-\alpha L,\text{real}}}$.

Figure 3.7: Practical identifiability of the phenomenological ODE model (Equations (3.32)–(3.34)) with $\sigma = 0.15$ in reduced parameter regions. Results from least squares estimation, when the parameters $\hat{k}_{-\alpha L}$, $\hat{P}$ and the noise levels vary in data generated with the phenomenological ODE model. $\hat{k}_{-\alpha L}$ is varied from 0.01 to 0.3981 and $\hat{P}$ from 10^{-3} to 10^2. Mean values and associated margin of errors for 95% confidence interval (MOE_{95}) for the ratio of inferred to real values of $\hat{k}_{-\alpha L}$ are presented in Panels (a) and (b) respectively. $R = 1.5, C = 1$. $\delta\tau = 10, T = 12000, M = 5, N = 100$. The values of the fixed parameters are stated in Table 2.7. We fix $n_\alpha(0) = C$ and use Equation (3.41) to determine $n_L(0)$, solving for S given the value of $\hat{P}$.

model. We vary R to determine how domain size affects the results. Data generated by the PDE model with different initial conditions for IL-2 are shown in Figure 2.2. Comparison between the ODE dynamics, using the estimated parameter values, and the PDE model which serves as the ground truth is shown in Figure 3.8. In Figure 3.9, we show how the estimated values of $\hat{k}_{-\alpha L}$ and $\hat{P}$ change as the domain size R varies.

We find that the steady states of the ODE model provide a good approximation to those of the 1D PDE model. However, initial transients in the 1D PDE model cannot be recovered by the ODE model. The ODE model approaches its steady state on a longer time-scale than the PDE model. The estimate of $\hat{k}_{-\alpha L}$ in the ODE model increasingly overestimates its value in the 1D PDE model as the domain size increases. This is because the difference between the average steady state concentration of IL-2 for the PDE model and its value on the cell membrane increases as R increases. The estimated value of $\hat{P}$ decreases as the domain size R increases because $\hat{P} = \lambda^2 n_L^\infty$ and the average concentration of IL-2 in the bulk for the PDE model, which is used to estimate n_L^∞, decreases with R. $\hat{k}_{-\alpha L}$ acquires an effective R dependence, indicating the limitations of this approach, especially for low cell densities (when R is large). Thus, the estimated parameters should be interpreted as effective quantities that encode the spatial effects of the PDE model rather than as intrinsic constants of the



(a) $R = 1.5$. Estimated $\hat{k}_{-\alpha L} = 0.0745$ and $\hat{P} = 5.7598$ in the ODE model. $n_L(r, 0) = S$.

(b) $R = 50$. Estimated $\hat{k}_{-\alpha L} = 0.08577$ and $\hat{P} = 5.2734$ in the ODE model. $n_L(r, 0) = S$.

Figure 3.8: Comparison between dynamics of the phenomenological ODE model (Equations (3.32)–(3.34)) and the PDE model (Equations (2.14)–(2.22)) with $\hat{k}_{-\alpha L}$ and $\hat{P}$ in the phenomenological ODE model estimated by matching its steady states with the PDE model. $\hat{k}_{-\alpha L} = 0.0745$ in the PDE model. Results for $R = 1.5$ and $R = 50$ are shown in Panels (a) and (b) respectively. Initial conditions: $n_L(r, 0) = S, n_\alpha(0) = C$. Results are also generated when the initial condition for IL-2 is $n_L(r, 0) = 0$ for $r \neq R$ and are consistent with the findings. We use $S = 10^4$, $C = 1$. The values of the other parameters are in Table 2.7.

ODE model.

We conclude that, although the phenomenological ODE model can reproduce the steady states, it cannot capture the transient behaviour of the 1D PDE model. The ODE model does not provide parameter values that are robust across changes in domain size, limiting its predictive accuracy and mechanistic interpretability.

3.3.5.2 Least squares estimation for the phenomenological ODE model using data generated by the 1D PDE model

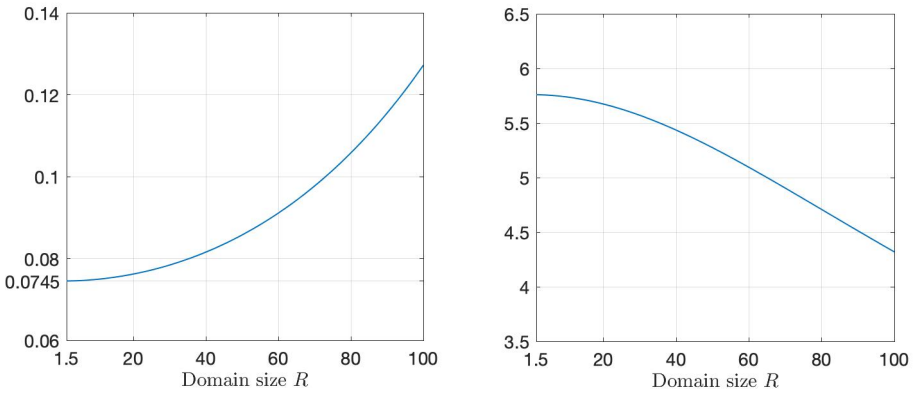
Given data for n_α and n_L generated by the 1D PDE model, we can also estimate $\hat{k}_{-\alpha L}$ and $\hat{P}$ in the ODE model using least squares estimation. As before, we generate synthetic noise-free time series data for n_α and n_L at P_τ time-points in the time range $[0, T]$ (times $\tau = 0, \delta\tau, 2\delta\tau, ..., (P_\tau - 1)\,\delta\tau$) using the PDE model and varying values of the domain size, R (1.5 to 100). We use average value of n_L in the bulk when

fitting to the ODE model. We estimate the values of $\hat{k}_{-\alpha L}$ and $\hat{P}$ by minimizing the relative squared error:

$$\text{Inferred } \left(\hat{k}_{-\alpha L}, \hat{P}\right) = \arg\min_{\left(\hat{k}_{-\alpha L}, \hat{P}\right)} \sum_{i=1}^{P_\tau} \left[\left(\frac{n_\alpha^{\text{obs}}(\tau_i) - n_\alpha^{\text{model}}(\tau_i; \hat{k}_{-\alpha L}, \hat{P})}{n_\alpha^{\text{obs}}(\tau_i)} \right)^2 + \left(\frac{n_{L,\text{avg}}^{\text{obs}}(\tau_i) - n_L^{\text{model}}(\tau_i; \hat{k}_{-\alpha L}, \hat{P})}{n_{L,\text{avg}}^{\text{obs}}(\tau_i)} \right)^2 \right], \tag{3.71}$$

where

$n_\alpha^{\text{obs}}(\tau_i)$	is the observed value of n_α at time $\tau_i = (i-1)\,\delta\tau$, generated by the 1D PDE model;
$n_\alpha^{\text{model}}(\tau_i; \hat{k}_{-\alpha L}, \hat{P})$	is the predicted value of n_α at time τ_j, given parameters $\hat{k}_{-\alpha L}$ and $\hat{P}$, generated by the phenomenological ODE model;
$n_{L,\text{avg}}^{\text{obs}}(\tau_i)$	is the observed value of the average concentration of IL-2 in the bulk, at time τ_i, generated by the 1D PDE model;
$n_L^{\text{model}}(\tau_i; \hat{k}_{-\alpha L}, \hat{P})$	is the predicted value of n_L, at time τ_i, given parameters $\hat{k}_{-\alpha L}$ and $\hat{P}$, generated by the phenomenological ODE model;
P_τ	is the total number of time points.



(a) Estimates of $\hat{k}_{-\alpha L}$. (b) Estimates of $\hat{P}$.

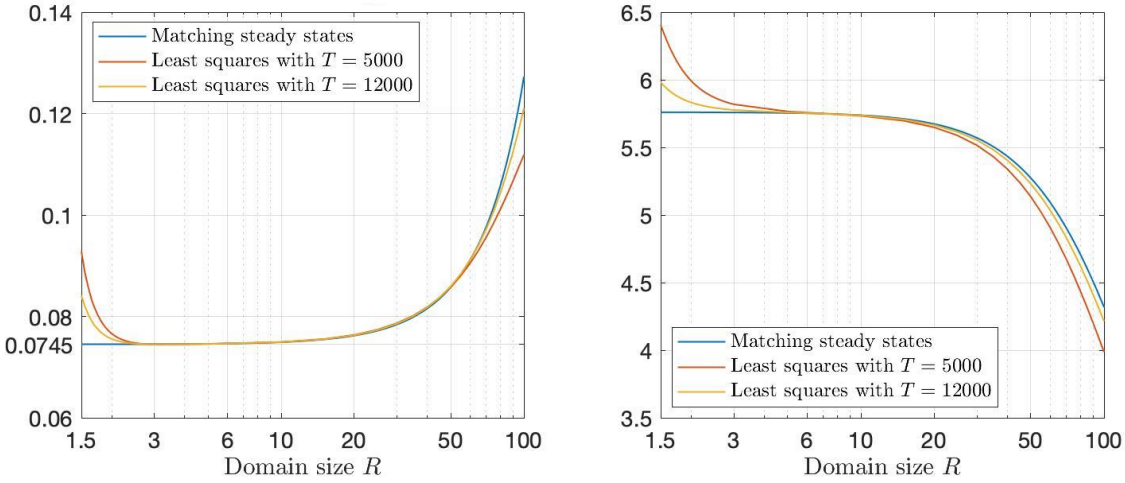
Figure 3.9: Estimated values of $\hat{k}_{-\alpha L}$ and $\hat{P}$ in the phenomenological ODE model (Equations (3.32)–(3.34)) as the domain size R varies by matching its steady states with the PDE model (Equations (2.14)–(2.22)). The expressions for the estimates are stated in Equations 3.69 and 3.70. $\hat{k}_{-\alpha L} = 0.0745$ in the PDE model. Initial conditions: $n_L(r, 0) = S, n_\alpha(0) = C$. We use $S = 10^4$, $C = 1$. The values of the other parameters are in Table 2.7.

We calculate the associated mean relative squared error (MRSE):

$$\text{MRSE} = \frac{1}{2P_\tau}\sum_{i=1}^{P_\tau}\left[\left(\frac{n_\alpha^{\text{obs}}(\tau_i) - n_\alpha^{\text{model}}(\tau_i;\hat{k}_{-\alpha L},\hat{P})}{n_\alpha^{\text{obs}}(\tau_i)}\right)^2 + \left(\frac{n_{L,\text{avg}}^{\text{obs}}(\tau_i) - n_L^{\text{model}}(\tau_i;\hat{k}_{-\alpha L},\hat{P})}{n_{L,\text{avg}}^{\text{obs}}(\tau_i)}\right)^2\right], \tag{3.72}$$

The estimated values of $\hat{k}_{-\alpha L}$ and $\hat{P}$ in the ODE model, along with the estimates from matching the steady states, are shown in Figure 3.10. We present estimates from least squares estimation using time ranges $T = 5000$ and $T = 12000$. The data generated by the 1D PDE model and the fitted curves using the ODE model are presented in Figure 3.11.

In Figure 3.10, we observe that the estimates of $\hat{k}_{-\alpha L}$ and $\hat{P}$ differ from those obtained by matching the steady states of the ODE and PDE models, particularly for small and large values of R. We note also that differences between the estimates decrease when a long time-scale ($T = 12000$) is used instead of a short one ($T = 5000$). This is because, in least squares estimation, the predicted concentration of IL-2 overshoots the steady state of the PDE model to minimize the cost function, as illustrated in Figure 3.11. When a long time-scale is used, more data points are collected closer to the steady state of the PDE model, decreasing the difference between the estimates. As before, the dependence of the estimated parameter values on the time-scale over which data are collected is a fitting artifact.



(a) Estimates of $\hat{k}_{-\alpha L}$.

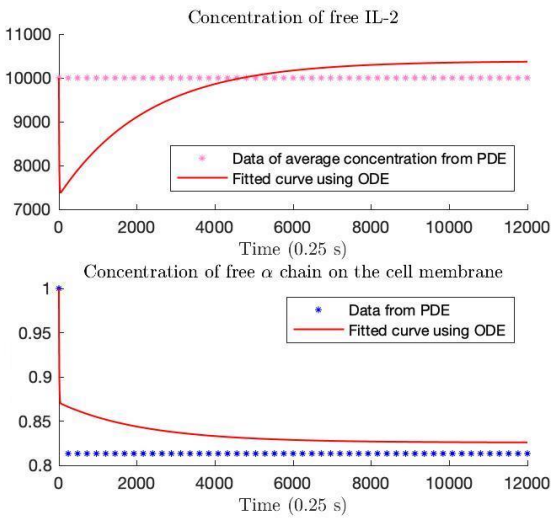
(b) Estimates of $\hat{P}$.

Figure 3.10: Estimated values of $\hat{k}_{-\alpha L}$ and $\hat{P}$ as the domain size R varies when the phenomenological ODE model (Equations (3.32)–(3.34)) is fitted to data generated by the 1D PDE model (Equations (2.14)–(2.22)). Estimates using time ranges $T = 5000$ and $T = 12000$ are presented together with those obtained by matching the steady states. $\hat{k}_{-\alpha L} = 0.0745$ in the PDE model. Fitted values of $\hat{k}_{-\alpha L}$ and $\hat{P}$ are shown in Panels (a) and (b) respectively. The values of R on the x-axis are presented on a logarithmic scale. $P_\tau = 51$. Initial conditions: $n_\alpha(0) = C$. $n_L(r, 0) = S$ for the PDE model; $n_L(0) = S$ for the ODE model. We use $S = 10^4$, $C = 1$. Values of the other parameters are in Table 2.7.

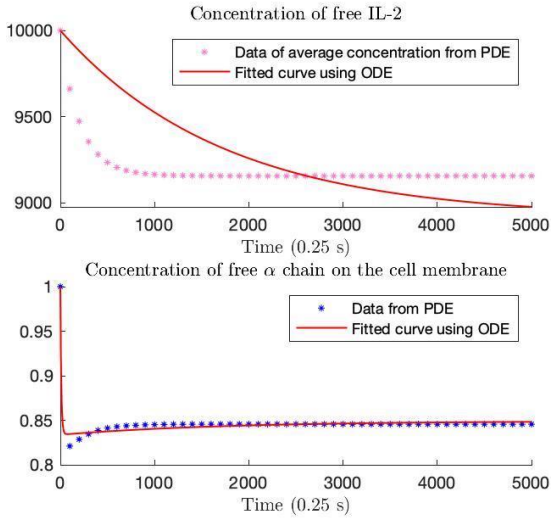
3.4 Comparison of the ODE models to the PDE model

To examine how well the two ODE models describe the 1D spatial model, we compare simulation results from the quasi-steady state model, the phenomenological ODE model and the 1D PDE model. Results with the same parameter values and quasi-steady initial conditions for the three models are shown in Figure 3.12 for two values of the domain size R. Comparison of the quasi-steady state model and the 1D PDE model, with non-quasi-steady initial conditions for the PDE model, is presented in Figure 3.13.

The quasi-steady state model provides a good approximation to the PDE model with quasi-steady initial conditions, even when the domain size is large ($R = 50$). When the PDE model is not initially at its quasi-steady state, the quasi-steady state model is a good representation of the PDE model only when the domain size R is small. This is because when the domain size is small, the concentration of IL-2 in the



(a) $R = 1.5$. Inferred $\hat{k}_{-\alpha L} = 0.0841$ and $\hat{P} = 5.9814$ in the phenomenological ODE model. Mean relative squared error is 2.976×10^{-3}.

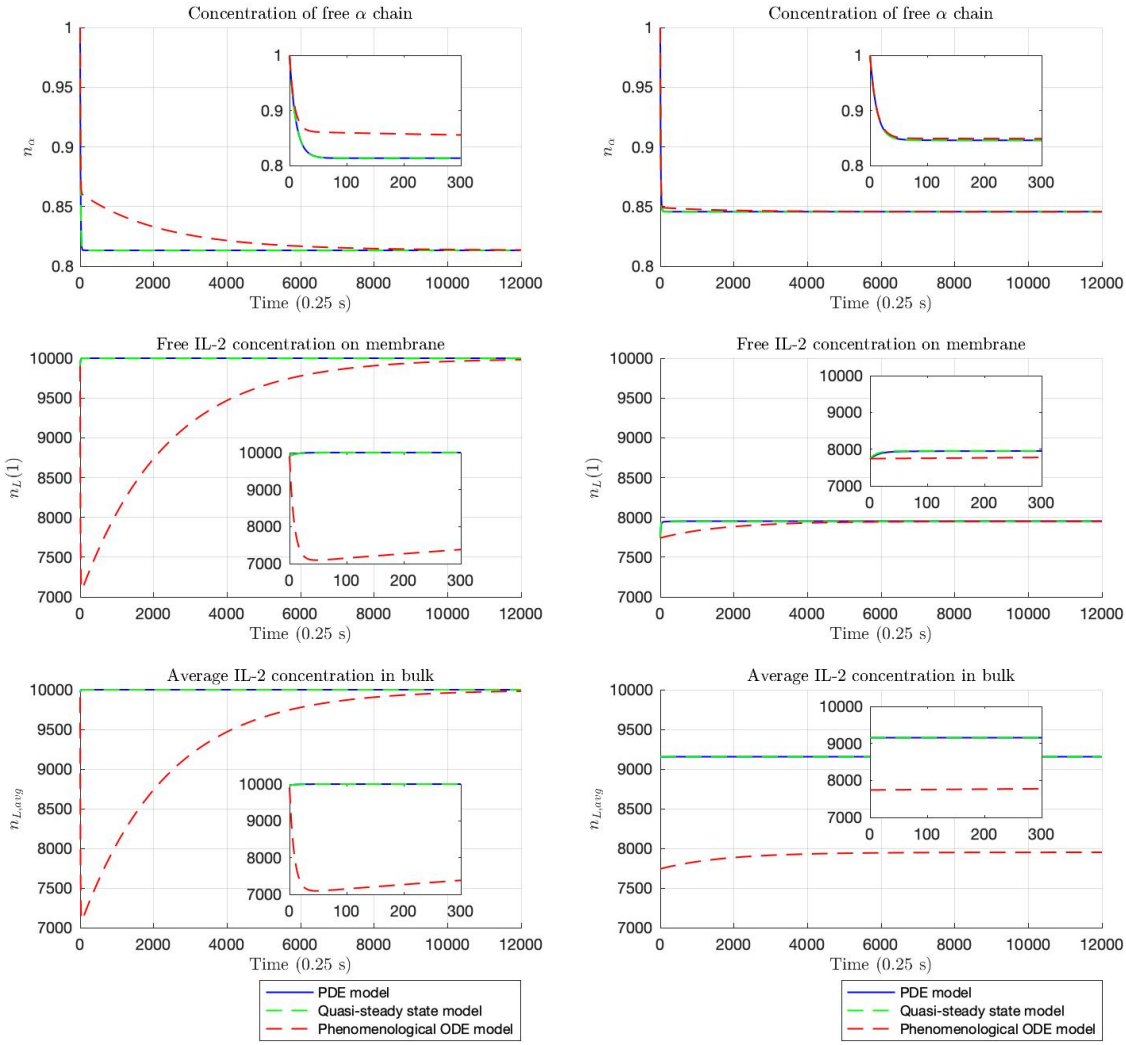


(b) $R = 50$. Inferred $\hat{k}_{-\alpha L} = 0.08581$ and $\hat{P} = 5.1349$ in the phenomenological ODE model. Mean relative squared error is 3.209×10^{-4}.

Figure 3.11: The data generated by the 1D PDE model (Equations (2.14)–(2.22)) and the fitted curves using the phenomenological ODE model (Equations (3.32)–(3.34)) by estimating $\hat{k}_{-\alpha L}$ and $\hat{P}$ using least squares estimation. Results for $R = 1.5$ and $R = 50$ are shown in Panels (a) and (b) respectively. Results for n_α and n_L are plotted. $\hat{k}_{-\alpha L} = 0.0745$ in the PDE model. $P_\tau = 51$. $T = 12000$ when $R = 1.5$; $T = 5000$ when $R = 50$. Initial conditions: $n_\alpha(0) = C$. $n_L(r, 0) = S$ for the PDE model; $n_L(0) = S$ for the ODE model. We use $S = 10^4$, $C = 1$. The values of the other parameters are in Table 2.7.

bulk rapidly approaches its quasi-steady state. More generally, the PDE model takes more time to relax to its steady state than the quasi-steady state model.

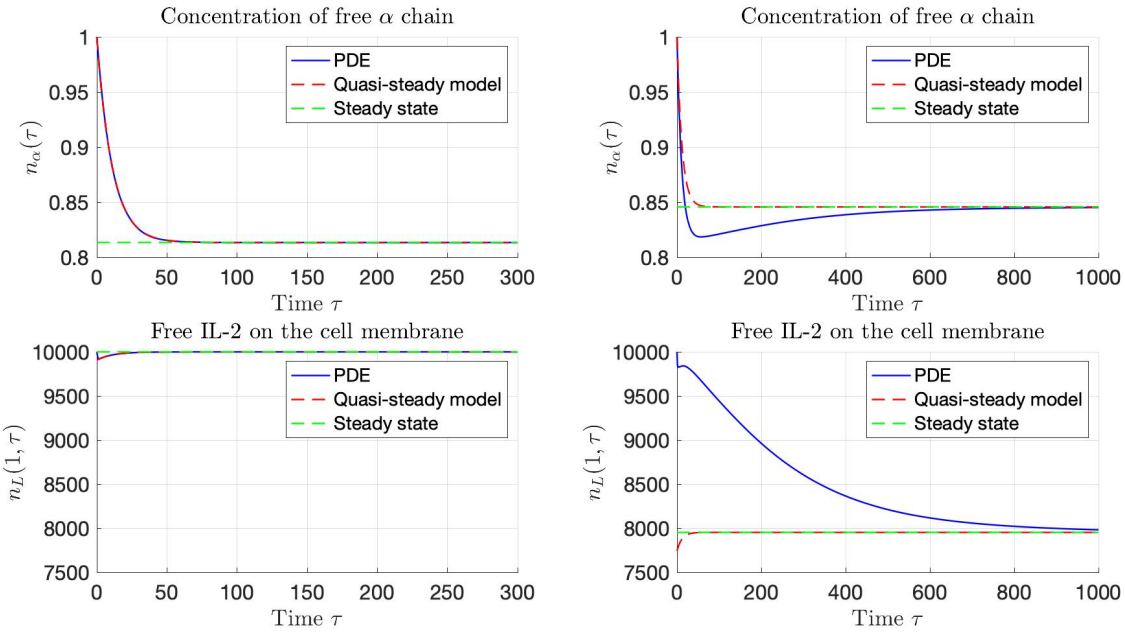
For the phenomenological ODE model, with the production rate $\hat{P}$ estimated from spatial information generated by the 1D model ($\hat{P} = \frac{S\lambda^3 R}{\sinh \lambda R}$ as from Section 3.3.2.2), the steady state values of the free α chain concentration and free IL-2 concentration are in good agreement with the free α chain concentration and free IL-2 concentration on the cell membrane from the PDE model as expected from the analysis in Section 3.3.2.2. However, the phenomenological model does not capture the initial transients in the PDE model. The concentration of free α chain and the concentration of free IL-2 evolve on a longer time-scale than for the PDE model. The decay rate for IL-2, λ^2, governs the time-scale on which the phenomenological ODE model relaxes to its steady state, which is consistent with the linear analysis of the ODE model (see Section 3.3.2.3). Also, when the domain size R is large, the phenomenological ODE



(a) $R = 1.5$. (b) $R = 50$.

Figure 3.12: Comparison of simulation results from the quasi-steady state model (Equations (3.10)–(3.13)) and the phenomenological ODE model (Equations (3.32)–(3.34)) to those of the PDE model (Equations (2.14)–(2.22)) with quasi-steady initial conditions with domain size $R = 1.5$ and $R = 50$. For both domain sizes, simulation results for the concentration of free α chain on the cell membrane, free IL-2 concentration on the cell membrane and average IL-2 concentration in the bulk are plotted as a function of time for each model. For the models: $n_\alpha(0) = 1$ and $n_L(r, 0)$ is calculated from the quasi-steady model. Parameter values in Tables 2.5 and 2.7 are used for the models. For the phenomenological ODE model, $\hat{P}$ is estimated by $\hat{P} = \frac{S\lambda^3 R}{\sinh \lambda R}$.

model does not accurately predict the average steady state concentration of IL-2 in the bulk from the PDE model. This is because when the domain size is large, the



(a) $R = 1.5$. $n_L(r,0) = S$ for the PDE model.

(b) $R = 50$. $n_L(r,0) = S$ for the PDE model.

Figure 3.13: Comparison of simulations from the quasi-steady state model (Equations (3.10)–(3.13)) to the PDE model (Equations (2.14)–(2.22)) with initial conditions that are not quasi-steady for the PDE model. For both models: $n_\alpha(0) = 1$. For the PDE model: $n_L(r,0) = S$. The initial conditions for IL-2 are not consistent for the two models. Parameter values in Tables 2.5 and 2.7 are used for the models. Results are similar when the initial condition for free IL-2 in the bulk in the PDE model is $n_L(r,0) = 0$ for $r \neq R$.

concentration of IL-2 on the cell membrane differs markedly from its average in the bulk; the phenomenological model is unable to capture this difference.

3.5 Discussion

This chapter assesses when the two simpler ODE models, the quasi-steady state model and the phenomenological ODE model, can approximate the spatial PDE model, and considers whether parameters from the simpler ODE models can be estimated, including the prospect of model misspecification.

For the phenomenological ODE model, we compared its steady state solutions to those of the 1D PDE model to see how this may constrain the phenomenological ODE model and to give a first indication of the quality of approximation that it provides. To understand the model's long-term behavior, we linearized the phenomenological

ODE model around its steady state. To guide experimental design and data collection to calibrate the two simpler models, we investigated their structural and practical identifiability. We examined structural identifiability of the models with different observables, using the scaling method and the generating series method by GenSSI 2.0 [14, 52]. To evaluate the practical identifiability of the models, we used the models themselves to generate synthetic data under various experimental conditions and then used a least squares approach to estimate the model parameters in each of these scenarios. By comparing the recovered parameters with their true values, we gained insights into how well the model can be identified under different conditions. To identify model misspecification, we used the 1D PDE model to generate synthetic data and estimated parameter values of the two simpler models by using a least squares approach. For the phenomenological ODE model, we also estimated the parameters of interest by matching its steady state solutions with those simulated by the PDE model. To investigate whether the two simpler models can represent the behaviour of the 1D spatial PDE model, we compared time-dependent simulation results from the three models.

For the phenomenological ODE model, with adjustment of the value of the production rate of IL-2 ($\hat{P}$), its steady states can match the bound α chain (or equivalently bound IL-2) and free IL-2 on the cell surface from the PDE model regardless of the domain size (R). From linearization of the phenomenological ODE model around its steady state, we find that the decay rate of IL-2, $\lambda^2 \ll 1$, governs the time-scale of relaxation to steady state in the ODE model, which explains why the time-scale is long when approaching the steady state of the system.

From structural identifiability analysis, we conclude that the quasi-steady state model maximizes the number of identifiable parameters when data for the concentration of α chains and the concentration of free IL-2 on the cell membrane are observable. Utilising the data for the average concentration of IL-2 reduces the number of parameters for which global identifiability can be established. When only the concentration of α chains can be observed, the model is least identifiable. However, obtaining data for the concentration of IL-2 on the cell membrane requires more advanced imaging techniques, which may not be readily accessible. Depending on the available data, some parameters need to be measured separately to ensure global structural identifiability of the model. The phenomenological ODE model is globally identifiable when data for both n_α and n_L are observed. When only one of n_α or n_L is observed, some model parameters must be measured separately to ensure

global structural identifiability of the phenomenological ODE model. From the practical identifiability analysis, we conclude that by strategically selecting the number of replicates, refining sampling strategies, and using accessible forms of data, $\hat{k}_{-\alpha L}$ in the quasi-steady state model and both $\hat{k}_{-\alpha L}$ and $\hat{P}$ in the phenomenological ODE model are practically identifiable under less-than-ideal conditions.

When estimating parameter values in the ODE models using data generated by the 1D PDE model, parameter values in the quasi-steady state model could be estimated accurately when the initial conditions for the PDE model are at its quasi-steady state. When the initial conditions for the IL-2 are not at quasi-steady state for the PDE model, the estimates of $\hat{k}_{-\alpha L}$ and the corresponding mean relative squared error get worse, with poor fitting to the initial transient as the domain size R increases. As the time span increases, the estimates for $\hat{k}_{-\alpha L}$ improve because the steady state solutions contribute more to the fitting. However, the fitting to the initial transient does not improve. For the phenomenological ODE model, when estimating parameter values by matching its steady state solutions with those from the PDE model, the estimate of $\hat{k}_{-\alpha L}$ deviates from its value in the PDE model and is larger as the domain size increases. This is because of the discrepancy between the value of average concentration of IL-2 and its value on the cell membrane. The estimated value of $\hat{P}$ decreases as the domain size R increases. This indicates difficulty with the phenomenological ODE model in terms of parameter estimation. The estimates of $\hat{k}_{-\alpha L}$ and $\hat{P}$ obtained from least squares estimation differ from those derived by matching the steady states of the ODE and PDE models. This is because, in least squares estimation, the predicted concentration of IL-2 overshoots the steady state of the PDE model to minimize the cost function. When a larger time-scale is used, more data points are collected at steady states of the PDE model, decreasing the difference between the estimates. This dependence of the estimated parameter values on the time-scale over which data are collected is again a fitting artifact.

From comparison of simulation results of the three models, we conclude that the quasi-steady state model accurately approximates the spatial model when the domain size is small or when the initial conditions are at a quasi-steady state. The quasi-steady state model describes the 1D PDE model well when the domain size is small because the concentration of IL-2 in the bulk approaches its quasi-steady state. If the initial conditions for the PDE model are not initially at quasi-steady state, the system takes longer to relax to its steady state than the quasi-steady state model. Although the phenomenological ODE model can match the steady state of the 1D

PDE model, it cannot capture its temporal behaviour, highlighting the importance of spatial effects for behavior on relatively fast timescales.

We conclude that whether to use one of the simpler ODE models or retain a spatial formulation depends on the specific research question. If the primary focus is on long-term receptor occupancy, the phenomenological ODE model may be sufficient. If the initial transients in the dynamics are important, such as when examining dosing strategies, spatial effects need to be preserved.

In chapters 2 and 3, we focused on IL-2 binding to α chains to isolate their specific role in capturing free IL-2 in the extracellular space and initiating the formation of the quaternary signalling complex (IL-2 bound to α, β and γ chains). However, to induce downstream signalling, IL-2 must bind to β and γ chains. In the next chapter, we will include the full binding kinetics, involving β and γ chains, in our mathematical models.

Chapter 4

1D PDE model with α, β, γ chains

4.1 Introduction

IL-2 stimulates T cells by binding to IL-2 receptors on their outer membrane. The building blocks of IL-2 receptors are α, β and γ chains (CD25, CD122 and CD132 respectively). In Chapters 2 and 3, we focused on the α chain for simplicity. In this chapter, we will consider models that have a higher fidelity to the biology by including β and γ chains.

Low and high doses of IL-2 have been used as immunotherapies to treat different diseases [3, 25]. Low doses of IL-2 are used to treat autoimmune and chronic inflammatory diseases, conditions characterized by reduced IL-2 signaling and relative dysfunction of regulatory T cells compared to effector T cells. Administration of low-dose IL-2 primarily activates regulatory T cells, helping to restore immune balance, although it may also stimulate some effector T cells. High doses of IL-2 predominantly stimulate and enhance the activity of effector T cells and natural killer (NK) cells. As such, high doses of IL-2 are used to treat metastatic cancer and immune deficiencies, including chronic HIV and other viral infections [21, 43].

T cells differ in their expression levels of different receptors [3]. Effector T cells express high levels of dimeric IL-2 receptors, consisting of β and γ chains; while regulatory T cells express high levels of α chains and intermediate levels of β and γ chains. Memory T cells do not possess α chains. We hypothesise that differences in the numbers of α, β and γ chains expressed by different types of T cells explain differences in their responses to IL-2.

As a step towards the rational development of IL-2-based immunotherapies to preferentially stimulate different types of T cells, this chapter compares the responses of different T cell types to IL-2 by extending the 1D PDE model from Chapter 2, to account for β and γ chains. For simplicity, we represent the β and γ chains as a

single β/γ dimer (henceforth referred to as the β chain), assuming that the γ chains are in excess and bind with IL-2 once it has bound with a β chain. We use the model to investigate how different types of T cells respond to different levels of IL-2, noting the variability of α and β chains for different types of T cells. The main quantities of interest are the concentrations of IL-2 complexes that contain the β chain because they induce downstream signalling. We examine the effects of changing the size of the domain to investigate the impact of different cell densities. We vary the production rate of β chains because estimates of its value are not well established and can be influenced by factors such as cell type, activation state, and external stimuli. We also examine the effects of simplified binding kinetics, as assumed in existing models in the literature [27, 45, 95], and identify when it is appropriate to neglect certain binding processes. To highlight critical parameters for experimental measurement and potential targets for intervention, we perform a global sensitivity analysis to investigate the parameters that most significantly influence the ability of IL-2 to stimulate downstream signalling for different types of T cells. These factors include the concentration of IL-2 in the extracellular space, the availability of α and β chains, the cell density and the kinetic rate constants.

The remainder of this chapter is organised as follows. In Section 4.2, we develop and parameterize the 1D PDE model with α and β chains. In section 4.3, we investigate how different types of T cells respond to different levels of IL-2, examine the effects of changing the synthesis rate of β chains and the domain size R, and consider different assumptions about the mechanisms involved in the formation of quaternary receptor complexes. In Section 4.4, we perform a global sensitivity analysis to assess the impact of parameter variations over their entire plausible ranges. We identify the parameters that have the strongest influence on the concentration of signalling complexes for different types of T cells. The chapter ends in Section 4.5, where we discuss our results and outline possible directions for future work.

4.2 Model development

4.2.1 Dimensional model

As further summarised in Figure 4.1, we inherit the geometry and extracellular IL-2 diffusion dynamics from Figure 2.1 in Chapter 2. We make the following modelling assumptions: IL-2 diffuses and decays in the extracellular space that surrounds the cell; α and β chains remain on the cell membrane. IL-2 binds reversibly to α and β chains, and the resulting complexes bind reversibly to whichever chain is left. [IL-2 : α] and

[IL-2 : β] complexes remain on the cell membrane; [IL-2 : α : β] complexes are internalised, and the α chain is recycled to the cell surface. β chains are synthesized.

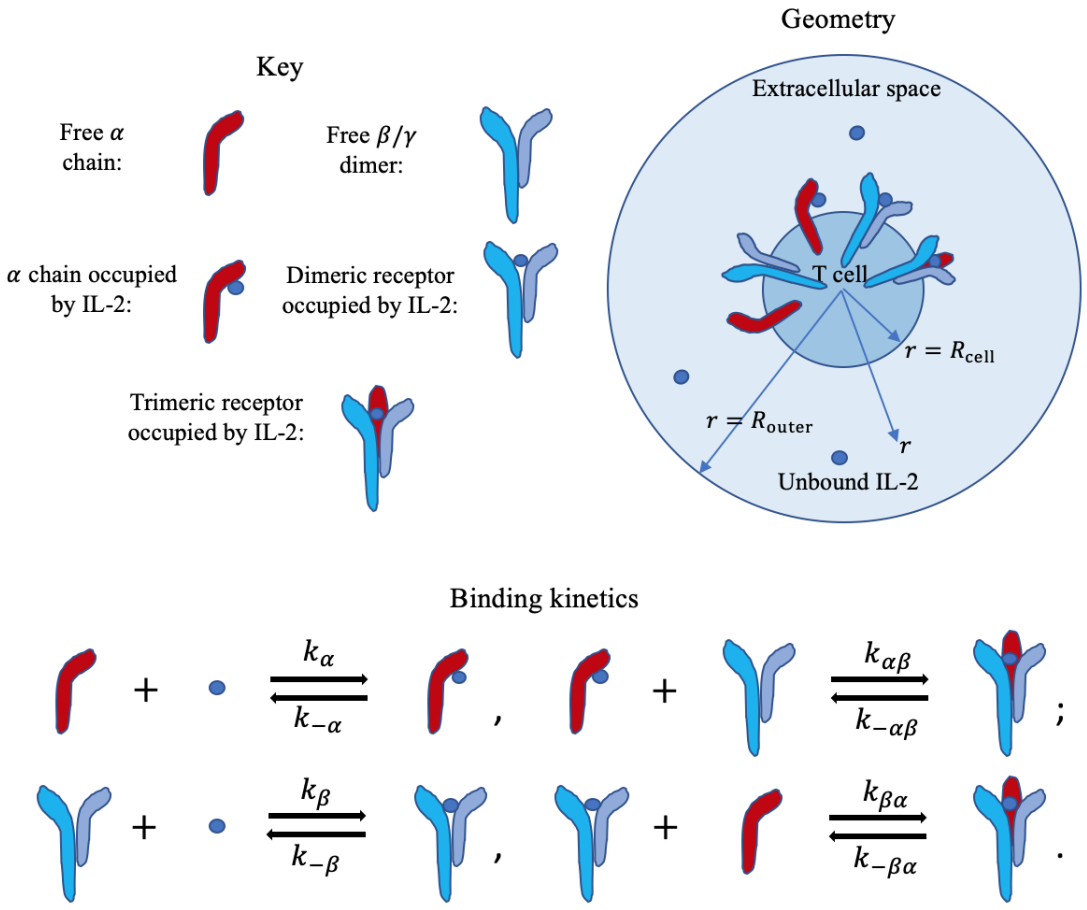


Figure 4.1: Schematic of geometry and binding kinetics for the 1D PDE model with α, β and γ chains. The key illustrates the different receptor configurations: free α chain, free β/γ dimer and their complexes with IL-2. The geometry depicts the T cell represented as a sphere of radius R_{cell} centered at the origin, embedded within a larger spherical extracellular domain of radius R_{outer}. Free IL-2 molecules diffuse in the extracellular space ($R_{\text{cell}} < r < R_{\text{outer}}$) and interact with receptors located on the cell membrane ($r = R_{\text{cell}}$). For the binding kinetics, IL-2 binds reversibly to α chains on the cell membrane, with on and off rates k_α and $k_{-\alpha}$ respectively; IL-2 binds reversibly to β chains on the cell membrane with on and off rates k_β and $k_{-\beta}$ respectively; β chains bind to [IL-2 : α] complexes reversibly with on and off rates $k_{\alpha\beta}$ and $k_{-\alpha\beta}$ respectively to form [IL-2 : α : β : γ] complexes; α chains bind to [IL-2 : β] complexes reversibly with on and off rates $k_{\beta\alpha}$ and $k_{-\beta\alpha}$ respectively to form [IL-2 : α : β : γ] complexes.

The dependent variables are $N_L(r, t)$ (the concentration of free IL-2 in the extra-

Variable	Interpretation	Unit
N_L	Concentration of free IL-2 in the bulk	Number/cm^3
N_α	Concentration of free α chain on the cell membrane	Number/cm^2
N_β	Concentration of free β chain on the cell membrane	Number/cm^2
$N_{\alpha L}$	Concentration of [IL-2 : α] complex	Number/cm^2
$N_{\beta L}$	Concentration of [IL-2 : β] complex	Number/cm^2
$N_{\alpha\beta L}$	Concentration of [IL-2 : α : β] complex	Number/cm^2

Table 4.1: Dependent variables and their units for the dimensional 1D PDE model with full binding kinetics.

Parameter	Interpretation	Unit
R_{cell}	Cell radius	cm
R_{outer}	Radius of the domain that the cell lies in (Distance between cells)	cm
D_L	Diffusion coefficient of IL-2 in the bulk	cm^2/s
Λ	Decay rate of IL-2	1/s
k_α	Binding on rate of IL-2 and α chain	cm^3/ (Number$\times$s)
$k_{-\alpha}$	Binding off rate of IL-2 and α chain	1/s
k_β	Binding on rate of IL-2 and β chain	cm^3/ (Number$\times$s)
$k_{-\beta}$	Binding off rate of IL-2 and β chain	1/s
$k_{\alpha\beta}$	Binding on rate of β chain and [IL-2 : α] complex	cm^2/ (Number$\times$s)
$k_{-\alpha\beta}$	Binding off rate of β chain and [IL-2 : α] complex	1/s
$k_{\beta\alpha}$	Binding on rate of α chain and [IL-2 : β] complex	cm^2/ (Number$\times$s)
$k_{-\beta\alpha}$	Binding off rate of α chain and [IL-2 : β] complex	1/s
I	Internalisation rate of the [IL-2 : α : β] complex	1/s
S_{outer}	Concentration of IL-2 at the outer boundary	Number/cm^3
$N_{\alpha,\text{TOT}}$	Total concentration of the α chain on the cell membrane	Number/cm^2
G_β	synthesis rate of the β chain	1/s
N_β^*	The concentration of the β chain in the absence of IL-2	Number/cm^2

Table 4.2: Parameters and their units for the 1D PDE model with full binding kinetics.

cellular space) with unit Number/cm^3, $N_\alpha(t)$, $N_\beta(t)$, $N_{\alpha L}(t)$, $N_{\beta L}(t)$ and $N_{\alpha\beta L}(t)$ (the concentrations of unbound α chains, unbound β chains, [IL-2 : α] complexes, [IL-2 : β] complexes and [IL-2 : α : β] complexes respectively), with units Number/cm^2. The physical interpretation and units of the dependent variables and model parameters are summarized in Tables 4.1 and 4.2 respectively.

By appealing to mass conservation and using the Law of Mass Action to model the binding kinetics, in a natural extension of the model from Chapter 2, it is straightforward to derive the following equations, which describe the evolution of the dependent

variables:

$$\frac{\partial N_L}{\partial t} = D_L \frac{1}{r^2}\frac{\partial}{\partial r}\left(r^2 \frac{\partial N_L}{\partial r}\right) - \Lambda N_L, \;\; R_{\text{cell}} < r < R_{\text{outer}}, \tag{4.1}$$

$$\frac{dN_\alpha}{dt} = -\left(k_\alpha N_L\left(R_{\text{cell}}, t\right) N_\alpha - k_{-\alpha} N_{\alpha L}\right) - \left(k_{\beta\alpha} N_{\beta L} N_\alpha - k_{-\beta\alpha} N_{\alpha\beta L}\right) + I N_{\alpha\beta L}, \tag{4.2}$$

$$\begin{aligned}\frac{dN_\beta}{dt} = &-\left(k_\beta N_L\left(R_{\text{cell}}, t\right) N_\beta - k_{-\beta} N_{\beta L}\right) - \left(k_{\alpha\beta} N_{\alpha L} N_\beta - k_{-\alpha\beta} N_{\alpha\beta L}\right) \\ &+ G_\beta\left(N_\beta^* - N_\beta - N_{\beta L} - N_{\alpha\beta L}\right),\end{aligned} \tag{4.3}$$

$$\frac{dN_{\alpha L}}{dt} = +\left(k_\alpha N_L\left(R_{\text{cell}}, t\right) N_\alpha - k_{-\alpha} N_{\alpha L}\right) - \left(k_{\alpha\beta} N_{\alpha L} N_\beta - k_{-\alpha\beta} N_{\alpha\beta L}\right), \tag{4.4}$$

$$\frac{dN_{\beta L}}{dt} = +\left(k_\beta N_L\left(R_{\text{cell}}, t\right) N_\beta - k_{-\beta} N_{\beta L}\right) - \left(k_{\beta\alpha} N_{\beta L} N_\alpha - k_{-\beta\alpha} N_{\alpha\beta L}\right), \tag{4.5}$$

$$\frac{dN_{\alpha\beta L}}{dt} = +\left(k_{\beta\alpha} N_{\beta L} N_\alpha - k_{-\beta\alpha} N_{\alpha\beta L}\right) + \left(k_{\alpha\beta} N_{\alpha L} N_\beta - k_{-\alpha\beta} N_{\alpha\beta L}\right) - I N_{\alpha\beta L}. \tag{4.6}$$

In Equation (4.1), IL-2 diffuses in the extracellular space with diffusion coefficient D_L (unit: cm^2/s), where it also undergoes linear decay with rate Λ (unit: s^{-1}). In Equation (4.2), α chains on the cell membrane bind reversibly with IL-2 on the cell membrane and also with [IL-2 : β] complexes. We assume that α chains are synthesised at the same rate as that at which [IL-2 : α : β] complexes are internalised at rate I (unit: s^{-1}). Similarly in Equation (4.3), β chains bind reversibly with IL-2 and [IL-2 : α] complexes on the cell membrane. We assume that β chains are produced at a rate proportional to the difference between the concentration of β chains in the absence of IL-2 (N_β^*, a constant with units Number/cm^2) and the total concentration of β chains in the system (i.e., free β chains and those in [IL-2 : β] and [IL-2 : α : β] complexes), with constant of proportionality G_β (unit: s^{-1}). In Equation (4.4), the [IL-2 : α] complex forms when IL-2 binds with an α chain; [IL-2 : α] complexes bind with β chains reversibly. Similarly in Equation (4.5), [IL-2 : β] complex forms when IL-2 binds with an β chain; [IL-2 : β] complexes bind with α chains reversibly. In Equation (4.6), the [IL-2 : α : β] complexes form when an α chain binds with a [IL-2 : β] complex and when a β chain binds with a [IL-2 : α] complex. [IL-2 : α : β] complexes are internalised at rate I (unit: s^{-1}).

We close Equations (4.1)–(4.6) by imposing the following boundary and initial conditions:

$$D_L \frac{\partial N_L}{\partial r}\left(R_{\text{cell}}, t\right) = +\left(k_\alpha N_L\left(R_{\text{cell}}, t\right) N_\alpha - k_{-\alpha} N_{\alpha L}\right) + \left(k_\beta N_L\left(R_{\text{cell}}, t\right) N_\beta - k_{-\beta} N_{\beta L}\right), \tag{4.7}$$

$$N_L\left(R_{\text{outer}}, t\right) = S_{\text{outer}}. \tag{4.8}$$

$$N_L(r,0) = S_{\text{outer}},\ R_{\text{cell}} < r < R_{\text{outer}},\ N_\alpha(0) = N_{\alpha,\text{TOT}},\ N_\beta(0) = N_\beta^*, \tag{4.9}$$

$$N_{\alpha L}(0) = 0,\ N_{\beta L}(0) = 0,\ N_{\alpha\beta L}(0) = 0. \tag{4.10}$$

Equation (4.7) balances the flux of IL-2 from the extracellular space with its net rate of binding to α and β chains on the cell surface (i.e. $r = R_{\text{cell}}$). In Equation (4.8), we assume further that the concentration of IL-2 at the outer boundary ($r = R_{\text{outer}}$) is maintained at the constant value S_{outer}.

Following from the stated ODEs, we have conservation of the total concentration of α chains, so that:

$$N_\alpha + N_{\alpha L} + N_{\alpha\beta L} = N_{\alpha,\text{TOT}}. \tag{4.11}$$

4.2.2 Non-dimensionalisation

We non-dimensionalise time with the time-scale for IL-2 to diffuse over a distance of R_{cell} ($\overline{\tau} = \frac{R_{\text{cell}}^2}{D_L}$) and distance r with the cell radius (R_{cell}). We rescale the concentration of IL-2 in the bulk (N_L) by a typical concentration ($\overline{N_L}$), and the concentration of α chains (N_α), β chains (N_β), [IL-2 : α] complexes ($N_{\alpha L}$), [IL-2 : β] complexes ($N_{\beta L}$) and [IL-2 : α : β] complexes ($N_{\alpha\beta L}$), with respect to a typical concentration of α chains on the cell membrane ($\overline{N_\alpha}$).

In summary, we have the following dimensionless independent variables for time and the radial component:

$$\tau = \overline{\tau} t,\ \text{where } \overline{\tau} = \frac{D_L}{R_{\text{cell}}^2},\ r^* = \frac{r}{R_{\text{cell}}}, \tag{4.12}$$

and the scalings:

$$n_L = \frac{N_L}{\overline{N_L}},\ n_i = \frac{N_i}{\overline{N_\alpha}},\ i \in \{\alpha,\ \alpha L,\ \beta,\ \beta L,\ \alpha\beta L\}. \tag{4.13}$$

We also introduce the following parameter groupings:

$$\begin{aligned}
&\hat{k}_\alpha = \overline{\tau}\overline{N_L}k_\alpha, \hat{k}_{-\alpha} = \overline{\tau}k_{-\alpha}, \hat{k}_\beta = \overline{\tau}\overline{N_L}k_\beta, \hat{k}_{-\beta} = \overline{\tau}k_{-\beta}, \hat{k}_{\beta\alpha} = \overline{\tau}\overline{N_\alpha}k_{\beta\alpha},\\
&\hat{k}_{-\beta\alpha} = \overline{\tau}k_{-\beta\alpha}, \hat{k}_{\alpha\beta} = \overline{\tau}\overline{N_\alpha}k_{\alpha\beta}, \hat{k}_{-\alpha\beta} = \overline{\tau}k_{-\alpha\beta}, n_\alpha^* = \frac{N_{\alpha,\text{TOT}}}{\overline{N_\alpha}}, \hat{G}_\beta = \overline{\tau}G_\beta,\\
&n_\beta^* = \frac{N_\beta^*}{\overline{N_\alpha}}, \lambda = \sqrt{\frac{R^2}{D_L}\Lambda}, \hat{I} = \overline{\tau}I, R = \frac{R_{\text{outer}}}{R_{\text{cell}}}, S = \frac{S_{\text{outer}}}{\overline{N_L}}, \hat{T} = \frac{\overline{N_\alpha}}{R_{\text{cell}}\overline{N_L}}.
\end{aligned} \tag{4.14}$$

Then, the model transforms to give:

$$\frac{\partial n_L}{\partial \tau} = \frac{1}{r^2}\frac{\partial}{\partial r}\left(r^2 \frac{\partial n_L}{\partial r}\right) - \lambda^2 n_L, \tag{4.15}$$

$$\frac{dn_\alpha}{d\tau} = -\left(\hat{k}_\alpha n_L\left(1,\tau\right) n_\alpha - \hat{k}_{-\alpha} n_{\alpha L}\right) - \left(\hat{k}_{\beta\alpha} n_{\beta L} n_\alpha - \hat{k}_{-\beta\alpha} n_{\alpha\beta L}\right) + \hat{I} n_{\alpha\beta L}, \tag{4.16}$$

$$\begin{aligned}\frac{dn_\beta}{d\tau} &= -\left(\hat{k}_\beta n_L\left(1,\tau\right) n_\beta - \hat{k}_{-\beta} n_{\beta L}\right) - \left(\hat{k}_{\alpha\beta} n_{\alpha L} n_\beta - \hat{k}_{-\alpha\beta} n_{\alpha\beta L}\right) \\ &+ \hat{G}_\beta\left(n_\beta^* - n_\beta - n_{\beta L} - n_{\alpha\beta L}\right),\end{aligned} \tag{4.17}$$

$$\frac{dn_{\alpha L}}{d\tau} = +\left(\hat{k}_\alpha n_L\left(1,\tau\right) n_\alpha - \hat{k}_{-\alpha} n_{\alpha L}\right) - \left(\hat{k}_{\alpha\beta} n_{\alpha L} n_\beta - \hat{k}_{-\alpha\beta} n_{\alpha\beta L}\right), \tag{4.18}$$

$$\frac{dn_{\beta L}}{d\tau} = +\left(\hat{k}_\beta n_L\left(1,\tau\right) n_\beta - \hat{k}_{-\beta} n_{\beta L}\right) - \left(\hat{k}_{\beta\alpha} n_{\beta L} n_\alpha - \hat{k}_{-\beta\alpha} n_{\alpha\beta L}\right), \tag{4.19}$$

$$\frac{dn_{\alpha\beta L}}{d\tau} = +\left(\hat{k}_{\beta\alpha} n_{\beta L} n_\alpha - \hat{k}_{-\beta\alpha} n_{\alpha\beta L}\right) + \left(\hat{k}_{\alpha\beta} n_{\alpha L} n_\beta - \hat{k}_{-\alpha\beta} n_{\alpha\beta L}\right) - \hat{I} n_{\alpha\beta L}, \tag{4.20}$$

with boundary conditions,

$$\frac{\partial n_L}{\partial r}\left(1,\tau\right) = +\hat{T}\left(\hat{k}_\alpha n_L\left(1,\tau\right) n_\alpha - \hat{k}_{-\alpha} n_{\alpha L}\right) + \hat{T}\left(\hat{k}_\beta n_L\left(1,\tau\right) n_\beta - \hat{k}_{-\beta} n_{\beta L}\right), \tag{4.21}$$

$$n_L\left(R,\tau\right) = S, \tag{4.22}$$

conservation of α chain,

$$n_\alpha + n_{\alpha L} + n_{\alpha\beta L} = n_\alpha^*, \tag{4.23}$$

and initial conditions,

$$n_L\left(r,0\right) = S,\ 1 < r < R, \tag{4.24}$$

$$n_\alpha(0) = n_\alpha^*,\ n_\beta(0) = n_\beta^*,\ n_{\alpha L}(0) = 0, \tag{4.25}$$

$$n_{\beta L}(0) = 0,\ n_{\alpha\beta L}(0) = 0. \tag{4.26}$$

We assume that at $\tau = 0$, the receptor system is in a steady state established prior to the introduction of IL-2. Thus, all α and β chains are initially unbound. To model the experimental condition of rapid ligand addition, we set the initial IL-2 concentration to be uniform throughout the domain at S. While this initialization is consistent with the Dirichlet boundary condition at the outer boundary, this idealized initial condition induces a fast initial transient at the cell surface as the boundary and initial conditions are not compatible.

4.2.3 Model parametrization

Where possible, we use data from the literature to parameterize our 1D PDE model. In Tables 4.3 and Table 4.4, we collate data for the parameters and typical values of the dependent variables. To the best of our knowledge, direct measurements of $k_{\alpha\beta}$, $k_{-\alpha\beta}$, $k_{\beta\alpha}$ and $k_{-\beta\alpha}$ are not available in the literature. The parameter values we use were obtained in [27, 45] by fitting mathematical models to in vitro experimental data. Values of dimensional parameters estimated from the available data are shown in Tables 4.5. The corresponding dimensionless parameter values are summarized in Table 4.6. As motivated in the introduction, the dimensionless parameters we will vary are R (size of the domain), $\hat{G}_\beta$ (synthesis rate of β chains), n^*_β (availability of β chains in absence of IL-2), S (level of IL-2 available) and n^*_α (availability of α chains).

Variable	Data	Data type	Description and Citation
N_L	$[10^{-4}, 10^4]$ pM	Range	IL-2 concentrations to which T cells are exposed in vitro [27]
	125 pM		Concentration of IL-2 used to culture PBMCs in vitro [39]
N_α	2000 per cell		In vitro activated human effector T cells [3]
	$[0,10^3]$ per cell	Range	In vitro human effector T cells with peptide stimulation [27]
	10^4 per cell	Geometric mean	In vitro human regulatory T cells [27]
N_β	$[10^2,10^4]$ per cell	Range	In vitro human effector and regulatory T cells with antigen stimulation [27]

Table 4.3: Typical values for N_L, N_α and N_β in the 1D PDE model with α and β chains.

Parameter	Data	Note	Description and Citation
R_{cell}	2.5–5 μm	Range	In vitro activated human T cells [39]
D_L	$9.2 \pm 2\,(10^{-7})$ cm^2/s	Mean ± SEM	Diffusion of human IL-2 from HEK 293 cell in live mouse lymph node tissue [76]
Λ	5–7 min	Range for half life of IL-2	In vivo half life of human IL-2 from a Jurkat cell line in serum [56]
	3.7 ± 0.8 min	Mean ± SD for half life of IL-2	In vivo half life of IL-2 in murine serum [22]
k_α	1.4×10^7 M^{-1}s^{-1}		In vitro for human IL-2 from E. coli, MT-1 cells [94]
	$1.06 \pm 0.02\,(10^7)$ M^{-1}s^{-1}	Mean ± SD	Biosensor analysis (surface plasmon resonance) for recombinant human IL-2 and α chain [55]
$k_{-\alpha}$	0.4 s^{-1}		In vitro for human IL-2 from E. coli, MT-1 cells [94]
	0.298 ± 0.004 s^{-1}	Mean ± SD	Biosensor analysis (surface plasmon resonance) for recombinant human IL-2 and α chain [55]
k_β	3.8×10^5 M^{-1}s^{-1}		In vitro for human IL-2 from E. coli, YT-2C2 membranes [94]
$k_{-\beta}$	2.5×10^{-4} s^{-1}		In vitro for human IL-2 from E. coli, YT-2C2 membranes [94]
I	15 min	Half life of [IL-2 : α : β]	In vitro for recombinant IL-2, a human tumor T cell line [23]
	1.1×10^{-3} s^{-1}		In vitro for recombinant IL-2, human T cell [30, 27, 31]
$k_{\alpha\beta}$	3×10^{-4} s^{-1} $\times A$		Fitting mathematical models to in vitro human/mice data [27]
	2.2×10^{-3} s^{-1} $\times A$		Fitting mathematical models to in vitro human/mice data [45]
$k_{-\alpha\beta}$	2.3×10^{-4} s^{-1}		Fitting mathematical models to in vitro human/mice data [27]
	3×10^{-3} s^{-1}		Fitting mathematical models to in vitro human/mice data [45]
$k_{\beta\alpha}$	0.6×10^{-2} s^{-1} $\times A$		Fitting mathematical models to in vitro human/mice data [45]
$k_{-\beta\alpha}$	0.6 s^{-1}		Fitting mathematical models to in vitro human/mice data [45]

Table 4.4: Data available in the literature for the parameters in the 1D model with α chain and β/γ dimer. $A = 4\pi R_{\text{cell}}^2$ is the area of the cell membrane with units cm^2.

Parameter	Units	Estimated value
R_{cell}	Length	5×10^{-4} cm
D_L	Length^2/Time	10^{-6} cm^2/s
Λ	1/Time	0.00231 s^{-1} (Half life of IL-2: 5 min)
k_α	Length^3/(Number$\times$Time)	1.760×10^{-14} cm^3/(Number$\times$s) $\left(1.06 \times 10^7 \text{ M}^{-1}\text{s}^{-1}\right)$
$k_{-\alpha}$	1/Time	0.298 s^{-1}
k_β	Length^3/(Number$\times$Time)	3.8×10^5 M^{-1}s^{-1}
$k_{-\beta}$	1/Time	2.5×10^{-4} s^{-1}
$k_{\alpha\beta}$	Length^2/(Number$\times$Time)	3×10^{-4} s^{-1} $\times A$
$k_{-\alpha\beta}$	1/Time	2.3×10^{-4} s^{-1}
$k_{\beta\alpha}$	Length^2/(Number$\times$Time)	0.6×10^{-2} s^{-1} $\times A$
$k_{-\beta\alpha}$	1/Time	0.6 s^{-1}
I	1/Time	1.1×10^{-3} s^{-1}
R_{outer}	Length	Varied
S_{outer}	Number/Length^3	Varied
$N_{\alpha,\text{TOT}}$	Number/Length^2	Varied
G_β	1/Time	Varied
N_β^*	Number/Length^2	Varied
$\overline{N_L}$	Number/Length^3	3.885×10^8 Number/cm^3 (IL-2 typical: 10 pg/ml, molecular weight of IL-2: 15.5 kDa [77])
$\overline{N_\alpha}$	Number/Length^2	3.183×10^9 Number/cm^2 (Number of α chains: 10^4)

Table 4.5: Reference values of the parameters for the 1D PDE model with α and β chains.

Parameter	Expression	Value
$\hat{k}_\alpha$	$\frac{R_{\text{cell}}^2}{D_L}\overline{N_L}k_\alpha$	1.710×10^{-6}
$\hat{k}_{-\alpha}$	$\frac{R_{\text{cell}}^2}{D_L}k_{-\alpha}$	0.0745
$\hat{k}_\beta$	$\frac{R_{\text{cell}}^2}{D_L}\overline{N_L}k_\beta$	6.13×10^{-8}
$\hat{k}_{-\beta}$	$\frac{R_{\text{cell}}^2}{D_L}k_{-\beta}$	6.25×10^{-5}
$\hat{k}_{\alpha\beta}$	$\overline{\tau}\overline{N_\alpha}k_{\alpha\beta}$	0.75
$\hat{k}_{-\alpha\beta}$	$\overline{\tau}k_{-\alpha\beta}$	5.75×10^{-5}
$\hat{k}_{\beta\alpha}$	$\overline{\tau}\overline{N_\alpha}k_{\beta\alpha}$	15
$\hat{k}_{-\beta\alpha}$	$\overline{\tau}k_{-\beta\alpha}$	0.15
$\hat{T}$	$\frac{\overline{N_\alpha}}{R_{\text{cell}}\overline{N_L}}$	1.639×10^4
λ	$\sqrt{\frac{R_{\text{cell}}^2}{D_L}\Lambda}$	0.024
$\hat{I}$	$\overline{\tau}I$	2.75×10^{-4}
R	$\frac{R_{\text{outer}}}{R_{\text{cell}}}$	Varied
$\hat{G}_\beta$	$\overline{\tau}G_\beta$	Varied
n_β^*	$\frac{N_\beta^*}{\overline{N_\alpha}}$	Varied
S	$\frac{S_{\text{outer}}}{\overline{N_L}}$	Varied
n_α^*	$\frac{N_{\alpha,\text{TOT}}}{\overline{N_\alpha}}$	Varied

Table 4.6: Dimensionless parameters in the 1D spatial model with full binding kinetics. The values are calculated using reference values of the dimensional parameters in Table 4.5.

4.3 Preferential stimulation of IL-2

Different types of T cells express different numbers of receptors, and each type has a different binding affinity for IL-2. These differences may explain why different types of T cells respond differently to IL-2. Estimates of the number of α and β chains on different types of T cells are given in Table 4.7 [3, 27]. In this section, we use our model to investigate how these differences affect the response of different types of T cells to different levels of IL-2. We also examine the effect of changing the domain size R, and the synthesis rate of β chains $\hat{G}_\beta$, for which data are not available, and the effect of simplifying the binding kinetics.

4.3.1 Preferential stimulation of different types of T cells with varying levels of IL-2

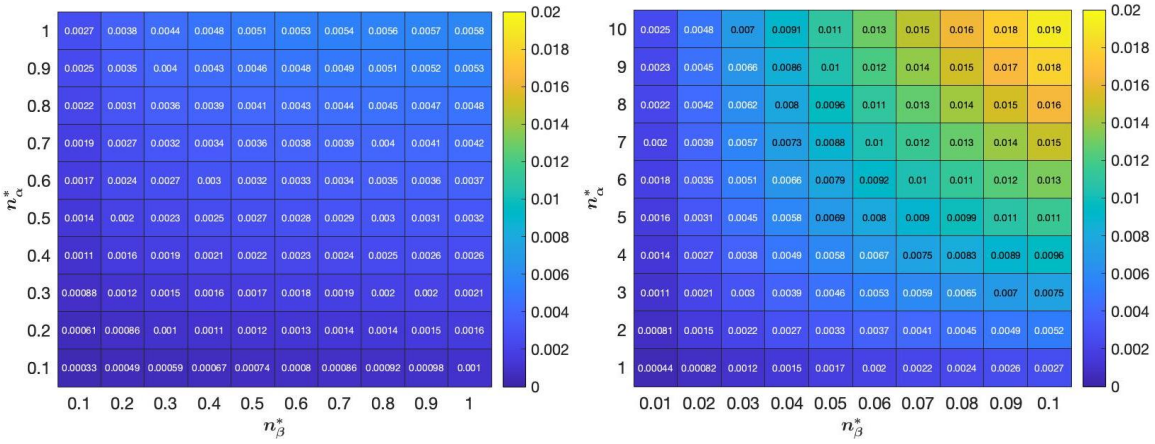
To examine how different types of T cells respond to different levels of IL-2, we obtain the steady state solutions of the 1D PDE model by numerically solving the steady nonlinear algebraic system in MATLAB with `vpasolve` (Symbolic Math Toolbox). To validate these solutions, we simulate the 1D PDE system over a sufficiently long time interval to ensure that the solution has converged to equilibrium and verify that the same steady state is obtained. The steady state solutions for the concentrations of [IL-2 : β] and [IL-2 : α : β] complexes are denoted as $n^\infty_{\beta L}$ and $n^\infty_{\alpha\beta L}$ respectively. The total concentration of the signalling complexes ($n^\infty_{\beta L} + n^\infty_{\alpha\beta L}$) induces downstream signalling and is thus the quantity of interest. We vary the total concentrations of α and β chains (n^*_α and n^*_β respectively) to represent different types of T cells using the values stated in Table 4.7. We control the concentration of IL-2 in the system by varying the value of S.

Heatmaps of the steady state solutions for the total concentration of the signalling complexes ($n^\infty_{\beta L} + n^\infty_{\alpha\beta L}$) for different types of T cells with $S = 1$ (low level of IL-2), $S = 100$ (intermediate level of IL-2) and $S = 10^4$ (high level of IL-2) are shown in Figures 4.2, Figures 4.3 and Figures 4.4 respectively. For each type of T cell, we vary the total concentration of α and β chains across their physical ranges. From Figure 4.2, we observe that at low concentrations of IL-2, regulatory T cells are preferentially stimulated. From Figure 4.3, we conclude that at intermediate concentrations of IL-2, effector T cells are preferentially stimulated, and memory CD8+ cells start to respond. From Figure 4.4, we observe that at high concentrations of IL-2, memory CD8+ and effector T cells are preferentially stimulated, with the signalling level of memory CD4+ T cells exceeding that of regulatory T cells. The heatmaps show that

T cell type	α chain	β chain
Effector T cell	$\sim 10^3 - 10^4$	$\sim 10^3 - 10^4$
Regulatory T cell	$\sim 10^4 - 10^5$	$\sim 10^2 - 10^3$
Memory CD4+ T cell	0	$\sim 10^2 - 10^3$
Memory CD8+ T cell	0	$\sim 10^3 - 10^4$

Table 4.7: Availability of α and β chains (Number/cell) for different types of T cells, estimated from literature [3, 27].

T cells of the same type can react differently to the same IL-2 levels, driven by the variability across the physiological ranges of α and β chain expression.



(a) Effector T cell.

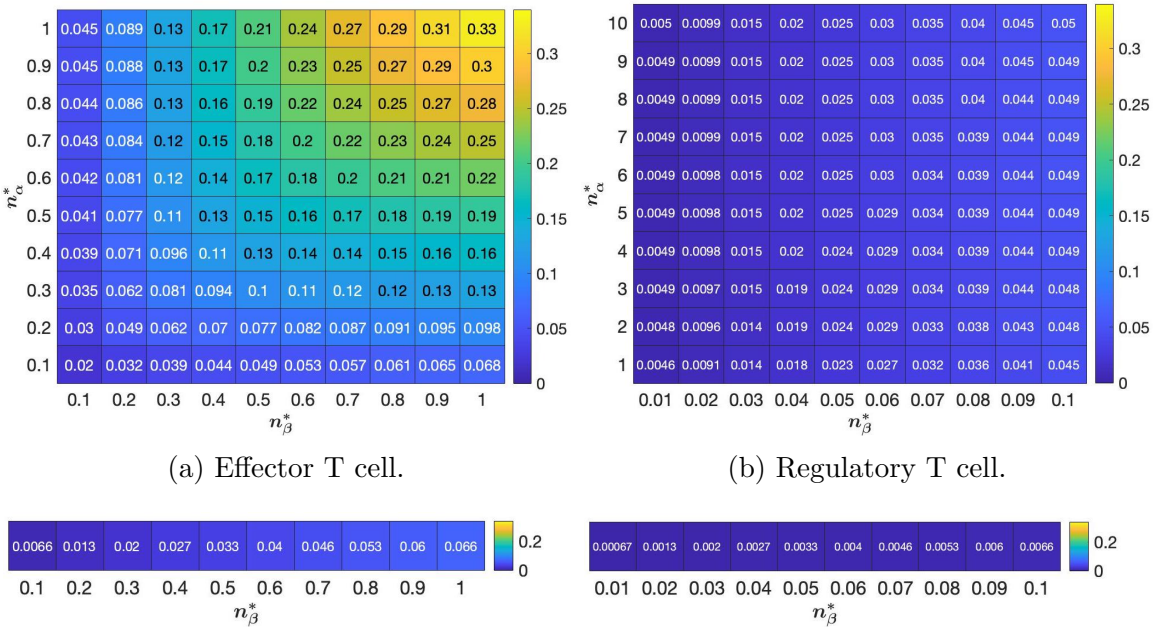
(b) Regulatory T cell.

(c) Memory CD8+ T cell.

(d) Memory CD4+ T cell.

Figure 4.2: Heatmaps of the steady state solutions for $n^\infty_{\beta L} + n^\infty_{\alpha\beta L}$ for the different types of T cells when $S = 1$ (low levels of IL-2). For each type of T cell, the availability of α chains (n^*_α) and β chains (n^*_β) are varied within the ranges specified in Table 4.7. Since memory T cells lack α chains, we only show how varying n^*_β affects $n^\infty_{\beta L}$ ($n^\infty_{\alpha\beta L} \equiv 0$). We fix $\hat{G}_\beta = 2.75 \times 10^{-4}$ and $R = 10$. Other parameter values are fixed as in Table 4.6.

In Figure 4.5, we plot the steady state solutions for $n^\infty_{\beta L}$ and $n^\infty_{\alpha\beta L}$ as S varies from 10^{-1} to 10^{10} for different types of T cells. We note that high IL-2 exposure is associated with substantial toxicities; $S \gtrsim 10^4$ is likely unphysiological and is only included for completeness. For each type of T cell, we fix the number of α and β chains. We plot the steady state solution for $n^\infty_{\beta L} + n^\infty_{\alpha\beta L}$ in Panel 4.5a, and in



(a) Effector T cell.

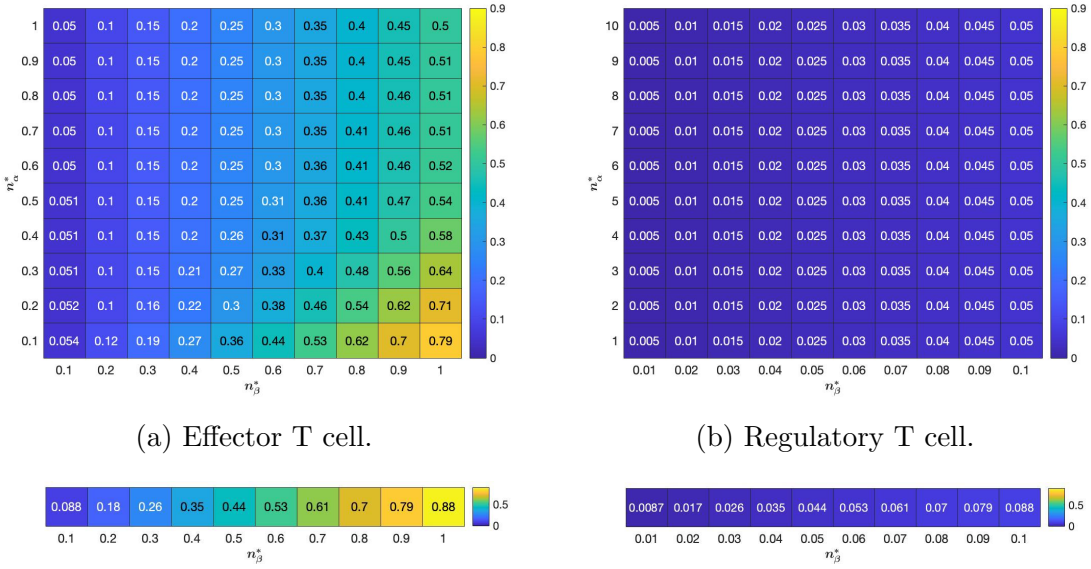
(b) Regulatory T cell.

(c) Memory CD8+ T cell.

(d) Memory CD4+ T cell.

Figure 4.3: Heatmaps of the steady state solutions for $n^{\infty}_{\beta L} + n^{\infty}_{\alpha\beta L}$ for the different types of T cells when $S = 100$ (intermediate levels of IL-2). For each type of T cell, the availability of α chains (n^*_α) and β chains (n^*_β) are varied within the ranges as specified in Table 4.7. Since memory T cells lack α chains, we only show how varying n^*_β affects $n^{\infty}_{\beta L}$ ($n^{\infty}_{\alpha\beta L} \equiv 0$). We fix $\hat{G}_\beta = 2.75 \times 10^{-4}$ and $R = 10$. Other parameter values are fixed as in Table 4.6.

Panel 4.5b, we plot the steady state solutions for $n^{\infty}_{\beta L}$ and $n^{\infty}_{\alpha\beta L}$. Figure 4.5 shows trends when different types of T cells are stimulated with IL-2. Similar behaviours are obtained for a range of values of n^*_α and n^*_β for the different types of T cells. At low levels of IL-2 ($0.1 \lesssim S \lesssim 10$), the regulatory T cells are preferentially stimulated. This is because regulatory T cells express the highest levels of α chains. When IL-2 levels are low, α chains are essential for capturing free IL-2 and facilitating the formation of the signalling complexes. At intermediate levels of IL-2 ($10 \lesssim S \lesssim 10^3$), the effector T cells are preferentially stimulated, and the signalling level of memory CD8+ T cells increases rapidly; at high levels of IL-2 ($S \gtrsim 10^3$), both memory CD8+ and effector T cells are strongly stimulated. The signalling levels of the memory CD4+ cells exceed those of the regulatory T cells. For large values of S, the steady state solutions for $n^{\infty}_{\beta L} + n^{\infty}_{\alpha\beta L}$ continue to increase with S for effector and regulatory T cells, approaching levels similar to those for memory CD8+ and memory CD4+ T cells respectively. Panel 4.5b shows that this is because when IL-2 is plentiful, β chains bind preferentially to IL-2 rather than the [IL-2 : α] complex and this reduces the number



(a) Effector T cell.

(b) Regulatory T cell.

(c) Memory CD8+ T cell.

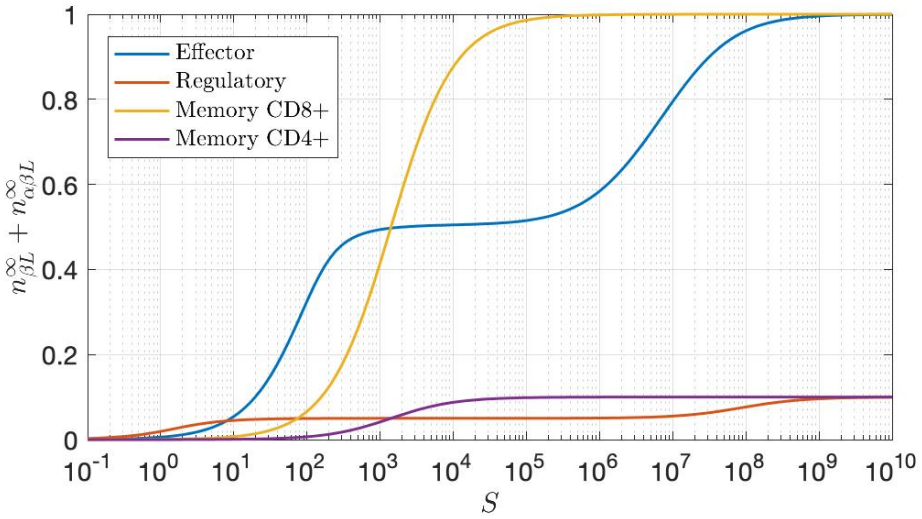
(d) Memory CD4+ T cell.

Figure 4.4: Heatmaps of the steady state solutions for $n^{\infty}_{\beta L} + n^{\infty}_{\alpha\beta L}$ for the different types of T cells when $S = 10^4$ (high levels of IL-2). For each type of T cell, the availability of α chains (n^*_α) and β chains (n^*_β) are varied within the ranges specified in Table 4.7. Since memory T cells lack α chains, we only show how varying n^*_β affects $n^{\infty}_{\beta L}$ ($n^{\infty}_{\alpha\beta L} \equiv 0$). We fix $\hat{G}_\beta = 2.75 \times 10^{-4}$ and $R = 10$. Other parameter values are fixed as in Table 4.6.

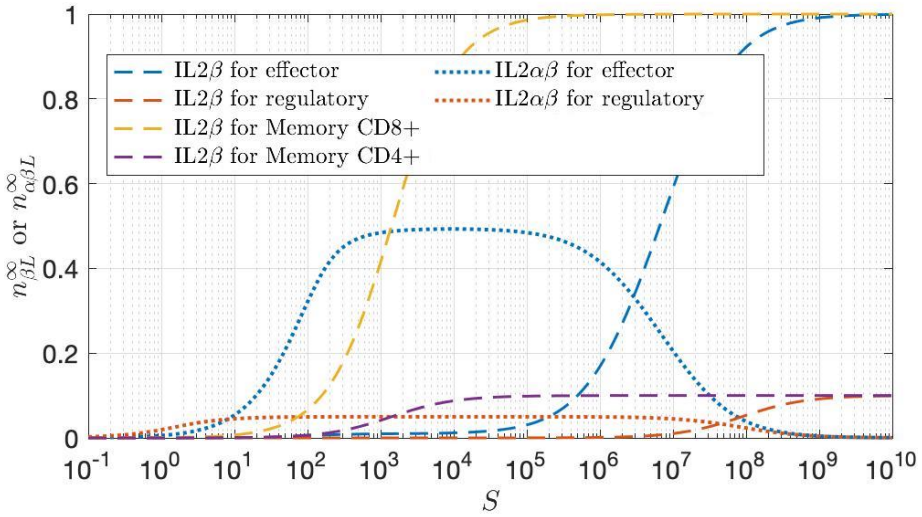
of signalling complexes being internalised. For effector T cells, the dominant signalling complex is [IL-2 : α : β] when $0.1 \lesssim S \lesssim 3 \times 10^6$ and [IL-2 : β] when $S \gtrsim 3 \times 10^6$. We observe a similar trend for regulatory T cells but with a higher transition point ($S \approx 5 \times 10^7$).

4.3.2 Effect of varying $\hat{G}_\beta$ and R across the range of S

The synthesis rate for β chains ($\hat{G}_\beta$) is not well known. Additionally, the domain size R dictates cell density (larger values of R correspond to more dilute cell populations). In this section, we investigate whether the conclusions drawn in the previous section are robust to changes in these parameters. Heatmaps of the steady state solutions for $n^{\infty}_{\beta L} + n^{\infty}_{\alpha\beta L}$ as $\hat{G}_\beta$ or R varies independently against the full spectrum of IL-2 source strengths (S) are generated for different types of T cells. For each type of T cell, the availability of α and β chains is fixed at a typical value. Results when varying $\hat{G}_\beta$ are shown in Figures 4.6. We present results for effector and regulatory T cells (since the number of β chains on memory cells is conserved, varying $\hat{G}_\beta$ does not affect their



(a) Steady state solutions for $n^{\infty}_{\beta L} + n^{\infty}_{\alpha\beta L}$ as S varies. Different line colours correspond to different cell types.

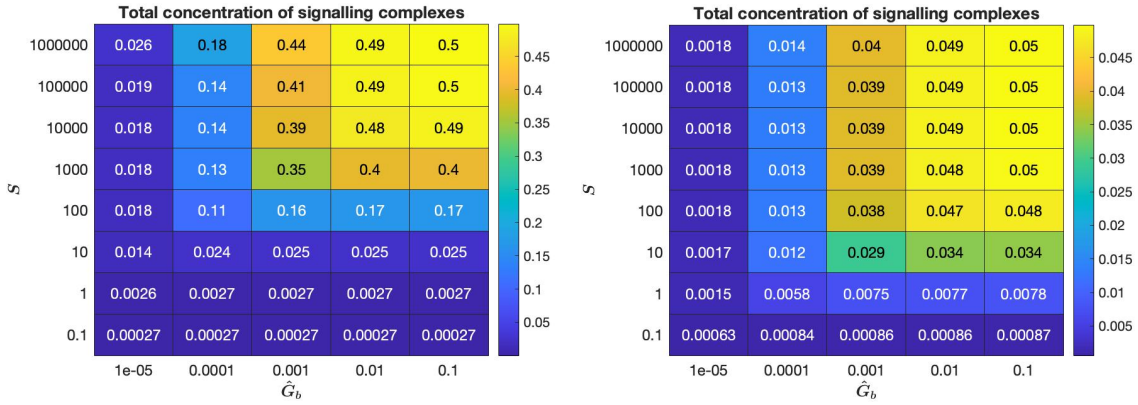


(b) Steady state solutions for $n^{\infty}_{\beta L}$ and $n^{\infty}_{\alpha\beta L}$. Different line colours correspond to different cell types. Dashed lines represent results for $n^{\infty}_{\beta L}$; dotted lines represent results for $n^{\infty}_{\alpha\beta L}$.

Figure 4.5: Steady state solutions for $n^{\infty}_{\beta L}$ and $n^{\infty}_{\alpha\beta L}$ as S varies for different types of T cells. Steady state solutions are obtained by solving the steady nonlinear algebraic system numerically, as described in Section 4.3.1. Steady state profiles for $n^{\infty}_{\beta L} + n^{\infty}_{\alpha\beta L}$ are shown in Panel (a); steady state solutions for $n^{\infty}_{\beta L}$ and $n^{\infty}_{\alpha\beta L}$ are shown in Panel (b). For each type of T cell, the availability of α and β chains are fixed at a typical value within the physical range to represent the behavior. For effector T cells: $n^{*}_{\alpha} = 0.5, n^{*}_{\beta} = 0.5$; for regulatory T cells: $n^{*}_{\alpha} = 5, n^{*}_{\beta} = 0.05$; for memory CD8+ T cells, $n^{*}_{\alpha} = 0, n^{*}_{\beta} = 0.5$; for memory CD4+ T cells, $n^{*}_{\alpha} = 0, n^{*}_{\beta} = 0.05$. We fix $\hat{G}_{\beta} = 2.75 \times 10^{-4}$ and $R = 10$. Other parameter values are fixed as in Table 4.6.

behaviour; results not shown). Results when varying R from 1.5 to 100 are not shown for brevity, as $n^{\infty}_{\beta L} + n^{\infty}_{\alpha\beta L}$ is insensitive to changes in R.

Figure 4.6 demonstrates that changing $\hat{G}_\beta$ does not alter the qualitative response of effector and regulatory cells to varying IL-2 source strengths (S). We observe that $\hat{G}_\beta$ primarily modulates the magnitude of the response rather than the trend; specifically, changes in $\hat{G}_\beta$ have a stronger effect when IL-2 source strengths are high, which is the regime where β chain availability becomes the rate-limiting factor for the formation of the signalling complexes.



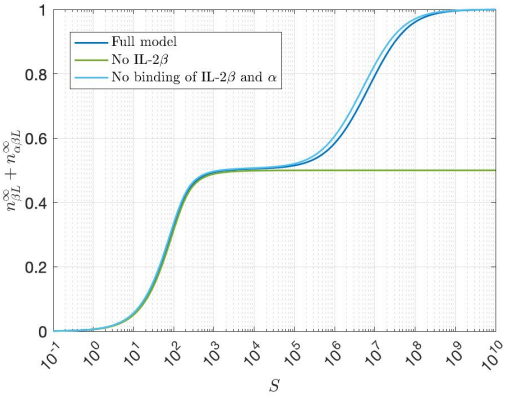
(a) Effector T cell.

(b) Regulatory T cell.

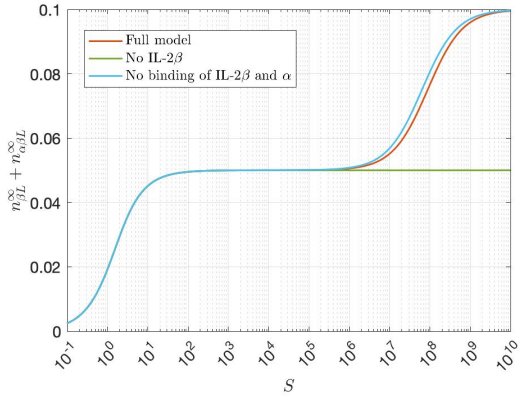
Figure 4.6: Heatmaps of the steady state solutions for $n^{\infty}_{\beta L} + n^{\infty}_{\alpha\beta L}$ as S and $\hat{G}_\beta$ vary for different types of T cells. For each type of T cell, the availability of α and β chains are fixed at a typical value within the physical range to represent the behavior. For effector T cells: $n^*_\alpha = 0.5, n^*_\beta = 0.5$; for regulatory T cells: $n^*_\alpha = 5, n^*_\beta = 0.05$. We fix $R = 10$. Other parameter values are fixed as in Table 4.6.

4.3.3 Results with different assumptions for the binding kinetics

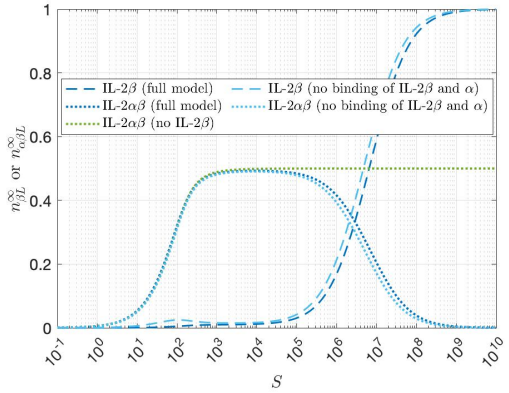
In many mathematical models, the binding kinetics are simplified. This raises the question of whether such reductions preserve the behavior of the full kinetic model. To assess this, we construct two model variants (Equations (4.15)–(4.26)) by removing (i) IL-2 binding to β chains and (ii) binding between α chains and [IL-2 : β] complexes. Operationally, we nullify the relevant kinetic terms in the governing equations. For (i), we set $\hat{k}_\beta = \hat{k}_{-\beta} = \hat{k}_{\beta\alpha} = \hat{k}_{-\beta\alpha} = 0$ and $n_{\beta L} \equiv 0$; for (ii), we set $\hat{k}_{\beta\alpha} = \hat{k}_{-\beta\alpha} = 0$. We then compare the steady state values of the signalling complexes ($n^{\infty}_{\beta L}, n^{\infty}_{\alpha\beta L}$ and $n^{\infty}_{\beta L} + n^{\infty}_{\alpha\beta L}$) for the simplified models to those for the full model. Results of this



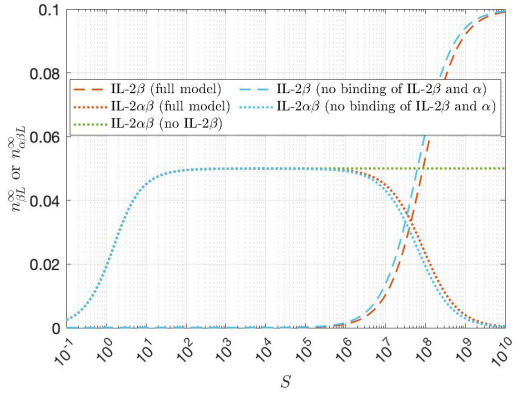
(a) $n^{\infty}_{\beta L} + n^{\infty}_{\alpha\beta L}$ for effector T cells.



(b) $n^{\infty}_{\beta L} + n^{\infty}_{\alpha\beta L}$ for regulatory T cells.



(c) $n^{\infty}_{\beta L}$ and $n^{\infty}_{\alpha\beta L}$ for effector T cells. Dashed lines represent results for $n^{\infty}_{\beta L}$; dotted lines represent results for $n^{\infty}_{\alpha\beta L}$.



(d) $n^{\infty}_{\beta L}$ and $n^{\infty}_{\alpha\beta L}$ for regulatory T cells. Dashed lines represent results for $n^{\infty}_{\beta L}$; dotted lines represent results for $n^{\infty}_{\alpha\beta L}$.

Figure 4.7: Comparison of models with different binding assumptions for effector and regulatory T cells. $n^{\infty}_{\beta L} + n^{\infty}_{\alpha\beta L}$ as S varies for effector and regulatory T cells are shown in Panels (a) and (b) respectively; the corresponding $n^{\infty}_{\beta L}$ and $n^{\infty}_{\alpha\beta L}$ as S varies for effector and regulatory T cells are shown in Panels (c) and (d) respectively. Steady state solutions for the full and simplified models are obtained by solving the corresponding steady nonlinear algebraic systems numerically, as described in Section 4.3.1. Different line colours correspond to different models (as indicated in the legend). For effector T cell: $n^*_\alpha = 0.5, n^*_\beta = 0.5$; for regulatory T cell: $n^*_\alpha = 5, n^*_\beta = 0.05$. We fix $\hat{G}_\beta = 2.75 \times 10^{-4}$, $R = 10$, and all other parameters at the values stated in Table 4.6.

comparison are shown in Figure 4.7 for effector and regulatory T cells, where S varies from 10^{-1} to 10^{10}.

Figures 4.7a and 4.7b show that neglecting binding between [IL-2 : β] complexes and α chains has a minimal effect on the levels of signalling complexes; the majority of the [IL-2 : α : β] complexes form via an α-first pathway, in which IL-2 binds the α

chain first and subsequently recruits the β chain; the β-first route contributes negligibly. The model that neglects binding of IL-2 to β chains is a good approximation to the full model when the IL-2 level is sufficiently small so that the [IL-2 : α : β] complex is the major signalling compound formed; here, IL-2 first binds to the α chain and then to the β chain. This level of IL-2 is $S = 10^4$ for effector T cells and $S = 10^6$ for regulatory T cells (see Panels 4.7c and 4.7d). As IL-2 levels increase, levels of [IL-2 : β] complexes increase and become the dominant signalling complex in the full model; in this case, the reduced model with no [IL-2 : β] complexes cannot capture the level of signalling complexes in the system.

4.4 Global sensitivity analysis for the 1D PDE model with full binding kinetics

Building upon the local sensitivity analysis conducted in the previous section, we now perform a global sensitivity analysis to investigate the factors that most significantly influence the steady-state values of the total concentration of signalling complexes for different T cell types.

As in Chapter 2, we perform eFAST [59] and Sobol sensitivity analysis [13]. The output of interest is the steady-state value of the total concentration of signalling complexes ($n_{\beta L}^{\infty} + n_{\alpha\beta L}^{\infty}$). The parameters of interest include those studied in the local sensitivity analysis ($R, \hat{G}_\beta, n_\beta^*, S, n_\alpha^*$), in addition to the binding off rates ($\hat{k}_{-\alpha}, \hat{k}_{-\beta}$,$\hat{k}_{-\alpha\beta}$ and $\hat{k}_{-\beta\alpha}$) because of their therapeutic potential. The ranges of the parameters that vary and the values of the fixed parameters are stated in Table 4.8. The parameters n_α^* and n_β^* are varied for different cell types as in Table 4.7. We sample S and $\hat{G}_\beta$ uniformly on a logarithmic scale; since they can vary over 6 orders of magnitude. This ensures that both small and large values are adequately represented in the analysis. The other parameters of interest are sampled uniformly within their specified ranges.

Parameter	Expression	Value
$\hat{k}_\alpha$	$\frac{R_{\text{cell}}^2}{D_L}\overline{N_L}k_\alpha$	1.710×10^{-6}
$\hat{k}_{-\alpha}$	$\frac{R_{\text{cell}}^2}{D_L}k_{-\alpha}$	$0.0745 \times [0.1, 10]$
$\hat{k}_\beta$	$\frac{R_{\text{cell}}^2}{D_L}\overline{N_L}k_\beta$	6.13×10^{-8}
$\hat{k}_{-\beta}$	$\frac{R_{\text{cell}}^2}{D_L}k_{-\beta}$	$6.25 \times 10^{-5} \times [0.1, 10]$
$\hat{k}_{\alpha\beta}$	$\overline{\tau}\overline{N_\alpha}k_{\alpha\beta}$	0.75
$\hat{k}_{-\alpha\beta}$	$\overline{\tau}k_{-\alpha\beta}$	$5.75 \times 10^{-5} \times [0.1, 10]$
$\hat{k}_{\beta\alpha}$	$\overline{\tau}\overline{N_\alpha}k_{\beta\alpha}$	15
$\hat{k}_{-\beta\alpha}$	$\overline{\tau}k_{-\beta\alpha}$	$0.15 \times [0.1, 10]$
$\hat{T}$	$\frac{\overline{N_\alpha}}{R_{\text{cell}}\overline{N_L}}$	1.639×10^4
λ	$\sqrt{\frac{R_{\text{cell}}^2}{D_L}\Lambda}$	0.024
$\hat{I}$	$\overline{\tau}I$	2.75×10^{-4}
R	$\frac{R_{\text{outer}}}{R_{\text{cell}}}$	[1.5,100]
$\hat{G}_\beta$	$\overline{\tau}G_\beta$	$[10^{-5}, 0.1]$
n_β^*	$\frac{N_\beta^*}{\overline{N_\alpha}}$	$[0.1, 1]$ for effector and memory CD8+ T cells; $[0.01, 0.1]$ for regulatory and memory CD4+ T cells
S	$\frac{S_{\text{outer}}}{\overline{N_L}}$	[0.1, 10^5]
n_α^*	$\frac{N_{\alpha,\text{TOT}}}{\overline{N_\alpha}}$	$[0.1, 1]$ for effector T cells; $[1, 10]$ for regulatory T cells; 0 for memory T cells

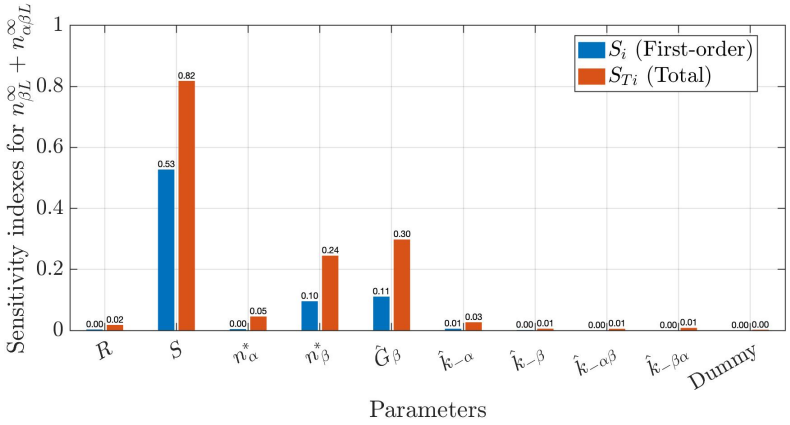
Table 4.8: Values and ranges of the parameters in the 1D spatial model with full binding kinetics for global sensitivity analysis. The binding off rates ($\hat{k}_{-\alpha}, \hat{k}_{-\beta}$,$\hat{k}_{-\alpha\beta}$ and $\hat{k}_{-\beta\alpha}$) are varied from one-tenth to ten times the values presented in Table 4.6. The parameters n_α^* and n_β^* are varied for different cell types according to their availabilities as in Table 4.7.

The results from eFAST in which we vary the 9 parameters ($R, \hat{G}_\beta, n^*_\beta, S, n^*_\alpha, \hat{k}_{-\alpha}$, $\hat{k}_{-\beta}$, $\hat{k}_{-\alpha\beta}, \hat{k}_{-\beta\alpha}$) are shown in Figure 4.8. These results are in good agreement with those from Sobol's method, suggesting that the algorithms are functioning correctly and confirming their reliability in our global sensitivity analysis; we present only results from eFAST to avoid redundancy. Results for CD4+ and CD8+ memory T cells exhibit negligible differences. For all types of T cells, S (the source strength of IL-2) contributes the most to the variance in the total concentration of signalling complexes, with increasing effects for regulatory T cells, effector T cells and memory T cells. The parameters relating to the availability of β chains (n^*_β and $\hat{G}_\beta$) also contribute to the output of interest, but to a lesser extent than S, with decreasing effects for regulatory T cells, effector T cells and only a small impact on memory T cells. This is because α chains facilitate the capture of IL-2 from the extracellular space; thus, cell types expressing higher levels of α chains are less dependent on variations in IL-2 levels than cell types expressing lower levels of α chains, and are more sensitive to the expression levels of β chains. Memory T cells are not sensitive to the production rate of β chains, $\hat{G}_\beta$, because their β chains are conserved. All other parameters have negligible impact on the variance of the steady-state solution for the total signalling complexes, with sensitivity indices comparable to the dummy parameter.

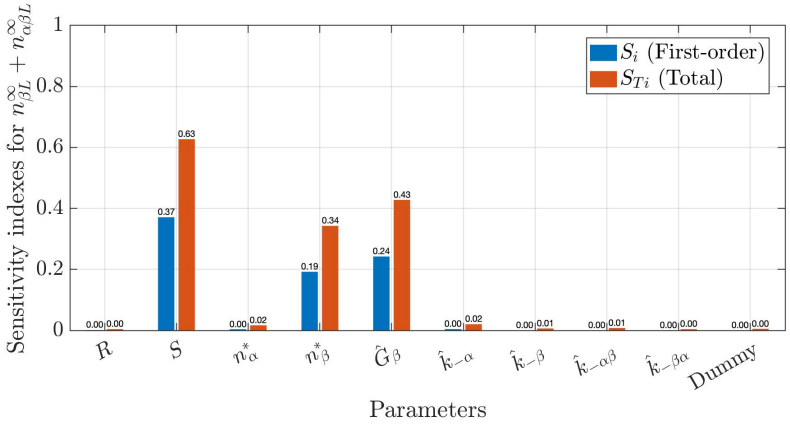
To investigate how parameter sensitivity depends on IL-2 availability, we fix the source strength (S) at specific values and perform a global sensitivity analysis on the remaining parameters for effector and regulatory T cells. The results in Figure 4.9 show that the parameters that contribute to the variance in the total concentration of signalling complexes are $n^*_\alpha, n^*_\beta, \hat{G}_\beta, \hat{k}_{-\alpha}$ and R (R only for effector T cells), the other parameters ($\hat{k}_{-\beta}$,$\hat{k}_{-\alpha\beta}, \hat{k}_{-\beta\alpha}$) have minimal effects, with sensitivity indices less than 0.1 for all values of S. We observe that at low levels of IL-2, both cell types are most sensitive to α chain-related parameters. Effector T cells are most sensitive to n^*_α when $S < 10$; $\hat{k}_{-\alpha}$ and n^*_β are the next in sensitivity ranking. Regulatory T cells are most sensitive to $\hat{k}_{-\alpha}$ for $S < 1$; n^*_α and n^*_β are the next in sensitivity ranking. The shift in sensitivity from n^*_α to $\hat{k}_{-\alpha}$ across the cell types is due to the higher expression levels of α chains on regulatory T cells. For effector T cells, R also exerts a measurable influence on the variance in the level of signalling complexes when $S < 10$. This is because the variance in the domain size will affect the concentration of IL-2 on the cell membrane. Since effector T cells express fewer α chains, they are more sensitive to the availability of IL-2 when IL-2 levels are low. For both cell types, as S increases, the significance of the parameters relating to the β chains (n^*_β and

$\hat{G}_\beta$) increases and the significance of those relating to the α chains decreases (n^*_α and $\hat{k}_{-\alpha}$). This is because when IL-2 levels are low, α chains play a key role in capturing free IL-2 from the bulk, while when IL-2 levels are high, the availability of β chains becomes limiting. When IL-2 levels are high (i.e. $S > 10^3$), both cell types are most sensitive to $\hat{G}_\beta$ and n^*_β.

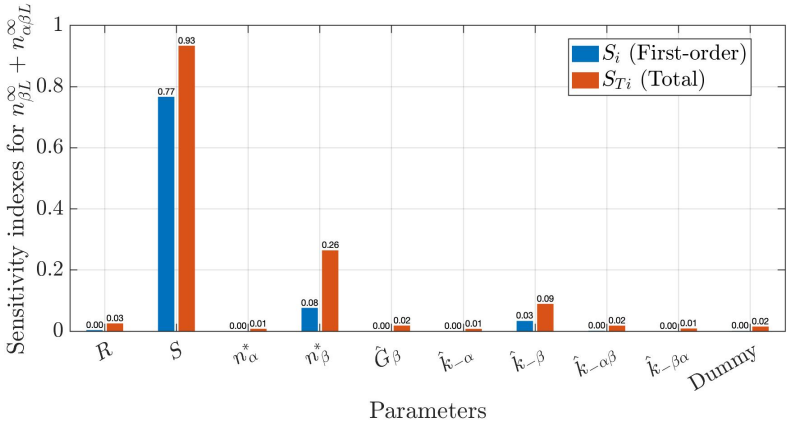
These results show that the parameters controlling the steady-state level of signalling complexes depend on both IL-2 availability and the type of T cell under consideration. Across all cell types, the source strength of IL-2, S, is the dominant contributor to the variance in the output, confirming that cytokine availability is the primary determinant of signalling. The analysis also reveals a clear shift across IL-2 regimes: at low IL-2 levels, signalling is governed mainly by processes associated with α chain-mediated ligand capture; whereas at high IL-2 levels, it is governed mainly by processes associated with the availability of β chains. Differences between cell types arise from their distinct receptor compositions. These findings identify the key processes controlling signalling across IL-2 regimes and T-cell types, and indicate which parameters should be prioritised for experimental quantification and therapeutic targeting.



(a) For effector cells.

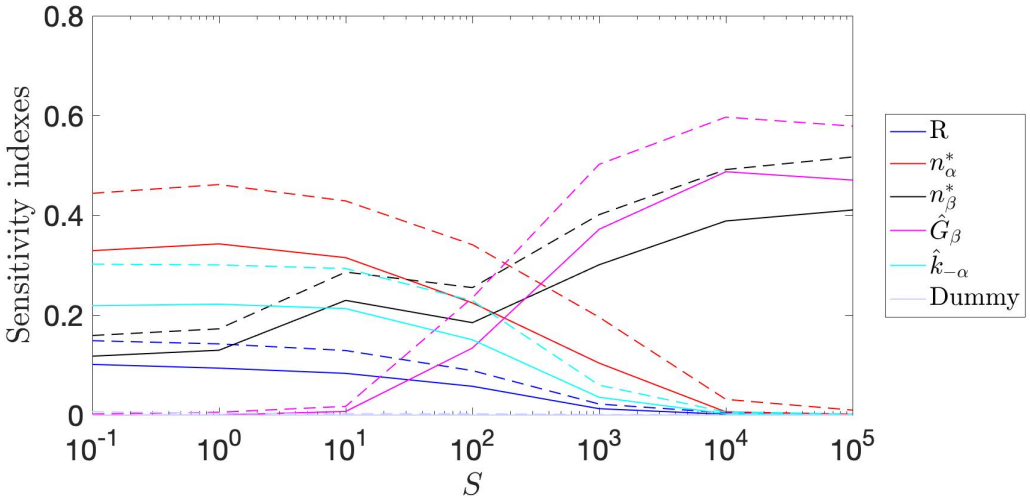


(b) For regulatory T cells.

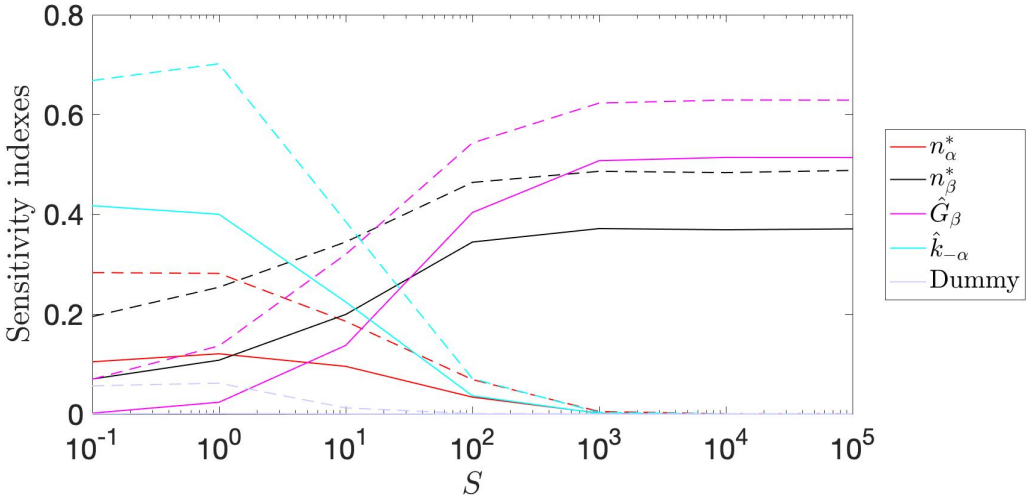


(c) For memory CD8+/CD4+ T cell.

Figure 4.8: Results of global sensitivity analysis from eFAST for different types of T cells varying 9 parameters. For each parameter, the first-order ($\mathcal{S}_i$) and total-order ($\mathcal{S}_{T_i}$) sensitivity indices are illustrated using bar charts, with the colors of the bars corresponding to those indicated in the legend. Results for effector, regulatory and memory T cells are shown in Panels (a), (b) and (c) respectively.



(a) For effector T cells.



(b) For regulatory T cells.

Figure 4.9: Results of global sensitivity analysis from eFAST for different types of T cells for different fixed values of S. Results for effector and regulatory T cells are presented in Panels (a) and (b) respectively. The varying parameters are R, n^*_α, n^*_β, $\hat{G}_\beta$ and all the off rates ($\hat{k}_{-\alpha}, \hat{k}_{-\beta}, \hat{k}_{-\alpha\beta}, \hat{k}_{-\beta\alpha}$). For each parameter, the first-order ($\mathcal{S}_i$) and total-order ($\mathcal{S}_{T_i}$) sensitivity indices are plotted in solid and dashed lines respectively, with the colors of the lines corresponding to parameters indicated in the legend. Results for parameters with sensitivity indexes less than 0.1 for all values of S are not presented for simplicity. Number of search curves = 10; Number of samples = 256.

4.5 Discussion

In this chapter, we extended our 1D PDE model to account for β and γ chains, which we treated as effective β/γ dimers ("β" chains). We used the model to simulate steady-state solutions for the signalling complexes for different types of T cells characterised by differential expression levels of α and β chains under varying levels of IL-2. We examined the effects of varying the synthesis rate of the β chains and the domain size. We evaluated simplified binding-kinetic assumptions that have been used in existing mathematical models [27, 45, 95]. We performed eFAST and Sobol global sensitivity analysis to investigate the factors that most significantly influence the ability of IL-2 to stimulate downstream signalling for different types of T cells.

Our model predicts and explains the preferential stimulation of different types of T cells at different IL-2 levels. Regulatory T cells are preferentially stimulated at low IL-2 levels because they possess more α chains, which capture IL-2 when its concentration is low and facilitates the formation of signalling complexes. Effector T cells are preferentially stimulated at intermediate and high levels of IL-2 because then the availability of β chains becomes the rate-limiting factor for regulatory T cells but not for effector T cells which possess more β chains. Memory CD8+ and CD4+ T cells lack α chains and thus start to respond at higher levels of IL-2. These predictions are consistent with experimental observations and are biologically plausible: low IL-2 levels favouring regulatory T cells is consistent with the role of IL-2 in maintaining immune tolerance and restraining inappropriate activation under homeostatic conditions, whereas higher IL-2 levels favouring effector and memory T cells is consistent with the need to amplify immune responses during active infection or inflammation [3, 40, 46, 82].

We also found that changes in the synthesis rate of β chains ($\hat{G}_\beta$) do not alter the qualitative response of the different types of T cells. Changes in $\hat{G}_\beta$ influence levels of β chains and have a more significant effect on the results when the availability of β chains is rate-limiting. Changes in $\hat{G}_\beta$ do not affect the formation of signalling complexes for the memory cells because they lack α chains and therefore their β chains are conserved (no internalisation of [IL-2 : α : β] complexes). Our conclusions regarding preferential stimulation of IL-2 do not depend on the synthesis rate for the β chains or the domain size when their values are within physiological ranges.

By making different simplifying assumptions about the binding kinetics, we showed that neglecting binding between [IL-2 : β] complexes and α chains has a negligible effect on the levels of signalling complexes; most [IL-2 : α : β] complexes form via an

α-first pathway, in which IL-2 binds the α chain before recruiting the β chain; the β-first route is negligible. The model that neglects IL-2 binding to β chains is a good approximation to the full model for effector and regulatory T cells when IL-2 levels are sufficiently small to ensure that the [IL-2 : α : β] complex is the dominant signalling complex. As IL-2 levels increase, when the level of [IL-2 : β] complexes increases and becomes the dominant signalling complex in the full model, the simpler model that neglects [IL-2 : β] complexes cannot capture the total level of signalling complex in the system. Given the toxicity of high doses of IL-2, neglecting IL-2 binding to β chains is expected to be adequate for effector and regulatory T cells in most physiologically relevant scenarios.

The results from eFAST in which 9 parameters were varied ($R, \hat{G}_\beta, n^*_\beta, S, n^*_\alpha, \hat{k}_{-\alpha}, \hat{k}_{-\beta}, \hat{k}_{-\alpha\beta}, \hat{k}_{-\beta\alpha}$) indicated that the source strength of IL-2 (S) is the dominant determinant of variance in the steady-state total concentration of signalling complexes across all T-cell subsets, with its influence increasing from regulatory to effector to memory cells. Parameters governing the availability of β chains (n^*_β and $\hat{G}_\beta$) also contribute to the output of interest, but to a lesser extent than S; their importance is greatest in regulatory cells, smaller in effector cells and minimal in memory cells. This pattern is consistent with the role of the α chain in ligand capture: subsets of cells with larger n^*_α are less supply-limited by S and correspondingly more sensitive to the availability of β chains. Sensitivity to $\hat{G}_\beta$ is negligible for memory T cells whose β chains are conserved (i.e., not synthesized). The remaining parameters have minimal impact on the variance of the steady-state output within the explored ranges. Fixing S at different levels and applying eFAST to the remaining parameters for effector and regulatory T cells revealed that variance in the steady-state total concentration of signalling complexes is driven primarily by n^*_α, n^*_β, $\hat{G}_\beta$, $\hat{k}_{-\alpha}$ and, for effector T cells only, the domain size R. In contrast, $\hat{k}_{-\beta}$, $\hat{k}_{-\alpha\beta}$, and $\hat{k}_{-\beta\alpha}$ exhibit uniformly small first-order and total-order indices (< 0.1) across all S. At low IL-2 levels, sensitivities are dominated by parameters related to α chains. Effector cells rank n^*_α highest (with $\hat{k}_{-\alpha}$ and n^*_β following), whereas regulatory cells rank $\hat{k}_{-\alpha}$ highest (followed by n^*_α and n^*_β). This difference is consistent with the higher α-chain expression in the regulatory subset. In the same low-S regime, R contributes detectably for effector T cells. As IL-2 levels increase, sensitivity shifts toward parameters related to β chains. $\hat{G}_\beta$ and n^*_β become the dominant factors in both subsets when IL-2 levels are high.

Through ablation of the IL-2 receptor kinetics, we have shown that the binding between α chains and [IL-2 : β] complexes can be neglected without loss of accuracy, as can the binding between IL-2 and β chains if IL-2 dosing is not too high. These

rules provide the first concrete blueprint for streamlining IL-2 signalling models while preserving predictive fidelity. From the global sensitivity analysis, we have identified the most important factors contributing to the steady-state values of the total concentration of signalling complexes in the full 1D PDE model, across different T cell types and varying availability of IL-2; to our knowledge, this constitutes the first such analysis for a model that captures IL-2 binding kinetics. These results improve our understanding of the underlying biological mechanisms and provide insight into critical parameters for experimental measurement and potential targets for intervention. Specifically, with the therapeutic aim of modifying binding off rates, our results indicate that the dissociation rate of IL-2 and the α chain ($\hat{k}_{-\alpha}$) may be a key parameter to manipulate because the level of IL-2 signalling is sensitive to it, but not the other binding off rates. As a future step, further analysis could be performed considering the variation of other parameters in the model, depending on the specific research questions of interest. Our model can be used to study the effectiveness of potential IL-2-modulatory therapeutics to preferentially stimulate certain types of T cells to promote or suppress immunity in relevant diseases. However, for our model to make quantitative and more precise predictions, consistent data will be needed for a single cell line to parameterise the model.

In the next chapter, we shift our focus from the single-cell perspective to the population level and consider competition for IL-2 between different types of T cells.

Chapter 5

Competition between T cell populations

5.1 Introduction

In Chapters 2, 3 and 4, we focused on single-cell models to understand how different types of T cells interact with IL-2. In practice, T cells do not operate in isolation; they exist within heterogeneous cell populations that interact with each other and compete for IL-2 [3, 31]. Effector T cells (conventional $CD4^+$ helper and $CD8^+$ cytotoxic T cells) are the principal executors of immunity - cytotoxic T cells kill infected or malignant cells, while helper T cells activate phagocytes. Effector T cells express relatively few α chains, and require higher extracellular IL-2 levels for activation. Regulatory T cells, by contrast, express high levels of α chains and signal robustly at low IL-2 levels; they efficiently capture and internalize IL-2, acting as an IL-2 sink that limits expansion of effector T cells and enforces self-tolerance. In this chapter, we extend the modelling to examine co-existing populations of different cell types in a well-mixed framework to consider how competition for IL-2 determines competitive outcomes and its influence on the induction of T cell signalling.

We formulate this problem with ODE models, which extend the ODE model from Chapter 3. We assume that all cells of a given phenotype are identical. The ODE setting is analytically tractable, which allows us to derive steady states and assess their linear stability, to derive threshold criteria for effector or regulatory T cell dominance and to compare mechanistic hypotheses without heavy computation. This balance - capturing the essential resource-competition dynamics while maintaining analytical tractability and computational efficiency - motivates our use of ODE models for the population-level study.

As in previous chapters, we begin by isolating the role of the α chain. α chains do not signal on their own, but they dominate the initial capture of IL-2: they bind IL-2 rapidly and concentrate IL-2 at the cell surface, from which β and γ chains can subsequently be recruited to form signalling complexes. These initial models track ligand capture and depletion and are used to understand how differential α chain densities skew partitioning of IL-2 between the two populations. Isolating this first step is useful because it yields a simpler submodel with closed-form occupancies and provides a baseline to assess how accounting for β and γ chains shifts dose-response. In the second step, we incorporate β and γ chains, allowing the formation of signalling complexes. This chapter aims to identify those features of the system which strongly influence competition between different cell-types and to provide design principles for therapeutic strategies that tilt competition in a desired direction. To our knowledge, this integrative analysis is novel.

The remainder of this chapter is organised as follows. In Section 5.2, we focus on α chains and develop three in vitro models describing different settings. We perform steady state analysis for the models to examine the proportion and absolute value of bound α chains. In Section 5.3, we extend the models to incorporate the full binding kinetics. We perform global and local sensitivity analysis to identify the parameters that govern the competition of IL-2 between effector and regulatory T cells and identify potential targets for intervention. The chapter ends in Section 5.4, where we discuss our results and outline possible directions for future work.

5.2 Models with only α chain

In this section, we focus on IL-2 binding to α chains, the initial step in the formation of the quaternary signalling complex. We develop models that describe different settings:

- **Model I:** incorporates IL-2 production, decay and internalisation for a population of both effector and regulatory T cells competing for a shared source of IL-2.
- **Model II:** a simplification of Model I, in which IL-2 is not internalised.
- **Model III:** a further simplification of Model I, in which IL-2 production, decay and internalisation are neglected, and IL-2 is introduced via the initial conditions as an exogenous bolus. This setting describes standard in vitro experi-

ments where a fixed dose of IL-2 is administered at the start of the observation period.

5.2.1 Model formulation

In this section, we formulate and non-dimensionalise Model I. With units and summaries given in Tables 5.1 and 5.2, the dependent variables are $N_L(t)$, the concentration of free IL-2 in the extracellular space, $N_\alpha^{\mathrm{i}}(t)$, the concentration of free α chain on the cell membrane, and $N_{\alpha L}^{\mathrm{i}}(t)$, the concentration of [IL-2 : α] complex on the cell membrane, where $\mathrm{i} \in \{\mathrm{E}, \mathrm{R}\}$ indicates whether the quantity corresponds to effector (E) or regulatory (R) T cells respectively. We suppose that IL-2 binds reversibly to α chains on the cell membrane, with on and off rates k_α and $k_{-\alpha}$ respectively. We further assume that [IL-2 : α] complexes are internalised at rates I^{E} and I^{R} for effector and regulatory T cells, respectively, with concomitant recycling of unbound α chains back to the cell membrane.

Variable	Interpretation	Unit
N_L	Concentration of free IL-2 in the bulk	Number/cm^3
N_α^{E}	Concentration of free α chain on a effector T cell	Number/cm^2
$N_{\alpha L}^{\mathrm{E}}$	Concentration of [IL-2 : α] complex on a effector T cell	Number/cm^2
N_α^{R}	Concentration of free α chain on a regulatory T cell	Number/cm^2
$N_{\alpha L}^{\mathrm{R}}$	Concentration of [IL-2 : α] complex on a regulatory T cell	Number/cm^2

Table 5.1: Dependent variables and their units for Models I which describe competition for IL-2 by α chains on effector and regulatory T cells (see Equations (5.1)–(5.5)).

Parameter	Interpretation	Units
P	Production rate of IL-2 in the bulk	Number/(cm^3×s)
Λ	Decay rate of IL-2	1/s
k_α	Binding on rate of IL-2 and α chain	cm^3/ (Number×s)
$k_{-\alpha}$	Binding off rate of IL-2 and α chain	1/s
I^{E}	Internalisation rate of the [IL-2 : α] complex for the effector T cells	1/s
I^{R}	Internalisation rate of the [IL-2 : α] complex for the regulatory T cells	1/s
$N^{\mathrm{E}}_{\alpha,\mathrm{TOT}}$	Total concentration of α chains on the cell membrane of a Teff	Number/cm^2
$N^{\mathrm{R}}_{\alpha,\mathrm{TOT}}$	Total concentration of α chains on the cell membrane of a Treg	Number/cm^2
M^{E}	Number of Teffs	Number
M^{R}	Number of Tregs	Number
V	Volume of the bulk	cm^3
A	Surface area of a Teff/Treg	cm^2
R_{cell}	Cell radius	cm

Table 5.2: Parameters and their units for models which describe competition for IL-2 by α chains on effector and regulatory T cells.

Based on these assumptions, the dynamics of the dependent variables are governed by the following system of ODEs:

$$\frac{dN_L}{dt} = -M^{\mathrm{E}}\frac{A}{V}\left(k_{\alpha L}N_L N_\alpha^{\mathrm{E}} - k_{-\alpha L}N_{\alpha L}^{\mathrm{E}}\right) - M^{\mathrm{R}}\frac{A}{V}\left(k_{\alpha L}N_L N_\alpha^{\mathrm{R}} - k_{-\alpha L}N_{\alpha L}^{\mathrm{R}}\right) - \Lambda N_L + P, \tag{5.1}$$

$$\frac{dN_\alpha^{\mathrm{E}}}{dt} = -\left(k_{\alpha L}N_L N_\alpha^{\mathrm{E}} - k_{-\alpha L}N_{\alpha L}^{\mathrm{E}}\right) + I^{\mathrm{E}}N_{\alpha L}^{\mathrm{E}}, \tag{5.2}$$

$$\frac{dN_\alpha^{\mathrm{R}}}{dt} = -\left(k_{\alpha L}N_L N_\alpha^{\mathrm{R}} - k_{-\alpha L}N_{\alpha L}^{\mathrm{R}}\right) + I^{\mathrm{R}}N_{\alpha L}^{\mathrm{R}}, \tag{5.3}$$

$$\frac{dN_{\alpha L}^{\mathrm{E}}}{dt} = +\left(k_{\alpha L}N_L N_\alpha^{\mathrm{E}} - k_{-\alpha L}N_{\alpha L}^{\mathrm{E}}\right) - I^{\mathrm{E}}N_{\alpha L}^{\mathrm{E}}, \tag{5.4}$$

$$\frac{dN_{\alpha L}^{\mathrm{R}}}{dt} = +\left(k_{\alpha L}N_L N_\alpha^{\mathrm{R}} - k_{-\alpha L}N_{\alpha L}^{\mathrm{R}}\right) - I^{\mathrm{R}}N_{\alpha L}^{\mathrm{R}}. \tag{5.5}$$

In Equation (5.1), free IL-2 in the extracellular space binds reversibly to α chains on effector T cells of population size M^{E} and regulatory T cells of population size M^{R}. The terms describing reversible binding include a prefactor $\frac{A}{V}$ which converts the cell surface concentration to a bulk concentration, where the area of the cell membrane A is estimated by $A = 4\pi R_{\mathrm{cell}}^2$, V is the volume of the bulk, and R_{cell} is the radius of the cell. We assume that IL-2 undergoes linear decay, with rate Λ, and that it is produced at a constant rate P. In Equations (5.2) and (5.3), α chains on the outer membrane of effector and regulatory T cells bind reversibly with IL-2 from the bulk and are recycled back to the cell membrane when [IL-2 : α] complexes are internalised. In Equations (5.4) and (5.5), [IL-2 : α] complexes form on effector and regulatory T cells when IL-2 binds to the associated α chains and are internalised.

Adding Equations (5.2) and (5.4) and Equations (5.3) and (5.5), we note that the total number of α chains on effector T cell and regulatory T cells is constant. We exploit these identities to eliminate $N_{\alpha L}^{\mathrm{E}}$ and $N_{\alpha L}^{\mathrm{R}}$ from the model as follows:

$$N_{\alpha L}^{\mathrm{E}}(t) = N_{\alpha,\mathrm{TOT}}^{\mathrm{E}} - N_\alpha^{\mathrm{E}}(t), \tag{5.6}$$

$$N_{\alpha L}^{\mathrm{R}}(t) = N_{\alpha,\mathrm{TOT}}^{\mathrm{R}} - N_\alpha^{\mathrm{R}}(t), \tag{5.7}$$

where the positive constants $N_{\alpha,\mathrm{TOT}}^{\mathrm{E}}$ and $N_{\alpha,\mathrm{TOT}}^{\mathrm{R}}$ are the total concentrations of α chains on the outer membranes of effector and regulatory T cells respectively.

We close Equations (5.1)–(5.3) by imposing the initial conditions,

$$N_L(0) = N_{L,0}, \tag{5.8}$$

$$N_\alpha^{\mathrm{E}}(0) = N_{\alpha,\mathrm{TOT}}^{\mathrm{E}}, \tag{5.9}$$

$$N_\alpha^{\mathrm{R}}(0) = N_{\alpha,\mathrm{TOT}}^{\mathrm{R}}. \tag{5.10}$$

Non-dimensionalisation

We introduce the following scalings:

$$\begin{aligned} \tau = \frac{t}{\overline{\tau}},\ n_L = \frac{N_L}{\overline{N_L}}, \\ n_\alpha^{\mathrm{E}} = \frac{N_\alpha^{\mathrm{E}}}{\overline{N_\alpha}},\ n_\alpha^{\mathrm{R}} = \frac{N_\alpha^{\mathrm{R}}}{\overline{N_\alpha}},\ n_{\alpha L}^{\mathrm{E}} = \frac{N_{\alpha L}^{\mathrm{E}}}{\overline{N_\alpha}},\ n_{\alpha L}^{\mathrm{R}} = \frac{N_{\alpha L}^{\mathrm{R}}}{\overline{N_\alpha}}, \end{aligned} \tag{5.11}$$

where $\overline{\tau}$ is a typical time-scale with units s, $\overline{N_L}$ (units: Number/cm^3) and $\overline{N_\alpha}$ (units: Number/cm^2) are typical values of the concentrations of free IL-2 in the bulk and free α chain on the cell membrane respectively. We also introduce the following dimensionless parameters,

$$\begin{aligned} \hat{k}_{\alpha L} = \overline{\tau}\overline{N_L}k_{\alpha L}, \hat{k}_{-\alpha L} = \overline{\tau}k_{-\alpha L}, \lambda^2 = \overline{\tau}\Lambda, \hat{P} = \frac{\overline{\tau}}{\overline{N_L}}P, \\ n_{\alpha,\mathrm{TOT}}^{\mathrm{E}} = \frac{N_{\alpha,\mathrm{TOT}}^{\mathrm{E}}}{\overline{N_\alpha}}, n_{\alpha,\mathrm{TOT}}^{\mathrm{R}} = \frac{N_{\alpha,\mathrm{TOT}}^{\mathrm{R}}}{\overline{N_\alpha}}, \hat{F} = \frac{A}{V}\frac{\overline{N_\alpha}}{\overline{N_L}}, \\ \hat{I}^{\mathrm{E}} = \overline{\tau}I^{\mathrm{E}}, \hat{I}^{\mathrm{R}} = \overline{\tau}I^{\mathrm{R}}, n_{L,0} = \frac{N_{L,0}}{\overline{N_L}}. \end{aligned} \tag{5.12}$$

Under these scalings, Equations (5.1)–(5.10) transform to give the following system of dimensionless ODEs:

$$\frac{dn_L}{d\tau} = -M^{\mathrm{E}}\hat{F}\left(\hat{k}_{\alpha L}n_L n_\alpha^{\mathrm{E}} - \hat{k}_{-\alpha L}n_{\alpha L}^{\mathrm{E}}\right) - M^{\mathrm{R}}\hat{F}\left(\hat{k}_{\alpha L}n_L n_\alpha^{\mathrm{R}} - \hat{k}_{-\alpha L}n_{\alpha L}^{\mathrm{R}}\right) - \lambda^2 n_L + \hat{P}, \tag{5.13}$$

$$\frac{dn_\alpha^{\mathrm{E}}}{d\tau} = -\left(\hat{k}_{\alpha L}n_L n_\alpha^{\mathrm{E}} - \hat{k}_{-\alpha L}n_{\alpha L}^{\mathrm{E}}\right) + \hat{I}^{\mathrm{E}}n_{\alpha L}^{\mathrm{E}}, \tag{5.14}$$

$$\frac{dn_\alpha^{\mathrm{R}}}{d\tau} = -\left(\hat{k}_{\alpha L}n_L n_\alpha^{\mathrm{R}} - \hat{k}_{-\alpha L}n_{\alpha L}^{\mathrm{R}}\right) + \hat{I}^{\mathrm{R}}n_{\alpha L}^{\mathrm{R}}, \tag{5.15}$$

where

$$n_{\alpha L}^{\mathrm{E}}(\tau) = n_{\alpha,\mathrm{TOT}}^{\mathrm{E}} - n_\alpha^{\mathrm{E}}(\tau), \tag{5.16}$$

$$n_{\alpha L}^{\mathrm{R}}(\tau) = n_{\alpha,\mathrm{TOT}}^{\mathrm{R}} - n_\alpha^{\mathrm{R}}(\tau), \tag{5.17}$$

and

$$n_L(0) = n_{L,0}, \tag{5.18}$$

$$n_\alpha^{\mathrm{E}}(0) = n_{\alpha,\mathrm{TOT}}^{\mathrm{E}}, \tag{5.19}$$

$$n_\alpha^{\mathrm{R}}(0) = n_{\alpha,\mathrm{TOT}}^{\mathrm{R}}. \tag{5.20}$$

The values of the dimensional and dimensionless parameters are stated in Tables 5.3 and 5.4 respectively.

With the same parameter and variable definitions, Model II is obtained from Model I by eliminating terms relating to the internalisation of [IL-2 : α] complexes, by setting $\hat{I}^{\mathrm{E}} = \hat{I}^{\mathrm{R}} = 0$; Model III is obtained by setting $\hat{P} = \lambda = \hat{I}^{\mathrm{E}} = \hat{I}^{\mathrm{R}} = 0$.

Parameter	Dimension	Value
P (Model I and II)	Number/(Length^3 $\times$Time)	Varied
Λ (Model I and II)	1/Time	0.00231 s^{-1} (Half life of IL-2: 5 min)
k_α	Length^3/(Number$\times$Time)	1.760×10^{-14} cm^3/(Number$\times$s) $\left(1.06 \times 10^7\ \mathrm{M}^{-1}\mathrm{s}^{-1}\right)$
$k_{-\alpha}$	1/Time	0.298 s^{-1}
I^{E} (Model I)	1/Time	Varied from 1.1×10^{-3} s^{-1}
I^{R} (Model I)	1/Time	Varied from 1.1×10^{-3} s^{-1}
$N^{\mathrm{E}}_{\alpha,\mathrm{TOT}}$	Number/Length^2	$3.183 \times [10^8, 10^9]$ Number/cm^2 Number per cell: $[10^3, 10^4]$
$N^{\mathrm{R}}_{\alpha,\mathrm{TOT}}$	Number/Length^2	$3.183 \times [10^9, 10^{10}]$ Number/cm^2 Number per cell: $[10^4, 10^5]$
M^{E}	Number	Varied
M^{R}	Number	Varied
V	Length^3	200 μL
R_{cell}	Length	5×10^{-4} cm
A	Length^2	3.14×10^{-6} cm^2
$\overline{\tau}$	Time	0.25 s
$\overline{N_L}$	Number/Length^3	3.885×10^8 Number/cm^3 (or $\sim 10^{-12}$ M) (IL-2 typical: 10 pg/ml, molecular weight of IL-2: 15.5 kDa [77])
$\overline{N_\alpha}$	Number/Length^2	3.183×10^9 Number/cm^2 (Number per cell: 10^4)

Table 5.3: Selected values of the dimensional parameters for Model I, II and III. $A = 4\pi R^2_{\mathrm{cell}}$ is the area of the cell membrane. $\overline{N_L}$ and $\overline{N_\alpha}$ are chosen typical values of N_L and N_α respectively to non-dimensionalise these two variables.

Steady state analysis

Steady state analysis for Model I

We determine the steady state solutions of Model I by setting the right hand side of Equations (5.13)–(5.15) to zero. It is straightforward to show that the proportions of

Parameter	Expression	Value
$\hat{P}$ (Model I and II)	$\hat{P} = \frac{\overline{\tau}}{\overline{N_L}} P$	Varied
λ (Model I and II)	$\sqrt{\overline{\tau}\Lambda}$	0.024
$\hat{k}_\alpha$	$\overline{\tau}\overline{N_L} k_\alpha$	1.710×10^{-6}
$\hat{k}_{-\alpha}$	$\overline{\tau} k_{-\alpha}$	0.0745
$\hat{I}^{\mathrm{E}}$ (Model I)	$\overline{\tau} I^{\mathrm{E}}$	Varied from 2.75×10^{-4}
$\hat{I}^{\mathrm{R}}$ (Model I)	$\overline{\tau} I^{\mathrm{R}}$	Varied from 2.75×10^{-4}
$n^{\mathrm{E}}_{\alpha,\mathrm{TOT}}$	$\frac{N^{\mathrm{E}}_{\alpha,\mathrm{TOT}}}{\overline{N_\alpha}}$	Varied
$n^{\mathrm{R}}_{\alpha,\mathrm{TOT}}$	$\frac{N^{\mathrm{R}}_{\alpha,\mathrm{TOT}}}{\overline{N_\alpha}}$	Varied
M^{E}		Varied
M^{R}		Varied
$\hat{F}$	$\frac{A}{V}\frac{\overline{N_\alpha}}{\overline{N_L}}$	1.287×10^{-4} ($V = 200$ μL)

Table 5.4: Values of the dimensionless parameters in the model describing competition with only α chain. The values are calculated using selected values for the dimensional parameters as in Table 5.3.

α chains bound to the two cell populations are:

$$\frac{n^{\mathrm{E}}_{\alpha L,\infty}}{n^{\mathrm{E}}_{\alpha,\mathrm{TOT}}} = \frac{n_{L,\infty}}{n_{L,\infty} + \theta_{\mathrm{E}}}, \tag{5.21}$$

$$\frac{n^{\mathrm{R}}_{\alpha L,\infty}}{n^{\mathrm{R}}_{\alpha,\mathrm{TOT}}} = \frac{n_{L,\infty}}{n_{L,\infty} + \theta_{\mathrm{R}}}, \tag{5.22}$$

where we have introduced the half-saturation parameters,

$$\theta_{\mathrm{E}} = \frac{\hat{k}_{-\alpha L} + \hat{I}^{\mathrm{E}}}{\hat{k}_{\alpha L}}, \theta_{\mathrm{R}} = \frac{\hat{k}_{-\alpha L} + \hat{I}^{\mathrm{R}}}{\hat{k}_{\alpha L}}.$$

Substituting for $n^{\mathrm{E}}_{\alpha,\infty}$ and $n^{\mathrm{R}}_{\alpha,\infty}$ in the steady-state IL-2 equation, we obtain the following non-linear equation for $n_{L,\infty}$:

$$\lambda^2 n_{L,\infty} \; + \; M^{\mathrm{E}} \hat{F} \hat{I}^{\mathrm{E}} n^{\mathrm{E}}_{\alpha,\mathrm{TOT}} \frac{n_{L,\infty}}{n_{L,\infty} + \theta_{\mathrm{E}}} \; + \; M^{\mathrm{R}} \hat{F} \hat{I}^{\mathrm{R}} n^{\mathrm{R}}_{\alpha,\mathrm{TOT}} \frac{n_{L,\infty}}{n_{L,\infty} + \theta_{\mathrm{R}}} \; = \; \hat{P}. \tag{5.23}$$

We note that the left-hand side of Equation (5.23) is a monotonically increasing function of $n_{L,\infty}$ that starts from 0 when $n_{L,\infty} = 0$ and increases linearly with $n_{L,\infty}$ as $n_{L,\infty} \to \infty$. Thus, the system has a unique physically realistic steady state solution.

Equation (5.23) shows that at steady-state, IL-2 levels are determined by balancing IL-2 production ($\hat{P}$), natural decay (λ^2), and uptake by effector and regulatory T cells. Equations (5.21) and (5.22) show that the proportions of bound α chains for the two cell types differ when their rates of internalisation of the [IL-2 : α] complex, $\hat{I}^{\mathrm{E}}$ and $\hat{I}^{\mathrm{R}}$, differ. The cell type with the lower internalisation rate binds IL-2 more avidly at low cytokine levels, tipping the balance toward immunoactivation ($\hat{I}^{\mathrm{E}} < \hat{I}^{\mathrm{R}}$) or immunosuppression ($\hat{I}^{\mathrm{E}} > \hat{I}^{\mathrm{R}}$).

Steady state analysis for Model II

With $I^{\mathrm{E}} = I^{\mathrm{R}} = 0$ in Equations (5.21), (5.22) and (5.23), the steady state solutions of Model II are:

$$n_{L,\infty} = \frac{\hat{P}}{\lambda^2}, \quad \frac{n^{\mathrm{E}}_{\alpha L,\infty}}{n^{\mathrm{E}}_{\alpha,\mathrm{TOT}}} = \frac{n^{\mathrm{R}}_{\alpha L,\infty}}{n^{\mathrm{R}}_{\alpha,\mathrm{TOT}}} = \left(1 + \frac{\hat{k}_{-\alpha L}}{\hat{k}_{\alpha L}} \frac{1}{n_{L,\infty}}\right)^{-1}. \tag{5.24}$$

The steady-state extracellular concentration of IL-2 ($n_{L,\infty}$) depends only on the balance between its rate of production ($\hat{P}$) and its rate of decay (λ^2), rendering it invariant to changes in receptor abundance. While the fractional occupancy of α chains is identical for the effector and regulatory T cells, the higher surface density of α chains on regulatory T cells (see Table 5.3) results in a correspondingly larger number of [IL-2 : α] complexes on this cell type.

Steady state analysis for Model III

For Model III, we obtain the following equation for the steady state solution of n_L, $n_{L,\infty}$:

$$n_{L,\infty} = n_{L,0} - \hat{F}\, \frac{\hat{k}_{\alpha L}\, n_{L,\infty}}{\hat{k}_{\alpha L}\, n_{L,\infty} + \hat{k}_{-\alpha L}}\, \Delta, \quad \text{where} \quad \Delta = M^{\mathrm{E}}\, n^{\mathrm{E}}_{\alpha,\mathrm{TOT}} + M^{\mathrm{R}}\, n^{\mathrm{R}}_{\alpha,\mathrm{TOT}}. \tag{5.25}$$

Rearranging Equation (5.25), we deduce that $n_{L,\infty}$ solves the quadratic:

$$\hat{k}_{\alpha L}\, (n_{L,\infty})^2 \;+\; \left(\hat{k}_{-\alpha L} \;-\; n_{L,0}\, \hat{k}_{\alpha L} \;+\; \hat{F}\, \hat{k}_{\alpha L}\, \Delta\right) n_{L,\infty} \;-\; n_{L,0}\, \hat{k}_{-\alpha L} \;=\; 0. \tag{5.26}$$

Steady state solutions for the other variables ($n^{\mathrm{E}}_{\alpha,\infty}$, $n^{\mathrm{R}}_{\alpha,\infty}$, $n^{\mathrm{E}}_{\alpha L,\infty}$, $n^{\mathrm{R}}_{\alpha L,\infty}$) can then be calculated and are all positive. In this case, the proportions of bound α chain at the steady state are the same for both populations:

$$\frac{n^{\mathrm{E}}_{\alpha L,\infty}}{n^{\mathrm{E}}_{\alpha,\mathrm{TOT}}} = \frac{n^{\mathrm{R}}_{\alpha L,\infty}}{n^{\mathrm{R}}_{\alpha,\mathrm{TOT}}} = \frac{n_{L,\infty}}{n_{L,\infty} + \frac{\hat{k}_{-\alpha L}}{\hat{k}_{\alpha L}}}. \tag{5.27}$$

Since regulatory T cells possess more α chains than effector T cells, we conclude that they possess more bound α chains than effector T cells.

To assess the stability of the physically realistic steady state solution, we perform a linear stability analysis. The Jacobian matrix of the two-dimensional system for n_α^{E} and n_α^{R} is:

$$J = \begin{pmatrix} -\hat{k}_{\alpha L}\left(M^{\mathrm{E}}\hat{F}\, n_{\alpha,\infty}^{\mathrm{E}} + n_{L,\infty}\right) - \hat{k}_{-\alpha L} & -\hat{k}_{\alpha L}\, M^{\mathrm{R}}\hat{F}\, n_{\alpha,\infty}^{\mathrm{E}} \\ -\hat{k}_{\alpha L}\, M^{\mathrm{E}}\hat{F}\, n_{\alpha,\infty}^{\mathrm{R}} & -\hat{k}_{\alpha L}\left(M^{\mathrm{R}}\hat{F}\, n_{\alpha,\infty}^{\mathrm{R}} + n_{L,\infty}\right) - \hat{k}_{-\alpha L} \end{pmatrix}. \tag{5.28}$$

The determinant D of J is:

$$D = \hat{k}_{\alpha L}^2\Big[n_L\big(M^E\hat{F}\, n_\alpha^E \;+\; M^R\hat{F}\, n_\alpha^R\big) \;+\; n_L^2\Big] \tag{5.29}$$

$$+\; \hat{k}_{\alpha L}\,\hat{k}_{-\alpha L}\Big[M^E\hat{F}\, n_\alpha^E \;+\; M^R\hat{F}\, n_\alpha^R \;+\; 2\, n_L\Big] \;+\; \hat{k}_{-\alpha L}^2. \tag{5.30}$$

It is straightforward to show that the $T = \mathrm{trace}(J) < 0$ and $D > 0$ is positive at the feasible steady state solution. Further more the discriminant $T^2 - 4D > 0$, and so we conclude that the unique feasible steady state solution is a stable node.

The main conclusion of this work is that regulatory T cells possess an advantage in IL-2 competition because their higher abundance of α chains leads to a larger number of [IL-2 : α] complexes at steady state when the occupancy fraction is the same across cell types, as in Models II and III. Model I shows that differential internalisation rate of the [IL-2 : α] complexes can modulate this competition: the cell type with the lower internalisation rate attains a higher proportion of bound α chains especially at low IL-2 levels, thereby biasing the balance towards immunoactivation or immunosuppression. Thus, the simplified α-chain models show that competition can be shaped both by receptor abundance and by trafficking, but that the baseline competitive advantage of regulatory T cells already arises from their greater availability of α chains.

5.3 Model with full binding kinetics

5.3.1 Model development

In Section 5.2, we developed ODE models of competition for IL-2 between effector and regulatory T cells which focused on IL-2 binding to α chains. In this section, we incorporate β and γ chains, again via a β/γ dimer, to more realistically describe the

binding kinetics. We also extend the ODE model for a single T cell to the population level.

We assume that IL-2 is produced and decays in the extracellular space that surrounds the cells. For each cell, we make the same assumptions for IL-2 binding kinetics as detailed in Section 4.2.1 (see Figure 4.1 for a schematic representation of the binding kinetics). The independent variable is time, t, with units s. The interpretations and the units of the dependent variables and parameters are summarized in Tables 5.5 and 5.6 respectively.

Variable	Interpretation	Unit
N_L	Concentration of free IL-2 in the bulk	Number/cm^3
N_α^{i}	Concentration of free α chain on a T cell	Number/cm^2
N_β^{i}	Concentration of free β chain on a T cell	Number/cm^2
$N_{\alpha L}^{\mathrm{i}}$	Concentration of [IL-2 : α] complex on a T cell	Number/cm^2
$N_{\beta L}^{\mathrm{i}}$	Concentration of [IL-2 : β] complex on a T cell	Number/cm^2
$N_{\alpha\beta L}^{\mathrm{i}}$	Concentration of [IL-2 : α]β complex on a T cell	Number/cm^2

Table 5.5: Dependent variables and their units for the dimensional ODE model describing competition for IL-2 by effector and regulatory T cells, assuming β/γ dimers. $\mathrm{i} \in \{\mathrm{E}, \mathrm{R}\}$ indicates whether the quantity corresponds to effector (E) or regulatory (R) T cells respectively.

Combining these modelling assumptions, we deduce that the dynamics of the dependent variables are governed by:

$$\frac{dN_L}{dt} = -M^{\mathrm{E}}\frac{A}{V}\left[R_1^{\mathrm{E}} + R_2^{\mathrm{E}}\right] - M^{\mathrm{R}}\frac{A}{V}\left[R_1^{\mathrm{R}} + R_2^{\mathrm{R}}\right] - \Lambda N_L + P, \tag{5.31}$$

$$\frac{dN_\alpha^{\mathrm{i}}}{dt} = -R_1^{\mathrm{i}} - R_3^{\mathrm{i}} + I^{\mathrm{i}} N_{\alpha\beta L}^{\mathrm{i}}, \tag{5.32}$$

$$\frac{dN_\beta^{\mathrm{i}}}{dt} = -R_2^{\mathrm{i}} - R_4^{\mathrm{i}} + G_\beta^{\mathrm{i}}\left(N_{\beta,*}^{\mathrm{i}} - N_\beta^{\mathrm{i}} - N_{\beta L}^{\mathrm{i}} - N_{\alpha\beta L}^{\mathrm{i}}\right), \tag{5.33}$$

$$\frac{dN_{\alpha L}^{\mathrm{i}}}{dt} = +R_1^{\mathrm{i}} - R_4^{\mathrm{i}}, \tag{5.34}$$

$$\frac{dN_{\beta L}^{\mathrm{i}}}{dt} = +R_2^{\mathrm{i}} - R_3^{\mathrm{i}}, \tag{5.35}$$

$$\frac{dN_{\alpha\beta L}^{\mathrm{i}}}{dt} = +R_3^{\mathrm{i}} + R_4^{\mathrm{i}} - I^{\mathrm{i}} N_{\alpha\beta L}^{\mathrm{i}}, \tag{5.36}$$

Parameter	Interpretation	Unit
k_β	Binding on rate of IL-2 and β chain	cm^3/ (Number×s)
$k_{-\beta}$	Binding off rate of IL-2 and β chain	1/s
$k_{\alpha\beta}$	Binding on rate of β chain and [IL-2 : α] complex	cm^2/ (Number×s)
$k_{-\alpha\beta}$	Binding off rate of β chain and [IL-2 : α] complex	1/s
$k_{\beta\alpha}$	Binding on rate of α chain and [IL-2 : β] complex	cm^2/ (Number×s)
$k_{-\beta\alpha}$	Binding off rate of α chain and [IL-2 : β] complex	1/s
I^{i}	Internalisation rate of the [IL-2 : α : β] complex	1/s
$N^{\text{i}}_{\beta,*}$	The concentration of β chains in the absence of IL-2	Number/cm^2
G^{i}_β	Synthesis rate of β chains	1/s

Table 5.6: Parameters and their units for the ODE model describing competition for IL-2 by effector and regulatory T cells, assuming β/γ dimers. The interpretations and units for the parameters $P, \Lambda, k_\alpha, k_{-\alpha}, N^{\text{i}}_{\alpha,\text{TOT}}, M^{\text{i}}, V, A, R_{\text{cell}}$ inherit from models developed in Section 5.2 and are listed in Table 5.2. $\text{i} \in \{\text{E}, \text{R}\}$ indicates whether the quantity corresponds to effector (E) or regulatory (R) T cells respectively.

where

$$R^{\text{i}}_1 = k_\alpha N_L N^{\text{i}}_\alpha - k_{-\alpha} N^{\text{i}}_{\alpha L}, \tag{5.37}$$

$$R^{\text{i}}_2 = k_\beta N_L N^{\text{i}}_\beta - k_{-\beta} N^{\text{i}}_{\beta L}, \tag{5.38}$$

$$R^{\text{i}}_3 = k_{\beta\alpha} N^{\text{i}}_{\beta L} N^{\text{i}}_\alpha - k_{-\beta\alpha} N^{\text{i}}_{\alpha\beta L}, \tag{5.39}$$

$$R^{\text{i}}_4 = k_{\alpha\beta} N^{\text{i}}_{\alpha L} N^{\text{i}}_\beta - k_{-\alpha\beta} N^{\text{i}}_{\alpha\beta L}, \tag{5.40}$$

and $\text{i} \in \{\text{E}, \text{R}\}$ for effector (E) and regulatory (R) T cells respectively.

The equations take the same form and have the same interpretation as Equations (5.1)–(5.5) with additional terms involving β/γ dimers. Those terms involving β/γ dimers have the same interpretation as Equations (4.2)–(4.6) with the additional cell types, as labelled by the superscript $\text{i} \in \{\text{E}, \text{R}\}$.

Adding Equations (5.32), (5.34) and (5.36), we note that the total number of α chains on effector and regulatory T cells is constant. We exploit this identity to eliminate $N^{\text{i}}_{\alpha\beta L}$ from the model, noting that:

$$N^{\text{i}}_{\alpha\beta L}(t) = N^{\text{i}}_{\alpha,\text{TOT}} - N^{\text{i}}_\alpha(t) - N^{\text{i}}_{\alpha L}(t), \tag{5.41}$$

where $N^{\text{i}}_{\alpha,\text{TOT}}$ is the total concentration of α chains on the membrane for a cell of type $\text{i} \in \{\text{E}, \text{R}\}$.

We close Equations (5.31) to (5.35) by imposing the initial conditions,

$$N_L(0) = N_{L,0}, \tag{5.42}$$
$$N^{\mathrm{i}}_{\alpha}(0) = N^{\mathrm{i}}_{\alpha,\mathrm{TOT}}, \tag{5.43}$$
$$N^{\mathrm{i}}_{\beta}(0) = N^{\mathrm{i}}_{\beta,*}, \tag{5.44}$$
$$N^{\mathrm{i}}_{\alpha L}(0) = 0, \tag{5.45}$$
$$N^{\mathrm{i}}_{\beta L}(0) = 0. \tag{5.46}$$

Non-dimensionalisation

We introduce the following scalings, with $\mathrm{i} \in \{\mathrm{E}, \mathrm{R}\}$:

$$\begin{gathered} \tau = \frac{t}{\overline{\tau}}, n_L = \frac{N_L}{\overline{N_L}}, \\ n^{\mathrm{i}}_{\alpha} = \frac{N^{\mathrm{i}}_{\alpha}}{\overline{N_\alpha}}, n^{\mathrm{i}}_{\beta} = \frac{N^{\mathrm{i}}_{\beta}}{\overline{N_\alpha}}, n^{\mathrm{i}}_{\alpha L} = \frac{N^{\mathrm{i}}_{\alpha L}}{\overline{N_\alpha}}, n^{\mathrm{i}}_{\beta L} = \frac{N^{\mathrm{i}}_{\beta L}}{\overline{N_\alpha}}, n^{\mathrm{i}}_{\alpha\beta L} = \frac{N^{\mathrm{i}}_{\alpha\beta L}}{\overline{N_\alpha}}, \end{gathered} \tag{5.47}$$

where $\overline{\tau}$ is a typical time-scale with units s, $\overline{N_L}$ and $\overline{N_\alpha}$ are typical values of the concentrations of free IL-2 in the bulk and free α chain on the cell membrane respectively. We also introduce the following dimensionless parameters:

$$\begin{aligned} &\hat{k}_{\alpha} = \overline{\tau}\,\overline{N_L} k_{\alpha}, \hat{k}_{-\alpha} = \overline{\tau} k_{-\alpha}, \\ &\hat{k}_{\beta} = \overline{\tau}\,\overline{N_L} k_{\beta}, \hat{k}_{-\beta} = \overline{\tau} k_{-\beta}, \\ &\hat{k}_{\beta\alpha} = \overline{\tau}\,\overline{N_\alpha} k_{\beta\alpha}, \hat{k}_{-\beta\alpha} = \overline{\tau} k_{-\beta\alpha}, \\ &\hat{k}_{\alpha\beta} = \overline{\tau}\,\overline{N_\alpha} k_{\alpha\beta}, \hat{k}_{-\alpha\beta} = \overline{\tau} k_{-\alpha\beta}, \\ &\lambda^2 = \overline{\tau}\Lambda, \hat{P} = \frac{\overline{\tau}}{\overline{N_L}} P, \hat{F} = \frac{A}{V}\frac{\overline{N_\alpha}}{\overline{N_L}}, \hat{G}^{\mathrm{i}}_{\beta} = \overline{\tau} G^{\mathrm{i}}_{\beta}, \\ &n^{\mathrm{i}}_{\alpha,\mathrm{TOT}} = \frac{N^{\mathrm{i}}_{\alpha,\mathrm{TOT}}}{\overline{N_\alpha}}, n^{\mathrm{i}}_{\beta,*} = \frac{N^{\mathrm{i}}_{\beta,*}}{\overline{N_\alpha}}, \hat{I}^{\mathrm{i}} = \overline{\tau} I^{\mathrm{i}}, n_{L,0} = \frac{N_{L,0}}{\overline{N_L}}. \end{aligned} \tag{5.48}$$

Under the above rescaling, Equations (5.31)–(5.46) transform to give the following dimensionless ODEs:

$$\frac{dn_L}{d\tau} = -M^{\mathrm{E}}\hat{F}\left[\hat{R}^{\mathrm{E}}_1 + \hat{R}^{\mathrm{E}}_2\right] - M^{\mathrm{R}}\hat{F}\left[\hat{R}^{\mathrm{R}}_1 + \hat{R}^{\mathrm{R}}_2\right] - \lambda^2 n_L + \hat{P}, \tag{5.49}$$
$$\frac{dn^{\mathrm{i}}_{\alpha}}{d\tau} = -\hat{R}^{\mathrm{i}}_1 - \hat{R}^{\mathrm{i}}_3 + \hat{I}^{\mathrm{i}} n^{\mathrm{i}}_{\alpha\beta L}, \tag{5.50}$$
$$\frac{dn^{\mathrm{i}}_{\beta}}{d\tau} = -\hat{R}^{\mathrm{i}}_2 - \hat{R}^{\mathrm{i}}_4 + \hat{G}^{\mathrm{i}}_{\beta}\left(n^{\mathrm{i}}_{\beta,*} - n^{\mathrm{i}}_{\beta} - n^{\mathrm{i}}_{\beta L} - n^{\mathrm{i}}_{\alpha\beta L}\right), \tag{5.51}$$
$$\frac{dn^{\mathrm{i}}_{\alpha L}}{d\tau} = \hat{R}^{\mathrm{i}}_1 - \hat{R}^{\mathrm{i}}_4, \tag{5.52}$$
$$\frac{dn^{\mathrm{i}}_{\beta L}}{d\tau} = \hat{R}^{\mathrm{i}}_2 - \hat{R}^{\mathrm{i}}_3, \tag{5.53}$$

where

$$R_1^{\mathrm{i}} = \hat{k}_\alpha n_L n_\alpha^{\mathrm{i}} - \hat{k}_{-\alpha} n_{\alpha L}^{\mathrm{i}}, \tag{5.54}$$

$$R_2^{\mathrm{i}} = \hat{k}_\beta n_L n_\beta^{\mathrm{i}} - \hat{k}_{-\beta} n_{\beta L}^{\mathrm{i}}, \tag{5.55}$$

$$R_3^{\mathrm{i}} = \hat{k}_{\beta\alpha} n_{\beta L}^{\mathrm{i}} n_\alpha^{\mathrm{i}} - \hat{k}_{-\beta\alpha} n_{\alpha\beta L}^{\mathrm{i}}, \tag{5.56}$$

$$R_4^{\mathrm{i}} = \hat{k}_{\alpha\beta} n_{\alpha L}^{\mathrm{i}} n_\beta^{\mathrm{i}} - \hat{k}_{-\alpha\beta} n_{\alpha\beta L}^{\mathrm{i}}, \tag{5.57}$$

and

$$n_{\alpha\beta L}^{\mathrm{i}}(\tau) = n_{\alpha,\mathrm{TOT}}^{\mathrm{i}} - n_\alpha^{\mathrm{i}}(\tau) - n_{\alpha L}^{\mathrm{i}}(\tau), \tag{5.58}$$

with initial conditions,

$$n_L(0) = n_{L,0}, \tag{5.59}$$

$$n_\alpha^{\mathrm{i}}(0) = n_{\alpha,\mathrm{TOT}}^{\mathrm{i}}, \tag{5.60}$$

$$n_\beta^{\mathrm{i}}(0) = n_{\beta,*}^{\mathrm{i}}, \tag{5.61}$$

$$n_{\alpha L}^{\mathrm{i}}(0) = 0, \tag{5.62}$$

$$n_{\beta L}^{\mathrm{i}}(0) = 0, \tag{5.63}$$

where we assume that all α and β chains are initially unbound.

The numbers of α and β chains expressed by effector and regulatory T cells are the same as for the single-cell model and are stated in Table 4.7. The values of the dimensional and dimensionless model parameters are stated in Tables 5.7 and 5.8 respectively.

Parameter	Dimension	Value
$k_{-\beta}$	1/Time	2.5×10^{-4} s^{-1}
$k_{\alpha\beta}$	Length^2/(Number×Time)	3×10^{-4} s^{-1} $\times A$
$k_{-\alpha\beta}$	1/Time	2.3×10^{-4} s^{-1}
$k_{\beta\alpha}$	Length^2/(Number×Time)	0.6×10^{-2} s^{-1} $\times A$
$k_{-\beta\alpha}$	1/Time	0.6 s^{-1}
I^{E}	1/Time	Varied from 1.1×10^{-3} s^{-1}
I^{R}	1/Time	Varied from 1.1×10^{-3} s^{-1}
$N^{\mathrm{E}}_{\beta,*}$	Number/Length^2	Varied
$N^{\mathrm{R}}_{\beta,*}$	Number/Length^2	Varied
G^{E}_{β}	1/Time	Varied
G^{R}_{β}	1/Time	Varied

Table 5.7: Selected values of the parameters for the model with full binding kinetics. The values of the parameters $P, \Lambda, k_\alpha, k_{-\alpha}, N^{\mathrm{i}}_{\alpha,\mathrm{TOT}}, M^{\mathrm{i}}, V, A, R_{\mathrm{cell}}, \overline{\tau}, \overline{N_L}, \overline{N_\alpha}$ are the same as for the models developed in Section 5.2 and are listed in Table 5.3. $\mathrm{i} \in \{\mathrm{E}, \mathrm{R}\}$ indicates whether the quantity corresponds to effector (E) or regulatory (R) T cells respectively. $A = 4\pi R^2_{\mathrm{cell}}$ is the area of the cell membrane.

Parameter	Expression	Value
$\hat{k}_\beta$	$\overline{\tau}\overline{N_L}k_\beta$	6.13×10^{-8}
$\hat{k}_{-\beta}$	$\overline{\tau}k_{-\beta}$	6.25×10^{-5}
$\hat{k}_{\alpha\beta}$	$\overline{\tau}\overline{N_\alpha}k_{\alpha\beta}$	0.75
$\hat{k}_{-\alpha\beta}$	$\overline{\tau}k_{-\alpha\beta}$	5.75×10^{-5}
$\hat{k}_{\beta\alpha}$	$\overline{\tau}\overline{N_\alpha}k_{\beta\alpha}$	15
$\hat{k}_{-\beta\alpha}$	$\overline{\tau}k_{-\beta\alpha}$	0.15
$\hat{I}^{\mathrm{E}}$	$\overline{\tau}I^{\mathrm{E}}$	Varied from 2.75×10^{-4}
$\hat{I}^{\mathrm{R}}$	$\overline{\tau}I^{\mathrm{R}}$	Varied from 2.75×10^{-4}
$n^{\mathrm{E}}_{\beta,*}$	$\frac{N^{\mathrm{E}}_{\beta,*}}{\overline{N_\alpha}}$	Varied
$n^{\mathrm{R}}_{\beta,*}$	$\frac{N^{\mathrm{R}}_{\beta,*}}{\overline{N_\alpha}}$	Varied
$\hat{G}^{\mathrm{E}}_{\beta}$	$\overline{\tau}G^{\mathrm{E}}_{\beta}$	Varied
$\hat{G}^{\mathrm{R}}_{\beta}$	$\overline{\tau}G^{\mathrm{R}}_{\beta}$	Varied

Table 5.8: Values of the dimensionless parameters in the model describing competition with full binding kinetics. The values are calculated using selected values for the dimensional parameters as in Table 5.7. The expressions and values of the parameters $\hat{P}, \lambda, \hat{k}_\alpha, \hat{k}_{-\alpha}, n^{\mathrm{E}}_{\alpha,\mathrm{TOT}}, n^{\mathrm{R}}_{\alpha,\mathrm{TOT}}, M^{\mathrm{E}}, M^{\mathrm{R}}, \hat{F}$ are the same as for the models developed in Section 5.2 and are listed in Table 5.4.

5.3.2 Steady-state behaviour under parameter variation

We now examine how changes in the values of selected parameters alter IL-2 binding, the distribution of signalling complexes and the balance between stimulation of effector and regulatory T cells. We simulate the model to its steady state using `ode45` in MATLAB. Results varying the bulk production rate of IL-2, $\hat{P}$, are shown in Figure 5.1.

To quantify the competitive outcome, we define the signalling balance ratio, denoted as ρ. This metric represents the relative abundance of signalling complexes on effector T cells compared with regulatory T cells at steady state:

$$\rho = \frac{n^{\mathrm{E}}_{\beta L,\infty} + n^{\mathrm{E}}_{\alpha\beta L,\infty}}{n^{\mathrm{R}}_{\beta L,\infty} + n^{\mathrm{R}}_{\alpha\beta L,\infty}}. \tag{5.64}$$

Given the therapeutic interest in $\hat{k}_{-\alpha L}$, we then examine how varying $\hat{k}_{-\alpha L}$ affects ρ for fixed values of $\hat{P}$; these results are shown in Figure 5.2. We also investigate how variation in other parameter values affects ρ, although these results are omitted for brevity.

From Figure 5.1(a), we observe that the proportion of bound IL-2 decreases as $\hat{P}$ increases. When IL-2 production rates are low ($\hat{P} \approx 10^{-4}$), more than one-third of the available IL-2 is captured by receptors. The bound fraction decreases monotonically as $\hat{P}$ increases and drops below 5% when $\hat{P} \gtrsim 10$. In this ligand-excess regime, receptor numbers are limiting. From Figure 5.1(b), we conclude the following, consistent with the findings of Chapter 4:

Preferential stimulation depends on IL-2 availability. When IL-2 production rates are low, ligand availability is limited, and regulatory T cells are preferentially stimulated because their high expression levels of α chains enables more efficient ligand capture. By contrast, when IL-2 production rates are high, ligand is more abundant, and effector T cells are preferentially stimulated because the availability of β chains becomes the limiting factor for the formation of signalling complexes.

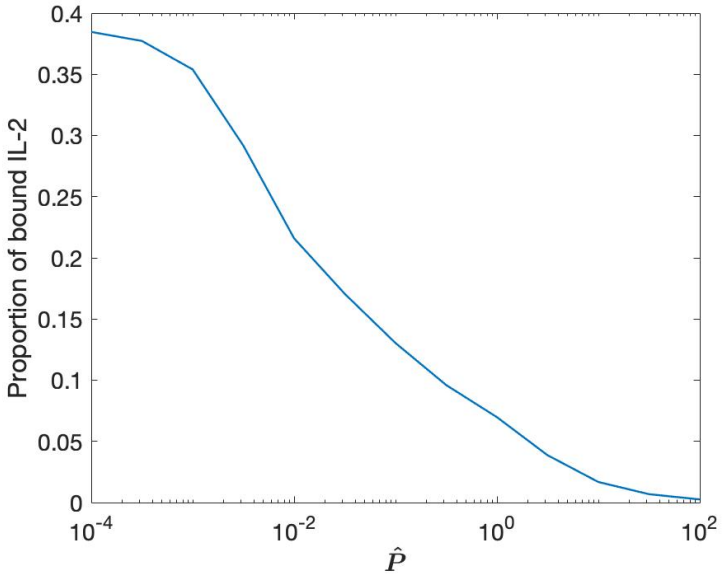
Regulatory T cells rely on initial binding of IL-2 to α chains. Across the entire range of $\hat{P}$ considered, the signalling complexes formed on regulatory T cells are predominantly [IL-2 : α : β]. The [IL-2 : β] complexes make a negligible contribution because the limited availability of β chains on regulatory T cells restricts formation through this pathway. Thus, regulatory T cells rely on α chains to capture IL-2.

Effector T cells switch from α chain dependent capture to β chain capture when $\hat{P}$ increases. For effector T cells, when IL-2 production rates are low, [IL-2 : α : β] complexes dominate; when IL-2 production rates are high, [IL-2 : β]

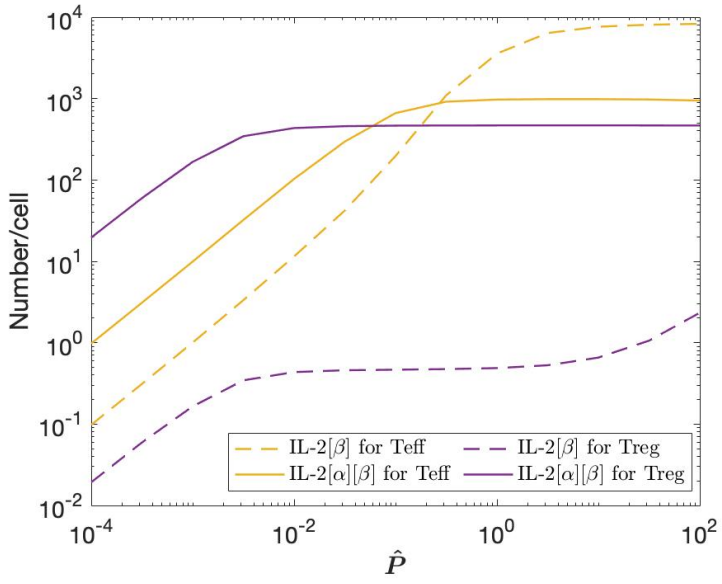
complexes dominate. When IL-2 is scarce, effector T cells rely on α chains to form signalling complexes; when IL-2 is plentiful, they can bypass α chains, and β chain binding becomes the dominant route. This shift indicates that the contribution of the α chain to complex formation decreases as IL-2 becomes more abundant.

From Figure 5.2, we conclude that variation in $\hat{k}_{-\alpha L}$ alters the balance of stimulation between effector and regulatory T cells, with the strongest effect observed when IL-2 production rates are low. In this regime, increasing $\hat{k}_{-\alpha L}$ shifts the signalling balance in favour of effector T cells. Increasing $\hat{k}_{-\alpha L}$ promotes dissociation of IL-2 from α chains, thus reducing the efficacy of the ligand capture pathway that plays a more prominent role in regulatory T cells.

Results obtained by varying other parameters (not shown) reveal that increasing the availability of β chains for a specific cell type promotes its competitive advantage. Specifically, increasing the availability of β chains on effector T cells (increasing $n^{\mathrm{E}}_{\beta,*}$) shifts the signalling balance in favor of effector T cells; increasing the availability of β chains on regulatory T cells (increasing $n^{\mathrm{R}}_{\beta,*}$ or $\hat{G}^{\mathrm{R}}_{\beta}$, decreasing $\hat{I}^{\mathrm{R}}$) enhances the stimulation of regulatory T cells. These results are biologically plausible and consistent with the model structure, since β chains are necessary for the formation of signalling complexes. Thus, greater availability of β chains allows a given cell type to make more effective use of the available IL-2. More generally, these results show that competitive outcome in the model depends not only on cytokine abundance, but also on the capacity of each cell type to assemble and maintain signalling complexes.



(a) Proportion of bound IL-2.



(b) Signalling complexes.

Figure 5.1: Effects of varying $\hat{P}$. Panel (a) presents results on how the proportion of bound IL-2 varies as the level of IL-2 ($\hat{P}$) increases in the system; Panel (b) presents results on how the distributions of signalling complexes for the two cell types change as $\hat{P}$ increases. The model is simulated to steady state using `ode45` in MATLAB, as described in Section 5.3.2. The proportion of bound IL-2 is the ratio of IL-2 held in any complex for both cell types to the total IL-2 in the system at steady state. Results for effector and regulatory T cells are plotted in dashed and solid lines respectively; results for [IL-2 : β] and [IL-2 : α : β] complexes are plotted in colours as indicated in the legend. $M_{\mathrm{E}} = 10^6$, $M_{\mathrm{R}} = 10^5$. $n^{\mathrm{E}}_{\alpha,\mathrm{TOT}} = 0.1, n^{\mathrm{R}}_{\alpha,\mathrm{TOT}} = 10$, $n^{\mathrm{E}}_{\beta,*} = 1, n^{\mathrm{R}}_{\beta,*} = 0.1$ ($\times 10^4$ gives number per cell). Other parameter values are stated in Table 5.8.

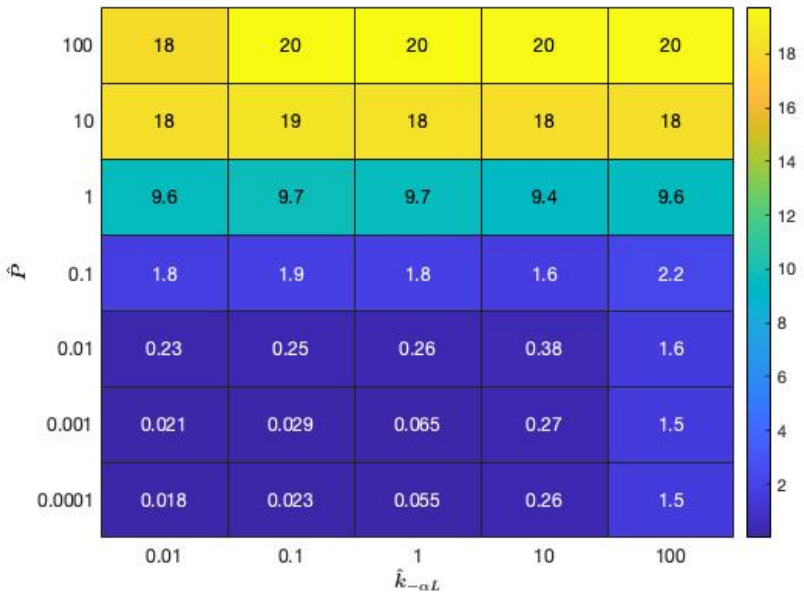


Figure 5.2: Ratio of signalling complexes for Teff/Treg when varying $\hat{k}_{-\alpha L}$ and $\hat{P}$. On the x-axis, we vary $\hat{k}_{-\alpha L}$ from 0.01 to 100; on the y-axis, we vary $\hat{P}$ from 0.0001 to 100. The ratios are drawn in colours according to the colour bar. $M_{\mathrm{E}} = 10^6, M_{\mathrm{R}} = 10^5$. $n^{\mathrm{E}}_{\alpha,\mathrm{TOT}} = 0.1, n^{\mathrm{R}}_{\alpha,\mathrm{TOT}} = 10$, $n^{\mathrm{E}}_{\beta,*} = 1, n^{\mathrm{R}}_{\beta,*} = 0.1$. Other parameter values are stated in Table 5.8.

5.3.3 Global sensitivity analysis

To further determine what model parameters drive competition for IL-2 between effector and regulatory T cells, we perform a global sensitivity analysis using the Extended Fourier Amplitude Sensitivity Test (eFAST). Whereas the parameter variations in the previous section assessed the effects of changing selected parameters individually, the global sensitivity analysis quantifies the relative importance of all parameters of interest simultaneously, including their interactions.

We again select the signalling balance ratio ρ (defined in Equation (5.64)) as the output of interest because it serves as a proxy for the net direction of the immune response; a high value of ρ indicates effector dominance (favoring activation), while a low value indicates regulatory dominance (favoring suppression). We vary 16 model parameters ($\hat{P}, \lambda, \hat{k}_{-\alpha}, \hat{k}_{-\beta}, \hat{k}_{-\alpha\beta}, \hat{k}_{-\beta\alpha}, \hat{I}^{\mathrm{E}}, \hat{I}^{\mathrm{R}}, n^{\mathrm{E}}_{\alpha,\mathrm{TOT}}, n^{\mathrm{R}}_{\alpha,\mathrm{TOT}}, n^{\mathrm{E}}_{\beta,*}, n^{\mathrm{R}}_{\beta,*}, \hat{G}^{\mathrm{E}}_{\beta}, \hat{G}^{\mathrm{R}}_{\beta}, M^{\mathrm{E}}, M^{\mathrm{R}}$) over the ranges specified in Table 5.9. The results are shown in Figure 5.3. Parameters with sensitivity indices lower than the dummy variable ($\hat{k}_{-\beta}, \hat{k}_{-\alpha\beta}, \hat{k}_{-\beta\alpha}, \hat{I}^{\mathrm{E}}, n^{\mathrm{E}}_{\alpha,\mathrm{TOT}}$, $n^{\mathrm{R}}_{\alpha,\mathrm{TOT}}, M^{\mathrm{E}}, M^{\mathrm{R}}$) are considered non-influential and are not shown in the figure for simplicity. To examine how the sensitivity to different parameters changes with the level of IL-2, we fix the value of $\hat{P}$ at different levels and perform eFAST varying the other 15 parameters. The results are shown in Figure 5.4. We present results for and focus our analysis on the five parameters with the highest sensitivity indices ($\hat{k}_{-\alpha}, \hat{I}^{\mathrm{R}}, n^{\mathrm{E}}_{\beta,*}, n^{\mathrm{R}}_{\beta,*}, \hat{G}^{\mathrm{R}}_{\beta}$) to highlight the primary sources of output uncertainty. Key observations from Figure 5.3 are:

Effects of population sizes are negligible. The negligible impact of population sizes ($M_{\mathrm{E}}, M_{\mathrm{R}}$) suggests that the system operates in a regime, for which the rate of natural cytokine decay ($\lambda^2 n_L$) significantly exceeds the net rate of cellular uptake. In this regime, the extracellular ligand concentration remains independent of cellular density, such that the competitive outcome is governed by the intrinsic kinetics and stoichiometry of the receptors on an individual cell basis, rather than by population-level competition for a finite resource.

Dominant influence of $\hat{G}^{\mathrm{R}}_{\beta}$. The synthesis rate of the β chain in regulatory T cells, $\hat{G}^{\mathrm{R}}_{\beta}$, is the most influential parameter, with first-order sensitivity index reaching $\mathcal{S}_i \approx 0.35$ and total-order sensitivity index reaching $\mathcal{S}_{T_i} \approx 0.8$. This strong influence is consistent with the structure of the model, since $\hat{G}^{\mathrm{R}}_{\beta}$ controls the replenishment of regulatory β chains for regulatory T cells, for which the availability of β chains is a limiting factor in the formation of signalling complexes. At present, $\hat{G}^{\mathrm{R}}_{\beta}$ remains weakly constrained because relevant data in the existing literature are scarce. Thus,

reducing uncertainty in this parameter should be a priority for improving the predictive reliability of the model, for example through experiments that quantify the replenishment rate of β chains in regulatory T cells, such as time-resolved measurements of surface expression of β chains following receptor internalisation or cytokine stimulation. Given its dominant influence on the signalling balance, $\hat{G}_\beta^{\mathrm{R}}$ highlights the availability of β chains for regulatory T cells as an important process for further experimental and pharmacological investigation.

Moderate, interaction-driven effects of $\hat{G}_\beta^{\mathrm{E}}$, $\hat{I}^{\mathrm{R}}$, $\hat{P}$, λ, $\hat{k}_{-\alpha}$, $n_{\beta,*}^{\mathrm{E}}$, and $n_{\beta,*}^{\mathrm{R}}$. These parameters exhibit moderate total-order sensitivity indices ($0.3 \lesssim \mathcal{S}_{T_i} \lesssim 0.45$) but small first-order indices ($\mathcal{S}_i < 0.15$), indicating that their influence on the model output arises mainly through interactions with other parameters rather than through strong independent effects. This suggests that they modulate the signalling balance indirectly, by shaping the ligand environment, receptor availability, ligand binding and complex turnover within the coupled network, rather than acting as primary control parameters on their own. Among the unbinding rates, only the dissociation rate of IL-2 from the α chain, $\hat{k}_{-\alpha}$, shows a non-negligible contribution ($\mathcal{S}_{T_i} \approx 0.38$), whereas the remaining off rates have negligible effects. This is consistent with findings in Chapter 4.

From Figure 5.4, we observe that the sensitivity of the model output to $\hat{k}_{-\alpha}$ decreases as the bulk IL-2 production rate $\hat{P}$ increases. When IL-2 production is low ($\hat{P} = 10^{-4}$), $\hat{k}_{-\alpha}$ is the dominant parameter, with $\mathcal{S}_i \approx 0.3$ and $\mathcal{S}_{T_i} \approx 0.8$. By contrast, when $\hat{P} = 1$, its influence becomes negligible (both sensitivity indices decrease to values comparable to those of the dummy variable). This behaviour is consistent with the biological interpretation of the model: under conditions of limited IL-2 production, the dissociation of IL-2 from the α chain has a substantial effect on ligand retention and, consequently, on downstream signalling. However, as IL-2 production increases, ligand availability increases, and the dissociation of IL-2 from the α chain has less effect on the competitive outcome. These results indicate that the IL-2–α interaction pathway is most influential in regimes of low IL-2 availability, and may accordingly constitute the most relevant target for perturbation under such conditions to alter IL-2 competition between effector and regulatory T cells.

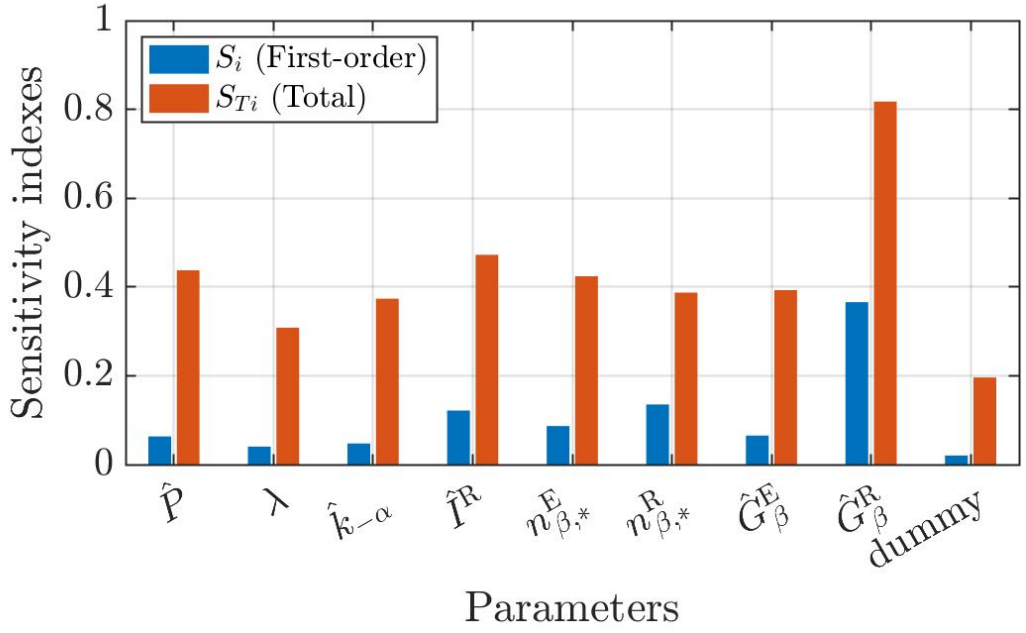
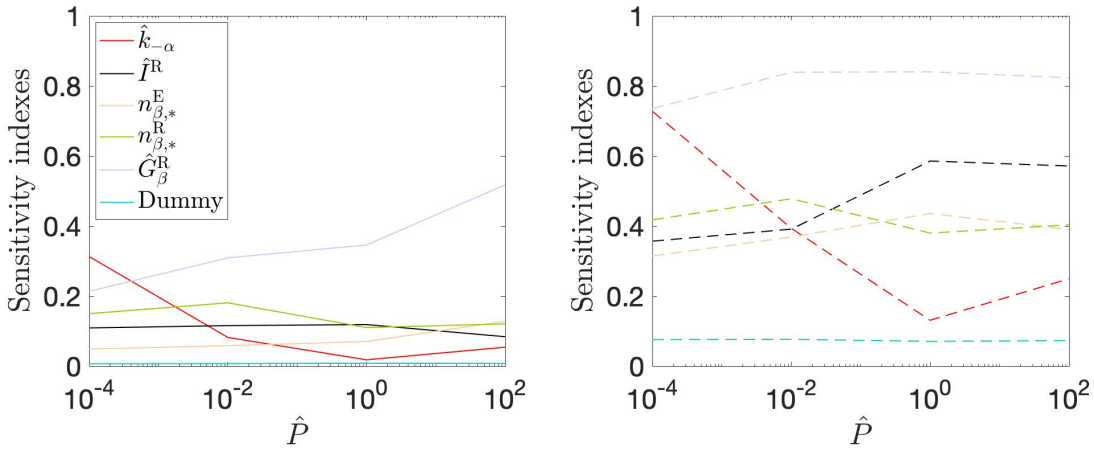


Figure 5.3: Results of global sensitivity analysis for the ratio of the total concentration of signalling complexes for Teff and Treg ($\frac{n^{\mathrm{E}}_{\beta L,\infty}+n^{\mathrm{E}}_{\alpha\beta L,\infty}}{n^{\mathrm{R}}_{\beta L,\infty}+n^{\mathrm{R}}_{\alpha\beta L,\infty}}$) as 16 model parameters $(\hat{P}, \lambda, \hat{k}_{-\alpha}, \hat{k}_{-\beta}, \hat{k}_{-\alpha\beta}, \hat{k}_{-\beta\alpha}, \hat{I}^{\mathrm{E}}, \hat{I}^{\mathrm{R}}, \ n^{\mathrm{E}}_{\alpha,\mathrm{TOT}}, n^{\mathrm{R}}_{\alpha,\mathrm{TOT}}, n^{\mathrm{E}}_{\beta,*}, n^{\mathrm{R}}_{\beta,*}, \hat{G}^{\mathrm{E}}_{\beta}, \hat{G}^{\mathrm{R}}_{\beta}, M^{\mathrm{E}}, M^{\mathrm{R}})$ vary. For each parameter, the first-order ($\mathcal{S}_i$) and total-order ($\mathcal{S}_{T_i}$) sensitivity indices are illustrated using bar charts (blue bars: $\mathcal{S}_i$, orange bars: $\mathcal{S}_{T_i}$). Results for parameters that have smaller effects than the dummy variable ($\hat{k}_{-\beta}, \hat{k}_{-\alpha\beta}, \hat{k}_{-\beta\alpha}, \hat{I}^{\mathrm{E}}, n^{\mathrm{E}}_{\alpha,\mathrm{TOT}}, n^{\mathrm{R}}_{\alpha,\mathrm{TOT}}, M^{\mathrm{E}}, M^{\mathrm{R}}$) are not shown. Number of search curves = 5; number of samples = 65. The parameter ranges used are summarized in Table 5.9.

Parameter	Expression	Value
$\hat{P}$	$\hat{P} = \frac{\overline{\tau}}{\overline{N_L}} P$	$[10^{-4}, 100]$
λ	$\sqrt{\overline{\tau}\Lambda}$	$[1.414 \times 10^{-3}, 0.03795]$ Half life: [2 min, 1 day]
$\hat{k}_\alpha$	$\overline{\tau}\overline{N_L}k_\alpha$	1.710×10^{-6}
$\hat{k}_{-\alpha}$	$\overline{\tau}k_{-\alpha}$	Varied 1000 fold from 0.0745
$\hat{k}_\beta$	$\overline{\tau}\overline{N_L}k_\beta$	6.13×10^{-8}
$\hat{k}_{-\beta}$	$\overline{\tau}k_{-\beta}$	Varied 1000 fold from 6.25×10^{-5}
$\hat{k}_{\alpha\beta}$	$\overline{\tau}\overline{N_\alpha}k_{\alpha\beta}$	0.75
$\hat{k}_{-\alpha\beta}$	$\overline{\tau}k_{-\alpha\beta}$	Varied 1000 fold from 5.75×10^{-5}
$\hat{k}_{\beta\alpha}$	$\overline{\tau}\overline{N_\alpha}k_{\beta\alpha}$	15
$\hat{k}_{-\beta\alpha}$	$\overline{\tau}k_{-\beta\alpha}$	Varied 1000 fold from 0.15
$\hat{I}^{\mathrm{E}}$	$\overline{\tau}I^{\mathrm{E}}$	Varied 10 fold from 2.75×10^{-4}
$\hat{I}^{\mathrm{R}}$	$\overline{\tau}I^{\mathrm{R}}$	Varied 10 fold from 2.75×10^{-4}
$n^{\mathrm{E}}_{\alpha,\mathrm{TOT}}$	$\frac{N^{\mathrm{E}}_{\alpha,\mathrm{TOT}}}{\overline{N_\alpha}}$	$[0.1, 1]$
$n^{\mathrm{R}}_{\alpha,\mathrm{TOT}}$	$\frac{N^{\mathrm{R}}_{\alpha,\mathrm{TOT}}}{\overline{N_\alpha}}$	$[1, 10]$
$n^{\mathrm{E}}_{\beta,*}$	$\frac{N^{\mathrm{E}}_{\beta,*}}{\overline{N_\alpha}}$	$[0.1, 1]$
$n^{\mathrm{R}}_{\beta,*}$	$\frac{N^{\mathrm{R}}_{\beta,*}}{\overline{N_\alpha}}$	$[0.01, 0.1]$
$\hat{G}^{\mathrm{E}}_\beta$	$\overline{\tau}G^{\mathrm{E}}_\beta$	$[10^{-5}, 0.1]$
$\hat{G}^{\mathrm{R}}_\beta$	$\overline{\tau}G^{\mathrm{R}}_\beta$	$[10^{-5}, 0.1]$
M^{E}		$[10^4, 10^7]$
M^{R}		$[10^4, 10^7]$
$\hat{F}$	$\frac{A}{V}\frac{\overline{N_\alpha}}{\overline{N_L}}$	1.287×10^{-4} ($V = 200$ μL)

Table 5.9: The parameter ranges used in eFAST to study the competition model with full binding kinetics.



(a) $\mathcal{S}_i$. (b) $\mathcal{S}_{T_i}$.

Figure 5.4: Results of global sensitivity analysis for different values of the rate of supply of IL-2 to system ($\hat{P} = 10^{-4}, 10^{-2}, 10^{0}, 10^{2}$). For each parameter, the first-order ($\mathcal{S}_i$) and total-order ($\mathcal{S}_{T_i}$) sensitivity indices are plotted in solid and dashed lines respectively, with the colors of the lines corresponding to parameters indicated in the legend. Results for the 5 parameters with highest sensitivity indexes are presented. Number of search curves = 3; number of samples = 65. The parameter ranges used are summarized in Table 5.9.

5.4 Discussion

In this chapter, we shifted focus from the cell scale to the population scale in which effector and regulatory cells compete for a shared, well-mixed IL-2 pool. We aimed to pinpoint parameters that most strongly impact competition between effector and regulatory T cells for IL-2, with the goal of identifying therapeutic targets that could shift the balance towards immunoactivation or immunosuppression and to highlight where new data are needed to tighten model predictions.

We first constructed three idealised models that focus on the α chain. In Model I, we incorporated IL-2 production, decay and internalisation; Model II is a reduction of Model I, in which internalisation of IL-2 is neglected; in Model III, IL-2 is dosed from the initial conditions and IL-2 production, decay and internalisation are neglected. For Model I, steady state analysis revealed that the cell type with a lower internalisation rate of the [IL-2 : α] complex exhibits a higher proportion of bound α chains especially when the IL-2 production rate is low, tipping the balance toward immunoactivation ($\hat{I}^{\mathrm{E}} < \hat{I}^{\mathrm{R}}$) or immunosuppression ($\hat{I}^{\mathrm{E}} > \hat{I}^{\mathrm{R}}$). For Models II and III, while the occupancy fraction of the α chains is identical for effector and regulatory T cells, the higher surface density of α chains on regulatory T cells results in a larger absolute number of [IL-2 : α] complexes on this cell type. These results show that regulatory T cells retain a competitive advantage through their greater availability of α chains, while differential internalisation can modulate the degree and direction of this competitive bias.

We then formulated the competition model, incorporating α, β and γ chains (assuming β/γ dimers). Local and global sensitivity analyses identified model parameters that strongly influence competition between the two cell types and showed how changes in those parameters tilt the competition in a desired direction. From the local sensitivity analysis, we conclude that preferential stimulation shifts with IL-2 availability. Our model reproduces and mechanistically explains this behaviour: when IL-2 levels are low, regulatory T cells are preferentially stimulated because their abundant α-chains enable efficient capture of scarce ligand, whereas at higher IL-2 levels the balance shifts towards effector T cells as the availability of β chains becomes the limiting factor. This interpretation is consistent with the single-cell results in Chapter 4, where regulatory T cells were shown to rely predominantly on α-chain-mediated capture, while effector T cells increasingly exploit the [IL-2 : β] route as IL-2 availability increases. We also predict that increasing $\hat{k}_{-\alpha L}$ favors IL-2 stimulation of effector T cells, and also that increasing the availability of β chains for effector

T cells (increasing $n^{\mathrm{E}}_{\beta,*}$) or for regulatory T cells (increasing $n^{\mathrm{R}}_{\beta,*}$ or $\hat{G}^{\mathrm{R}}_{\beta}$, decreasing $\hat{I}^{\mathrm{R}}$) respectively induces the preferential stimulation of effector T cells or regulatory T cells.

From global sensitivity analysis, we conclude that the synthesis rate of the β chains for regulatory T cells ($\hat{G}^{\mathrm{R}}_{\beta}$) is the most influential parameter. Because $\hat{G}^{\mathrm{R}}_{\beta}$ is weakly constrained due to lack of data, tightening its confidence interval by performing relevant experiments should be a priority for the model to achieve reliable predictive accuracy. Altering the IL-2-α chain dissociation rate (but not the other unbinding rates) is predicted to be a potential target for intervention under conditions of limited IL-2 availability, such as low-dose IL-2 administration or weak endogenous IL-2 production. In this regime, signalling is sensitive to α-chain-mediated IL-2 capture. Modifying the interaction between IL-2 and α chains can alter how the available ligand is distributed between effector and regulatory T cells, thereby shifting the relative abundance of signalling complexes formed in the two cell types.

Taken together, the results of this chapter show that, at the population level, competition for a shared IL-2 pool is shaped not only by receptor abundance but also by the kinetic processes governing ligand capture, retention and signalling-complex formation in each cell type. While this is consistent with the single-cell findings in Chapter 4, the new insight gained in this chapter is that these mechanisms translate into a competitive balance between effector and regulatory T cells that depends on the availability of a shared cytokine resource and can shift as IL-2 levels vary. In particular, this chapter identifies which parameters most strongly control this population-level competition, thereby clarifying which biological processes are most relevant for tilting the balance towards immunoactivation or immunosuppression. These findings provide a foundation for understanding IL-2-mediated competition in heterogeneous T-cell populations and motivate future work to determine whether spatial effects, neglected here under the well-mixed assumption, can also influence competition at the population level.

Chapter 6

Discussion

6.1 Summary of results

In this thesis, we developed a mechanistic modelling framework that links IL-2 availability and receptor stoichiometry to cell type-specific stimulation. We demonstrated how this framework can be used to (i) determine when spatial modelling is necessary, (ii) explain dose-dependent preferential stimulation and (iii) identify parameters and intervention points that most strongly influence competition between effector and regulatory populations. Across Chapters 2–5, we achieved these aims by connecting spatially-resolved models of binding to single cells, related ODE approximations and population-level competition models. Further by combining analysis, identifiability and sensitivity methods, we showed how the mechanistic structure of the models can be translated into insights that can inform model selection, parameter estimation and the design of IL-2-based therapeutic strategies.

In Chapter 2, we developed and analysed a 1D, radially symmetric spatial PDE model capturing the initial binding of IL-2 with α chains on the membrane of a single T cell. The model describes the spatial distribution of IL-2 in the bulk and treats the α chain and the [IL-2:α] complex as uniform, surface-averaged membrane concentrations. We used a variety of techniques including steady state analysis and numerical simulations to investigate the model. We also performed global parameter sensitivity analysis including Extended Fourier amplitude sensitivity testing (eFAST) and Sobol sensitivity analysis to examine the importance of bulk spatial effects (spatial heterogeneity of IL-2 and its changes with cell density) and identify those model features, including IL-2 levels, the availability of α chains and cell density, that primarily impact the temporal dynamics and steady state levels of IL-2 bound to α chains. We concluded that the density of bound α chains is insensitive to spatial constraints, providing a strong rationale for non-spatial approximations. In Chapter

3, we developed and analysed two distinct ODE models, a quasi-steady state model (assuming the concentration of IL-2 is at its quasi-steady state) and a phenomenological model. We investigated the structural and practical identifiability of the two simpler ODE models to guide experimental design and data collection to calibrate them. We identified conditions under which the simpler ODE models can (and cannot) be used to describe the steady-state behaviour and full system dynamics of the spatial model. We found that for models that capture IL-2 binding to α chains on the membrane of a single T cell, whether to use one of the simpler ODE models or retain a spatial formulation depends on the specific research question. If the primary focus is on long-term receptor occupancy, the phenomenological ODE model may be sufficient. If the initial transients in the dynamics are important, such as when examining dosing strategies, spatial effects need to be preserved. The quasi-steady state model provides an accurate approximation of the 1D PDE model when the domain size is small or when the initial conditions reside near the quasi-steady manifold. In these regimes, diffusion-mediated equilibration of the IL-2 field is sufficiently rapid relative to the binding kinetics, allowing for a valid separation of timescales. The identifiability analysis provides a rigorous roadmap for experimental calibration by defining the observational requirements for parameter structural identifiability and the sampling and replication strategies required to ensure robust parameter recovery under practical, less-than-ideal conditions.

In Chapter 4, we extended the 1D PDE model to incorporate β and γ chains (treated as effective β/γ dimers), providing a mechanistic basis for the dose-dependent selectivity observed across different types of T cells [3]. We evaluated simplified binding-kinetic assumptions commonly used in existing mathematical models [27, 45, 95]. We performed eFAST and Sobol global sensitivity analysis to investigate the factors that most significantly influence the ability of IL-2 to stimulate downstream signalling for different types of T cells. Our simulation results suggested that at low IL-2 levels, α chain-mediated capture drives the preferential stimulation of regulatory T cells. At intermediate IL-2 levels, the availability of β chains becomes the rate-limiting factor, leading to the preferential stimulation of effector T cells with higher β chain expression. Memory T cells initiate a response at high IL-2 levels as a consequence of their minimal α-chain expression. Analysis of the receptor assembly pathways revealed the binding between α chains and [IL-2 : β] complexes can be neglected without loss of accuracy, as can the binding between IL-2 and β chains when IL-2 levels are sufficiently small to ensure that the [IL-2 : α : β] complex is the dominant signalling complex formed. Global sensitivity analysis identified the

dominant determinants of steady-state signalling across different types of T cells and IL-2 regimes. Notably, from a therapeutic engineering perspective, the dissociation rate of IL-2 and α chain emerged as the primary kinetic parameter for modulating signalling output, whereas the other binding off rates exhibited negligible effects. This suggests that engineering IL-2 variants with modified α-chain affinity provides the most effective mechanism for fine-tuning signalling responses.

In Chapter 5, we shifted the focus from the individual cell-scale to a population perspective in which effector and regulatory T cells compete for a shared, well-mixed IL-2 pool. We first constructed three highly idealised models that focused on the initial binding of IL-2 to α chains to examine how the differential α chain expression levels by effector and regulatory T cells dictated the allocation of IL-2. We then introduced a spatially well-mixed mathematical model incorporating α, β and γ chains (assuming β/γ dimers) which we used to investigate how competition between effector and regulatory T cells affects the response of a heterogeneous population of T cells to stimulation with IL-2. We performed local and global sensitivity analysis to identify parameters that strongly influence competition between the two cell types and examined how changes in those parameters tilt the competition in a desired direction. From global sensitivity analysis, we concluded that the synthesis rate of the β chains for regulatory T cells is the most influential parameter that tilts the IL-2 competition between effector and regulatory T cells. Because this parameter is currently weakly constrained due to lack of data in the literature, tightening its confidence interval by performing relevant experiments should be a priority for the model to achieve reliable predictive accuracy. Altering the IL-2-α chain dissociation rate (but not the other unbinding rates) is predicted to be a potential target for intervention when the production rate of IL-2 is low. From local sensitivity analysis, we concluded that preferential stimulation is predicted to reverse from regulatory T cells to effector T cells as IL-2 levels increase, which is a long-appreciated experimental observation. We also predicted that increasing IL-2-α chain dissociation rate favors IL-2 stimulation of effector T cells, and also that increasing the availability of β chains for effector T cells or for regulatory T cells respectively by changing related parameters induces the preferential stimulation of effector T cells or regulatory T cells.

6.2 Novelty and contributions

The novelty of this thesis lies in the model development, in the criteria derived for choosing between the models and in the immunological understanding that follows.

Model development and relation to existing work. Existing IL-2 models are typically either well-mixed ODE frameworks for receptor activation and population dynamics or spatial PDE descriptions of cytokine diffusion and capture. The contribution of this thesis is to extend existing modelling by integrating these viewpoints into a single framework and to use the spatial model as a reference for assessing the accuracy and limitations of related ODE descriptions. Our study is the first to establish practical criteria for deciding when a well-mixed ODE model can faithfully substitute for a spatially resolved model of IL-2 binding to α chains on a single T cell. Our work suggests that model choice should be driven by the timescale and the research question of interest, not by a blanket preference for spatial or non-spatial modelling. Through theoretical ablation of the IL-2 receptor kinetics, we have shown which reactions can be omitted without loss of accuracy and which reactions are indispensable. These rules for different cell types provide the first blueprint for streamlining IL-2 signalling models while preserving predictive fidelity.

Implications for IL-2-based therapeutics. Our work supports a mechanistic view of how IL-2 engineering and dosing can bias responses towards regulatory or effector T cells — towards immunoactivation in cancer and chronic infection or towards immunosuppression in autoimmunity and transplantation. The novelty here is twofold: first, the dose-dependent preferential stimulation of different types of T cells is obtained from a spatial model at the single-cell scale, in which receptor binding is coupled to the diffusion of IL-2 in the extracellular space, rather than from a model in which IL-2 is assumed to be spatially uniform; second, global sensitivity analysis is applied for the first time to models of IL-2 binding to its receptors, pinpointing the parameters that most strongly shift the balance of cell-type stimulation and the experimental measurements that would most improve the model predictions. In low-dose regimes, α chain-mediated capture dominates and favours regulatory T cells; at intermediate doses, β-subunit availability becomes increasingly limiting for regulatory cells and effector stimulation becomes competitive; at high doses, multiple T cell types can be strongly activated, but such regimes are often constrained by toxicity. A consistent finding across the single-cell and population-level models is that the IL-2–α chain dissociation rate is a particularly influential kinetic lever, whereas several other dissociation parameters contribute comparatively little within the explored ranges. This aligns with current IL-2 engineering strategies that tune receptor bias, including α chain-dependent IL-2 muteins designed to preferentially expand regulatory T cells (e.g. CUG252 [49]; efavaleukin alfa/AMG 592 [88]), and IL-2 variants engineered to

reduce α chain engagement while promoting $\beta\gamma$-mediated activation of $CD8^+$ cytotoxic T cells and NK cells (e.g. SAR-444245, formerly THOR-707 [57]; nemvaleukin alfa/ALKS 4230 [89]; and the long-acting IL-2 superkine MDNA11 [63]). The present framework therefore provides a quantitative basis for evaluating how receptor-biasing designs and dosing strategies shift dose-response behaviour and competitive outcomes across T-cell types.

Broader applicability. Although the thesis focuses on IL-2, the modelling approach is readily transferable to other cytokines that signal through related receptor architectures, particularly members of the common γ-chain cytokine family, such as IL-7, IL-15 and IL-21 [12, 37, 53, 64]. More broadly, the strategy of combining spatial single-cell descriptions, reduced ODE approximations and population-level competition provides a general template for analysing how ligand transport, receptor stoichiometry and competition shape selective signalling in immunological systems.

6.3 Limitations and future work

Several assumptions constrain the interpretation of the results and delineate natural directions for extension.

Identifiability and biological robustness. The requirement that model parameters be identifiable is in tension with the robustness of biological processes, and the distinction between structural and practical identifiability matters in reconciling the two. For ODE models, structural identifiability is an algebraic property of the state equations and the specified output map, and carries no implication about the sensitivity of the system it represents. Practical identifiability does: a parameter can be estimated from finite, noisy data only if the observed output responds appreciably to it, while biological signalling networks typically maintain stable qualitative behaviour despite variation in the underlying rates [5, 41]. While this tension cannot be removed, it is a partial one, since a model may be robust in its qualitative behaviour while remaining identifiable in the parameters that set the quantitative detail. This is the case for the framework developed in this thesis. The global sensitivity analyses sample parameters across wide ranges rather than perturbing them locally, and the reversal of preferential stimulation from regulatory to effector T cells persists throughout. This reversal follows from the relative expression of α chains and β/γ dimers by the two cell types, rather than from particular values of the rate constants; the

parameters identified as influential affect only the quantitative details, namely where the crossover occurs and how sharply.

The mapping from receptor occupancy to signalling output. Throughout Chapters 4 and 5, the steady-state density of complexes containing a β/γ dimer is used as a measure of the signalling output of a cell. Since our conclusions are drawn at steady state, it makes no difference whether this density or its integral over time is taken as the measure. A more consequential assumption concerns the relationship between this measure and the functional response of a cell, such as proliferation or survival. We do not model this response, and so leave the form of the relationship unspecified. The comparisons on which our main conclusions rest are relative rather than absolute: which cell type forms more signalling complexes at a given IL-2 concentration, and how that ordering changes as IL-2 availability varies. Provided the functional response is strictly increasing in the density of signalling complexes, this ordering is preserved, and the reversal of preferential stimulation from regulatory to effector T cells is unaffected. Thresholds and plateaus, however, would introduce flat regimes where the strict ordering fails to hold: below a threshold neither cell type responds, while within a plateau both respond maximally. In either case, the predicted difference in signalling complex formation produces no functional distinction. The predicted reversal of preferential stimulation would then be observable only over the range of IL-2 concentrations for which the response is graded. Within this graded range, a threshold would sharpen the transition between regimes, while a plateau would compress differences at high IL-2 levels and draw the signalling balance ratio ρ towards unity. When a threshold or plateau response is expected from experimental data, steady-state signalling complex density should not serve as a direct proxy for functional output. The model output should instead be passed through a phenomenological transfer function, such as a sigmoidal Hill curve calibrated against dose-response assays, or the receptor model should be coupled to an explicit downstream signalling module (e.g. a JAK/STAT pathway culminating in STAT5 activation). The latter approach would allow activation thresholds and saturation limits to emerge directly from the represented biochemistry rather than being imposed.

Parameter consistency and quantitative calibration. A central limitation is that parameter values are assembled from diverse sources and experimental contexts.

While this is appropriate for establishing mechanistic principles and exploring qualitative regimes, quantitative prediction for a particular biological system would require a consistent dataset for a single cell line (or well-defined experimental preparation), ideally measured under matched conditions. Thus, a key future step is end-to-end calibration of the receptor-kinetic and competition models to a coherent experimental dataset, so that model predictions can be interpreted quantitatively in a specific setting relevant to therapy design.

Qualitative agreement with existing data and required model extensions. Although the models developed here have not been calibrated against a dataset, several of their predictions admit qualitative comparison with published measurements. Chapters 4 and 5 predict that preferential stimulation shifts from regulatory to effector T cells as IL-2 availability increases; this is consistent with dose-resolved measurements in co-cultured T cell populations [11, 27]. Such comparisons are limited by a mismatch between the quantities produced by the models' output and those reported by experimental assays: predictions are expressed as the density of signalling complexes, whereas the measurements report STAT5 phosphorylation. The mismatch does not preclude all quantitative comparison. Provided that pSTAT5 is a monotonic function of the density of signalling complexes, the relative ordering of the dose-response curves for the different T cell types, as well as the direction and relative magnitude of the shift in half-maximal response between them, may be compared with model predictions without explicitly representing the intervening cascade. Quantitative use of such data would require extending the model so that occupied receptors drive an explicit downstream module (e.g. a JAK/STAT pathway culminating in STAT5 activation), so that predicted signalling complex densities may be related to measured pSTAT5 levels directly.

Data requirements and generation techniques. The models developed here are formulated in terms of the concentration of free IL-2 and the surface densities of free and occupied α chains and β/γ dimers. Calibrating the unextended models rests on measurements of these state variables and of the rates governing their interconversion. These experimental measurements may be obtained from a number of established techniques, each reporting a different subset of the model variables:

- **Binding rate constants.** Surface plasmon resonance (SPR) quantifies the binding of free IL-2 to receptor chains immobilised on a sensor chip. Sensorgrams record local refractive index changes near the chip surface, which serve as

a real-time proxy for the concentration of bound IL-2 as a function of time. Association and dissociation rate constants can then be inferred by fitting binding models to sensorgrams collected across a range of IL-2 concentrations [34].

- **Average IL-2 concentration:** Enzyme-linked immunosorbent assay (ELISA) measures free cytokine concentrations via specific antibody binding; when applied to cell-free supernatants sampled at successive time points, it yields a time-course trajectory of the volume-averaged extracellular IL-2 concentration [26].

- **Spatial distribution of IL-2.** Fluorescence microscopy resolves the distribution of labelled IL-2 in the vicinity of individual T cells via fluorophore-probe binding, and absolute concentrations may be recovered by calibration, providing spatial data relevant to the models in Chapters 2 and 4 [36].

- **Receptor densities and bound IL-2.** Multicolour flow cytometry uses fluorophore-conjugated antibodies and labelled cytokines to quantify, at single-cell resolution across distinct cell subsets, the surface densities of α chains and β/γ dimers and the amount of IL-2 bound to them [1, 32]. Calibration against beads of known antibody-binding capacity converts the measured fluorescence intensity into receptor numbers per cell [81]. Sampling at successive time points gives the trajectories of receptor expression and bound IL-2.

Which of these observables are required, in what combination and at what sampling times, and whether they must be acquired within a single experiment or assembled from separate ones, can be determined by the structural and practical identifiability of the model under consideration.

Downstream signalling and feedback. Throughout the thesis, outputs are defined primarily in terms of receptor occupancy and signalling-competent complex formation rather than explicit intracellular signal transduction. A natural extension is to couple surface binding to a module for downstream signalling and feedback, so that predictions address function rather than receptor occupancy alone. In such a framework, occupied IL-2 receptors would drive a minimal downstream signalling module (e.g. a JAK/STAT pathway culminating in STAT5 activation) and transcriptional programmes. In this setting, two feedback loops merit explicit inclusion: (i) a negative feedback loop in effector T cells in which IL-2 signalling induces the transcription of B lymphocyte-induced maturation protein 1 (Blimp1), encoded by the

gene Prdm1, which represses IL-2 production and reduces the cytokine supply; and (ii) a positive loop, present in multiple T cell types, in which IL-2 signalling upregulates α chains, increasing receptor availability and promoting further IL-2 capture and consumption [3]. Incorporating these feedback loops would allow direct comparison with functional readouts such as pSTAT5 and would enable mechanistic investigation of how signalling-dependent regulation reshapes dose response and competition.

Spatial idealisations at the single-cell scale. The spatial models assume spherical symmetry and treat membrane species as spatially well mixed (surface-averaged concentrations), thus neglecting lateral receptor transport, clustering and asymmetric stimulation. This approximation is reasonable when extracellular IL-2 exposure is approximately uniform and lateral mixing on the membrane is fast relative to binding and trafficking. However, in settings with spatially localised stimulation (e.g. synaptic contacts) or receptor microdomain formation, lateral heterogeneity could influence local capture, binding pathways and effective uptake. A future extension is to add a surface reaction-diffusion description for receptor species on the membrane, enabling systematic assessment of when membrane heterogeneity alters IL-2 capture, complex formation or the kinetic parameters inferred from data.

Receptor architecture and subunit availability. In Chapter 4 and Chapter 5, β and γ chains were treated as effective β/γ dimers, corresponding to the assumption that the common γ chain is not limiting. While this is a widely used simplification, it may fail in regimes where γ chain availability becomes limiting or where competition for γ chains among cytokines that share the common γ chain (e.g. IL-7 and IL-15) is relevant. A natural extension is to model β and γ chains as distinct species with explicit assembly into signalling complexes, which would allow the framework to identify when the dimer approximation remains valid and to explore regimes in which γ chain limitation reshapes subset selectivity.

Population-level simplifications and heterogeneity. The population models treat the extracellular milieu as well mixed and assume that all cells of a given phenotype are identical. These assumptions facilitate mechanistic interpretation and sensitivity analysis but neglect spatial organisation within tissues and heterogeneity in receptor expression, activation state and trafficking. Extensions that incorporate distributions of receptor availability and/or structured microenvironments (e.g. multiple compartments or spatially explicit multi-cell configurations) would allow closer

connection to heterogeneous experimental systems and could quantify how shielding, clustering or tissue architecture modulates competition.

Towards QSP models and cross-species comparison. Extending the present mechanistic framework to a quantitative systems pharmacology (QSP) model raises challenges in scale, compartmental structure and parameter transferability. A QSP formulation would need to couple receptor-level binding and competition to whole-body pharmacokinetics, including IL-2 distribution and clearance across relevant compartments (e.g. blood and tissues), explicit dosing regimens and tissue distribution/penetration that determines local cytokine exposure. It would also require organ- and subset-specific information on cell densities and receptor expression to link local signalling to systemic outcomes. Cross-species translation introduces further uncertainty, since receptor abundances and cytokine clearance can differ between preclinical models and humans, and these differences may shift dose-response behaviour and subset selectivity. Thus, the models developed in this thesis are best viewed as mechanistic building blocks and design principles that can be incorporated into larger PK/PD frameworks once appropriate species- and context-matched data are available.

Taken together, this thesis develops a mechanistic modelling framework for IL-2 signalling that links spatial single-cell binding, simpler ODE descriptions and population-level competition. Across Chapters 2–5, it identifies when spatial modelling is necessary, explains dose-dependent preferential stimulation across different types of T cells, and determines the parameters and mechanisms that govern competition between effector and regulatory T cells. These results provide a basis for model selection, experimental design and the development of IL-2-based therapeutics.

Bibliography

[1] A. Adan, G. Alizada, Y. Kiraz, Y. Baran, and A. Nalbant. Flow cytometry: basic principles and applications. *Critical Reviews in Biotechnology*, 37(2):163–176, 2016.

[2] I. F. Amado, J. Berges, R. J. Luther, M. P. Mailhé, S. Garcia, A. Bandeira, C. Weaver, A. Liston, and A. A. Freitas. IL-2 coordinates IL-2-producing and regulatory T cell interplay. *Journal of Experimental Medicine*, 210:2707–2720, 2013.

[3] N. Arenas-Ramirez, J. Woytschak, and O. Boyman. Interleukin-2: biology, design and application. *Trends in Immunology*, 36(12):763–777, 2015.

[4] E. Balsa-Canto, A. A. Alonso, and J. R. Banga. An iterative identification procedure for dynamic modeling of biochemical networks. *BMC Systems Biology*, 4(11), 2010.

[5] N. Barkai and S. Leibler. Robustness in simple biochemical networks. *Nature*, 387(6636):913–917, 1997.

[6] R. Bellman and K. J. Åström. On structural identifiability. *Mathematical Biosciences*, 7(3):329–339, 1970.

[7] G. Bellu, M. P. Saccomani, S. Audoly, and L. D'Angiò. DAISY: a new software tool to test global identifiability of biological and physiological systems. *Computer Methods and Programs in Biomedicine*, 88(1):52–61, 2007.

[8] E. T. Boder and K. D. Wittrup. Optimal screening of surface-displayed polypeptide libraries. *Biotechnology Progress*, 14(1):55–62, 1998.

[9] O. Boyman and J. Sprent. The role of interleukin-2 during homeostasis and activation of the immune system. *Nature Reviews Immunology*, 12(3):180–190, 2012.

[10] A. P. Browning, M. Taşcă, C. Falcó, and R. E. Baker. Structural identifiability analysis of linear reaction–advection–diffusion processes in mathematical biology. *Proceedings of the Royal Society A*, 480:20230911, 2024.

[11] D. Busse, M. de la Rosa, K. Hobiger, K. Thurley, M. Flossdorf, A. Scheffold, and T. Höfer. Competing feedback loops shape IL-2 signaling between helper and regulatory T lymphocytes in cellular microenvironments. *Proceedings of the National Academy of Sciences*, 107(7):3058–3063, 2010.

[12] M. Cai, X. Huang, X. Huang, D. Ju, Y. Z. Zhu, and L. Ye. Research progress of interleukin-15 in cancer immunotherapy. *Frontiers in Pharmacology*, 14:1184703, 2023.

[13] F. Cannavo. Sensitivity analysis for volcanic source modeling quality assessment and model selection. *Computers & Geosciences*, 44:52–59, 2012.

[14] M. Castro and R. J. de Boer. Testing structural identifiability by a simple scaling method. *PLOS Computational Biology*, 16(11):e1008248, 2020.

[15] D. Charych, S. Khalili, V. Dixit, P. Kirk, T. Chang, J. Langowski, W. Rubas, S. K. Doberstein, M. Eldon, U. Hoch, and J. Zalevsky. Modeling the receptor pharmacology, pharmacokinetics, and pharmacodynamics of NKTR-214, a kinetically controlled interleukin-2 (IL2) receptor agonist for cancer immunotherapy. *PLOS ONE*, 12(7):e0179431, 2017.

[16] G. Cheng, A. Yu, and T. R. Malek. T-cell tolerance and the multi-functional role of IL-2R signaling in T-regulatory cells. *Immunological Reviews*, 241(1):63–76, 2011.

[17] O.-T. Chiş, J. R. Banga, and E. Balsa-Canto. GenSSI: a software toolbox for structural identifiability analysis of biological models. *Bioinformatics*, 27(18):2610–2611, 2011.

[18] O.-T. Chiş, J. R. Banga, and E. Balsa-Canto. Structural identifiability of systems biology models: a critical comparison of methods. *PLOS ONE*, 6(11):e27755, 2011.

[19] R. Clynes, C. Key, Y. Ding, L. Li, J. Woo, B. Sadler, J. Kanodia, H. Sun, and R. Zitnik. A novel potency-reduced IL-2 Fc fusion protein selectively expands regulatory T cells: results from a single ascending dose study in healthy adult volunteers. *Annals of the Rheumatic Diseases*, 82:275, 2023.

[20] R. I. Cukier, H. B. Levine, and K. E. Shuler. Nonlinear sensitivity analysis of multiparameter model systems. *Journal of Computational Physics*, 26(1):1–42, 1978.

[21] C. Cunningham-Rundles, L. Mayer, E. Sapira, and L. Mendelsohn. Restoration of immunoglobulin secretion in vitro in common variable immunodeficiency by in vivo treatment with polyethylene glycol-conjugated human recombinant interleukin-2. *Clinical Immunology and Immunopathology*, 64(1):46–56, 1992.

[22] J. H. Donohue and S. A. Rosenberg. The fate of interleukin-2 after in vivo administration. *The Journal of Immunology*, 130(5):2203–2208, 1983.

[23] V. Duprez, V. Cornet, and A. Dautry-Varsat. Down-regulation of high affinity interleukin 2 receptors in a human tumor T cell line. Interleukin 2 increases the rate of surface receptor decay. *Journal of Biological Chemistry*, 263:12860–12865, 1988.

[24] V. Duprez and A. Dautry-Varsat. Receptor-mediated endocytosis of interleukin 2 in a human tumor T cell line. Degradation of interleukin 2 and evidence for the absence of recycling of interleukin receptors. *Journal of Biological Chemistry*, 261(33):15450–15454, 1986.

[25] J. P. Dutcher, D. J. Schwartzentruber, H. L. Kaufman, S. S. Agarwala, A. A. Tarhini, J. N. Lowder, and M. B. Atkins. High dose interleukin-2 (Aldesleukin) – expert consensus on best management practices-2014. *Journal for ImmunoTherapy of Cancer*, 2(1):26, 2014.

[26] E. Engvall and P. Perlmann. Enzyme-linked immunosorbent assay, ELISA. III. Quantitation of specific antibodies by enzyme-labeled anti-immunoglobulin in antigen-coated tubes. *The Journal of Immunology*, 109(1):129–135, 1972.

[27] O. Feinerman, G. Jentsch, K. E. Tkach, J. W. Coward, M. M. Hathorn, M. W. Sneddon, T. Emonet, K. A. Smith, and G. Altan-Bonnet. Single-cell quantification of IL-2 response by effector and regulatory T cells reveals critical plasticity in immune response. *Molecular Systems Biology*, 6:437, 2010.

[28] V. Golubovskaya and L. Wu. Different subsets of T cells, memory, effector functions, and CAR-T immunotherapy. *Cancers*, 8(3):36, 2016.

[29] B. Greene. pde1dM. `https://github.com/wgreene310/pde1dm`, 2023. GitHub software package, compatible with `pdepe` syntax and supporting coupled ODEs.

[30] A. Hemar, A. Subtil, M. Lieb, E. Morelon, R. Hellio, and A. Dautry-Varsat. Endocytosis of interleukin 2 receptors in human T lymphocytes: distinct intracellular localization and fate of the receptor alpha, beta, and gamma chains. *Journal of Cell Biology*, 129(1):55–64, 1995.

[31] T. Höfer, O. Krichevsky, and G. Altan-Bonnet. Competition for IL-2 between regulatory and effector T cells to chisel immune responses. *Frontiers in Immunology*, 3:268, 2012.

[32] S. Hoshino, K. Oshimi, M. Tsudo, M. Miyasaka, M. Teramura, M. Masuda, T. Motoji, and H. Mizoguchi. Flow cytometric analysis of expression of interleukin-2 receptor β chain (p70-75) on various leukemic cells. *Blood*, 76(4):767–774, 1990.

[33] E. Hsu, X. Cao, B. Moon, J. Bae, Z. Sun, Z. Liu, and Y. Fu. A cytokine receptor-masked IL2 prodrug selectively activates tumor-infiltrating lymphocytes for potent antitumor therapy. *Nature Communications*, 12(1), 2021.

[34] S. A. Hunter and J. R. Cochran. Cell-binding assays for determining the affinity of protein-protein interactions: technologies and considerations. *Methods in Enzymology*, 580:21–44, 2016.

[35] J. Huo, Y. Wang, W. Fu, N. Lu, and Z. Liu. The promising immune checkpoint LAG-3 in cancer immunotherapy: from basic research to clinical application. *Frontiers in Immunology*, 13:956090, 2022.

[36] H. Ishikawa-Ankerhold, R. Ankerhold, and G. P. C. Drummen. Advanced fluorescence microscopy techniques—FRAP, FLIP, FLAP, FRET and FLIM. *Molecules*, 17(4):4047–4132, 2012.

[37] G. I. G. Isvoranu and M. C. Chiritoiu-Butnaru. Therapeutic potential of interleukin-21 in cancer. *Frontiers in Immunology*, 15:1369743, 2024.

[38] M. J. W. Jansen. Analysis of variance designs for model output. *Computer Physics Communications*, 117(1–2):35–43, 1999.

[39] X. Jiang, S. Dudzinski, K. E. Beckermann, K. Young, E. McKinley, J. O. McIntyre, J. C. Rathmell, J. Xu, and J. C. Gore. MRI of tumor T cell infiltration in response to checkpoint inhibitor therapy. *Journal for ImmunoTherapy of Cancer*, 8:e000328, 2020.

[40] V. Kalia and S. Sarkar. Regulation of effector and memory CD8 T cell differentiation by IL-2—a balancing act. *Frontiers in Immunology*, 9:2987, 2018.

[41] H. Kitano. Biological robustness. *Nature Reviews Genetics*, 5(11):826–837, 2004.

[42] B. Knoechel, J. G. Lohr, E. Kahn, J. A. Bluestone, and A. K. Abbas. Sequential development of interleukin 2-dependent effector and regulatory T cells in response to endogenous systemic antigen. *Journal of Experimental Medicine*, 202(10):1375–1386, 2005.

[43] J. A. Kovacs, S. Vogel, J. M. Albert, J. Falloon, R. T. Davey, R. E. Walker, M. A. Polis, K. Spooner, J. A. Metcalf, M. Baseler, G. Fyfe, and H. C. Lane. Controlled trial of interleukin-2 infusions in patients infected with the human immunodeficiency virus. *New England Journal of Medicine*, 335:1350–1356, 1996.

[44] C. Kreutz, A. Bangert, M. Schilling, and J. Timmer. An error model for protein quantification. *Bioinformatics*, 23(20):2747–2753, 2007.

[45] K. León, K. García-Martínez, and T. Carmenate. Mathematical models of the impact of IL2 modulation therapies on T cell dynamics. *Frontiers in Immunology*, 4:439, 2013.

[46] S. Létourneau, C. Krieg, G. Pantaleo, and O. Boyman. IL-2- and CD25-dependent immunoregulatory mechanisms in the homeostasis of T-cell subsets. *Journal of Allergy and Clinical Immunology*, 123(4):758–762, 2009.

[47] A. Levin, D. Bates, A. Ring, C. Krieg, J. Lin, L. Su, I. Moraga, M. Raeber, G. Bowman, P. Novick, V. Pande, C. Fathman, O. Boyman, and K. C. Garcia. Exploiting a natural conformational switch to engineer an interleukin-2 "superkine". *Nature*, 484(7395):529–533, 2012.

[48] F. Li, Y. Sun, J. Huang, W. Xu, J. Liu, and Z. Yuan. CD4/CD8+ T cells, DC subsets, Foxp3, and IDO expression are predictive indictors of gastric cancer prognosis. *Cancer Medicine*, 8(17):7330–7344, 2019.

[49] L. Li, M. Grewal, Y. Liu, S. Fang, T. Wang, J. Lu, D. Sun, B. Deng, and S. Ye. OP0316 Emerging best-in-class IL-2 variant highlights Treg-directed therapy for autoimmune disease. *Annals of the Rheumatic Diseases*, 79(Suppl 1):195, 2020.

[50] W. Liao, J. X. Lin, and W. J. Leonard. IL-2 family cytokines: new insights into the complex roles of IL-2 as a broad regulator of T helper cell differentiation. *Current Opinion in Immunology*, 23(5):598–604, 2011.

[51] W. Liao, J. X. Lin, and W. J. Leonard. Interleukin-2 at the crossroads of effector responses, tolerance, and immunotherapy. *Immunity*, 38(1):13–25, 2013.

[52] T. S. Ligon, F. Fröhlich, O. T. Chiş, J. R. Banga, E. Balsa-Canto, and J. Hasenauer. GenSSI 2.0: multi-experiment structural identifiability analysis of SBML models. *Bioinformatics*, 34(8):1421–1423, 2018.

[53] J. X. Lin and W. J. Leonard. The common cytokine receptor γ chain family of cytokines. *Cold Spring Harbor Perspectives in Biology*, 10(9):a028449, 2018.

[54] X. Lin, K. Kang, P. Chen, Z. Zeng, G. Li, W. Xiong, M. Yi, and B. Xiang. Regulatory mechanisms of PD-1/PD-L1 in cancers. *Molecular Cancer*, 23:108, 2024.

[55] S. F. Liparoto, D. G. Myszka, Z. Wu, B. Goldstein, T. M. Laue, and T. L. Ciardelli. Analysis of the role of the interleukin-2 receptor γ chain in ligand binding. *Biochemistry*, 41(8):2543–2551, 2002.

[56] M. T. Lotze, L. W. Frana, S. O. Sharrow, R. J. Robb, and S. A. Rosenberg. In vivo administration of purified human interleukin 2. I. Half-life and immunologic effects of the Jurkat cell line-derived interleukin 2. *The Journal of Immunology*, 134(1):157–166, 1985.

[57] L. Ma, N. V. Acuff, J. L. Ptacin, C. E. Caffaro, K. M. San Jose, H. R. Aerni, R. W. Herman, Y. Pavlova, M. J. Pena, D. B. Chen, et al. SAR-444245, an engineered not-alpha IL-2 leveraging synthetic biology, modulates critical components of the immune system for durable anti-tumoral activity. *The Journal of Immunology*, 214(10):2781–2795, 2025.

[58] A. MacDonald, T. Wu, and C. Hung. Interleukin 2-based fusion proteins for the treatment of cancer. *Journal of Immunology Research*, 2021:7855808, 2021.

[59] S. Marino, I. Hogue, C. Ray, and D. Kirschner. A methodology for performing global uncertainty and sensitivity analysis in systems biology. *Journal of Theoretical Biology*, 254(1):178–196, 2008.

[60] A. Marquis, A. Arnold, C. Dean-Bernhoft, B. E. Carlson, and M. S. Olufsen. Practical identifiability and uncertainty quantification of a pulsatile cardiovascular model. *Mathematical Biosciences*, 304:9–24, 2018.

[61] J. S. Marshall, R. Warrington, W. Watson, and H. L. Kim. An introduction to immunology and immunopathology. *Allergy, Asthma & Clinical Immunology*, 14:49, 2018.

[62] MathWorks. pdepe: solve 1-D parabolic and elliptic PDEs. `https://www.mathworks.com/help/matlab/ref/pdepe.html`, 2026. MATLAB documentation.

[63] R. Merchant, C. Galligan, M. A. Munegowda, L. B. Pearce, P. Lloyd, P. Smith, F. Merchant, and M. D. To. Fine-tuned long-acting interleukin-2 superkine potentiates durable immune responses in mice and non-human primate. *Journal for ImmunoTherapy of Cancer*, 10(1):e003155, 2022.

[64] M. Morre and S. Beq. Interleukin-7 and immune reconstitution in cancer patients: a new paradigm for dramatically increasing overall survival. *Targeted Oncology*, 7(1):55–68, 2012.

[65] P. Murer, B. Brannetti, J. Rondeau, L. Petersen, N. Egli, S. Popp, C. Régnier, K. Richter, A. Katopodis, and C. Huber. Discovery and development of ANV419, an IL-2/anti-IL-2 antibody fusion protein with potent CD8+ T and natural killer cell-stimulating capacity for cancer immunotherapy. *mAbs*, 16(1):2381891, 2024.

[66] B. H. Nelson. IL-2, regulatory T cells, and tolerance. *The Journal of Immunology*, 172(7):3983–3988, 2004.

[67] J. Nie, L. Zhou, W. Tian, and T. Forsthuber. Deep insight into cytokine storm: from pathogenesis to treatment. *Signal Transduction and Targeted Therapy*, 10:112, 2025.

[68] B. T. Orcutt-Jahns, P. C. Emmel, E. M. Snyder, S. D. Taylor, and A. S. Meyer. Multivalent, asymmetric IL-2-Fc fusions show enhanced selectivity for regulatory T cells. *Science Signaling*, 16(807):eadg0699, 2023.

[69] W. Overwijk, M. Tagliaferri, and J. Zalevsky. Engineering IL-2 to give new life to T cell immunotherapy. *Annual Review of Medicine*, 72(1):281–311, 2021.

[70] L. F. Ponce, K. García-Martínez, and K. León. Quantitative contribution of IL2Rγ to the dynamic formation of IL2-IL2R complexes. *PLOS ONE*, 11(5):e0155684, 2016.

[71] A. Quijano-Rubio, M. Bhuiyan, H. Yang, I. Leung, E. Bello, L. Ali, K. Zhangxu, J. Perkins, J. Chun, W. Wang, M. Lajoie, R. Ravichandran, Y. Kuo, S. Dougan, S. Riddell, J. Spangler, M. Dougan, D. Silva, and D. Baker. A split, conditionally active mimetic of IL-2 reduces the toxicity of systemic cytokine therapy. *Nature Biotechnology*, 41(4):532–540, 2022.

[72] M. E. Raeber, D. Sahin, U. Karakus, and O. Boyman. A systematic review of interleukin-2-based immunotherapies in clinical trials for cancer and autoimmune diseases. *eBioMedicine*, 90:104539, 2023.

[73] I. Raphael, S. Nalawade, T. N. Eagar, and T. G. Forsthuber. T cell subsets and their signature cytokines in autoimmune and inflammatory diseases. *Cytokine*, 74(1):5–17, 2015.

[74] D. Rosen, A. Kvarnhammar, B. Laufer, T. Knappe, J. Karlsson, E. Hong, Y. Lee, D. Thakar, L. Zúñiga, K. Bang, S. Sabharwal, K. Uppal, J. Olling, K. Kjærgaard, T. Kurpiers, M. Schnabel, D. Reich, P. Glock, J. Zettler, M. Krusch, A. Bernhard, S. Heinig, V. Konjik, T. Wegge, Y. Hehn, S. Killian, L. Viet, J. Runz, F. Faltinger, M. Tabrizi, K. Abel, V. Breinholt, S. Singel, K. Sprogøe, and J. Punnonen. TransCon IL-2 β/γ: a novel long-acting prodrug with sustained release of an IL-2Rβ/γ-selective IL-2 variant with improved pharmacokinetics and potent activation of cytotoxic immune cells for the treatment of cancer. *Journal for ImmunoTherapy of Cancer*, 10(7):e004991, 2022.

[75] S. A. Rosenberg, M. T. Lotze, L. M. Muul, A. E. Chang, F. P. Avis, S. Leitman, W. M. Linehan, C. N. Robertson, R. E. Lee, J. T. Rubin, C. A. Seipp, C. G. Simpson, and D. E. White. A progress report on the treatment of 157 patients with advanced cancer using lymphokine-activated killer cells and interleukin-2 or high-dose interleukin-2 alone. *New England Journal of Medicine*, 316(15):889–897, 1987.

[76] A. E. Ross and R. R. Pompano. Diffusion of cytokines in live lymph node tissue using microfluidic integrated optical imaging. *Analytica Chimica Acta*, 1000:205–213, 2018.

[77] S. H. Ross and D. A. Cantrell. Signaling and function of interleukin-2 in T lymphocytes. *Annual Review of Immunology*, 36:411–433, 2018.

[78] A. Saltelli. Making best use of model evaluations to compute sensitivity indices. *Computer Physics Communications*, 145(2):280–297, 2002.

[79] A. Saltelli, P. Annoni, I. Azzini, F. Campolongo, M. Ratto, and S. Tarantola. Variance based sensitivity analysis of model output. Design and estimator for the total sensitivity index. *Computer Physics Communications*, 181(2):259–270, 2010.

[80] A. Saltelli, S. Tarantola, and K. P.-S. Chan. A quantitative model-independent method for global sensitivity analysis of model output. *Technometrics*, 41(1):39–56, 1999.

[81] S. Serke, A. van Lessen, and D. Huhn. Quantitative fluorescence flow cytometry: a comparison of the three techniques for direct and indirect immunofluorescence. *Cytometry*, 33(2):179–187, 1998.

[82] A. N. Shouse, K. M. LaPorte, and T. R. Malek. Interleukin-2 signaling in the regulation of T cell biology in autoimmunity and cancer. *Immunity*, 57(3):414–428, 2024.

[83] R. D. Skeel and M. Berzins. A method for the spatial discretization of parabolic equations in one space variable. *SIAM Journal on Scientific and Statistical Computing*, 11(1):1–32, 1990.

[84] K. S. Smigiel, S. Srivastava, J. M. Stolley, and D. J. Campbell. Regulatory T-cell homeostasis: steady-state maintenance and modulation during inflammation. *Immunological Reviews*, 259(1):40–59, 2014.

[85] I. M. Sobol'. Sensitivity estimates for nonlinear mathematical models. *Mathematical Modelling and Computational Experiment*, 1(4):407–414, 1993.

[86] J. Spangler, J. Tomala, V. Luca, K. Jude, S. Dong, A. Ring, P. Votavová, M. Pepper, M. Kovář, and K. C. Garcia. Antibodies to interleukin-2 elicit selective T

cell subset potentiation through distinct conformational mechanisms. *Immunity*, 42(5):815–825, 2015.

[87] A. Taylor, J. Verhagen, K. Blaser, M. Akdis, and C. A. Akdis. Mechanisms of immune suppression by interleukin-10 and transforming growth factor-beta: the role of T regulatory cells. *Immunology*, 117(4):433–442, 2006.

[88] N. Tchao, K. S. Gorski, T. Yuraszeck, S. J. Sohn, K. Ishida, H. Wong, and K. Park. AMG 592 is an investigational IL-2 mutein that induces highly selective expansion of regulatory T cells. *Blood*, 130(Suppl 1):696, 2017.

[89] U. N. Vaishampayan, J. Muzaffar, I. Winer, S. D. Rosen, C. J. Hoimes, A. Chauhan, A. Spreafico, K. D. Lewis, D. S. Bruno, O. Dumas, et al. Nemvaleukin alfa, a modified interleukin-2 cytokine, as monotherapy and with pembrolizumab in patients with advanced solid tumors (ARTISTRY-1). *Journal for ImmunoTherapy of Cancer*, 12(11):e010143, 2024.

[90] J. van der Veeken, A. J. Gonzalez, H. Cho, A. Arvey, S. Hemmers, C. S. Leslie, and A. Y. Rudensky. Memory of inflammation in regulatory T cells. *Cell*, 166(4):977–990, 2016.

[91] A. F. Villaverde and G. Massonis. On testing structural identifiability by a simple scaling method: relying on scaling symmetries can be misleading. *PLOS Computational Biology*, 17(10):e1009032, 2021.

[92] H. M. Wainwright, S. Finsterle, Y. Jung, Q. Zhou, and J. T. Birkholzer. Making sense of global sensitivity analyses. *Computers & Geosciences*, 65:84–94, 2014.

[93] L. S. Walker. Treg and CTLA-4: two intertwining pathways to immune tolerance. *Journal of Autoimmunity*, 45:49–57, 2013.

[94] H. M. Wang and K. A. Smith. The interleukin 2 receptor: functional consequences of its bimolecular structure. *Journal of Experimental Medicine*, 166(4):1055–1069, 1987.

[95] R. S. Waters, J. S. A. Perry, S. Han, B. Bielekova, and T. Gedeon. The effects of interleukin-2 on immune response regulation. *Mathematical Medicine and Biology: A Journal of the IMA*, 35(1):79–119, 2018.

[96] A. M. Weissman, J. B. Harford, P. B. Svetlik, W. L. Leonard, J. M. Depper, T. A. Waldmann, and R. D. Klausner. Only high-affinity receptors for interleukin 2 mediate internalization of ligand. *Proceedings of the National Academy of Sciences*, 83(5):1463–1466, 1986.

[97] J. M. Zhang and J. An. Cytokines, inflammation, and pain. *International Anesthesiology Clinics*, 45(2):27–37, 2007.